

Geology, Structure and Geochemistry of the Mazenod Lake Volcanic Complex

by

Mark Hamilton

Faculty of Graduate Studies
Department of Geology

Submitted in partial fulfillment
of the requirements for the degree of
Master of Science

Brandon University
Brandon, Manitoba, Canada

Copyright © 2017 by Mark Hamilton

Brandon University
FACULTY OF SCIENCE

The undersigned certify that they have read, and recommended to the Senate for acceptance, a **MASTER'S THESIS** entitled:

Geology, Structure, and Geochemistry of the Mazenod Lake IOCG Hydrothermal System

Submitted by: **Mark Hamilton**

In partial fulfillment for the requirements for the degree of

MASTER OF SCIENCE (ENVIRONMENTAL AND LIFE SCIENCES)

Date: December 12, 2017
Month - Day - Year

A. H. Mumin
Supervisor: Dr. A. H. Mumin

Date: Nov 22, 2017
Month - Day - Year

Dr. A. Gulliver
Committee Member: Dr. A. Gulliver

Date: Nov-22-2017
Month - Day - Year

Dr. A. Somarin
Committee Member: Dr. A. Somarin

Date: Nov 22, 2017
Month - Day - Year

Dr. P. Alexandre
External Examiner: Dr. P. Alexandre

Abstract

This study examines the geology, structure, hydrothermal alteration and mineralization from the Mazenod Lake volcanic complex in the Great Bear Magmatic Zone (GBMZ), Northwest Territories, Canada. Field work and geochemical data indicate that the Faber Group volcanic lithology is comprised of pervasively metasomatized, calc-alkaline, intermediate to felsic ignimbrite flows.

Analysis of lineaments derived from a high-resolution satellite image and measured vertical gradient (MVG) aeromagnetic data delineate tectonic blocks defined by strike-slip faults, including two sets of NE-trending right-lateral faults ($\sim N50^{\circ}E$ and $\sim N20E^{\circ}$) and one set of left-lateral NW-oriented ($\sim N30^{\circ}W$) faults. Mass balance and several diagnostic residual alteration indices (RAIs) characterize the nature, intensity and distribution of hydrothermal alteration. Spatial analysis of the RAIs reveals a direct correlation between locally significant structures and centers of intense alteration at Dan Island, Nod Hill and the central Bea area. The geology, structure and pervasive alteration are characteristic of a magmatic-hydrothermal iron oxide copper-gold (MH-IOCG) system.

Keywords: Great Bear Magmatic Zone, Mazenod Lake, Faber Group, IOCG, hydrothermal alteration, metasomatism, mass balance, alteration indices, RAI

Acknowledgements

I would like to acknowledge the very generous support of Dawn Zhu and BFR Copper & Gold for providing the necessary data and funds to make this study possible. Their trust in me is sincerely appreciated, and it is my earnest hope that they succeed in all their exploration endeavors.

Thank you to the editors and fellow geoscientists for instruction and advisement provided in the review and revision process. I would also like to thank fellow geologist colleagues that have contributed to this study by publishing related cited material. The many students and colleagues that provided insight into this investigation are too many to mention but deserve an acknowledgement as well. Without the support of my advisor Dr. Hamid Mumin there is no chance I would have been able to complete a project of this magnitude. I would also like to acknowledge the support of my committee members including Dr. Alireza K. Somarin, Dr. Austin F. Gulliver, the external reviewer Dr. Paul Alexander, and other individuals involved in the defense of this thesis. I would particularly like to recognize the significant contribution of all field mappers, students and contributors that took part in the extensive 2013 field work including: Dr. Hamid Mumin, Scott Ryan, John Shmyr, Kyle Reid, Kevan Bender, Shane Gleeson and Rashid Mumin. This thesis is dedicated to the memory of our camp manager, facilitator and personal friend Howard Stewart. He brought our camp to life with his unfailing enthusiasm and made it a place we all came to consider home. Thank you, Howard.

Table of Contents

Abstract	iii
Acknowledgements	iv
List of Tables	xi
List of Figures	xii
Chapter I: Introduction	1
Location, Physiography and Climate	2
Chapter II: Previous Work in the Mazenod Lake Area	7
Chapter III: Iron Oxide Copper-Gold Deposits	10
Economic Importance	10
Morphology & Structural Controls	13
Spatial & Geologic Context	14
Hydrothermal Alteration	14
(a) <i>Sodic Alteration</i>	17
(b) <i>Iron Oxide Alterations</i>	18
(c) <i>Potassic Alteration</i>	19
(d) <i>Tourmaline Alteration</i>	20
(e) <i>Phyllic and other Hydrolytic Alterations</i>	20
(f) <i>Silicification</i>	21

(g) <i>Other Associated Alteration Effects</i>	21
Genesis	22
Chapter IV: Regional Geology and Tectonic Setting of the GBMZ	28
Structure and Tectonics	32
Chapter V: Geology of the Mazenod Lake Region	36
Local Geologic Setting.....	36
Paleozoic Sediments.....	41
Great Bear Intrusive Rocks	41
(a) <i>Sarah Lake Granite</i>	43
(b) <i>Marian River Batholith</i>	44
Faber Lake Volcanic Rocks	41
(a) <i>Volcanic Sediments</i>	45
(b) <i>Dianne Lake assemblage</i>	45
(c) <i>Lou Lake assemblage</i>	48
(d) <i>Squirrel Lake assemblage</i>	50
(e) <i>Bea Lake assemblage</i>	50
(f) <i>Mazenod Lake assemblage</i>	51
Hydrothermal Alteration	52
(a) <i>Magnetite ± actinolite (MA) alteration</i>	52
(b) <i>Potassic alteration</i>	55

(c) <i>Tourmaline alteration</i>	56
(d) <i>Hematite alteration</i>	56
(e) <i>Phyllic alteration</i>	57
(f) <i>Epidote alteration</i>	57
(g) <i>Silicification</i>	58
Mineralization	58
Chapter VI: Structural Analysis	61
Lineament Definition	61
Methodology	62
(a) <i>Lineament and lineament intersection delineation</i>	62
(b) <i>Analysis of lineament orientations</i>	63
(c) <i>Analysis of the population density</i>	63
Satellite Image.....	62
Aeromagnetic Data.....	62
Digital Elevation Model (DEM)	62
Field Mapping	62
Satellite Image Lineaments	70
Magnetic Lineaments	73
Lineament Density Models	76
(a) <i>Satellite image lineament population density</i>	76

(b) <i>MVG data lineament density</i>	76
(c) <i>MVG data lineament intersections density</i>	79
Chapter VII: Geochemical Data Analysis	81
Filtering Data and Handling Detection Limits	83
Least Altered Representative Samples	84
Geochemical Classification	87
(a) <i>Tectonomagmatic Classification</i>	90
(b) <i>Trace Element Discrimination of Granitic Rocks</i>	90
Element Mobility	90
Mass Balance Analysis	95
Isocons of Mineralized Samples	97
(a) <i>Site 1, Dan Island</i>	97
(b) <i>Site 2, NE of Nod Hill</i>	99
(c) <i>Site 3, Bea area</i>	100
(d) <i>Site 4, Nod Hill</i>	100
Quantitatively Assessing Hydrothermal Alteration	102
(a) <i>Magnetite \pm Actinolite (MA) Alteration</i>	103
(b) <i>Potassic Alteration</i>	105
(c) <i>Tourmaline Alteration</i>	105
(d) <i>Propylitic Alteration</i>	108

(e) <i>Hematite Alteration</i>	108
(f) <i>Silicification</i>	111
Alteration Indices	111
Residual Alteration Indices	115
(a) <i>Sodium Enrichment Index</i>	115
(b) <i>Iron Alteration Index</i>	115
(c) <i>Ca-Fe Alteration Index</i>	120
(d) <i>Potassic Alteration Indices</i>	123
(e) <i>Silica Alteration Index</i>	128
Chapter VIII: Discussion	132
Stratigraphy	133
Structure	134
Hydrothermal Alteration	142
(a) <i>Sodic Alteration</i>	145
(b) <i>Magnetite ± Actinolite (MA) Alteration</i>	145
(c) <i>Potassic Alteration</i>	146
(d) <i>Tourmaline Alteration</i>	146
(e) <i>Hematite Alteration</i>	147
(f) <i>Phyllic Alteration</i>	147
(g) <i>Propylitic Alteration</i>	148

<i>(h) Silicification</i>	148
Residual Alteration Indices (RAIs)	148
Mineralization	150
Implications for Exploration	150
Chapter IX: Conclusions	152
References	157
Appendix I: Petrographic Analysis	175
Appendix II: Formulas	195
Appendix III: Sample Descriptions	197
Appendix IV: Common Indicator Element Concentrations	204
Appendix V: Mass Balance Data	216
Curriculum Vitae	232

List of Tables

TABLE 1. History of work completed within vicinity of Mazenod Lake.....	8
TABLE 2. Defining characteristics of magmatic-hydrothermal IOCGs, modified from Richards and Mumin (2013a, b).....	12
TABLE 3. Adjustments made to values in the geochemical data under the detection limit	83
TABLE 4: Selected least altered representatives of lithology	85
TABLE 5. Residual Alteration Indices (RAIs) applied to the Mazenod Lake region	114
TABLE 6. Dominant faults in the Mazenod Lake region and their estimated horizontal offset	138
TABLE 7. Typical element mobility associated with the some of the most common Mazenod Lake regions hydrothermal alteration types	144
TABLE 8. Hand sample and thin section analysis of selected rocks	177
TABLE 9. SEM analysis of sample 98197	188
TABLE 10. Sample descriptions amalgamated from sample booklet data, field notes and later observations for those samples undergone mass balance analysis in this study	198
TABLE 11. Mass balance data	217

List of Figures

Figure. 1. Regional location of the Mazenod Project, NWT.	5
Figure. 2. Geographic location of the study region within the Northwest Territories.....	6
Figure. 3. Schematic cross-sectional model of a magmatic-hydrothermal system.....	15
Figure. 4. Schematic cross-sectional diagram illustrating the fluid pathways and hydrothermal characteristics for the different IOCG genetic models	24
Figure. 5. The Great Bear Magmatic Zone (GBMZ).....	29
Figure. 6. Stratigraphic column of the Hottah terrane–Great Bear volcano-plutonic continuum .	33
Figure. 7. Tectono-magmatic models for the evolution of the Wopmay Orogen.....	34
Figure. 8. Geology of the Mazenod Lake region	37
Figure. 9. Geology of Mazenod Lake area, NWT.	38
Figure. 10. Geology of Dan Island and surrounding area, Mazenod Lake region, NWT.....	39
Figure. 11. Geology of the Bea area, south of Mazenod Lake, NWT.	40
Figure. 12. Outcrop photographs of selected intrusive rocks discussed in this thesis	42
Figure. 13. Outcrop photographs of volcanic assemblage rocks discussed in this thesis	46
Figure. 14. Outcrop photographs of several different facies and textures of volcanoclastic sediments (VS) that are discussed in this thesis.....	47
Figure. 15. Outcrop photographs of hydrothermal alteration types discussed in this thesis	53
Figure. 16. Geo-eye 1 satellite image of the Mazenod Lake region	64
Figure. 17. Close-up image of Net Ridge, Mazenod Lake region, NWT	65
Figure. 18. Magnetic vertical gradient (MVG) data layered over Geoeye-1 satellite image.....	67
Figure. 19. Structural diagrams compiled from field work measurements.....	68
Figure. 20. Digital elevation data and lake/river outlines on Geoeye-1 satellite image	69

Figure. 21. Mazenod Lake area satellite image lineament interpretation	71
Figure. 22. Lineaments drawn on Net Ridge, Mazenod Lake region, NWT.....	72
Figure. 23. Magnetic vertical gradient (MVG) data lineament interpretation layered over Geoeye-1 satellite image.....	74
Figure. 24. Kernel density model showing the population density of lineaments per square kilometer, derived from the satellite image.	77
Figure. 25. Kernel density model showing the population density of lineaments per square kilometer, derived from the MVG data.....	78
Figure. 26. Kernel density model showing the population density of lineament intersections per square kilometer, derived from the MVG data	80
Figure. 27. Spatial locations of geochemical data points.....	82
Figure. 28. Volcanic rock geochemical discrimination diagrams.....	88
Figure. 29. Geochemical discrimination of rocks from the Mazenod Lake area.....	89
Figure. 30. Granite geochemical discrimination diagrams	91
Figure. 31. Binary diagrams of typical immobile elements and zircon geochemical data	93
Figure. 32. Binary diagrams of major element oxides and zircon geochemical data	94
Figure. 33. Location map showing where lithogeochemical samples originated that have been mass balance analyzed	96
Figs. 34a, b. Isocon diagrams.....	98
Figure. 35a, b. Isocon diagrams	98
Figure. 36a, b. Isocon diagrams	101
Figure. 37a, b. Isocon diagrams	101
Figure. 38. Graph of calculated concentration changes for MA-altered samples.....	104

Figure. 39. Graph of calculated concentration changes for potassic altered	106
Figure. 40. Graph of calculated concentration changes for samples tourmaline altered	107
Figure. 41. Graph of calculated concentration changes for samples propylitic altered.....	109
Figure. 42. Graph of calculated concentration changes for samples hematite altered.....	110
Figure. 43. Graph of calculated concentration changes for samples silicified	112
Figure. 44. Bubble plot map of sodium enrichment intensity.....	116
Figure. 45. Interpolation of sodium enrichment intensity.....	117
Figure. 46. Bubble plot map of iron enrichment intensity.....	118
Figure. 47. Interpolation of iron enrichment intensity	119
Figure. 48. Bubble plot map of Ca-Fe enrichment intensity.....	121
Figure. 49. Interpolation of Ca-Fe enrichment intensity.....	122
Figure. 50. Bubble plot map of potassic alteration intensity	124
Figure. 51. Interpolation of potassium alteration intensity	125
Figure. 52. Bubble plot map of potassic alteration intensity	126
Figure. 53. Interpolation of potassium alteration intensity	127
Figure. 54. Bubble plot map of silica enrichment intensity.....	130
Figure. 55. Interpolation of silica enrichment intensity	131
Figure. 56. Satellite image and aerial phot of Net Ridge giant quartz vein.....	134
Figure. 57. Interpretation of major structures in the Mazenod Lake region	136
Figure. 58. Locations of measurement for estimated lateral displacements of major faults	137
Figure. 59. Map of tectonic blocks shown on MVG data.....	140
Figure. 60. Potassic RAI I contours overlain on Dan Island	149
Figure. 61. Thin section images of selected analyzed samples.....	184

Figure. 62. Backscattered electron microprobe images of selected sites in sample 98197	192
Figure. 63. Distribution of silver concentrations in the Mazenod Lake region	205
Figure. 64. Distribution of arsenic concentrations in the Mazenod Lake region.....	206
Figure. 65. Distribution of gold concentrations in the Mazenod Lake region.....	207
Figure. 66. Distribution of bismuth concentrations in the Mazenod Lake region	208
Figure. 67. Distribution of copper concentrations in the Mazenod Lake region	209
Figure. 68. Distribution of cobalt concentrations in the Mazenod Lake region	210
Figure. 69. Distribution of mercury concentrations in the Mazenod Lake region.....	211
Figure. 70. Distribution of lanthanum concentrations in the Mazenod Lake region	212
Figure. 71. Distribution of molybdenum concentrations in the Mazenod Lake region.....	213
Figure. 72. Distribution of tungsten concentrations in the Mazenod Lake region	214
Figure. 73. Distribution of uranium concentrations in the Mazenod Lake region.....	215

Chapter I: Introduction

This thesis is a geological, geochemical and structural investigation of the Mazenod Lake volcano-plutonic suite, located in the southern Great Bear Magmatic Zone (GBMZ), Northwest Territories (NWT) (Fig. 1). The Mazenod Lake region is an exceptional example of a well-exposed interior system of a magmatic-hydrothermal iron oxide copper-gold (MH-IOCG) complex. This makes it an excellent area for detailed investigations with an aim of gaining an improved understanding of an MH-IOCG type system.

Mazenod Lake is within the southern portion of the GBMZ, between two regionally important IOCG deposits. The Proterozoic NICO gold-cobalt-bismuth-copper deposit is located ~8 km to the southeast and Sue-Dianne copper-gold-silver deposit ~4 km to the north (Goad et al., 2000; Mumin et al., 2010). Both deposits are positioned within the same continental volcanic belt that also includes the Mazenod project area.

Generous support by BFR Copper and Gold Inc. (BFR) and Dawn Zhou, president of BFR, facilitated this work with the provision of research funding, scholarships, geological information, satellite imagery, geophysical and geochemical data. In addition, BFR also provided the opportunity to spend nearly three months at Mazenod Lake with the purpose of carrying out detailed mapping and geological sampling. The fieldwork was carried out by Scott Ryan and John Shmyr, Kyle Reid, Dr. H. Mumin, Rashid Mumin, Shane Gleeson and Mark Hamilton. Fieldwork forms the foundation for subsequent analyses and interpretations presented in this thesis. Compilation, analytical work and interpretations were completed at the Brandon University Laboratory for Applied Research in Resource Geology and the Brandon University Micro-Analytical Facility.

The thesis is presented in 9 chapters, beginning with an introduction and historical outline of work accomplished in the Mazenod Lake area, followed by a synthesis of current knowledge on IOCGs. The next chapters cover the detailed work completed for this project with an in depth look at geology, structure and geochemistry. The final chapters summarize and discuss, then interpret the results of the research. The thesis ends with a set of conclusions and recommendations.

Location, Physiography and Climate

Mazenod Lake is located in the Northwest Territories approximately 185 km to the northwest of Yellowknife (Fig. 1). The lake lies along the drainage path of the Marian River within the Mackenzie District. Nearby communities include Gam'et'i and Wha't'I, which are respectively ~48 km north and ~63 km south of the study area. Both communities are members of the Tłıchō First Nations government, which has title to ~39,000 km² of land between Great Slave Lake and Great Bear Lake, including both surface and subsurface rights (Indian and Northern Affairs Canada, 2003).

Year-round access to this area is limited to float planes or helicopters. During the winter months, the federal government maintains an ice road that runs directly across Mazenod Lake. The Northwest Territories and Tłıchō governments have made some progress with discussions to develop an all-weather road to service the nearby Tłıchō First Nations communities. The planned 94-km road would lead to Gam'et'i to the north of Mazenod Lake and would likely replace portions of the existing ice road. The proposed road would also run within close proximity to Mazenod Lake and the Mazenod project area.

Climate within the study region is generally temperate during the relatively short summer months (average of approximately 18°C in July), and bitterly cold during the winter (average of

approximately -27°C in January, Environment Canada, 2015). This region is within the physiographic division of Canada known as the Canadian Shield, which is generally covered by boreal forest that includes common deciduous and coniferous trees such as spruce, pine, alder, willow and birch. Undergrowth has extensive moss cover in the swampy areas. Labrador tea plants are present throughout most of the study area wherever there is available soil and/or moss cover. Lichen growth on rock is very common although not ubiquitous in large part due to a recent forest fire that removed much of the vegetation from a large portion of the study area.

The study region has a moderate to rugged relief of between 195 to 350 meters above sea level. Mazenod Lake is relatively shallow with few isolated deep areas. Bathymetric mapping performed during field operations indicated a depth of less than 5 feet to greater than 350 feet, and an estimated average of approximately 35 - 40 feet of water.

Outcrops are generally well exposed on islands and terrain surrounding Mazenod Lake. Further from the lake, muskeg and bog become more common, while outcrops become scarce and difficult to access. Approximately 80% of the study area is covered by swamp and water, while approximately 20% contains exposed outcrop. Less than half of the exposed outcrop within the study region has undergone ground-based studies described in this work.

The study area has been divided into two distinct physiographic and geologic zones of interest which are often discussed separately in this thesis (Fig. 2). These zones are referred to as the Mazenod and Bea areas, which comprise the northern two thirds of the project area and the southern zone respectively. Both areas were named after the dominant lakes of their respective regions. A finger of Paleozoic sedimentary cover partially separates these two areas.

The coordinate system used to reference several of the maps displayed in this thesis is UTM (Universal Transverse Mercator) NAD (North American Datum) 1983, zone 11. Some

maps constructed as part of this research also include location reference by Latitude and Longitude. The center of Mazenod Lake is located at geographic coordinates 63°40'N, 117°1'W, while most field work took place in the areas outlined in Figure 2.

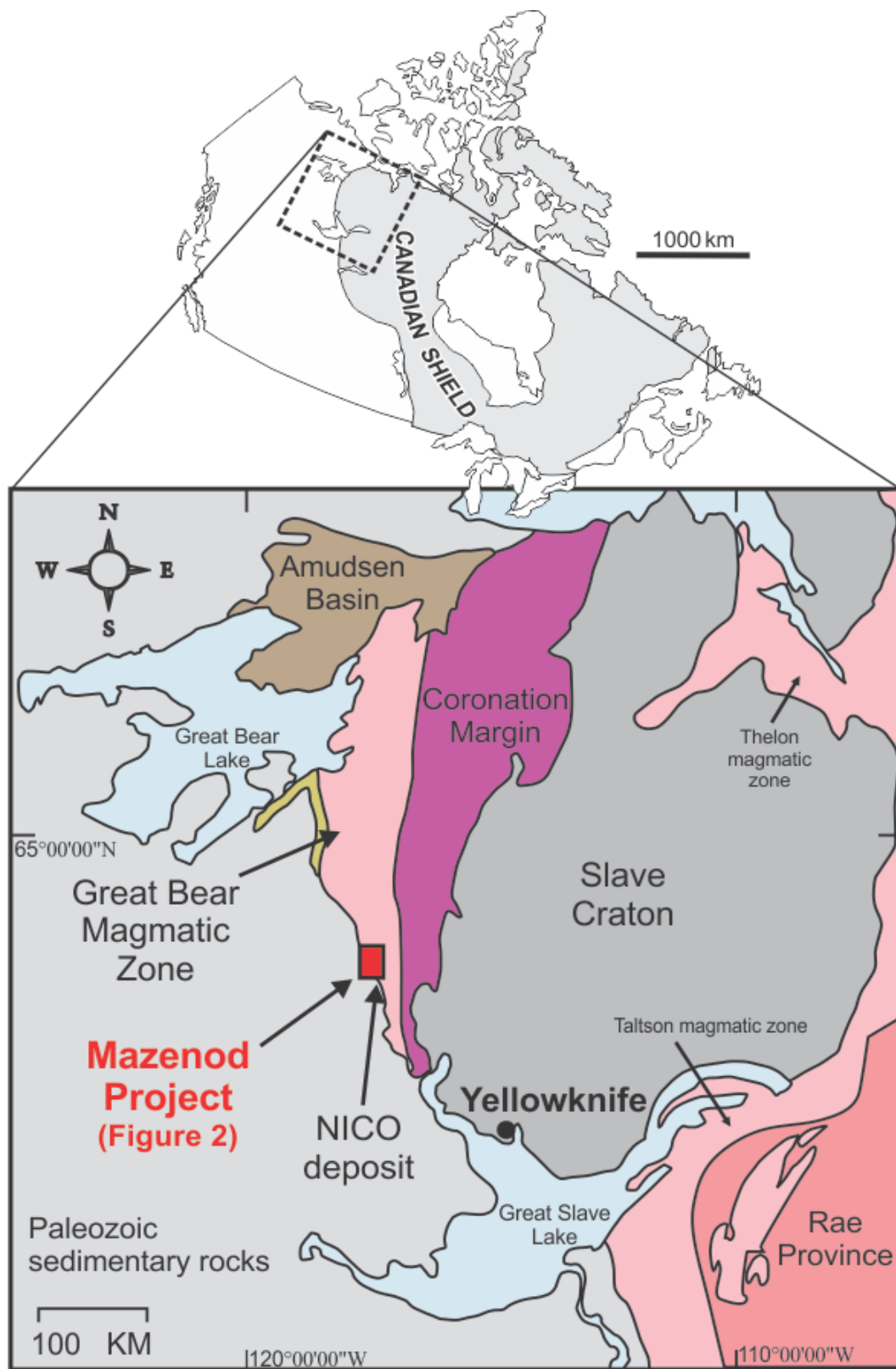


Fig. 1. Regional location of the Mazenod Project, NWT, after Mumin et al. (2014).

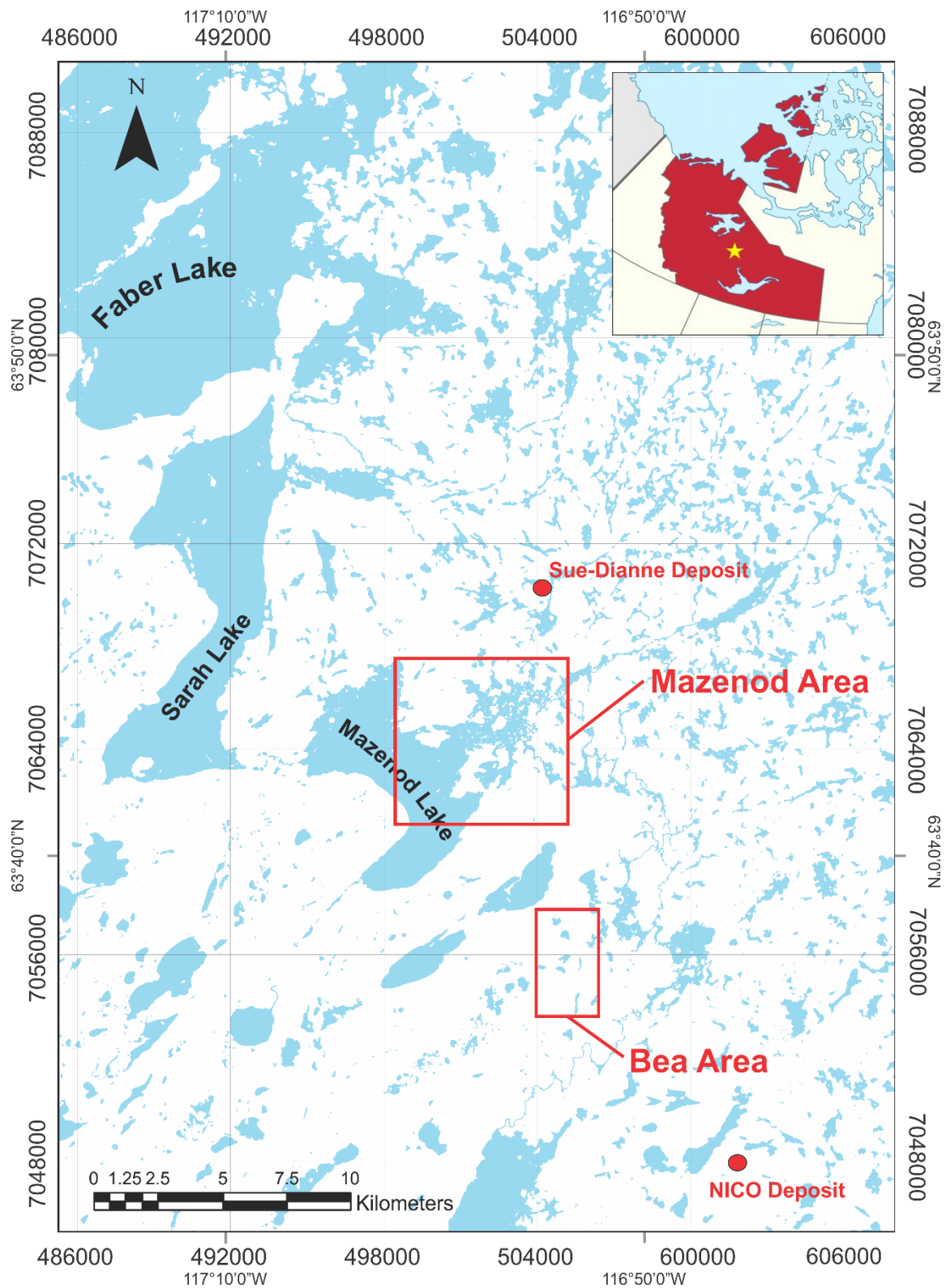


Fig. 2. Geographic location of the study region within the Northwest Territories. Areas where field work took place are highlighted with red squares.

Chapter II: Previous Work in the Mazenod Lake Area

The Geological Survey of Canada (GSC) has conducted numerous studies in the Mazenod Lake area, from reconnaissance mapping by Lord (1942) and McGlynn (1979) to the more recent metallogenic surveys by Sunil Gandhi (Gandhi, 1994; Gandhi et al., 1996; 2001). The most recent work by the GSC was accomplished due in large part to a surge in interest of IOCG deposits that took place in the 90s, a consequence of recognition of the relatively new class of mineral deposits. The studies conducted have resulted in numerous publications including those reviewing the geology at Mazenod Lake and surrounding regions as well as a regional 1:50000-scale map produced by Gandhi (2013).

Despite the work completed by the GSC, the Mazenod Lake area has experienced rather limited exploration. Noranda originally staked a large part of the area surrounding Mazenod Lake in 1974. It has since been explored by several independent companies including the Western Mining Corporation (WMC), Moss Resources in coordination with Xemac Resources, Alberta Star Mining Corporation and Phelps Dodge Corporation of Canada Limited. Independent junior exploration company BFR Copper & Gold is the only exploration company presently performing exploration activities in the area.

Only nine drill holes have been completed within the Mazenod claims, all within a relatively concentrated area near the eastern perimeter of Mazenod Lake. Phelps Dodge drilled the most significant holes, up to 266.7 m, with the best results returning 12 m @ 1525 ppm Cu including 3 m @ 4308 ppm Cu (Kulla, 2004). Highest copper values were hosted in an altered magnetite-rich meta-sediment.

BFR Copper & Gold Inc. acquired claims previously held by Freeport McMoRan in 2011 and has since performed additional exploration at Mazenod. Exploration activities have included

geophysical surveys, geophysical modeling, acquisition of high-resolution satellite imagery, ground reconnaissance, detailed field mapping and a lithogeochemical sampling program. These activities were carried out in preparation for drilling within the Mazenod Lake region.

Industry and government activities related to the exploration of geology and mineral potential within the study region are summarized further in Table 1:

TABLE 1. History of work completed within vicinity of Mazenod Lake

Year	Company / Involved Parties	Activity
1942	Geological Survey of Canada (GSC)	-Reconnaissance mapping by C. S. Lord ¹
1974-81	Noranda	-Diamond drilling for uranium in a quartz vein zone on the east shore of Mazenod Lake -Staking and ground exploration with a focus on the northern part of the property -Exploration at Nod Hill including mapping, ground magnetics, induced polarization (IP), and percussion drilling of 9 holes -Exploration of Dan Island including mapping and ground magnetics ^{1 2}
1979	Geological Survey of Canada (GSC)	Reconnaissance mapping by J. McGlynn
1994	Western Mining Corporation (WMC)	-Staked and completed surface exploration predominantly on the islands to the northeast and stream sediment testing (no anomalies reported) ¹
1994	Geological Survey of Canada (GSC)	-Regional metallogenic survey by S. S. Gandhi
1996	Moss Resources and Xemac Resources	-Property optioned, completed surface exploration and diamond drilling of 4 holes ¹
1996	Geological Survey of Canada (GSC)	-Regional metallogenic survey by S. S. Gandhi

1998	Alberta Star Mining Corporation	-Acquired 60% interest in the property and partially completed mapping, prospecting and ground magnetics of the Bea Lake grid and re-logging of core at the Nod prospect before returning claims to WMC ¹
2001	Geological Survey of Canada (GSC)	-Regional metallogenic survey by S. S. Gandhi ¹
2001-02	Phelps Dodge Corporation of Canada, Limited	-Reconnaissance, prospecting, lithogeochemical and soil sampling and prospect evaluation ¹ -1150 m of diamond drilling (5 drill holes). Program cut short due to budget and weather constraints ²
2011- Present	BFR Copper & Gold Inc.	-Mining leases transferred from Freeport McMoRan Inc. to BFR ³ -Geophysical data remodeling by SJ Geophysics -Historical compilation of previous work by Greg Kulla, P.Geo. -IP-Mag survey on Nod Hill by SJ Geophysics -Site prospecting by BFR geologists and consulting geologist Dr. Hamid Mumin -Fixed wing magnetic gradiometer, radiometric & VLF EM survey flown by Goldak Airborne Surveys -Undergraduate project identifying mineralogy, alteration and their relationships of samples acquired during site prospecting tour -1:2000 scale field mapping and lithogeochemical surveying -M.Sc. thesis performing geology, structure and geochemical compilation, analysis and interpretations

¹(Skanderbeg, 2001); ²(Kulla, 2004); ³(Bender, 2013)

Chapter III: Iron Oxide Copper-Gold Deposits

Hitzman et al. (1992) was the first to discuss IOCGs as a unique class of deposits with their own physical and genetic characteristics. These deposits are hydrothermal in origin and are characterized by enrichments of Fe, Cu \pm Au and abundant (< 15 - 20 wt. %) low-Ti hydrothermal iron oxides. The IOCG group of deposits can also have important concentrations of Fe, Ag, U, Nb, Co or Bi and rare earth elements (REEs) and may contain anomalous amounts of Ba, F, P, W, Se, Hg, Te, Sn, Mo and Y. The substantial economic potential makes IOCG deposits appealing for both research and commercial motives (Hitzman, 2000; Porter, 2000; Williams et al., 2005, 2010; Skirrow, 2010).

Williams (2010) divided IOCG deposits into a family of related subtypes, the most important of which are the Magnetite Group (e.g. Candelaria-Chile, Ernest Henry-Australia, Salobo-Brazil) and Hematite Group (e.g. Olympic Dam-Australia, Prominent Hill-Australia, Mantoverde-Chile) subtypes. They are characterized by their dominant iron oxide and are known as IOCG deposits *sensu stricto*. The next most important sub-group are the iron-oxide apatite (IOA) deposits (e.g. Kiruna-Sweden, Port Radium-Canada, Pea Ridge-USA, El Romeral-Chile), which is dominated by Na \pm Ca alteration and hydrothermal breccias cemented by magnetite, actinolite and apatite. Table 2 highlights some of the defining characteristics of magmatic-hydrothermal IOCG deposits (Richards and Mumin, 2013a, b).

Economic Importance

Globally IOCG deposits have a major economic impact, particularly for Fe, Cu, Au, U and REEs (Williams et al., 2005). They can be a junior or major exploration companies defining discovery, containing ore bodies hosting deposits of 10s of Mt (e.g. NICO) to >2000 Mt (e.g. Olympic Dam) of ore (Corriveau et al., 2010). Metal contents on average are relatively moderate

to low compared to some deposit types (e.g. SEDEX, VMS, MVT), but there are exceptions, such as the Osborne deposit within the Cloncurry district in Australia that in 2008 had a reserve of 15.2 Mt at 3% Cu and 1.05 g/t Au (Fisher et al., 2008). Probably the most well-known IOCG deposit is the Olympic Dam (Cu-U-Au) Mesoproterozoic deposit in South Australia, with a current total measured resource of 1330 Mt at 0.96% Cu, 0.29 kg/t U₃O₈, 0.40 g/t Au and 2 g/t Ag (BHP Billiton, 2015 Annual Report, www.bhp.com). The Olympic Dam deposit is the world's largest single resource of U and a major global source of Cu and Au (Skirrow et al., 2007).

Of more immediate importance for the purposes of this thesis are the IOCG deposits that occur within the GBMZ. Past producing mines include the Echo Bay Mine (Ag-Cu), Eldorado Mine (U-Ag-Cu-Co-Ni-Pb-Ra-Po), Contact Lake Mine (Ag-U), El Bonanza Mine (Ag), Terra Mine (Ag), Norex Mine (Ag), Ray Rock Mine (U), Damp Mine (U) and Tatie Mine (U). Closer to Mazenod Lake and within an 8 km radius are two IOCG-type deposits owned by Fortune Minerals Limited. South of Mazenod Lake is the NICO deposit that contains combined underground and open pit proven mineral reserves of 33 Mt at 0.04% Cu, 1.03 g/t gold, 0.11% Co and 0.14% Bi (Burgess et al., 2014). Only 4 km to the north of Mazenod Lake is the Sue-Dianne deposit which contains an indicated 8.4 Mt resource at 0.8% Cu, 0.07 g/t Au, 3.2 g/t Ag (Fortune Minerals, 2009). Both deposits are located within the same NNW trending volcanic belt and hosted within Faber group volcanic rocks.

TABLE 2. Defining characteristics of magmatic-hydrothermal IOCGs, modified from Richards and Mumin (2013a, b).

Characteristics	IOCG deposit type
Major metal association	Fe, Cu, Au
Minor metal association	U, REE, Co, Ag
Sulfur content	Low relative to porphyry copper deposits
Common ore mineralogy	Magnetite, hematite, chalcopyrite, bornite, chalcocite
Ore fluid	H ₂ O-CO ₂ -NaCl-KCl-CaCl ₂ (10-50 wt. % NaCl equivalent)
Oxidation; pH	Oxidized; neutral to mildly acidic, rarely acidic
Source of magmas	Subduction-modified lithosphere
Source of fluid	Magmatic predominant \pm crustal (basin/surface) \pm metamorphic derived
Source of metals	Evolved/subduction modified lithosphere and fluxing from host rocks
Alteration geochemistry	Na-K-Fe-P-Ca-CO ₂ -SiO ₂ -B
High-temperature alteration mineralogy (<~400°C-350°C)	Na-rich: Albite, scapolite, amphibole, pyroxene Na-Ca-Fe-rich: Magnetite, actinolite, apatite, alkali feldspar K-Fe-rich: K-feldspar, magnetite, biotite, amphibole
Low-temperature alteration mineralogy (>~400°C-350°C)	K-Fe-Ca-CO ₂ -rich: Hematite, sericite, chlorite, epidote, carbonate, quartz, phyllic and/or propylitic in some deposits SiO ₂ -Fe-CO ₂ -rich: Quartz, hematite \pm carbonate
Diameter of high-temperature alteration	1 to \geq 7 km (and possibly greater)
Depth of formation	Surface to \geq 5 km
Geothermal gradient	Elevated gradient
Regional metamorphism	Low to high grade
Magma composition	Calc-alkaline to alkaline; oxidized; mafic to felsic; I or A-type
Tectonic setting	Distal, back-arc or post-subduction
Kinematic setting	Extension to transtension
Common controls on deposit formation	Regional structures, nearby intrusions
Age range	Dominant in Precambrian, but not restrictive to age

Morphology & Structural Controls

There are many examples of different morphologies for the IOCG clan of deposits. Deposit examples exist that are stratabound sheets (e.g. Magnitogorsk deposit, Russia; Gandhi, 2003), stockwork zones (e.g. Kwyjibo deposit, Canada; Perreault and Lafrance, 2015), breccias (e.g. Olympic Dam deposit, Australia; Williams et al., 2005) and disseminated (e.g. Osborne and Starra deposits, Australia; Williams et al., 2005) varieties, which can be stratiform or discordant. The various deposits all have their own unique form; however, they are exclusively hydrothermal replacement and infill deposits where ore and alteration minerals have replaced host rocks and infilled open spaces hosted in fractures and brecciated rocks.

IOCG deposits universally exhibit strong structural control, a quality that all hydrothermal deposits share (Williams et al., 2005). Faults, fractures or other permeable structures make ideal conduits for the flow and spread of fluids necessary to form hydrothermal ore deposits. Magmas, which provide the heat source and much of the volatiles and metals that is necessary for mineralization in IOCG deposits, also intrudes along these structural zones. For these reasons, IOCG deposits are usually found at intersections of major crustal structures, which typically have a tensional or transtensional component (Richards and Mumin, 2013a, b).

Metal deposition sites include dilational jogs (e.g. Olympic Dam), duplexes, splays on faults (e.g. Carajas district and Monakoff deposit), en echelon extensional fractures, shear zones, cavities of folds (e.g. Tennant Creek district) or form from the interactions between differentially permeable lithologies (Sillitoe, 2003; Williams and Skirrow, 2000; Corriveau et al., 2007). Consequently, major crustal structures have a direct influence on the formation of deposits on a regional and local scale. Exploration and research strategies (such as in this study) will therefore often emphasize the importance of structure.

Spatial & Geologic Context

With the exception of Antarctica, known IOCG deposits are distributed across all continents and include representative examples from Archean to Cenozoic age (Barton, 2014). Their relative economic importance is not partial to any of the locations or ages, which demonstrates the variety of their geologic setting.

The geology and tectonic setting for IOCG deposits is also quite diverse. IOCG districts have been located in Precambrian shields, along active orogenic belts and in back-arc and other post-subduction settings (Williams et al., 2005; Richards and Mumin, 2013b). Where magmatic associations are recognized, they are typically of calc-alkaline to mildly alkaline character (Richards and Mumin, 2013a, b). Despite the diversity of tectonic setting, the kinematics of IOCG deposits tend to demonstrate extensional or in transtensional tectonics within intracratonic or continental-arc zones. IOCG deposits are often spatially and genetically associated with epithermal and skarn deposits or mineralization (Mumin et al., 2007, 2010) and those IOCGs known to have a magmatic-hydrothermal association are similar in many aspects to porphyry-Cu deposits, notwithstanding distinct and important differences (Mumin et al., 2007, 2010; Richards and Mumin, 2013a, b).

Hydrothermal Alteration

The most diagnostic hydrothermal alteration indicative of the core of IOCG systems is alkali-iron enrichment (Na-K-Fe) (Hitzman et al., 1992; Mumin et al., 2007, 2010) (Fig. 3). Typical alteration zones in IOCG hydrothermal systems generally exhibit progressive alteration mineral assemblages, from high-temperature, relatively reduced, neutral pH assemblages closest to the source to progressively distal lower-temperature, oxidized, lower pH assemblages (Mumin

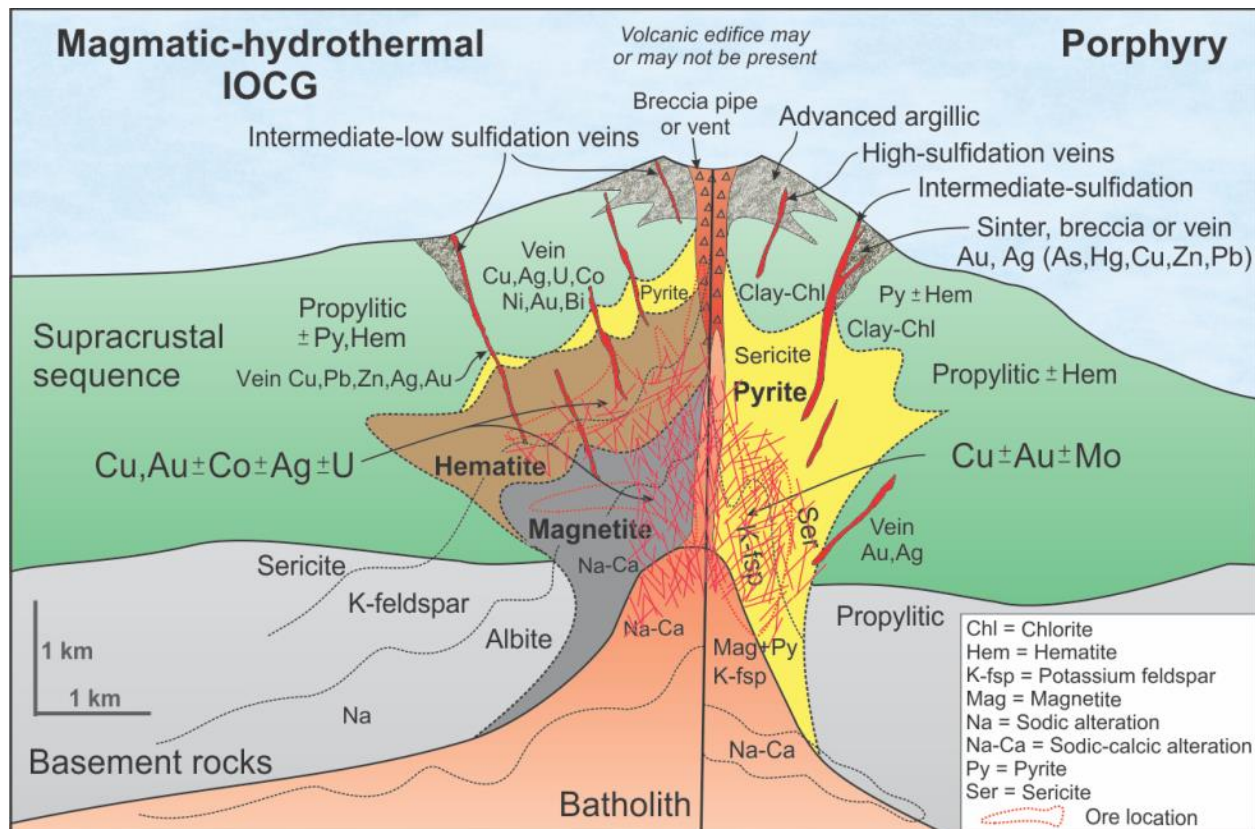


Fig. 3. Schematic cross-sectional model of a magmatic-hydrothermal system that illustrates the hydrothermal alteration zoning pattern and relationships between S-rich porphyry $\text{Cu} \pm \text{Mo} \pm \text{Au}$ deposits and S-poor MH-IOCG deposits (Richards and Mumin, 2013b).

et al., 2007, 2010; Richards and Mumin, 2013a, b). All the typical alteration zones do not necessarily have to form or may not be preserved after periods of erosion (e.g. Somarin and Mumin, 2013). Unique alteration types may also evolve that reflect the geologic diversity of their setting. These hydrothermal systems tend to be spatially extensive, extending to wide zones that can range from a few meters to 100s of km (Corriveau et al., 2007). Multiple hydrothermal cells often overlap, which may be difficult to differentiate as they combine alteration types and effects. The illustration in Figure 3 demonstrates the unique paragenetic sequence of alteration that is a distinguishing factor in defining IOCGs from other ore-forming systems.

Mass gains and losses in altered host rocks around IOCGs illustrate exchanges in elemental abundances of most major and minor elements with varying degrees of mobility that depend upon physio-chemical conditions of mineral formation. The most common whole-rock composition changes include both additions and depletions in Na, K, Ca, Fe and Si. Changes in framework silicate mineralogy are the most common observable manifestation, with K-feldspar \pm biotite forming in potassic altered areas and albite forming in sodic (albitic) altered zones. These changes in mineralogy often include tiny inclusions of hematite within the rock which imparts a characteristic reddish to reddish-brown color, colloquially known as ‘red rock’ alteration (Wenner and Taylor, 1987; Williams, 1994). Fe-enrichment manifests as magnetite in high-temperature proximal areas and hematite in lower-temperature parts of the system. Silica enrichment can occur as widespread silicification of host rocks, and /or as distal or late-stage massive (giant) quartz veins and/or stockworks.

Textural changes may or may not occur during hydrothermal alteration. Pseudomorphic replacement is a common method of altering mineralogy from one state to another without completely changing the rock texture. Alteration may also be texturally destructive, with often a complete change in texture and chemistry of the original host, which makes identifying the protolith a difficult task. In most instances replacement is spatially selective, and dependent upon local permeability conditions and available conduits for hydrothermal fluid migration.

One of the important aspects of understanding hydrothermal alteration for exploration of mineral deposits is its representation of the migration of fluid. Seemingly disparate alteration effects may in fact be parts of an overall hydrothermal system. For IOCGs, and similar hydrothermal ore deposits, the alteration zones are obvious expressions of physio-chemical

gradients that can potentially be traced to proximal zones of ore deposition (Corriveau et al., 2010).

IOCG-type hydrothermal alteration is generally defined in terms of elemental and/or mineral changes. The major alteration zones common to most IOCG systems are described below and include: Sodic, magnetite \pm actinolite \pm apatite (MAA), potassic, phyllic, tourmaline, carbonate and silicification.

(a) Sodic Alteration

Sodic (or albitic) alteration is known to involve the relative addition of Na to country rock. Typically, these alteration zones are also found to be regions of element leaching, where predominantly K and other alkali or alkali earth metals being depleted (Barton, 2014). Sodic altered rock usually results in host rock that experiences a change in framework silicates, where feldspars convert to their sodium phase (albite). The alteration can be either texturally destructive or preservative depending on the host rocks chemistry, intensity of alteration and degree of stress. Intense sodic alteration may generate albitites, composed of dominantly sodic-rich plagioclase, which may grade outwards from the source intrusion to a ‘patchy’ albitization. (Corriveau et al., 2010).

Several authors have associated high-temperature albitic alteration with the cores of IOCG hydrothermal cells (Corriveau et al., 2010; Richards and Mumin 2013b; Barton, 2014). Spatially this type of hydrothermal alteration is within the highest temperature zone, proximal to the heat source (igneous or otherwise). In some (possibly rare) instances it may indicate a source of abundant Na in the host rocks (e.g. evaporite). While this alteration can be intense due to proximity of a heat and Na source, it can also be spatially very extensive. Temperatures of

formation are estimated at ~600° to ~400°C (Mumin et al., 2007, 2010; Corriveau et al., 2010; Mumin and Richards, 2013a; Somarin and Mumin, 2013).

Base and precious metals in the Na-alteration zone can be significantly depleted (Williams, 1994; Menard, 1995; Barton and Johnson, 1996, 2000; de Jong et al., 1998; Oliver et al., 2004, 2008; Richards and Mumin, 2013a, b). In contrast to this proximal zone of IOCG systems, porphyry-Cu hydrothermal systems have potassic cores, commonly associated with metal enrichments (Sillitoe, 2010); however, Richards and Mumin (2013a, b) have shown that Na alteration can occur in porphyry systems deep below the potassic core.

(b) Iron Oxide Alterations

High temperature and low temperature varieties of hydrothermal iron oxide alteration are diagnostic of IOCG systems. Most of the important IOCG deposits are directly associated with extensive iron oxide enrichment (e.g. Candelaria, Olympic Dam, NICO, Carajas district, Ernest Henry; Goad et al., 2000; Williams et al., 2005). Typically, mineral exploration efforts often begin with an application of regional magnetic and gravity surveying to target unique physical properties associated with iron oxide alteration. Geophysical anomalies that are considered to be potential zones of iron oxide enrichment are then further inspected for their potential economic potential. The iron oxide alteration can be subdivided into two distinct categories in recognition of their predominant mineral characteristics, magnetite-actinolite-apatite (MAA) and hematite.

Magnetite is the high temperature variant of iron oxide and is commonly associated with actinolite ± apatite ± albite ± K-feldspar minerals (Richards and Mumin, 2013a, b). Texturally MAA alteration can be coarse grained and massive (e.g. Mag Hill from Somarin and Mumin, 2013), but finer-grained replacements and breccias are also common. The alteration may also manifest as veins or veinlets.

Like the above discussed sodic alteration, MAA alteration develops in relative proximity to heat sources. In a schematic model of an MH-IOCG hydrothermal system by Richards and Mumin (2013b), the MAA alteration is placed sequentially adjacent to sodic alteration progressing outwards from a potential heat and fluid source intrusion. In a few instances MAA type alteration has been known to form the wall rock of IOA deposits, such as in the Kiruna district, and Chilean and Peruvian iron belts, or the wall-rock for magnetite group IOCGs (e.g. Osborne, Ernest Henry, Salobo deposits) (Williams, 2010).

The lower temperature variant of alteration produced by Fe-saturated hydrothermal fluids is hematite \pm sericite \pm chlorite \pm carbonate \pm quartz. Hematite is a more distal, lower temperature and more oxidized alteration product, which may form adjacent to or above magnetite-bearing zones, or instead be a late superposition on magnetite alteration (Skirrow, 2010). Precious and base metals, REEs and/or uranium enrichments have been known to be concentrated within this alteration zone and can form impressive deposits (e.g. Olympic Dam, Prominent Hill; Williams et al., 2005). Hematite cemented breccias and stockworks are the characteristic textural variety these deposits.

(c) Potassic Alteration

K-alteration occurs in both high and low temperature forms in IOCG systems, each with their own distinct characteristics. A hydrothermal system that evolves beyond sodic alteration may form a high temperature K-Fe stage that contains potassic \pm ferroan minerals (K-feldspar \pm biotite \pm magnetite \pm amphibole) (Corriveau et al., 2010). This particular type of alteration is host for mineralization in magnetite-type IOCG deposits such as the Cu-Au deposits Ernest-Henry, Salobo, Candelaria, Aittik and NICO. It is also one of the more difficult alteration

assemblages to identify, as both lower temperature varieties and sodic alteration zones can appear similar in color and texture.

The distal, lower temperature phase of potassic alteration may occur with or be spatially associated with hydrolytic (acidic) and/or hematite alteration. This phase of alteration is further from the core of the hydrothermal cell and can extend for several kilometers. The most common mineral representation of this type of alteration is K-feldspar and hematite, often with sericite and can include chlorite and/or calcite. Specularite, a coarse crystalline variety of hematite often occurs in this alteration zone. Several globally important deposits are constrained within this alteration zone, including Olympic Dam and Prominent Hill (Williams et al., 2005).

(d) Tourmaline Alteration

Tourmaline alteration is common in some IOCG systems and typically forms the Fe-rich end member schorl or Mg-rich dravite species of minerals (e.g. Copiapó, Chile; Collins, 2010). This type of alteration has been linked to emplacement of granitic magmas that are boron-rich or from boiling-induced boron-rich residual fluid (Pirajno, 2009). Syn-volcanic episodes of hydrothermal alteration at temperatures of $\sim 300^\circ$ and 1-3 km depth of a highly saline and boron-rich fluid are the optimal conditions to induce tourmaline precipitation. At that temperature and depth tourmaline alteration is generally distal or intermediate to the core of an IOCG hydrothermal cell.

(e) Phyllic and other Hydrolytic Alterations

Hydrolytic alteration involves the decomposition of H_2O into H^+ and OH^- ions. The ions are consumed during reactions with silicate minerals, resulting in phyllosilicate mineral assemblages including those found in sericite, phyllic (quartz + sericite \pm pyrite) and argillic (clay mineral) alteration zones. In IOCGs the source of H^+ ions may be subsolidus reactions

during alkali metasomatism with hydrogen bearing fluids, such as H₂O, HCl or H₂S. Reactions result in the transformation of framework silicates to phyllosilicates and may be accompanied with a release of metal ions into solution.

The acidic alterations are a distal product of IOCG hydrothermal cell development. Hydrothermal fluids that escape from magmas have an initial neutral to mildly alkaline pH. As fluids cool, and sulphate in the magmatic fluid dissociates, residual fluids may become enriched in H⁺. This results in mildly acidic to acidic pH reactions distal from the source of the hydrothermal fluid, and typically leads to conversion of feldspar to sericite.

(f) Silicification

Pervasive silica alteration results in replacement of rock material with quartz or silica. It is the most distal and/or late stage hydrothermal alteration of an IOCG hydrothermal cell and can extend into the epithermal environment (Hitzman et al., 1992; Richards and Mumin, 2013b; Somarin and Mumin, 2013). In the GBMZ, widespread stockworks, breccias and silica flooding (massive quartz replacement) occur along transcurrent faults and other fracture zones. The Sue-Dianne deposit in the southern GBMZ can be traced along the axis of one of these silicified faults (Camier, 2002). Richards and Mumin (2013b) explain the presence of pervasive quartz as a result of leached and mobilized silica in a large MH-IOCG system that became soluble during prograde alteration and subsequently was deposited during retrograde alteration.

(g) Other Associated Alteration Effects

Skarns are common in many large IOCG systems (Hitzman et al., 1992). Formation of a skarn is not dependent on the presence of an IOCG system and instead is necessitated by the reaction of hydrothermal fluids, from any high-temperature heat source with carbonate-rich rocks (Corriveau et al., 2010; Barton, 2014). Skarn mineral assemblages include garnet (grossularite or

andradite) and clinopyroxene (diopside) \pm magnetite \pm vesuvianite \pm epidote \pm hornblende \pm sulphides \pm scapolite minerals. Although not common, there are examples of IOCG-related skarn deposits that are mined for copper, such as the Pumpkin Hollow deposit in Nevada (Schottenfeld, 2012).

IOCG systems have also been identified in proximity and association with epithermal conditions (Mumin et al., 2010; Somarin and Mumin, 2014). Mumin et al. (2010) and Richards and Mumin (2013b) suggest that epithermal style mineralization and alteration are part of the expected normal magmatic-hydrothermal IOCG system. They have cited spatial and temporal relationships within the GBMZ and elsewhere as evidence. Epithermal style mineralization is commonly characterized by quartz, quartz-hematite and quartz-hematite-carbonate dominant mineral assemblages in near-surface veins, breccias and stockworks.

Genesis

Several distinct and current hypotheses on the genetic development of IOCG hydrothermal systems have been discussed in modern literature (Hitzman, 2000; Pollard, 2000; Williams and Skirrow, 2000; Barton and Johnson, 2004; Richards and Mumin, 2013a, b). In large part, the differences in origin of each deposit type are due to their geologic diversity (Williams, 2010). Most genetic hypotheses include the association of an igneous (magmatic) source; however, as the intrusions are not always visually apparent and/or spatially close to the hydrothermal system in question, some researchers have proposed several other ideas. Three models are predominant in the literature for characterizing IOCGs based on principal fluid sources, and they can be grouped into two genetic families: magmatic and non-magmatic fluid sources. Both fluid types are relatively saline, sulfur deficient, neutral pH and oxidized;

however, there are several distinct possibilities as to where the fluid came from and how it travelled. The different possibilities are explained further below:

(1) *Magmatic-hydrothermal model*: The first model and most widely accepted considers a magmatic-hydrothermal source of fluids as the key source and transport mechanism for enrichment of metals and elements that alter and mineralize country rocks (Hauck, 1990; Pollard, 2000, 2006; Groves and Vielreicher, 2001; Williams et al., 2001; Sillitoe, 2003; Mumin et al., 2007; 2010; Richards and Mumin, 2013a, b) (Fig. 4). This theory suggests that hot, saline, metal bearing and relatively sulphur poor fluids are exsolved from a cooling, crystallizing magma in the subvolcanic environment. Volatiles such as H₂O, CO₂, H₂S, B become more enriched in the magma and derived fluids as it solidifies, fractionates and partitions. When the melt reaches saturation of volatile components exsolution occurs and many metals preferentially partition into the fluid fraction. Structural weaknesses in the surrounding country rock then act as conduits through which the volatiles migrate. The fluid cools and reacts with the host rock through which it permeates, leaching, transporting and depositing various metals in different parts of the system. This model is considered to be the best fit for GBMZ IOCG deposits, as well as many others worldwide (Richards and Mumin, 2013b).

(2) *Basin/surface derived fluids model*: In this model saline fluids are derived from an evaporitic source, i.e. coeval or older brine source (Barton and Johnson, 1996, 2000; Haynes et al., 1995, Haynes, 2000). Evaporites that supply NaCl have been used in literature to explain the abundance of Na wall rock alteration or Cl-bearing silicates such as scapolite. Convection of fluids in this model is considered to be driven by an igneous heat source or other crustal heat source, and in part by the density of the brines.

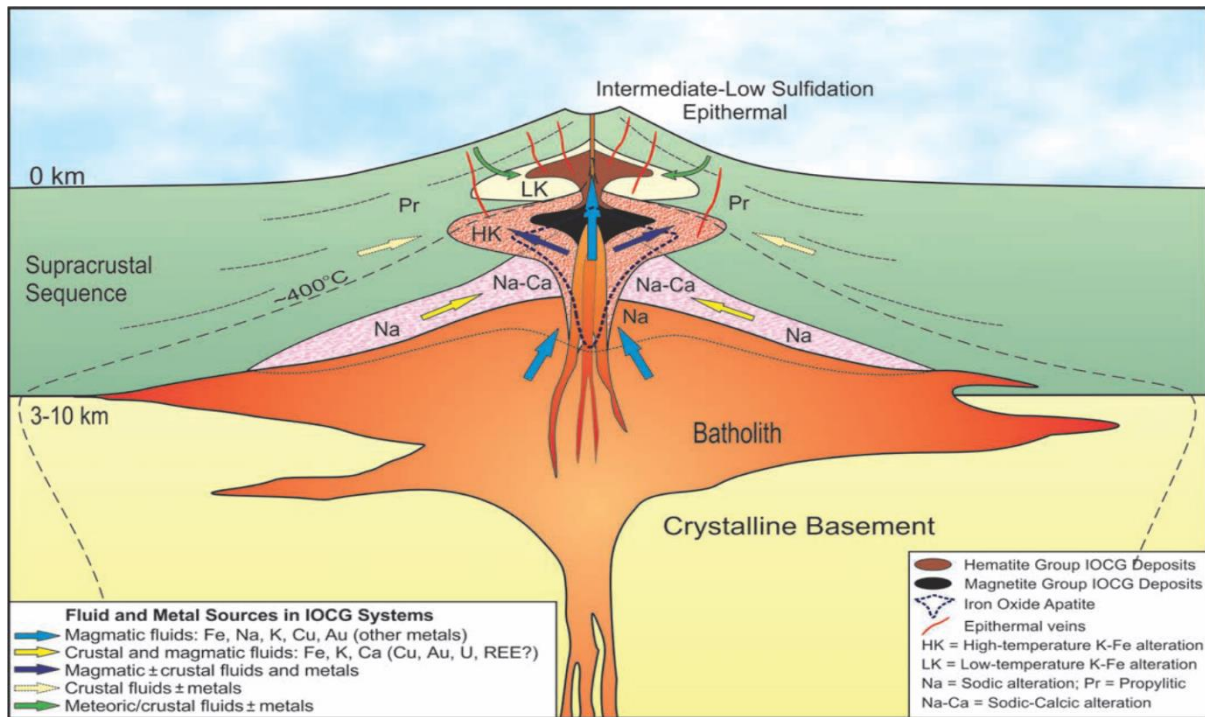


Fig. 4. Schematic cross-sectional diagram illustrating the fluid pathways and hydrothermal characteristics for the different IOCG genetic models (Richards and Mumin, 2013b).

Proponents of the model cite proximity of alteration to evaporite rocks in order to explain a high chloride/sulphur ratio, as well as a lack of evidence for a proximal intrusion; however, for many well documented IOCGs there is an unmistakable association with subvolcanic intrusions. Examples include the IOCGs located within the GBMZ (Richards and Mumin, 2013a, b) or the Gawler craton (Williams et al., 2005). In at least some IOCG settings (again the GBMZ) there is a complete lack of evidence for any nearby evaporites (Barton and Johnson, 1996).

(3) *Metamorphic-hydrothermal fluids model*: The primary source of fluid in this model is metamorphic derived fluids, where fluids originated from dehydration, decarbonation and desulphidation reactions of hydrous, carbonate and sulphur-bearing minerals (Oreskes and Einaudi, 1992; Williams, 1994; de Jong et al., 1998; Hitzman, 2000; Pollard, 2000).

There is not a necessary connection to an igneous source. Barton (2014) lists a number of

possible examples of IOCGs that may be metamorphic-hosted systems that may fit within this model including hydrothermal systems from Cloncurry and Tennant Creek districts. Hunt et al. (2007) explains the Wernecke breccias in the Yukon Territory as metamorphic driven IOCG systems. Alteration that occurs as a result of migrating fluid in this model reflects the chemical composition of the fluid source, which can include any regionally metamorphosed rocks. Authors that propose metamorphism as the dominant source of fluid in an IOCG system suggest there may be some mixing of fluids with a magmatic, basinal brine source or both (Williams, 1994; Hitzman, 2000; Barton and Johnson, 2004; Hunt et al., 2007).

Whatever the primary source of fluid, most investigators present evidence of fluid mixing in many IOCG systems as a critical mechanism for metal precipitation (Oreskes and Einaudi, 1992; Baker, 1998; Requia and Fontbote, 2000; Marschik and Fontbote, 2001; Ullrich et al., 2001; Mark et al., 2006; Davidson et al., 2007; Kendrick et al., 2008; Richards and Mumin, 2013b; Somarin and Mumin, 2014). The essential concept behind fluid mixing is that formation of an IOCG deposit involves the interaction of two or more different fluids. In these situations, lower temperature, oxidized fluids (most likely meteoric) interact with hotter, saline fluids (basinal brine or more likely magmatic) which creates conditions suitable for metal precipitation (Reeve et al, 1990; Haynes et al., 1995; Hayward and Skirrow, 2010; Skirrow 2010).

Richards and Mumin (2013a, b) convincingly suggest that the deficiency of sulfur in IOCG deposits and source fluids can be explained by a secular variation in oceanic sulfate content going back in geologic time. The S^{2-} anion of sulphide minerals in porphyry magmatic hydrothermal systems is known to have been sourced from seawater sulphate, which is scavenged by arc magmas following subduction and devolatilization of the oceanic lithosphere (de

Hoog et al., 2001; Wallace and Edmonds, 2011). Subduction of the oceanic lithosphere into the mantle includes significant amounts of H₂O, yet very low concentrations of sulfate during the Proterozoic and Archean because of a lack of sulfate content in the ocean prior to oxygenation of the atmosphere (Prouteau and Scaillet, 2013). During subduction, the slab underwent devolatilization reactions under progressively higher temperature and pressure conditions, fluidizing the overlying mantle wedge and helping to initiate mantle melting and formation of arc magmas. Interaction of the mantle melt with the base of the crust generated evolved, hydrous, oxidized, calc-alkaline magmas that were sulfate-deficient during the Proterozoic and Archean, and sulfate-rich during the Phanerozoic (Richards, 2009; Mumin and Richards, 2012, 2013; Richards and Mumin, 2013a, b). The paucity of sulphate explains the predominance of IOCGs in the Precambrian, while abundant sulphate during the Phanerozoic can explain the predominance of porphyry Cu deposits in the younger rocks. Those IOCG deposits formed in the Phanerozoic (such as the Mesozoic Mantoverde deposit) that also lack significant sulfur content are explained as a result of magmas generated from partial melting of relatively S-poor asthenospheric or subduction-modified lithospheric sources linked to periods of deep ocean anoxia (Richards and Mumin, 2013a, b).

The source of metals in IOCG systems is another debated topic, because of the range of possible sources. The most common explanation is that metals are directly sourced from the magma (Pollard, 2000; Sillitoe, 2003). Fluids derived from magma can contain relatively high concentrations of metals through preferential metal partitioning into the fluid phase (although the absolute concentration of metals is actually quite low) (Pirajno, 2009). Another source of potential metals includes elements leached directly from country rock during wall-rock interactions with hydrothermal fluids (Richards and Mumin, 2013b). Hot reactive fluid is capable

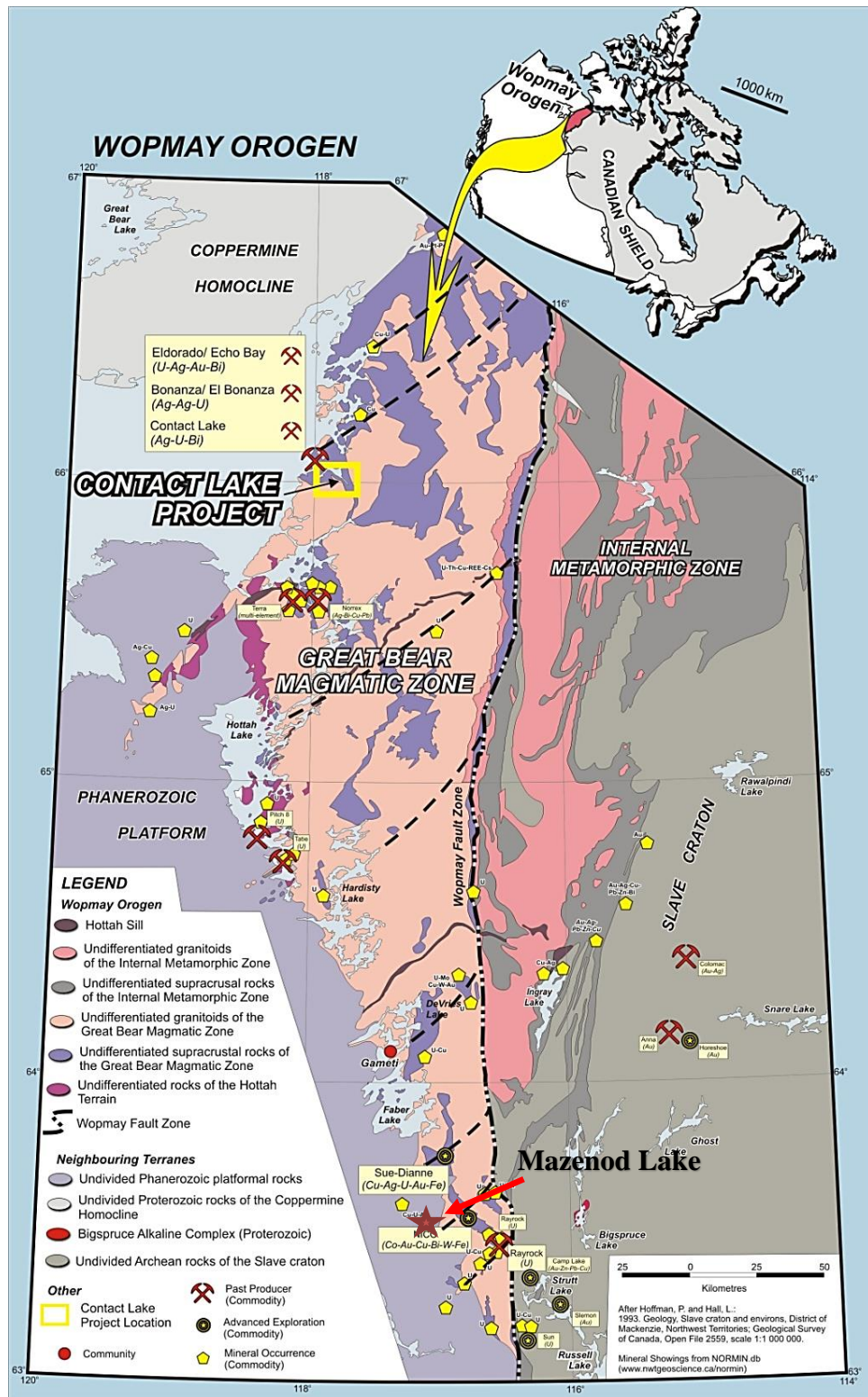
of, leaching, mobilizing and concentrating metal in country rock during migration of fluid in a hydrothermal system. All alteration zones in IOCG hydrothermal systems experience varying degrees of metal leaching, enrichment and redistribution.

Research is ongoing to explain the genesis of IOCGs. This thesis attempts to contribute to our growing understanding of the IOCG deposit type by updating our current knowledge on the geology, structure and geochemical relationships, characteristics and constraints, with a focus on the Mazenod Lake region in the southern GBMZ.

Chapter IV: Regional Geology and Tectonic Setting of the GBMZ

The GBMZ forms the western segment of the Wopmay orogen and is a regional subdivision of the Proterozoic Bear Province of the Canadian Shield, Northwest Territories, Canada (Fig. 1). Volcanic, plutonic and sedimentary rocks that comprise the Wopmay orogen were developed or emplaced during the time period between 1970 to 1890 Ma (Gandhi et al., 2001). Within the Wopmay orogen there are several divisions separated by similar rocks and tectonic significance. From east to west these divisions include the Coronation margin, Calderian foredeep, Turmoil Klippe and the focus for this investigation, the Great Bear magmatic zone (GBMZ) (Hildebrand et al., 2010; Gandhi, 2013; Mumin et al., 2014). The western edge of the GBMZ is bounded by the Hottah Terrane continental volcanic arc and the eastern border is bounded by the Slave craton.

The GBMZ is a north-south trending continental magmatic belt. The belt is exposed for a length of ~450-km and up to ~100-km wide, that is essentially parallel to the western margin of the Slave craton. For another approximately 500-km to the southwest and 300-km north-west, the volcanic belt extends beneath a relatively thin layer of Paleozoic cover (Coles et al., 1976; Hildebrand and Bowring, 1984; Hoffman, 1987; Hildebrand et al., 2010). Previous investigators have considered the GBMZ to be a typical analogue for an Andean-type continental magmatic terrane (Hildebrand et al., 1987). Volcanism within the belt is known to have occurred over a relatively short period of time with continental volcanism and associated plutonism dated at ~1875 to 1840 Ma (Hoffman and Bowring, 1984; Bowring, 1985; Bowring and Grotzinger, 1992; Gandhi et al., 2001; Ootes et al., 2015).



GBMZ stratigraphy is comprised of several supracrustal groups of volcanic rocks categorized as the McTavish Supergroup. Unconformities separate the McTavish Supergroup into the Labine, Dumas, Faber and Sloan volcanic groups (Gandhi et al., 2001; Hildebrand et al., 2010; Ootes et al., 2015). The northern Labine, Sloan and Dumas groups range up to 10 km thick. The southern Faber group rocks are made of ~5 km thick layers of volcanic assemblages, sediments and intrusive rocks.

Oldest of the volcanic assemblages is the LaBine Group, which is exposed along the western flank of the GBMZ (Fig. 2). An unconformity divides the LaBine Group from the metavolcanic and metasedimentary rocks that make up the Hottah terrane. The Labine volcanic group consists primarily of basalt and bedded tuff at the base of the stratigraphy and andesite in the upper units. Exposed along the east margin of the GBMZ near the Medial Zone (aka Wopmay Fault Zone) is the Dumas group. Relatively coeval to the LaBine Group, the Dumas Group contains alternations of mafic to intermediate rocks, felsic ignimbrites and flows as well as autochthonous sediments. The central area of the GBMZ contains the Sloan Group of rocks which is the youngest supracrustal sequence in the GBMZ and unconformably separated from the LaBine Group. Sloan group stratigraphy comprises dacite, rhyodacite and rhyolite flows and ignimbrites along with relatively small amounts of andesitic lava flows. Complex calderas, remnants of andesitic stratovolcanoes and associated subvolcanic diorite plutons have been mapped by investigators extensively within the Sloan Group (Hildebrand, 1982; Mumin et al., 2014). The Faber Group is located in the southern GBMZ and contains the Mazenod Lake area, which is the focus of this investigation. Faber Group lithology consists primarily of andesitic type volcanic and volcanoclastic rocks but ranges from basaltic andesites to rhyodacite ignimbrites along with associated flows, high level intrusions and autochthonous volcanic

sediments. Gandhi et al. (2001) determined the age of the Faber Group to be ~1865 Ma - roughly equivalent in age to both the LaBine and Dumas Groups. A chronostratigraphic column demonstrating the age relationships of the aforementioned geology is illustrated in Figure 6.

One of the last major events in the GBMZ was post-volcanic plutonism at about 1866-1840 Ma (Hoffman and Bowring, 1984, Gandhi et al, 2001). At this time period, the GBMZ was intruded by calc-alkaline to alkaline plutons across the length of the magmatic zone (Hoffman and Bowring 1984; Bowring, 1985; Hildebrand et al., 2010). These intrusions are extensive and occur as either plug-like bodies such as the Faber Lake rapakivi granite (~ca. 1856 Ma) or long tabular intermediate to felsic intrusions such as the Marian River batholith (~ca. 1866 Ma; Gandhi et al., 2001). These intrusions are often coarse-grained, massive and monotonously homogeneous, but often with differentiated marginal phases (Mumin et al., 2007). The granitic plutons include a compositional range of diorite, granodiorite, monzogranite or syenogranite that formed both concordant and discordant to the north-westerly trend of the volcanic belts (Hildebrand et al., 2010; Mumin et al., 2014). Largest of these intrusions is the Marian River batholith, a combination of undifferentiated intrusions that engulf Faber Group volcanic rocks. This giant pluton fences in the Faber Group on the east and west and is considered by some experts whom have worked in the area to be the source intrusion for the volcanic assemblages (Goad et al., 2000; Mumin et al., 2007). Coeval to the above intrusions, a sequence of small diorite to microdiorite dykes intruded into the GBMZ. The southern portion of the GBMZ dykes generally intruded lithology concurrent to northeast trending transcurrent faults and sometimes filled existing fault structures (Gandhi et al., 2001).

Although not of major relevance to this thesis because the Hottah terrane pre-dates the volcanic and sedimentary rocks of the GBMZ, the Hottah rocks have importance to this

discussion because they constrain the evolution of the magmatic zone. Prior to the extrusion of GBMZ volcanic supracrustal rocks a sedimentary sequence was emplaced on top of the Hottah terrane basement rock (Gandhi et al., 2001, Gandhi, 2013). This now metasedimentary group was first named by Gandhi et al. (2001) as the Treasure Lake Group. Metamorphic grade and deformation of this group increases in intensity towards the Medial Zone to the point of upper greenschist facies. The Hottah terrane is generally believed to form the basement rocks of the GBMZ. Despite the general consensus, basement rocks for the Treasure Lake Group have not been observed at surface in the southern GBMZ. The Hottah terrane that is exposed at surface has been age dated at ca. 2.5 – 2.0 Ga (Ootes et al., 2015). The terrane is mostly considered by experts working in the area to be a continental magmatic arc comprising calc-alkaline volcano-plutonic rocks with associated volcanic sediments and intrusions (Hildebrand et al., 1987; Clowes, 1997). Recent chronostratigraphic work and interpretations by Ootes et al. (2015) has indicated that the Hottah rocks migrated from the south of its current position due to extension-driven transtensional shearing (i.e. terrane translation). This notion contrasts previous widely used models advocating the Hottah terrane was a microcontinent accreted to the Slave craton and formed over a west-dipping subduction of the Coronation ocean crust (Hoffman et al., 2011).

Structure and Tectonics

The GBMZ is separated from the Coronation margin by a major crustal linear feature called the Wopmay fault zone, or in more recent literature it is referred to as the Medial Zone (Hildebrand et al., 1990). The Medial Zone is a major area of crustal deformation where rocks have been folded and faulted along a northern axial trace (Hildebrand et al., 1987; Hildebrand and Bowring, 1988; Hayward and Corriveau, 2014). Hildebrand et al. (1990) suggested the fault zone formed due to an oblique angle of subduction and subsequent tectonic shifting along a

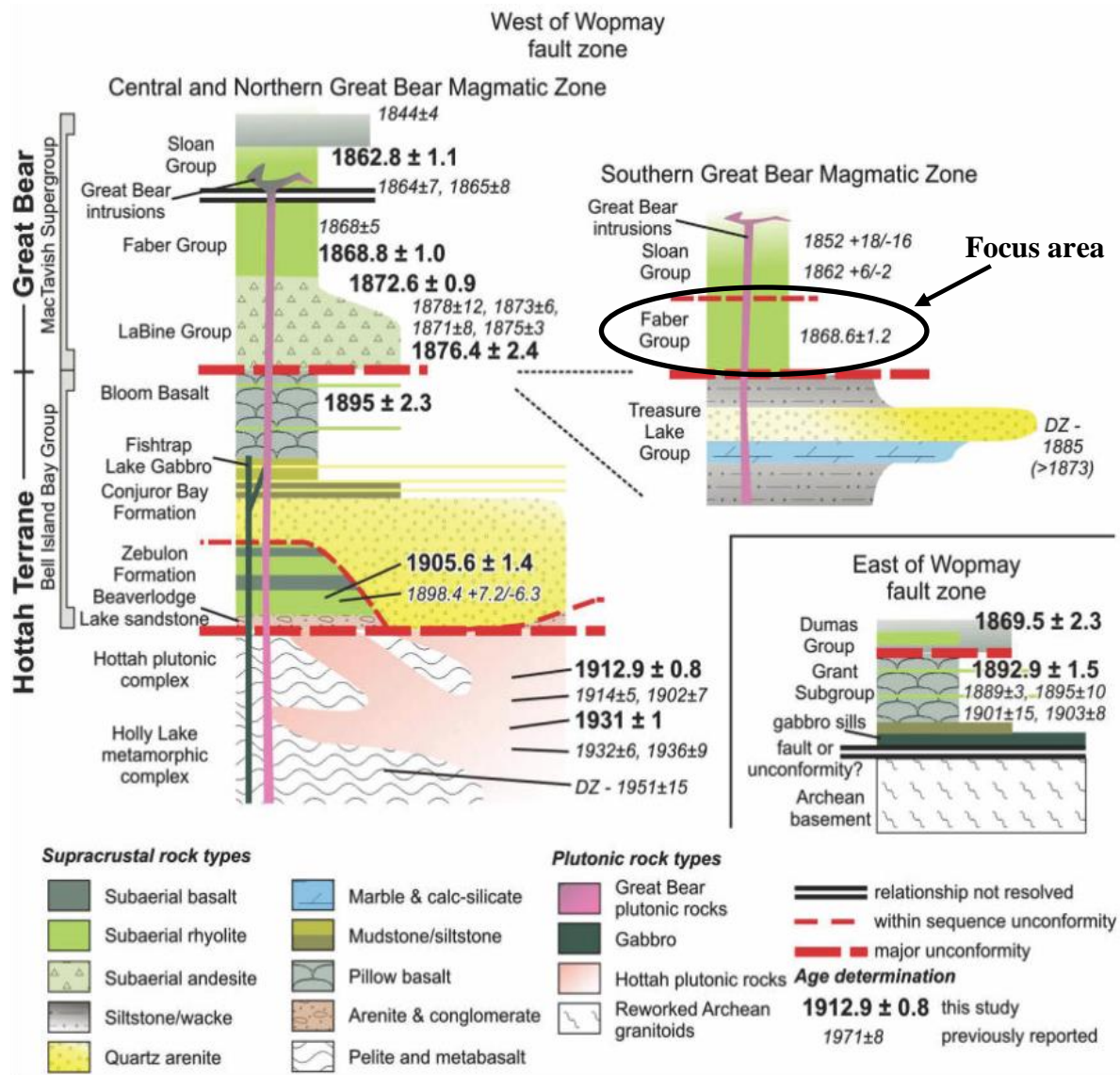


Fig. 6. Stratigraphic column of the Hottah terrane – Great Bear volcano-plutonic continuum (no vertical scale implied). (Ootes et al., 2015).

horizontal plane (Fig. 7). Another more recent theory included the possibility that the Medial Zone is a result of translation along a horizontal plane; essentially large-scale strike-slip movement, similar to the San Andreas Fault zone (Ootes et al., 2015).

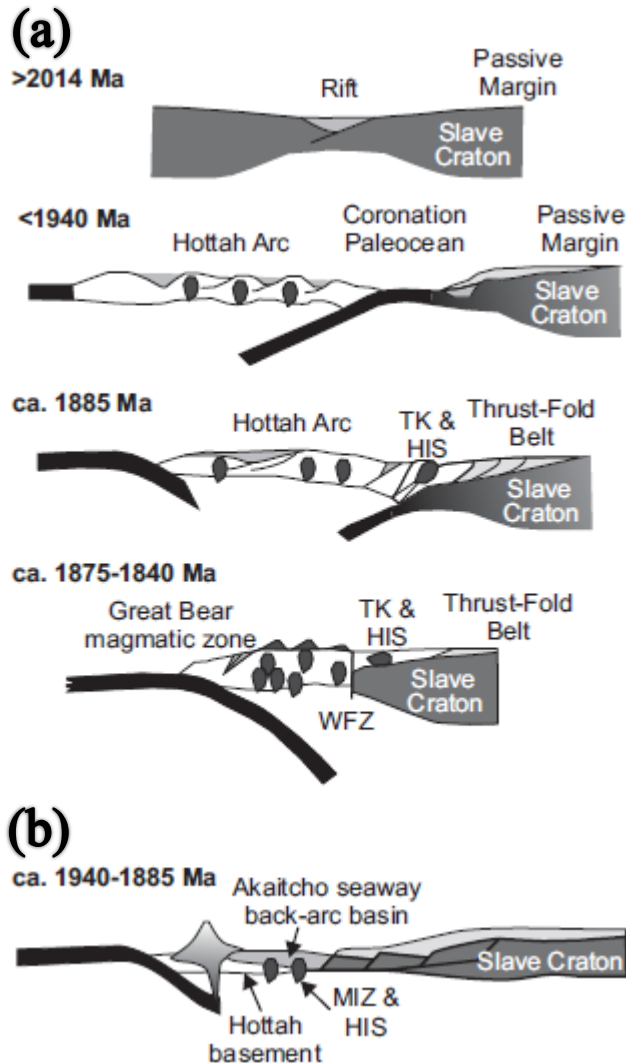


Fig. 7. Tectono-magmatic models for the evolution of the Wopmay Orogen and the GBMZ (after Ootes et al., 2015). (a) Accretion of the exotic Hottah terrane to the western Slave craton ca. 1880 Ma., subsequent arc magmatism resulting from eastward-directed subduction and formation of the GBMZ. (b) Back-arc basin formation and magmatism along a convergent plate boundary ca. 1940-1885 Ma. HIS, Hepburn intrusive suite; MIZ, metamorphic internal zone; TK, Turmoil klippe; WFZ, Wopmay fault zone.

cause of why the major crustal breaks formed has included the suggestion that they are a result of an eastward directed terminal terrane collision with the Hottah terrane by the Nahanni-Fort Simpson terranes (Hayward and Corriveau, 2014). Not supporting this hypothesis, Ootes et al.

Sometime after the GBMZ formed a regional set of NE-SW trending right-lateral transcurrent faults with km-scale strike-slip displacements offset and segmented the entirety of the continental magmatic belt. These prominent linear physiographic features are regional structural distortions that have been well defined by magnetic depletion, topography, and field geology work (Gandhi et al., 2001; Mumin et al., 2014; Hayward and Corriveau, 2014). The transcurrent right lateral faults appear to mostly terminate at or near the Medial Zone on the eastern side of the GBMZ.

Interpretations of regional magnetic variance also indicate that the transcurrent faults extend under Paleozoic cover past the western edge of the GBMZ to an unknown limit. Research as to the

(2015) pointed out that brittle deformation actually post-dates the Nahanni terrane emplacement, specifically referring to the major dextral transcurrent McDonald fault. In a different investigation of the GBMZ by Mumin et al. (2014) a suggestion was made that the transcurrent faulting was likely coeval to Great Bear volcanism. This proposal advocated that transcurrent faulting was a result of, or re-activated by pull-apart domains formed during a NE-SW oriented extension phase. While evidence of synvolcanic and post-volcanic faulting within the GBMZ has been discussed in literature there is no conclusive evidence to point to a single tectonic precursor event. At present, most experts working in the Great Bear agree that pre-volcanic tectonic activity is related to east-verging subduction along the western margin of the Slave craton (Hildebrand, 1990; Mumin et al., 2014).

Chapter V: Geology of the Mazenod Lake Region

Throughout this chapter are summary descriptions of the Mazenod Lake area lithology, hydrothermal alteration and mineralization. The observations described herein are based on 2013 field operations supported with an analysis of lithogeochemical data, remotely sensed imagery, and past reports that discuss the geology of the region (Gandhi et al., 2001, Skanderbeg, 2001; Kulla, 2004; Gandhi, 2013). The following maps included in this chapter illustrate interpretations of the geology described herein; including: Geology of the Mazenod Lake Region (Fig. 8), Geology of the Mazenod Lake Area (Fig. 9), Geology of Dan Island (Fig. 10) and Geology of the Bea Area (Fig. 11).

Local Geologic Setting

Geology in the Mazenod Lake area (Figs. 8-11) consists of predominantly ca. 1.865 Ga felsic to intermediate calc-alkaline volcanic rocks of the Faber Group. These volcanic rocks include numerous flows, tuffs, agglomerates and breccias (hydrothermal and volcanoclastic). The volcanic belt consists of lithology arranged in a predominantly NNW curvilinear orientation, constrained from the east and west within a suite of extensive coeval intrusive rocks. These plutonic rocks are compositionally diverse and typically range from granite to monzonite (Gandhi et al. 2001; Gandhi, 2013). Autochthonous sediments are conformable with the volcanic belt, while Paleozoic allochthonous sedimentary rocks are discordant, overlying the volcanic belt along an unconformity. Lithology from the Faber Group encompass a significant proportion of the study area, but also extends to greater than 16 km north along the Kemaz fault (Mar fault of Camier, 2002 and Mumin et al., 2014) and another approximately 17 km southeast. The stratigraphic group is subdivided into several volcanic assemblages of similar chemical composition and mineralogy. Some volcanic assemblages that have been previously included in

the Faber Group stratigraphy are located outside of the study area (Gandhi et al., 2001), which are not described in this thesis.

Several new rock units have been identified because of field work performed as part of this thesis project. The newly recognized units have necessitated some new nomenclature for the stratigraphy, described in the following sub-sections. An attempt was made in this thesis to remain consistent with previous research completed on the Mazenod Lake region (Hetu et al., 1994; Gandhi et al., 2001; Camier, 2002; Gandhi et al., 2014; Mumin et al., 2014).

Despite the detailed nature of the 2013 field mapping, some uncertainties remain regarding the stratigraphy. There were several isolated areas that could not be covered in the time permitted or were not directly accessible.

Paleozoic Sediments

Paleozoic sediments (PC, Figs. 8, 9) cover a significant proportion of the project area. The sediments comprise a relatively thin (< 100 m) sub-horizontal sequence of sandstones, conglomerates, argillaceous sediments and dolomitic rocks (Gandhi, 2013). Previous discussions by Gandhi (2013) described the sediments as a Cambrian marine transgression over the Great Bear and Great Slave Lakes region. Sedimentary units are considered undivided in this work, because they were not mapped in detail and they are not of significant importance to this investigation.

Great Bear Intrusive Rocks

Gandhi et al. (2001) succinctly described the intrusions of the Mazenod Lake area (Fig. 12), some of which is expanded upon in this report. The medium to coarse grained plutonic rocks are calc-alkaline, texturally massive, spatially extensive and usually have an orange color on

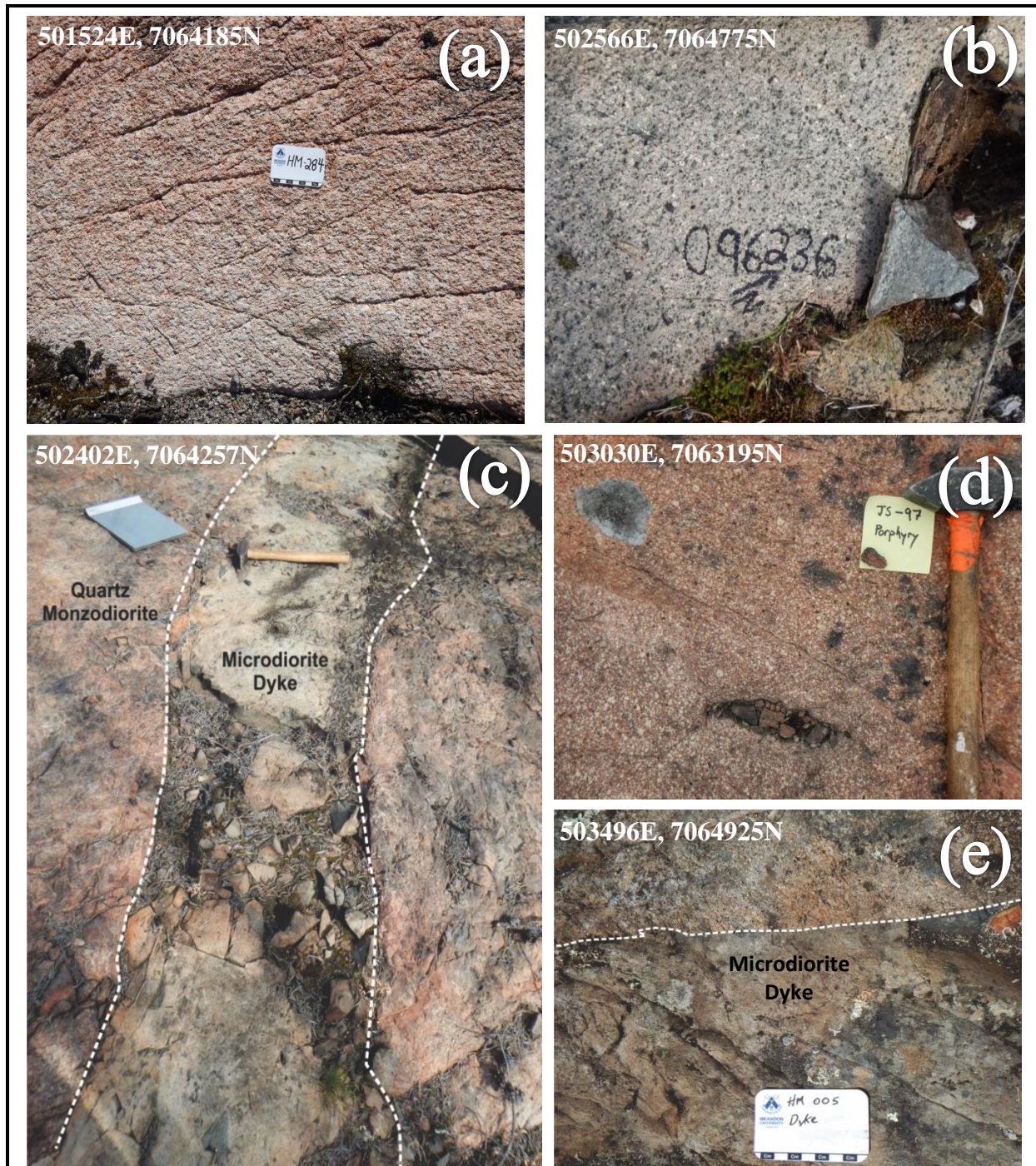


Fig. 12. Outcrop photographs of selected intrusive rocks discussed in this thesis: (a) HM284: Coarse grained monzogranite (SM) on the north side of NET ridge, (b) HM062: Porphyritic monzodiorite (MD) with distinctive ‘white’ feldspars and mafic (pyroxenes?) minerals located on the south side of Dan Island, (c) SR227: Microdiorite dyke that has penetrated the older quartz monzodiorite (SM) from the NE edge of NET ridge, (d) JS097: Porphyritic monzodiorite (MD), typical orange hue to the rocks found surrounding Mazenod Lake, (e) HM005: Microdiorite dyke that has penetrated a andesite crystal tuff ignimbrite. Reference system for coordinate data is UTM NAD83 zone 11.

weathered surfaces that contrasts well with the surrounding rocks. The intrusions have a compositional range that includes granite, granodiorite, monzogranite and quartz monzonite. Spatially and temporally, these intrusions surround, cut across and intrude into the volcanic assemblages.

At least one significant high-level (sub-volcanic) monzodiorite intrusion is exposed at surface in the project area. Unlike the volcanic rocks, the subvolcanic intrusion has no identifiable volcanic textures or specific orientation and appears to outcrop at surface in an irregular shape. The monzodiorite is texturally fine to medium grained, porphyritic and similar in appearance to the ignimbrites. It could easily be misinterpreted as a flow or pyroclastic unit yet is distinguishable by the uniform distribution of phenocrysts, which includes a higher percentage of ferromagnesian (predominantly pyroxene) minerals.

Dykes within the study region also have a composition range from intermediate to felsic. Most of the dykes are very fine-grained diorite with lesser amounts of the more felsic varieties. The dykes are typically approximately a meter wide but can range up to several meters. One uniquely large intermediate-felsic dyke in the Bea area is ~160 m wide, infilling an obvious major dextral fault structure (Figs. 8, 11). There is a consistent orientation for most of the dykes in the NE-SW direction from an azimuth of ~029° to 065°. The most prominent plutons from the Mazenod Lake area are described further below:

(a) Sarah Lake Granite

The Sarah Lake granite (SM, Figs. 8, 9, 11) is compositionally a monzogranite within the study area and acts as the western border of the volcanic belt. The granitic rock is mostly homogeneous and grades from medium to coarse-grained, west to east. Mineralogy includes abundant phenocrysts of quartz, feldspars, and relatively minor amounts of hornblende ± biotite

(Gandhi, 2013). The intrusion has a prominent right-lateral offset of ~1200 m along the Marian River fault in the central area of Mazenod Lake (Figs. 8, 9). Aplitic dykes of similar composition to the Sarah Lake granite intrude the adjoining rhyodacite.

(b) Marian River Batholith

The eastern extent of the volcanic belt is constrained by the Marian River batholith (MB, Figs. 8, 9). Composition of the batholith ranges from granite to granodiorite (felsic – intermediate). It forms the eastern boundary of the entire Faber volcanic belt and is present throughout most of the GBMZ between the Medial Zone and volcanic belt. Gandhi et al. (2001) described the batholith as granodiorite characterized by euhedral feldspar crystals set in a medium to coarse-grained matrix of feldspar, quartz, hornblende, biotite and accessory minerals. The Marian River batholith was not of significant interest during field mapping; consequently, it was not examined in detail.

Faber Lake Volcanic Rocks

The Faber Group consists of volcanic and volcanoclastic rocks (Figs. 13, 14) that form an approximately 85 km long and 10 km wide belt (Gandhi et al., 2001). Most of the lithology is intermediate in composition but ranges from basaltic andesite to rhyodacite (see Chapter 7 for chemical classifications). The suites of rocks are calc-alkaline in chemical character and have been extensively hydrothermally altered (Gandhi, 1994). Metamorphic grade is generally sub-greenschist facies and there is little to no penetrative foliation visible in the rocks. Despite limited internal fabric, the Faber Group rocks are intensely structurally broken. Typical examples of brittle and ductile deformation are visible in outcrops throughout the region. In this thesis, volcanic lithology within the project area is subdivided and discussed as five unique volcanic assemblages.

(a) Volcanic Sediments

Volcanoclastic sediments (VS, Figs. 8, 9, 11) are a coeval suite of rocks derived directly from the local volcanic rocks (Fig. 14). These rocks consist of detrital and pyroclastic material reworked into sediments that range from claystone to conglomerate types- although the most common beds are fine-grained. They contain excellent preserved structures from which to measure bedding planes and obtain geopetal indicators (way-up structures). Previous mapping by Gandhi (2013) grouped these rocks with adjoining volcanic assemblages. The sediments have been separated on maps included with this thesis to emphasize the nonconformity they represent between the sub-parallel series of volcanic assemblages.

(b) Dianne Lake Assemblage

The Dianne Lake assemblage (DL, Figs. 8 - 10) had been referred to as a series of rhyolitic rocks and a sub-volcanic intrusive assemblage related to the Lou Lake assemblage (Gandhi et al., 1996, 2001, 2013). Analysis of geochemical data reveal a compositional range, with more intermediate rocks on the west and felsic rocks on the east. The geochemical trend is interpreted to represent evidence of a change in magma composition over time. Unfortunately, a lack of chronologic indicators prevents conclusive interpretations of how the magma changed composition over time (i.e. intermediate to felsic or felsic to intermediate composition). The few bedding measurements taken from layers of ash and preserved fiammé correspond with an average dip of $\sim 70^\circ$ to the east.

Each of the different rock layers (ignimbrite sheets) within the Dianne Lake assemblage has similar mineralogy and textures. The rocks contain 10 – 40% feldspars that range from ~ 1 – 4 mm in diameter and contain trace to 4% quartz phenocrysts that range from ~ 1 – 2 mm. The more felsic ignimbrite sheets contain a small percentage of fine to medium grained biotite

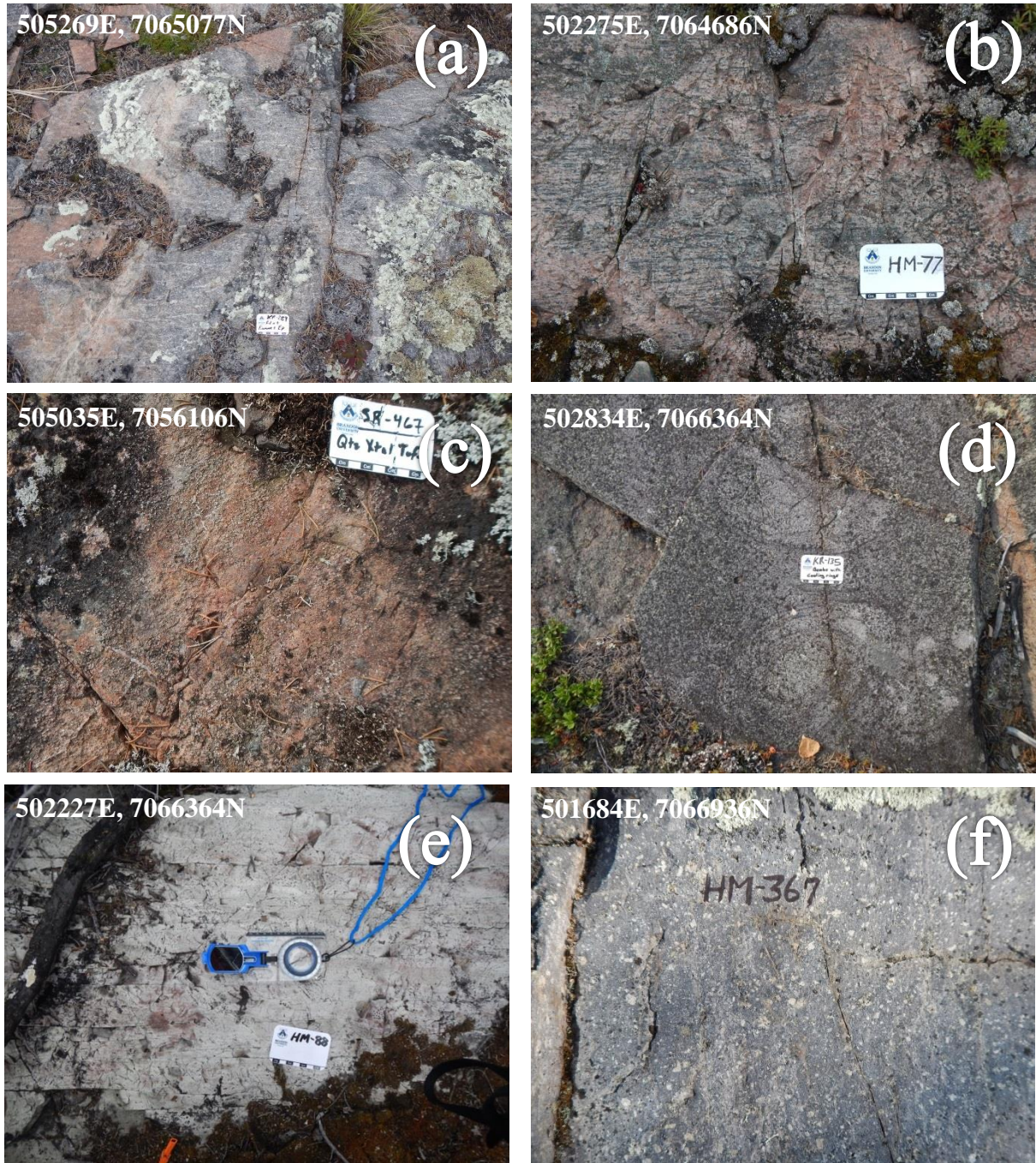


Fig. 13. Outcrop photographs of volcanic assemblage rocks discussed in this thesis: (a) KR289: Rhyodacite crystal tuff (LL) containing fiammé oriented $289^{\circ}/71^{\circ}$, (b) HM077: Andesite quartz-feldspar crystal tuff (BL) with fiammé oriented 327° , (c) SR467: Quartz amygdules in a fine-grained andesite (SL), (d) KR135: Andesite volcanic breccia (DL) with cooling rings, volcanic bombs are ~30-40cm, (e) HM088: Finely laminated bedded rhyodacite ash tuff (DL) with a bedding orientation of $228^{\circ}/55^{\circ}$, (f) HM367: Welded crystal tuff (ML) with distinct bedding orientation $189^{\circ}/60^{\circ}$. Reference system for coordinate data is UTM NAD83 zone 11.

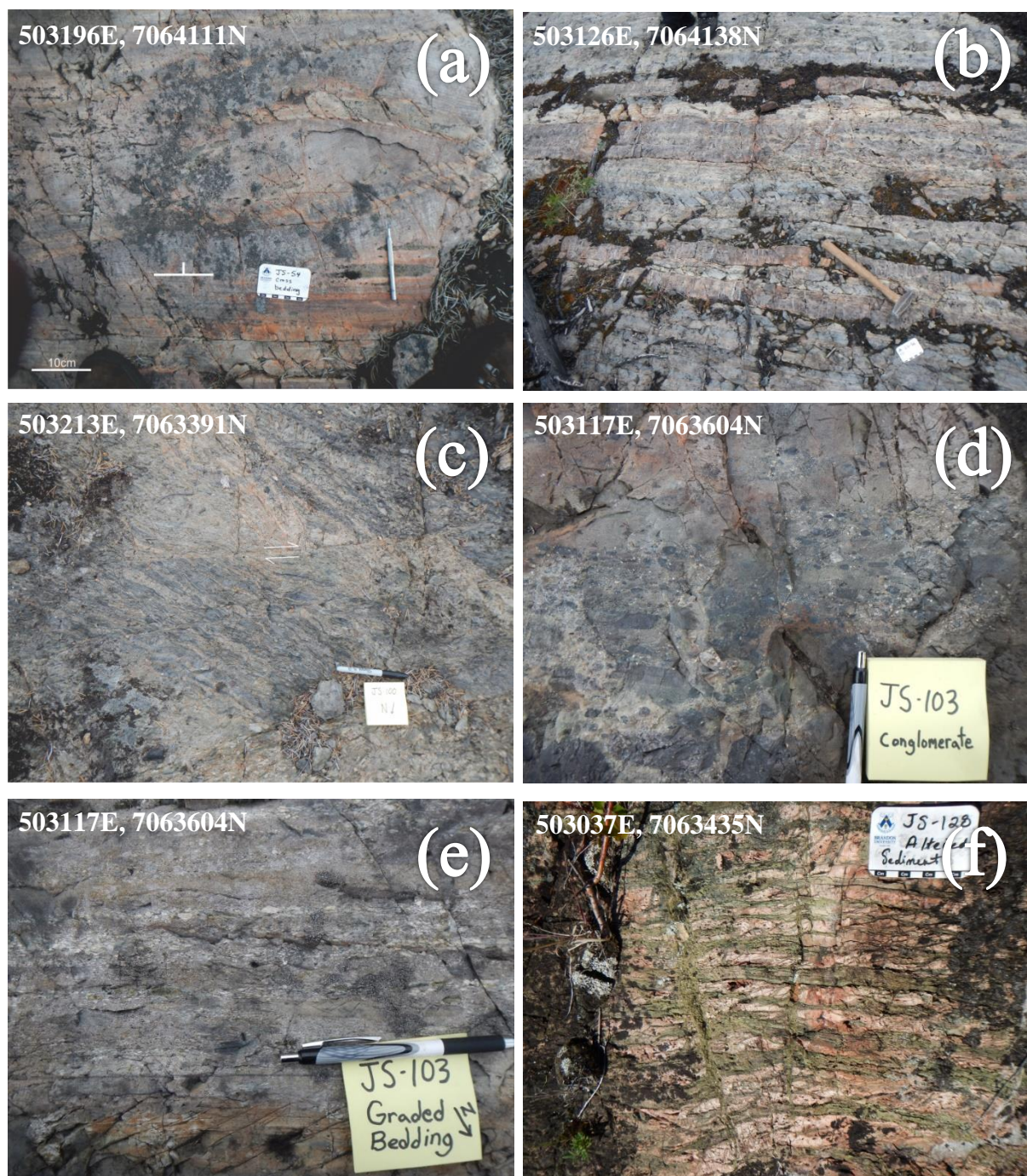


Fig. 14. Outcrop photographs of several different facies and textures of volcanoclastic sediments (VS) that are discussed in this thesis: (a) JS054: Cross bedded arkosic siltstone with beds of cherty muds. (b) JS056: Interbedded tuffaceous unit of fine-grained ash and mud. (c) JS100: Right laterally displaced, deformed thin bedded sediment. (d) JS103: Well bedded, strongly magnetic, matrix supported, monomictic conglomerate. (e) JS103: Same outcrop as previous with stratigraphic indications highlighted. (f) JS128: Selective alteration and replacement of sedimentary layers with epidote. Reference system for coordinate data is UTM NAD83 zone 11.

phenocrysts- typically ~1 – 3%. Several facies of the ignimbrite sheets are visible in the outcrops including ash tuffs, crystal tuffs and volcanic breccias. Macroscopic trachytic textures are also visible in several outcrops within most of the ignimbrite layers (Gandhi et al., 2001).

(c) Lou Lake Assemblage

The main exposed extent of the Lou Lake volcanic assemblage (LL, Figs. 8, 9, 11) is south of the study area, near the NICO deposit and in vicinity of Lou Lake (Gandhi et al., 1996, 2001). At the southeastern end of Mazenod Lake, the Lou Lake assemblage is the eastern and western limit of the local volcanic belt. The chemical composition of these rocks is transitional between rhyodacite and andesite. Textural variations include forms of ash, lapilli and crystal tuffs. Locally stretched fiammé and eutaxitic textures are commonly visible in outcrop. Measurements of the volcaniclastic textures taken from the western portion of the Lou Lake rocks dip ~75° NE while the eastern rocks dip in the opposite direction at ~75° SW. The rocks typically contain 5 – 30% phenocrysts of feldspars that are 0.5 – 3 mm in size and 3 – 4% quartz crystals that are microscopic to 2 mm in size. Within the explored outcrops, very fine-grained biotite crystals are present in minor to trace amounts. At the northern border of the assemblage it is intruded by a monzogranite pluton and right laterally offset by the Marian River fault.

Nod Hill rocks are grouped with the Lou Lake assemblage in the geologic maps (Figs. 8, 9), consistent with their spatial association and a pre-existing mapping interpretation of Gandhi et al. (2001, 2013). Despite the similar grouping demonstrated in the geologic maps for this report, the Nod Hill rocks have a unique chemical composition. Their distinctiveness is defined by a deficiency of REEs as compared to other rocks in the region (see Chapter 7, Fig. 28.).

Most of Nod Hill is intensely hydrothermally altered, making specific and accurate descriptions of the precursor rock difficult. The following lithology descriptions are derived from

the southern portion of Nod Hill where the least altered rocks are visible. The representative samples from Nod Hill are rhyodacite crystal tuffs that contain 7 – 12% phenocrysts of 1 – 2 mm feldspars as well as 2 - 3% quartz phenocrysts that are 2 - 3 mm in size. The phenocrysts are hosted within an aphanitic matrix that is greyish on the fresh surface. Weathered surfaces of the rock are generally pinkish orange to a brick red color. The intensity of alteration is strongest at the northern portion of the hill in close spatial association with faults that cut across Nod Hill. This area is an excellent example of the spatial association between hydrothermal alteration and faults, where intensity of alteration has a direct correlation to proximity and intensity of faulting. The strength of the hydrothermal alteration is exemplified by large-scale actinolite breccias that transition to massive magnetite and magnetite-cemented breccias exposed on the face of a fault-generated scarp. Crackle breccias are a common structural observation in the higher-intensity alteration zones. The breccias are typically cemented with either massive magnetite and/or a coarse-grained to megacrystic actinolite, often accompanied by quartz. The brecciated and intensely altered rock lies along a dextral shear zone, a continuation of the Kemaz fault (Ketcheson Lake-Mazenod Lake fault), that trends NNE-SSW and terminates at the Sue-Dianne deposit (Gandhi et al., 2001). This transverse right lateral fault bisects the center of Nod Hill with an offset of a few 10s of meters. The unique rocks from Nod Hill appear to be entirely constrained within the Lou Lake volcanic assemblage, although they may extend further to the south and/or southwest below overburden.

Unconformably separating the western portion of the Lou Lake assemblage from the younger Squirrel Lake assemblage is an almost 2 km wide range of volcanic derived sedimentary rocks. The eastern portion of the Lou Lake assemblage has a direct contact to both the Squirrel

Lake assemblage and the Dianne Lake assemblage. Geopetal markers show that the Squirrel Lake and Dianne Lake assemblages are stratigraphically younger than the Lou Lake assemblage.

(d) Squirrel Lake Assemblage

The Squirrel Lake assemblage (SL, Figs. 8-11) refers to a newly identified dacite ignimbrite flow. Typical exposed outcrops of this volcanoclastic assemblage are massive crystal tuff facies, with textures that are sometimes seriate and locally trachytic. Exposed lapilli and breccia volcanoclastic facies exist in the southwestern portion of the Bea area (Fig. 11). There is also at least one example of a layer of the dacite containing quartz amygdules. The assemblage is consistently rich in 2 – 5 mm diameter plagioclase phenocrysts that range from 15 - 30% modal abundance. Often the rock contains biotite up to 5 modal % and 1 - 2 mm in diameter.

Volcanic breccia found in the southwestern portion of the Squirrel Lake assemblage is monomictic, containing subangular clasts from 1 - 40 cm in size. It is mostly matrix supported but locally clast supported. Dark grey-black clasts make up ~20% of the breccia and are very strongly magnetic (~70% magnetite estimated volume), unlike the red-grey matrix material. Feldspar phenocrysts within the clasts are oriented along the same axial direction as the clasts.

(e) Bea Lake Assemblage

The Bea Lake volcanic assemblage (BL, Figs. 8-11) occupies the center of the volcanic belt. It is comprised of a relatively mineralogically uniform andesite ignimbrite. The extent of the assemblage ranges from almost 3 km southeast of Sarah Lake to approximately 1 km north of Lou Lake (Gandhi et al., 1996, 2001). Volcanoclastic rock facies vary from ash tuff, to lapilli tuff, to pyroclastic breccia. The Bea Lake assemblage had previously been identified as rhyodacite by Gandhi et al. (2014), but has been reclassified in this work as andesite to reflect the classification schemes of Pearce (1996) (Chapter 7, Figure 28). Bedding measurements show

a consistent dip of $\sim 70^\circ$ NE on the east and south end of Mazenod Lake, whereas it dips $\sim 70^\circ$ in a more northerly direction west of the lake.

The typical andesite within the Bea Lake assemblage contains up to 30% plagioclase euhedral phenocrysts that range from 1 – 6 mm in size. The andesite also contains varying quantities of quartz phenocrysts from 5 - 30% that are 1 – 6 mm in diameter. Phenocrysts are hosted within a light to dark grey aphanitic matrix.

On Dan Island, the contact between the andesite and rhyodacite is difficult to define as the entire island is intensely and pervasively hydrothermally altered. Many of the outcrops on the island are intensely potassic altered. The most intense of the potassic altered rocks are found in rocks at the highest elevation, near the center of the island and adjacent to part of the Kemaz fault. There are also several other examples on the island of other hydrothermal alteration products, including varying quantities of tourmaline, magnetite, hematite and/or epidote. Less abundant, although still present throughout the island in differing concentrations are sulphides such as pyrite, chalcopyrite and pyrrhotite.

(f) Mazenod Lake Assemblage

The exact stratigraphic position of the Mazenod Lake assemblage (ML, Figs. 8-9) is not clear from the 2013 field mapping; however, previous work of Gandhi et al. (2001) and Camier (2002) suggest the volcanic assemblage is the oldest product of volcanic activity exposed at surface. These volcanic rocks extend from the northern shore of Mazenod Lake to almost 4 km north, near Dianne Lake. The surface showing of the Sue-Dianne deposit is constrained within the Mazenod Lake volcanic assemblage (Goad et al., 2000; Gandhi et al., 2001; Camier, 2002; Mumin et al., 2010; Gandhi, 2013).

The explored portion of the Mazenod Lake assemblage is dominantly comprised of rhyodacite crystal tuff. On average, these rocks contain ~10 – 15% feldspar phenocrysts that are ~1 – 3 mm in diameter within a light grey aphanitic matrix. In local areas, pitting was identified indicating weathering of sulphides. The fresh surface of the rock is generally a light grey color. No significant structures were observed in the outcrops during the 2013 mapping project; however, Gandhi (2013) reported shallow bedding in the rhyodacites oriented at 25 – 30° NE.

Hydrothermal Alteration

Rocks in the Mazenod Lake region have been pervasively affected by hydrothermal alteration (Fig. 15). Field observations include examples of magnetite \pm actinolite (MA), potassic, sodic, hematite, magnetite, phyllic, tourmaline, propylitic and silica alteration types. Silication is also visible in core samples that originate from a drill program completed by Phelps Dodge in 2005. These alteration types are all commonly associated with IOCG systems, which are also present throughout the GBMZ (Mumin et al., 2007; Corriveau et al., 2010; Mumin et al., 2010; Montreuil et al., 2013).

(a) Magnetite \pm actinolite (MA) alteration

Magnetite \pm actinolite (MA) alteration occurs in several different mineralogical combinations and textural forms in local areas throughout the Mazenod Lake region (Figs. 15a, 15b, 15c). Most often this alteration is visible as veinlets of very fine-grained dark green actinolite often accompanied with trace amounts of magnetite. Alteration visibly strengthens in intensity from a minor presence of veinlets to areas with more widespread veining and examples of megacrystic actinolite resembling pegmatite. This occurs significantly at Nod Hill where

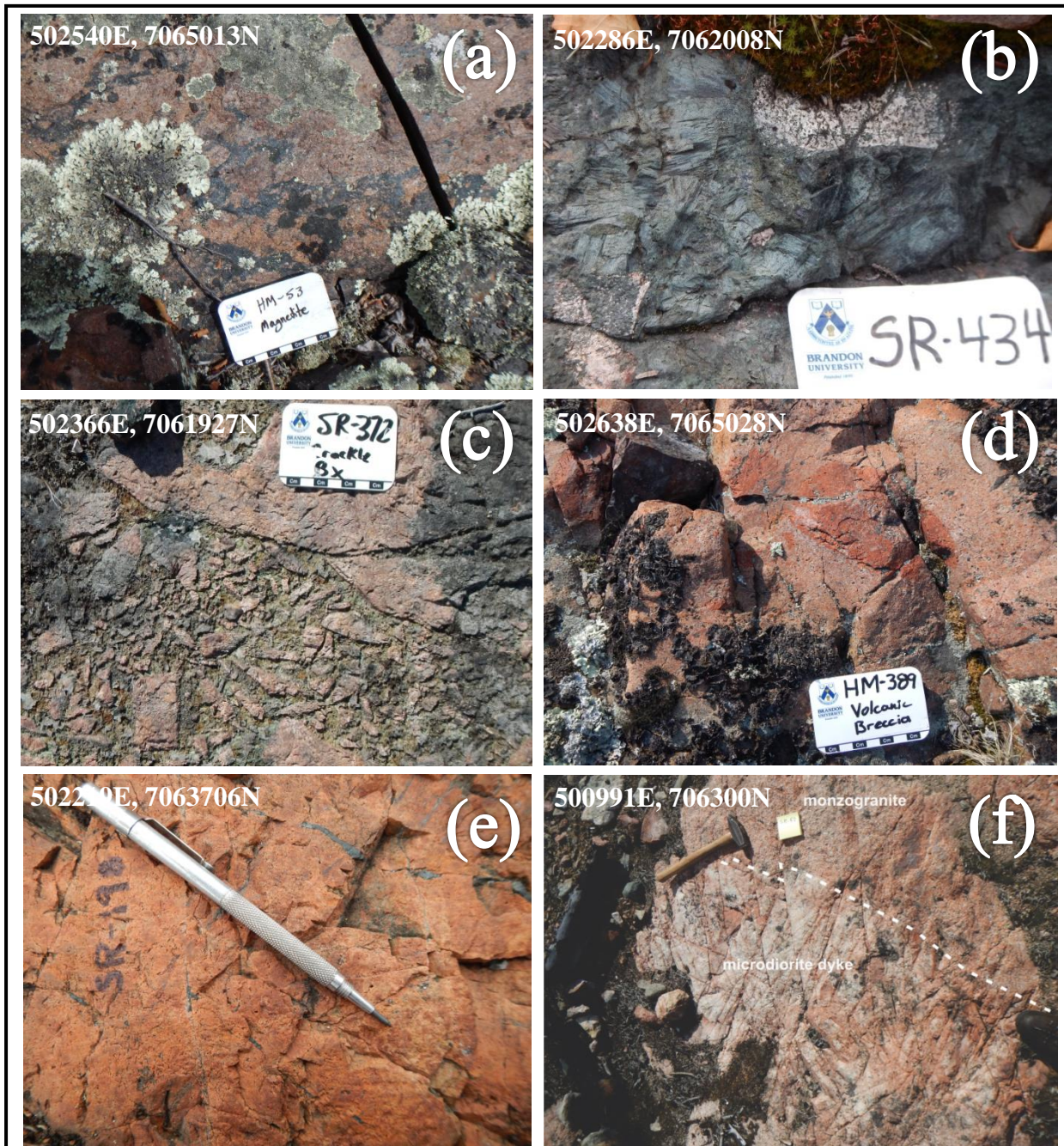


Fig. 15. Outcrop photographs of hydrothermal alteration types discussed in this thesis: (a) HM053: Crystal tuff containing magnetite veins throughout the rock, up to >5cm in diameter, (b) SR434: Megacrysts of actinolite form in zone of MA alteration; the host rock is largely brecciated and cemented with predominantly massive actinolite, (c) SR372: Crackle breccia that is cemented by actinolite-quartz-magnetite alteration minerals, (d) HM389: Fractured volcanic breccia with a strong potassic alteration overprint that affects more permeable volcanic bombs greater than host rock, (e) SR198: Brick red hue from a micro-dusting of hematite within a dacite ignimbrite. Also contains veins of specular hematite, (f) SR052: Pervasive potassic alteration and chemical weathering that affects both the monzogranite and an intruding dyke.

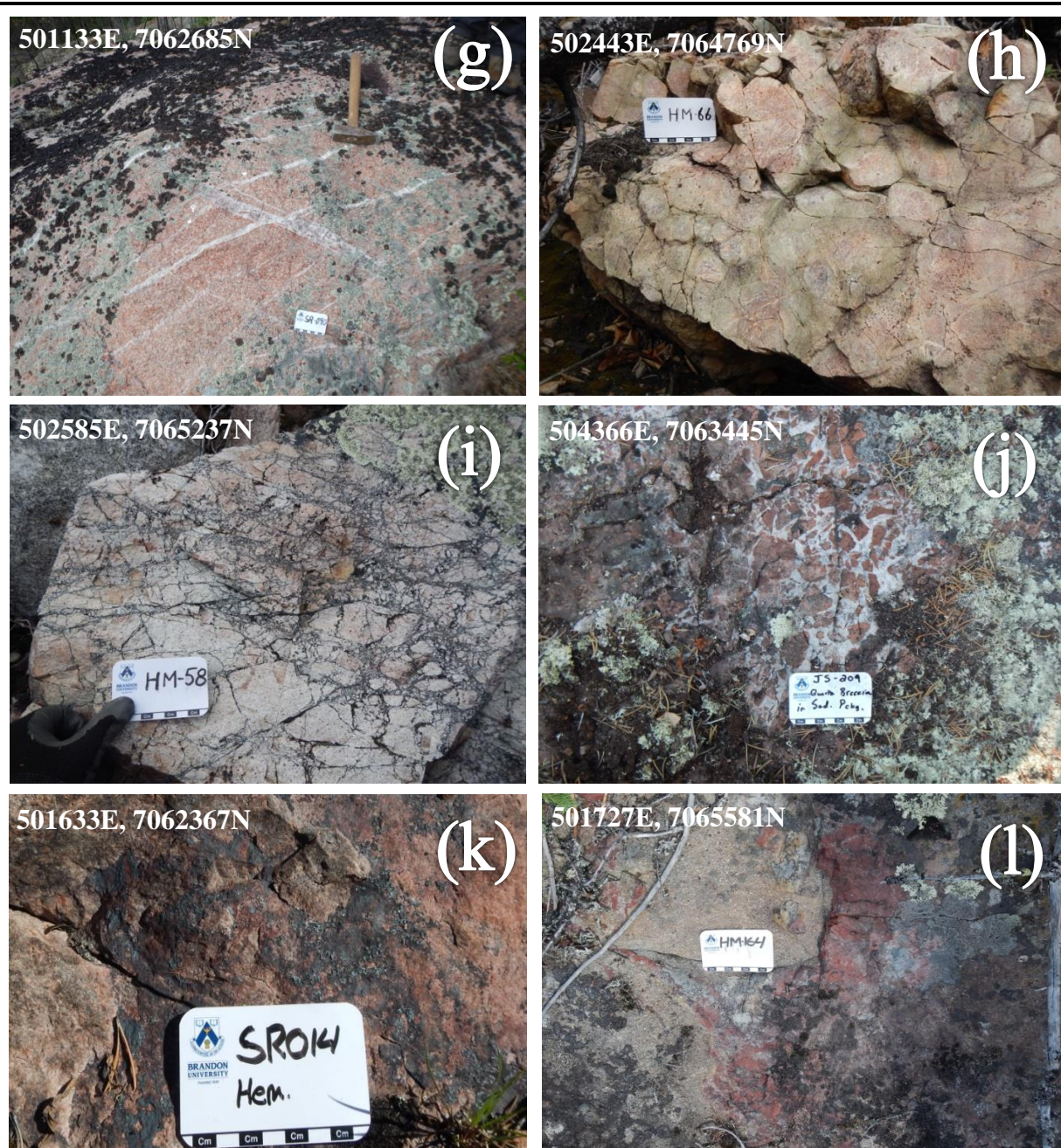


Fig. 15 (cont.). (g) SR090: Coarse grained monzogranite inundated by a stockwork of quartz veins and silica flooding, (h) HM066: Green staining along fractures representing epidote alteration within an intersection zone between two conjugate fracture sets, (i) HM058: Tourmaline cemented crackle breccia. Host crystal tuff was potassic altered prior to being brecciated and cemented, (j) JS209: Autochthonous sedimentary rock brecciated and cemented with quartz, (k) SR014: Specular hematite associated with fractures in a crystal tuff, also contains trace amounts of magnetite, (l) HM164: Jasper stockwork within a crystal tuff, also associated with local quartz-epidote veining. Reference system for coordinate data is UTM NAD83 zone 11.

abundant stocks, veins and masses of actinolite \pm magnetite \pm quartz replace and cross-cut the rhyodacite host rock. The most extreme cases of MA alteration are large crackle breccias, where megacrysts of actinolite \pm magnetite \pm quartz cement fractured host rock. While magnetite and actinolite are often found together they also exist independent of each other.

The most commonly associated accessory mineral observed with MA alteration is epidote, which typically rims actinolite or directly cross-cuts of MA altered rocks. Outcrops also often contain trace amounts of pyrite \pm chalcopyrite \pm pyrrhotite that coexist with MA alteration. The mineralization generally occurs as clots of subhedral sulphides, occurring within or along the outer edge of veins of actinolite \pm magnetite.

(b) Potassic alteration

Potassic alteration (K-feldspar \pm magnetite \pm biotite \pm hematite \pm sericite) is ubiquitous throughout the Mazenod Lake region, although it varies in intensity (Figs. 15d, 15e, 15f, 15g, 15h, 15i). Typically, the potassic alteration is recognizable as a pinkish color, orangey-brown, or bright orange hue. The altered rocks visibly change shades of color according to intensity and style of potassic alteration. Locally, potassic alteration occurs as K-feldspar veins and/or veinlets. All other types of alteration identified in the field exist in conjunction with the widespread potassic alteration or occur independently. Paragenetic evidence from cross-cutting and overprinting features that replace the pervasive K-feldspar alteration indicate there was an early regional phase of widespread potassic alteration (Fig. 15e).

The highest recorded scintillometer readings (K: 8.6 wt. %) and highest reported lithogeochemical values of K₂O content (12.8 wt.%) were identified at Dan Island and correlate with observations of the most intensely potassic altered rocks. At Dan Island, the alteration reaches greatest intensity at the highest elevation near the Kemaz fault, which crosses the center

of the island. Spatial association between intensity of potassic alteration and this significant fault suggests that it was major hydrothermal fluid conduit. Camier (2002) made a similar interpretation of the Kemaz fault another 4 km NE of Dan Island at the Sue-Dianne deposit.

(c) Tourmaline alteration

Tourmaline alteration typically occurs as black sooty veins and veinlets that range from mm to cm scale, with few local examples of massive replacements. The alteration is found locally throughout the study region in all types of rocks, but is dominant in the Bea area and NW end of Dan Island. Potassic, epidote and/or hematite alterations are often associated with or proximal to tourmaline altered rocks. Pyrite and lesser chalcopyrite sulphides are also commonly associated with tourmaline alteration in the Bea area. The mineralization locally occurs as clots of subhedral sulphides or disseminated within massive tourmaline in trace quantities.

One of the most intense tourmaline altered zones is along the northwest side of Dan Island, where the tourmaline occurs as cement for a crackle breccia (\pm hematite) overprinting potassic altered rocks (Fig. 15i). In the Bea area, the tourmaline alteration is more wide-spread, with local bodies of a massive replacement of host ignimbrites that can be greater than 5 m².

(d) Hematite alteration

Hematite alteration occurs as a local massive replacement, fracture/vein fill or as disseminated specularite throughout the region, in all rock types (Figs. 15a, 15k, 15l). Veins and disseminated instances of hematite are typically a black, dark brown or reddish-brown color, locally accompanied by a reddish oxidized stain surrounding the minerals. Hematite alteration is also manifest in outcrops by a brick red color that occurs in the vicinity of fractures and encompassing wide zones at Dan Island, Nod Hill and in other local areas. The red color is

thought to be a result of submicron inclusions of hematite within K-feldspar and possibly other minerals.

Local hematite alteration exists independently of other alteration minerals, occurs along with magnetite veins, within tourmaline crackle breccia, and in conjunction with silicified rocks across the study region. Jasper (quartz with embedded hematite) also occurs, dispersed throughout the field mapped area in comparatively rare instances.

(e) Phyllic alteration

Phyllic (sericite, quartz \pm pyrite) alteration occurs locally throughout the Mazenod Lake region. More often, quartz and sericite occur together or independently and typically absent of any sulphides. Thin section studies of on both igneous and volcanic rocks show that microscopic sericite \pm quartz is widespread as pseudomorphic replacement of groundmass and feldspars phenocrysts. This microscopic sericite is not visually identifiable in hand sample. For example, hand samples taken from the intrusion immediately west of Net Ridge contain apparently euhedral feldspar phenocrysts; however, thin section analysis shows the feldspars to be strongly sericitized. Partial sericite pseudomorphs after feldspar indicate that the presence of sericite is a result of destruction of feldspars.

(f) Epidote alteration

Epidote alteration (epidote \pm quartz \pm carbonate \pm chlorite \pm sericite) is one of the more common alteration types found in the Mazenod Lake region (Fig. 15h). Epidote alteration usually occurs as mm to cm-scale ‘pistachio’ green veins, which exists locally throughout the study region. In relatively rare cases, massive epidote replacements and hydrothermal breccias exist, which are typically only a few square meters. For example, approximately 350 m SW of Dan Island is another island that contains a crackle breccia cemented by massive epidote.

The microscopic studies have identified epidote veins that cross-cut and replace pre-existing actinolite veins and recrystallized K-feldspar, suggesting that epidote alteration is a younger alteration than MA and potassic alteration.

(g) Silicification

The most predominant silicification occurs along NE-SW oriented transcurrent faults, which are cemented by silica to form giant quartz veins. Along the faults and in proximity to them are milky white quartz stockworks, hydrothermal breccias, veins, and massive pseudomorphic replacements (silica flooding) (Figs. 15g, 15j). Any other silicification within the region is typically associated with subsidiary fractures/faults adjoining the transcurrent faults. Hematite (as specularite) is an associated hydrothermal alteration mineral, which occurs disseminated along the giant quartz veins. Sulphides are typically distinctly absent from zones of silicification; however, a uraninite showing on the western side of Net Ridge along the Marian River transcurrent fault was drilled by Noranda in the 1970's. There is also a small quartz flooded outcrop a few square meters in size located at UTM NAD83 zone 11 499931E, 7064456N (± 5 m) that contains 1-2% euhedral pyrite grains.

Mineralization

Several varieties of mineralization have been observed across the extent of the Mazenod Lake region, although not in significant quantities. Over the course of the regions exploration history Cu, Mo and Co as well as U and LREE-bearing minerals have been discovered. Chalcopyrite (CuFeS_2) is the most common metal-bearing mineral observed in the region. Concentrations of the chalcopyrite and other metal-bearing minerals is typically minor. The highest recorded values of chalcopyrite occur in a few isolated portions of outcrops, estimated up to 5% by volume. The rest of the metal-bearing minerals, such as cobaltite (CoAsS) and

uraninite (UO_2) are present in minor to trace amounts, also within isolated areas. The copper and cobalt sulphides are characteristically accompanied by their weathered mineral products including malachite ($\text{Cu}_2\text{CO}_3(\text{OH})_2$) and erythrite ($\text{Co}_3(\text{AsO}_4)_2 \cdot 8\text{H}_2\text{O}$), respectively. For field identification, distinctive patches of gossans that are rusty in appearance are a good indication of sulphides (typically trace amounts of pyrite, FeS_2) within a few cm of the surface.

Cobaltite and erythrite was discovered during the course of 2013 field work on an island <1 km northeast of Dan Island (Fig. 9, 10). The Co-bearing minerals are accompanied by chalcopyrite and pyrite, all of which are in trace quantities and hosted in the Bea Lake assemblage andesite crystal tuff. Cobalt minerals are restricted to the islands east of Dan Island; however, the pyrite and chalcopyrite have also been found on several of the surrounding islands. Equant pitting is abundant in these areas, particularly on the eastern side of Dan Island, indicating weathering of pyrite and potentially other sulphides.

A minor amount of uraninite is visible at surface at the SW portion of Net Ridge (Fig. 9). The uranium mineralization is located at the contact between the Lou Lake volcanic assemblage and the Sarah Lake monzogranite, along the Marian River fault. Exploration trenches expose the showing of mm-scale veins of uraninite. Local alteration surrounding the showing includes the presence of drusy quartz and specular hematite.

The LREE-bearing mineral allanite ($(\text{Ce,Ca,Y,La})_2(\text{Al,Fe}^{+3})_3(\text{SiO}_4)_3(\text{OH})$) is recognizable in core samples originating from the Phelps Dodge 2002 drill program (Hamilton, 2013). Extent and quantity of allanite within the drill core is currently unknown.

Several magnetite-garnet –pyroxene skarn sections were identified in the core as well, which contain notable quantities of pyrite, chalcopyrite and pyrrhotite. Core logging performed by Phelps Dodge geologists had previously incorrectly identified the skarns as magnetite-

amphibole-epidote altered rocks (Kulla, 2004). A forest fire resulted in damage to the core samples and boxes that prevents correlation of the core samples to depth of drilling and drill collar location.

Molybdenite (MoS_2) was observed by Gandhi (2013) at UTM coordinates 500010E, 7064478N (± 5 m), on an island west of Dan Island. The molybdenite was not encountered during 2013 field work, and the extent of the mineralization is not known.

Chapter VI: Structural Analysis

Crustal structures play an important role in the formation and location of IOCG-type mineralization and hydrothermal alteration (Williams et al., 2000; Williams et al., 2005; Richards and Mumin, 2013b; Mumin et al., 2014). This chapter presents the analysis of the Mazenod Lake region structural framework with an examination of lineaments derived from remotely sensed imagery. These linear features generally represent surface expressions of geologic features, alteration effects and/or structural disruptions within the subsurface. As a consequence, local supracrustal deformation can be partially revealed by maps and diagrams that illustrate the distribution of lineaments. With a basic understanding of structure in the lithosphere and geology of the region interpretations can be made with respect to geotectonic setting and evolution. Knowledge of the structural framework also provides evidence of tectonic conditions at the time of magmatism, hydrothermal alteration, and ore deposition.

Lineament Definition

Lineaments have long been acknowledged and used for their representation of structure in the lithosphere (Richards, 2000). Definitions of lineaments have arisen from a number of investigations (e.g. Hobbs, 1904; O’Leary et al., 1976; Gabrielsen et al., 2002; Galkin, 2010; Soto-Pinto, 2013); however, a slightly modified definition from Galkin (2010) represents the most useful characterization of lineaments for this study. In this thesis, lineaments are interpreted and derived from satellite images, airborne magnetic survey data and digital elevation data as linear and arcuate visually contrasting features.

Methodology

Interpretations of possible structural features within bedrock are based on a visual inspection of lineaments from a satellite image, aeromagnetic data and digital elevation model. Lineaments unrelated to geologic structure (such as anthropogenic features) are not included in structural interpretations. The subjective determination and classification of lineaments is corroborated by structural data acquired during the 2013 field season and correlation between the remotely sensed images. This is a necessary step for validating lineaments reflecting real anomalous physical properties on the earth, such as individual rock bodies (e.g. dykes, sills, layers or intrusions) or fault ruptures. Human bias and error precludes every structure being drawn accurately in this subjective interpretation; however, it is an effective method of deriving an understanding of the local structural framework.

An overview of the methods used in this study to derive and analyze lineaments is described in more detail below:

(a) Lineament and lineament intersection delineation

The process of identifying and extracting lineaments is a manual process. Linear and curvilinear features are drawn directly on geophysical or satellite images with the use of both CorelDraw and ArcMap software. To prevent any systematic errors, no automated techniques for extracting lineaments are applied in this study. Lineaments are categorized on the basis of calculated vertical gradient on the aeromagnetic map or extent of topographic features from the satellite image. Selection of lineaments is based on their importance to the local tectonic framework, i.e. anthropogenic features are not included as a lineament. The lineament intersections are extracted using the Arcmap intersect tool, which creates a map of georeferenced points where lines intersect.

(b) Analysis of lineament orientations

To analyze and portray preferred orientations and directional data of lineaments a circular histogram (rose diagram) is depicted along with each lineament map. The radial distance on the rose diagrams indicates relative frequency of a lineament at a specific azimuth. Orientation data of the lineaments (called polylines in ArcMap) is extracted by use of a custom-made ArcMap function. The function reports in spreadsheet format (.csv) the angle of each polyline relative to north, from the beginning of a polyline and every 5 m to the end of the same polyline. The orientation data includes all orientations within curved lines as well as straight lines, without adding any significance to any one type of line preferentially. The spreadsheet data is then imported into the freeware program GeoRose that generates rose diagrams for each category of lineament (Georose v. 0.51, 2014).

(c) Analysis of the population density

Lineament intersections are derived from the lineaments using the intersect tool in ArcMap software. ArcMap uses a kernel function based on the quadratic kernel function developed by Silverman (1986) to calculate density fields. The line (lineaments or polylines) and point kernel density functions in ArcMap conceptually fits a smooth curved surface around each lineament or point. Greatest density is in areas containing the most length of lineaments or points per square km. The search radius parameter is set to 1 km, which produces a more generalized density raster. Selected output cell size parameter is the aerial extent of the environment analyzed, which is set to the area within the satellite image. Individual lines and points are weighted equally.

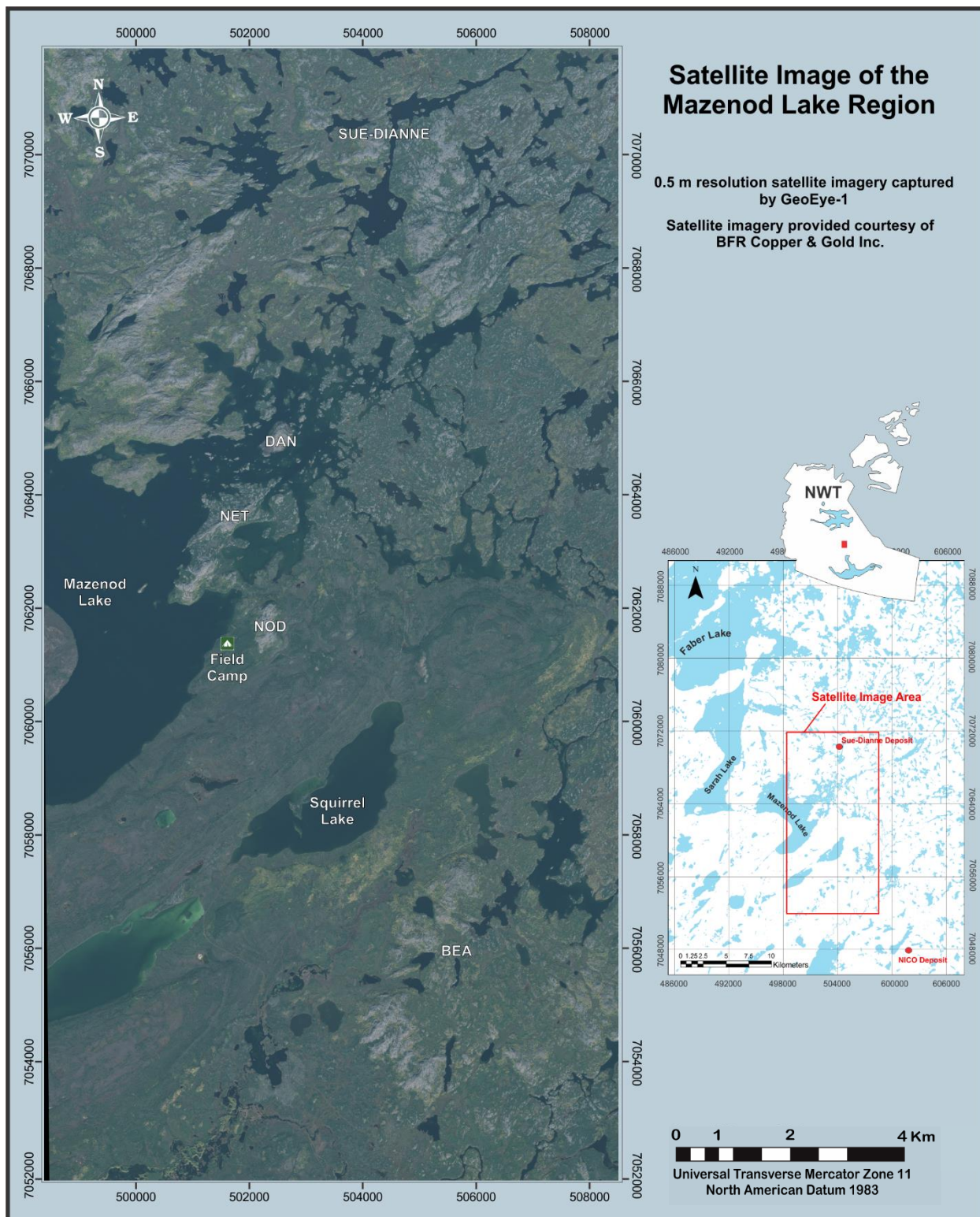


Fig. 16. Geo-eye 1 satellite image of the Mazenod Lake region.

Satellite Image

BFR purchased the GeoEye-1 satellite image in 2012 and provided it for use in this investigation (Fig. 16). Spatial resolution of the satellite image is 0.5 m. Details visible on the satellite image are to the extent that individual trees and, more importantly, geologic structures can be identified with the naked eye with little difficulty. Bedrock exposure in the Mazenod Lake area is excellent, although still less than 25% overall coverage within the extent of the satellite image. The exposed bedrock tends to be concentrated in the northern portion of the satellite image and southeastern corner. Lakes and rivers are also shown to cover approximately 25% of the study area. The rest of the satellite image shows that the ground is mostly covered with forest

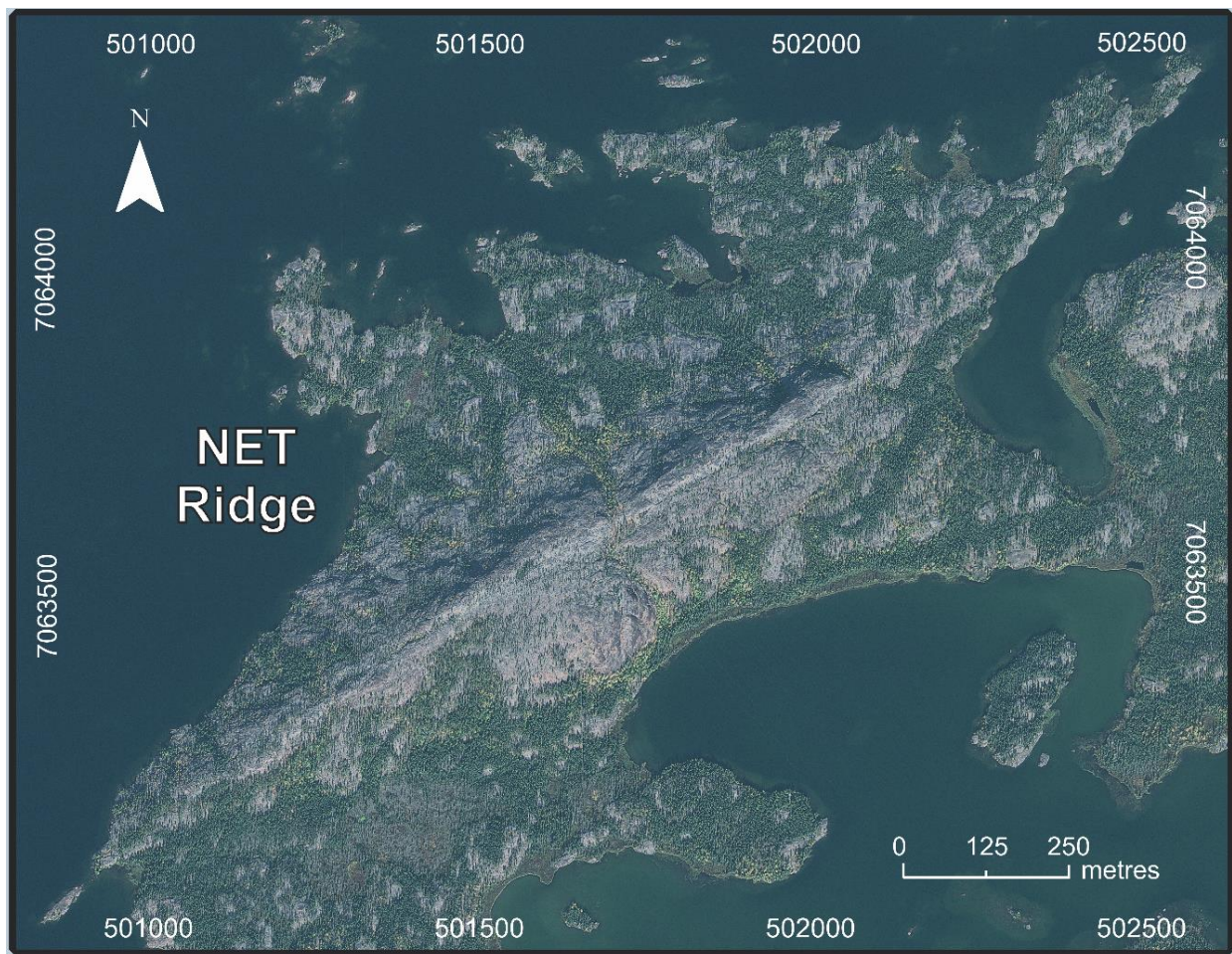


Fig. 17. Close-up image of Net Ridge, Mazenod Lake region, NWT.

and swamp. The degree of satellite image detail is better illustrated in the close-up image of Net Ridge shown in Figure 17.

Aeromagnetic Data

Aeromagnetic surveys are important for geologists because of the general correlation of magnetic susceptibility data to subsurface geology, structure and hydrothermal alteration. Unlike the satellite image, this magnetic data has a uniform coverage of the area surveyed and is not dependent on the presence of outcrop for providing useful information.

Goldak Airborne Surveys flew a high-resolution airborne magnetic survey in the fall of 2012. The survey was flown at 60 m height with traverse line spacing of 50 m and control line spacing 500 m. Direction of the traverse was $90^{\circ}/270^{\circ}$ with a control direction at $0^{\circ}/180^{\circ}$. The magnetic system on the plane utilized two vertically separated tail mounted and two wing tip mounted cesium vapour magnetometers arranged in a three-axis gradiometer configuration. Goldak Airborne Surveys also performed final processing, leveling, gridding and production of illustrated aeromagnetic data. Processing of the magnetic data included generation of a measured vertical gradient (MVG) map (Fig. 18), which is better at displaying near surface magnetic sources than total magnetic field measurements. The magnetic field gradient data has a greater variance than total field magnetism; therefore, it shows a higher spatial resolution and is useful for delineating linear surface features. Although there have been high-resolution aeromagnetic surveys completed within the Mazenod Lake region prior to this investigation, spatial resolution is significantly more detailed in this new data (see Hetu R.J. et al., 1994 open file 2806 for regional aeromagnetic data). BFR provided the aeromagnetic data for use in this study.

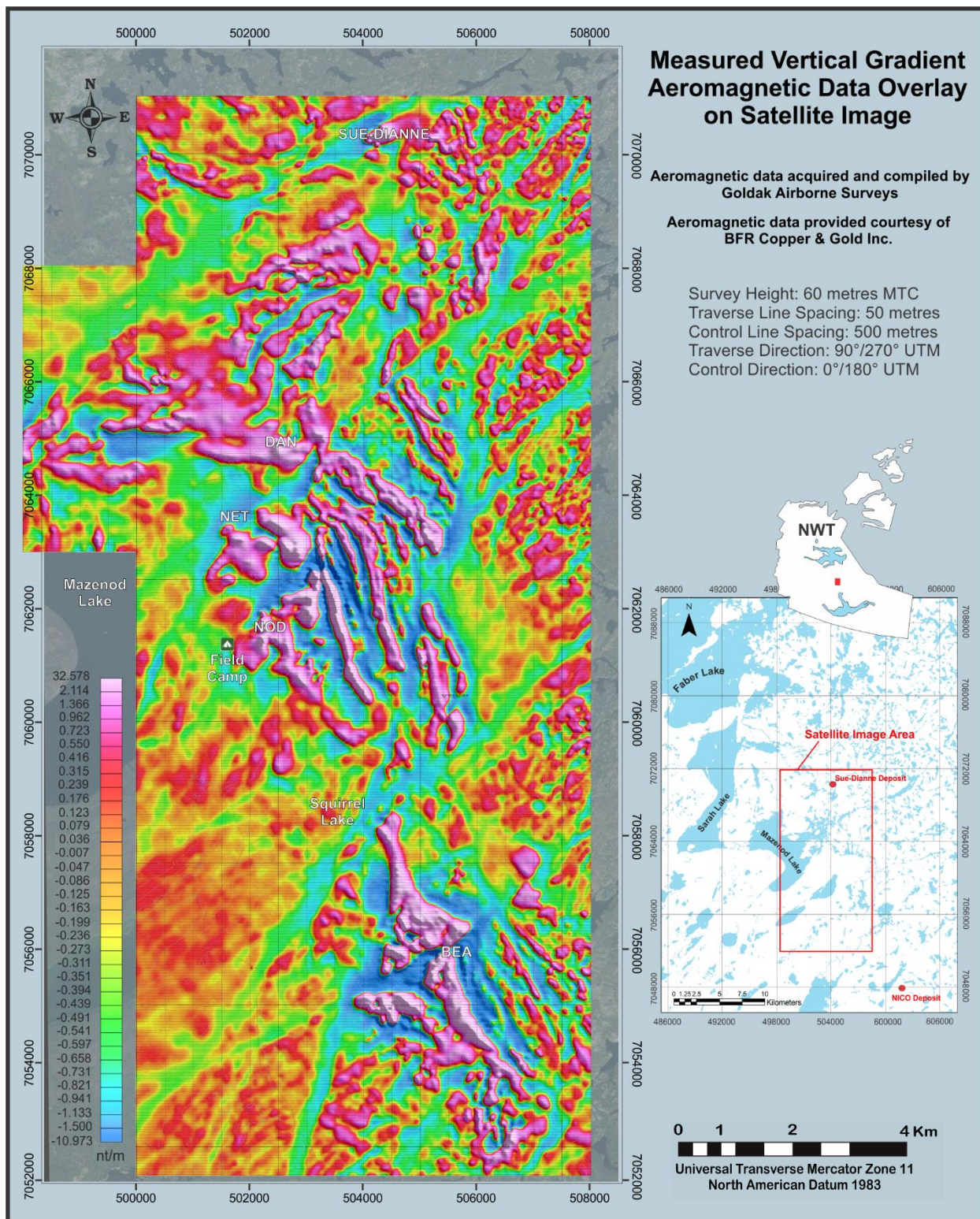


Fig. 18. Magnetic vertical gradient (MVG) data layered over Geoeye-1 satellite image.

Digital Elevation Model (DEM)

Digital elevation data was also provided for this study by BFR. Areas with differential relief are significantly more distinct on the DEM than the satellite image (e.g. Paleozoic strata). The contrasting elevation data is used in this study to link topographic relief to physical and magnetic data lineations. A visual representation of the differential relief also allows for the delineation of lineaments that would otherwise be invisible and can improve the accuracy of orientations of lineaments derived from the satellite imagery. ArcMap software was used to construct the digital elevation model (Fig. 20).

Elevation in the Mazenod Lake area ranges from 194.7 m to 348.9 m above sea level. Highest elevation features include quartz cemented fault structures, areas covered by Paleozoic strata and a few isolated circular features with pervasive hydrothermal alteration, such as Dan Island. Lowest elevation areas include Mazenod Lake, rivers and the southwestern portion of the DEM.

Field Mapping

Without a reliable geologic understanding of a region, it would be impossible to accurately correlate the satellite image and geophysical data to real supracrustal structures. A 1:2000-scale field mapping program resulted in the construction of several detailed geologic maps (Chapter 5, Figs. 8 to 11). These maps, along with field notes and field experience form the basis for correlation of lineaments and geologic structures. Field structural observations are summarized in Figs. 19a, b.

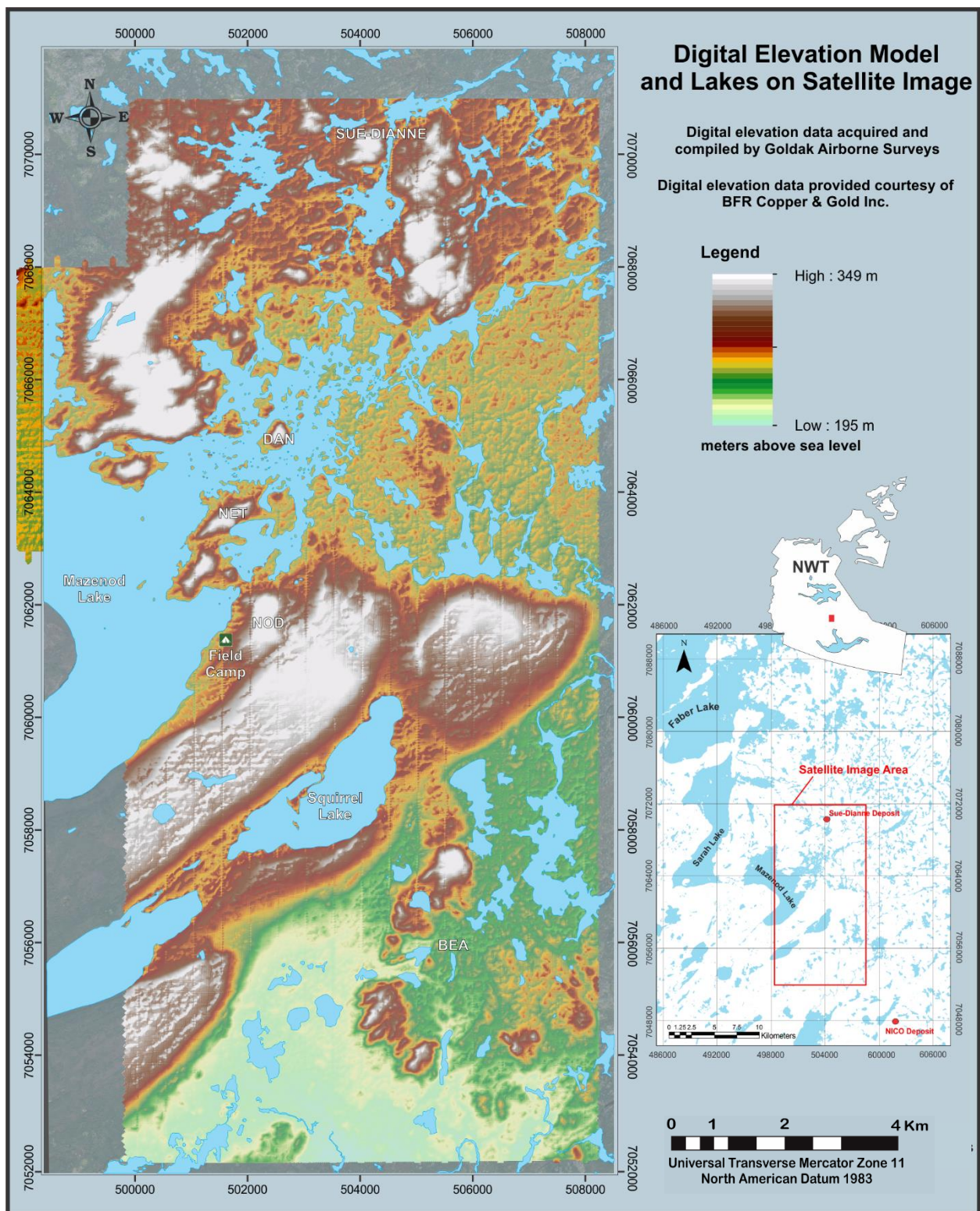


Fig. 20. Overlay of digital elevation data and lake/river outlines on Geoeye-1 satellite image.

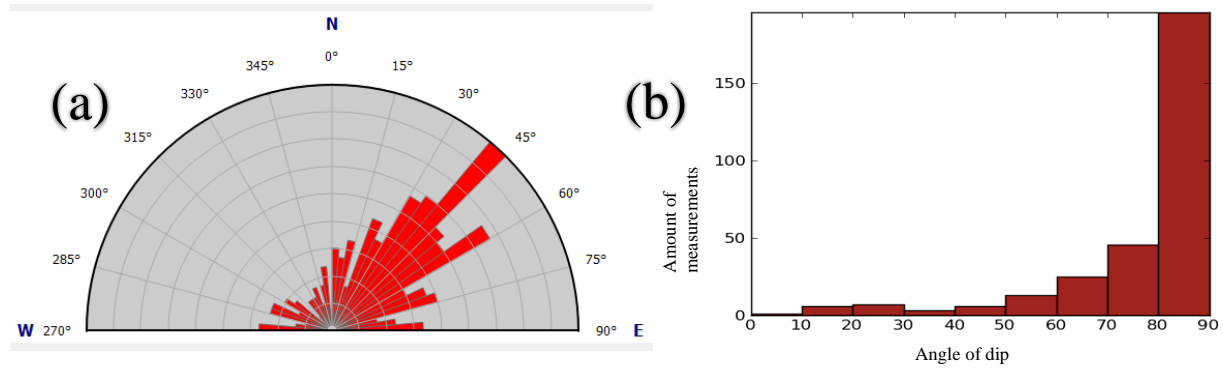


Fig. 19. (a) Half rose diagram showing the frequency of strike direction measurements taken in the field for faults, fractures and vein structures. (b) Histogram diagram showing the frequency of dip angle measurements taken in the field for fault, fracture and vein structures. N=303.

Satellite Image Lineaments

Lineaments extracted from the high-resolution satellite image occur as linear and curvilinear features that represent topographic features, such as: ridges, valleys, depressions, lake/island morphology, or shallows (Fig. 21). The linear features are easily recognizable by visually distinct expressions of topography (e.g. rivers, shallows, depressions and prominent elevation contrasts). Similar studies have shown that lineaments extracted from satellite images correlate well with geological features at all scales of observation (Mumin et al., 2014). The lineaments are commonly considered to be a result of different rates of erosion and weathering over long periods of time (predominantly from glaciation, but also from interglacial weathering) that highlights contrasting competency across the lithology. The excellent outcrop exposure in the Mazenod Lake area is particularly effective at revealing structure. Therefore, lineaments on remotely sensed images will often represent faults, shear zones, brecciated structures, differentially hydrothermally altered rock, and/or lithological contacts. The interpretation of lineaments as geologic features is further verified with corroborating evidence from field mapping.

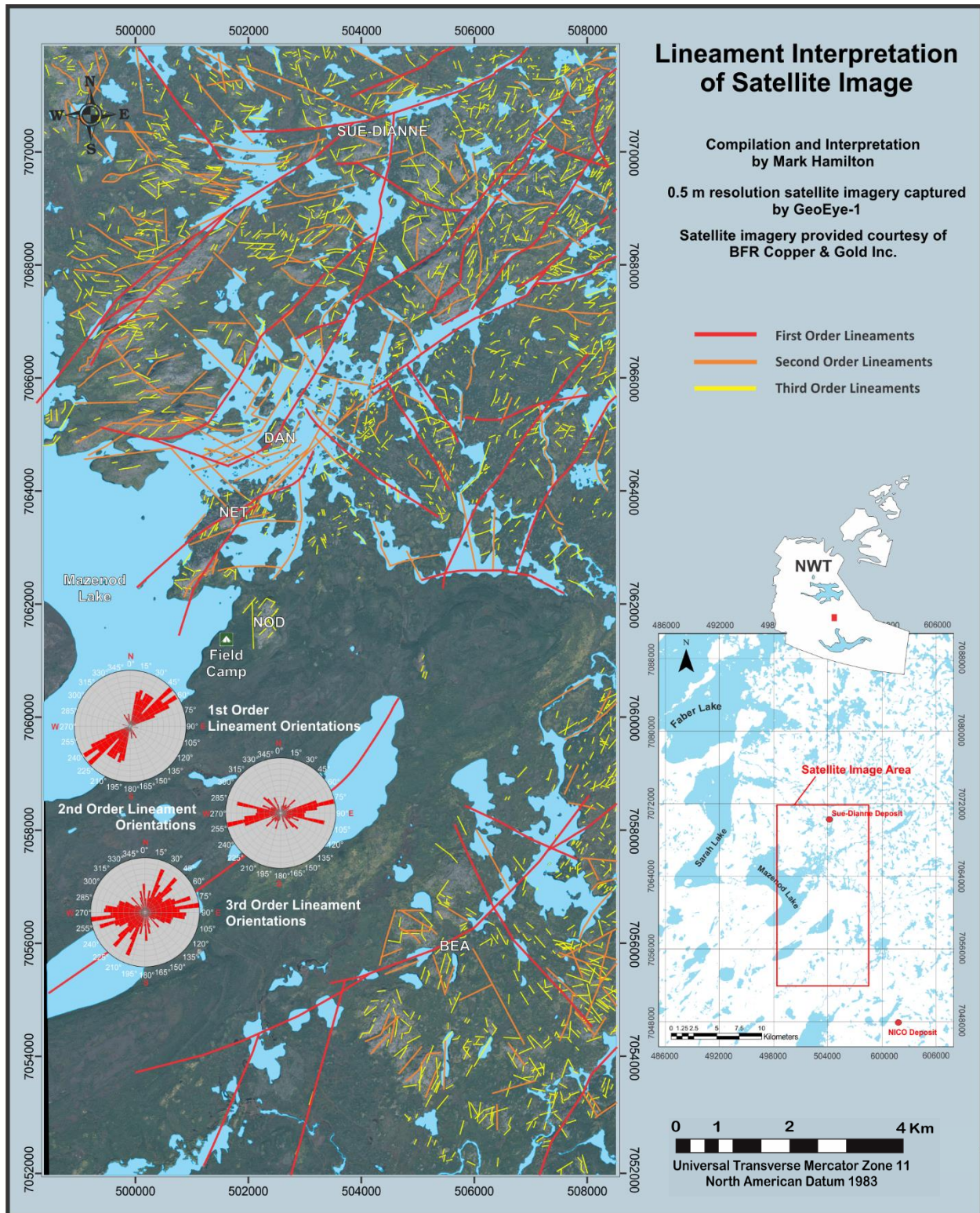


Fig. 21. Mazenod Lake area satellite image lineament interpretation. Anthropogenic features (cut-lines, roads) have been removed from this interpretation.

Any lack of discernible lineaments tends to be reflective of areas with lesser amount of rock exposure. Proterozoic lineaments of structural features are obscured by sedimentary cover and overburden. In a few areas, geomorphic features accentuate certain structures, such as faults that control the direction of rivers. Although there are many distinct long linear features that stand out on the satellite image, there is a large variation in length, width, depth and orientation across the scope of all the lineaments. To show the different characteristics of lineaments they are classified based on a subjective determination of length and prominence. The first order lineaments are the longest trending and most prominent linear features, while second orders are mid-range lineaments and third orders are the shortest linear features identified on the satellite image. Rose diagrams show the unique trends associated with each classification of lineament.

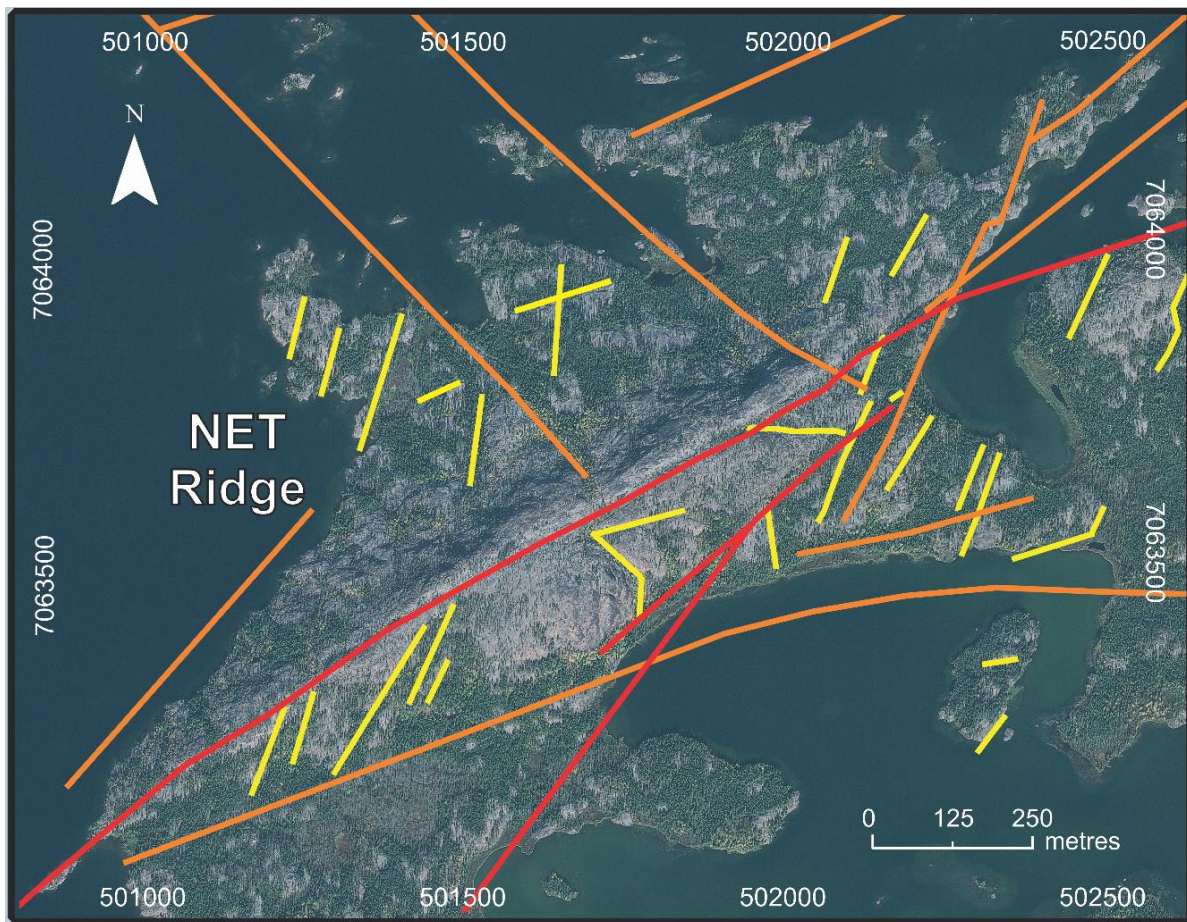


Fig. 22. Close-up image with lineaments drawn on Net Ridge, Mazenod Lake region, NWT.

First order lineaments have three main directional tendencies that are oriented at $\sim 050^\circ$, $\sim 020^\circ$ and to a lesser extent $\sim 330^\circ$. These orientations correspond with the major regional tectonic fabric that have a notable manifestation in the topography. Second order lineaments predominate in the general E-W direction. Third order lineaments have a large diversity of orientations; however, they do closely match the first and second order lineament orientations in relative abundance. The degree of satellite image detail is better illustrated in the close-up image of Net Ridge shown in Figure 22.

Magnetic Lineaments

Magnetic lineaments in this study are defined by the magnetic vertical gradient (MVG) - high and low intensity anomalies. The MVG lineaments have many similarities to lineaments recognized on the satellite image and to the distribution of geologic units recognized in the field (Fig. 23). For example, NW-trending MVG high intensity lineaments correspond with unique volcanic rock types mapped in the field. Most of these features have an almost tabular shape on the aeromagnetic data, with mostly equivalent orientations. There is a definite pattern to the MVG high lineaments that follows the NW orientation of the volcanic belt with a slight oblique-curve shape. In the northern portion of the aeromagnetic data this general trend is reversed, where the magnetic anomalies and mapped geology follow NE and NW orientations.

The high resolution MVG aeromagnetic data correlates well with belt-scale structures. Four of the most prominent, MVG low intensity, NE oriented lineaments occur along faults (Dianne Lake fault, Marian River fault, Squirrel Lake fault and Bea fault). These lineaments have a similar orientation with an average azimuth of $\sim 050^\circ$. Low MVG intensity lineaments also trend in two other dominant orientations at $\sim 330^\circ$ and 020° which correspond with similar orientations of the Kemaz and Cross Lakes faults. In general, directional tendencies of the main

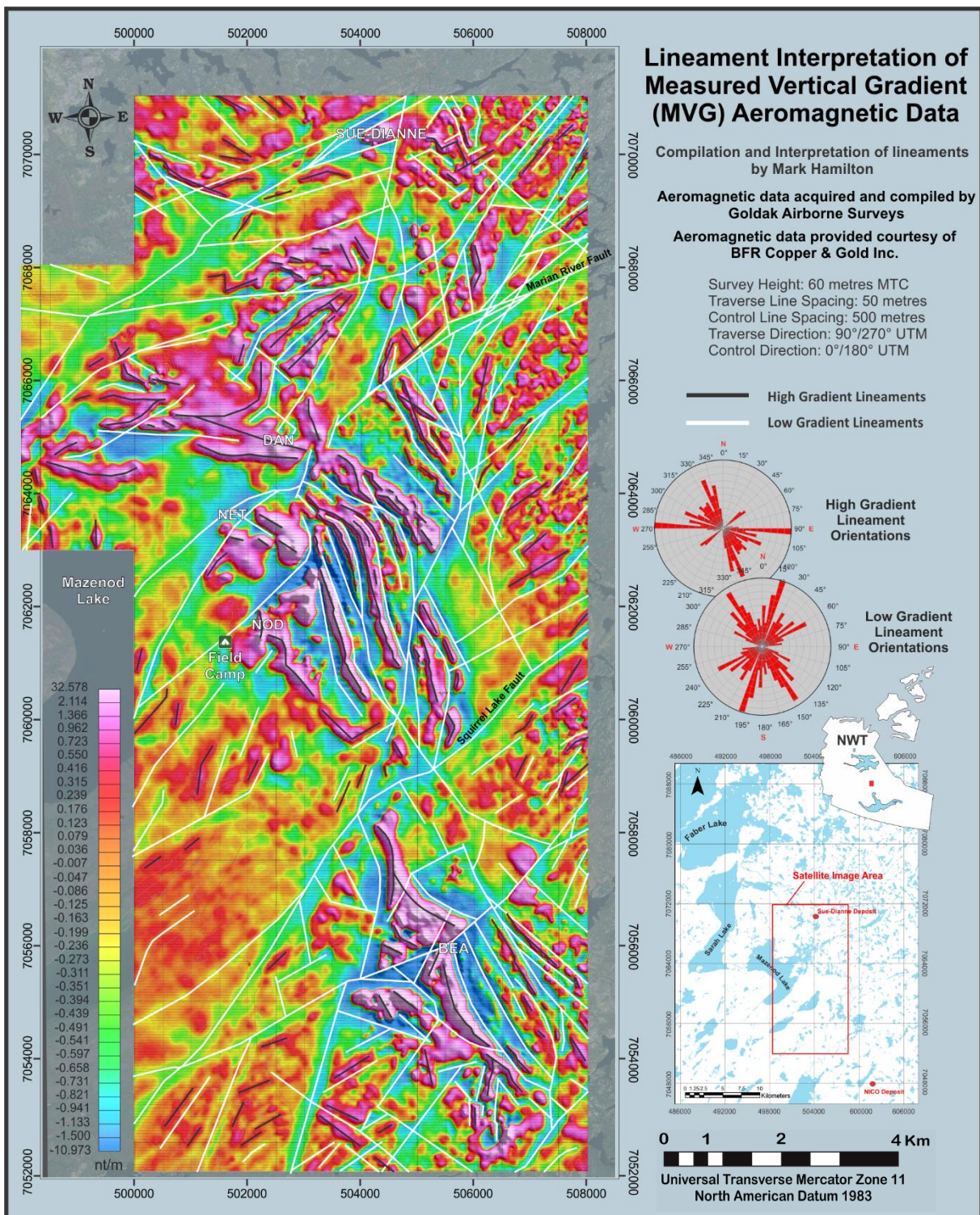


Fig. 23. Magnetic vertical gradient (MVG) data lineament interpretation layered over GeosEye-1 satellite image.

MVG low intensity lineaments correspond well with Tier 1 lineaments derived from the satellite image and regionally occurring faults mapped in the field.

There are three distinct zones where lineaments that have similar orientations to each other dominate, including the area north of the Marian River fault, the area between the Marian River fault and the Squirrel Lake fault, and the area south of the Squirrel Lake fault. South of the Marian River fault within the volcanic terrain the majority of lineaments orient $\sim 330^\circ$. The remaining lineaments mostly trend towards $\sim 016^\circ$ and 065° . Above the Marian River fault there is a higher variance to the directional trend of high and low MVG lineaments. The main orientations of note trend at $\sim 95^\circ$, $\sim 050^\circ$, $\sim 325^\circ$ and $\sim 016^\circ$.

Felsic intrusions are typically MVG low magnetic intensity features that have mostly no linear characteristics. The few lineaments that occur within areas underlain by felsic intrusions typically orient at $\sim 050^\circ$ and 020° , in conjunction with known faults. Dykes are normally too small-scale to be identified on the aeromagnetic data.

Impact of hydrothermal alteration on the magnetic signature of the Mazenod Lake region is significant on both a volcanic belt-scale and a local scale. The dominant NE-SW oriented MVG low intensity lineaments are underlain by giant hydrothermal quartz veins, stockworks and silicification. These quartz-rich structures form prominent aeromagnetic lows because of the low magnetic susceptibility of quartz in contrast to the surrounding rocks. The low intensity magnetism of the quartz veins is also obvious on regional magnetic survey data (Hetu, R.J. et al., 1994). There are also examples on the aeromagnetic data of high magnetic intensity lineaments that correlate with previously noted field observations of hydrothermal magnetite (Camier, 2002). This observation includes the semi-circular magnetic high Sue-Dianne deposit. Previous work has shown the high magnetic intensity signature of the deposit is a result of abundant

hydrothermal magnetite at depth within the deposit. There are several other prominent magnetic anomalies in the aeromagnetic data that are similar in shape and magnetic intensity to the Sue-Dianne deposit, including Dan Island, Nod Hill and a few isolated smaller-scale magnetic anomalies. Most of these MVG highs are semi-circular features that occur in areas with high relief.

Lineament Density Models

The purpose of a lineament density model is to illustrate lineament and lineament intersection population density. Zones that have a great density of lineaments and intersections are often associated with areas of greatest strain and permeability for fluid flow (Galkin, 2010). Identifying these areas is important for determining potential locations that have the space necessary for fluid migration and ore deposition.

(a) Satellite image lineament population density

The population density map of lineaments derived from the satellite image (Fig. 24) distinctly shows the correlation between the abundance of lineaments and outcrops. They are most abundant in the northern and southeastern portions of the study area, and least abundant in areas overlain with Paleozoic sediments and part of Mazenod Lake. Some of Mazenod Lake contains a dense zone of lineaments, where lines were drawn along outcrops on islands, along shorelines and similarly oriented (shaped) islands. This data is highly skewed towards areas with high outcrop exposure; therefore, any interpretation of the lineament density population would be significantly biased.

(b) MVG data lineament density

The most abundant MVG lineaments follow the trend of the volcanic belt (Fig. 25). Areas with less presence of lineaments correspond to locations known to contain Proterozoic granitoid

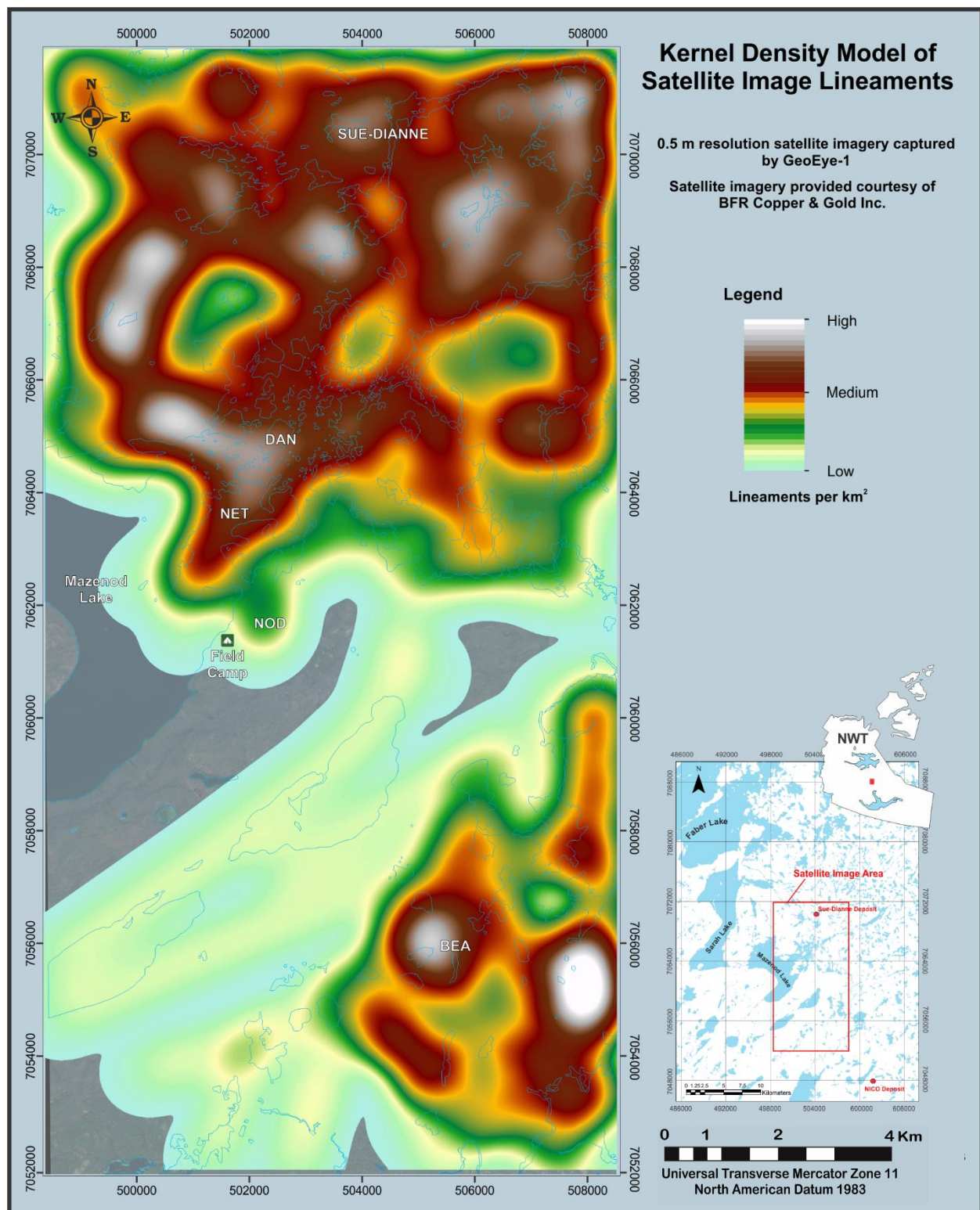


Fig. 24. Kernel density model showing the population density of lineaments per square kilometer, derived from the satellite image.

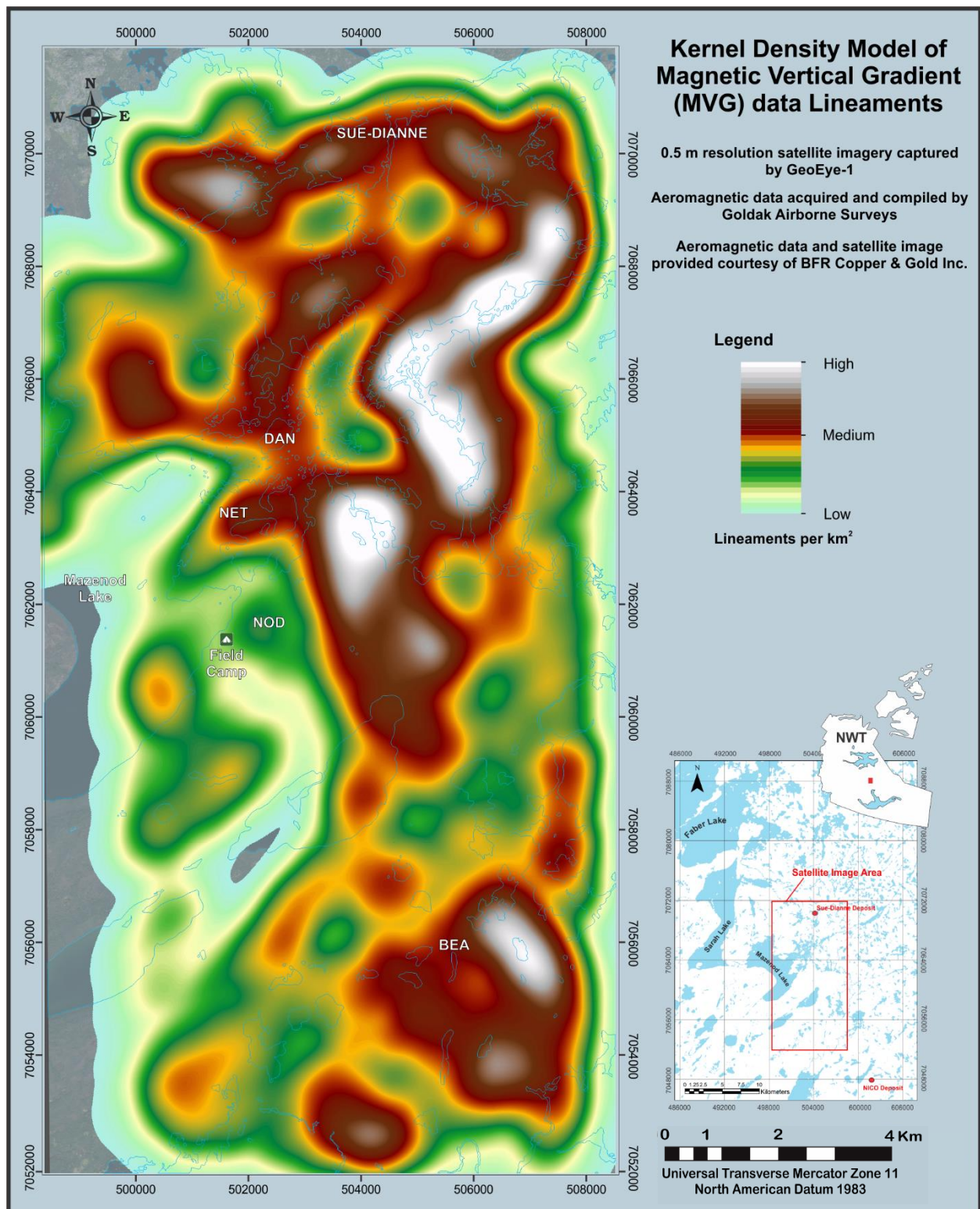


Fig. 25. Kernel density model showing the population density of lineaments per square kilometer, derived from the MVG data.

batholiths. Whether this pattern continues underneath areas overlain with Paleozoic cover remains unknown, but is suspected. An important observation is that there is no significant correlation between the abundance of lineaments and the presence of Paleozoic strata. Instead, the density of MVG lineaments highlights the difference between younger plutonic (lower density of lineaments) and older volcanic rocks (higher density of lineaments).

(c) MVG data lineament intersections density

Stretched contours showing the concentration of MVG lineament intersections per square kilometer show similar anomalies to the MVG lineament density map (Fig. 26). Along the Marian River and Cross Lakes fault in the northern part of the study region are relatively large high-density lineament intersections anomalies. This zone also exists along the contact between the Marian River batholith and Faber Group volcanic rocks. Similarly, in the Bea area a smaller dense zone of lineament intersections occurs at the eastern contact of the Marian River batholith and Faber Group volcanic rocks. The Bea fault also intersects the high-density anomaly. In general, the medium density anomalies coexist along recognized regionally cross-cutting faults. Low densities of lineament intersections typically occur outside of the volcanic belt, within the granitoid batholiths. The western part of Mazenod Lake has no presence of lineament intersections.

Similar to the other lineament population density maps, the data is skewed towards areas with higher outcrop exposure. Any interpretations derived from this data would be highly biased towards these areas.

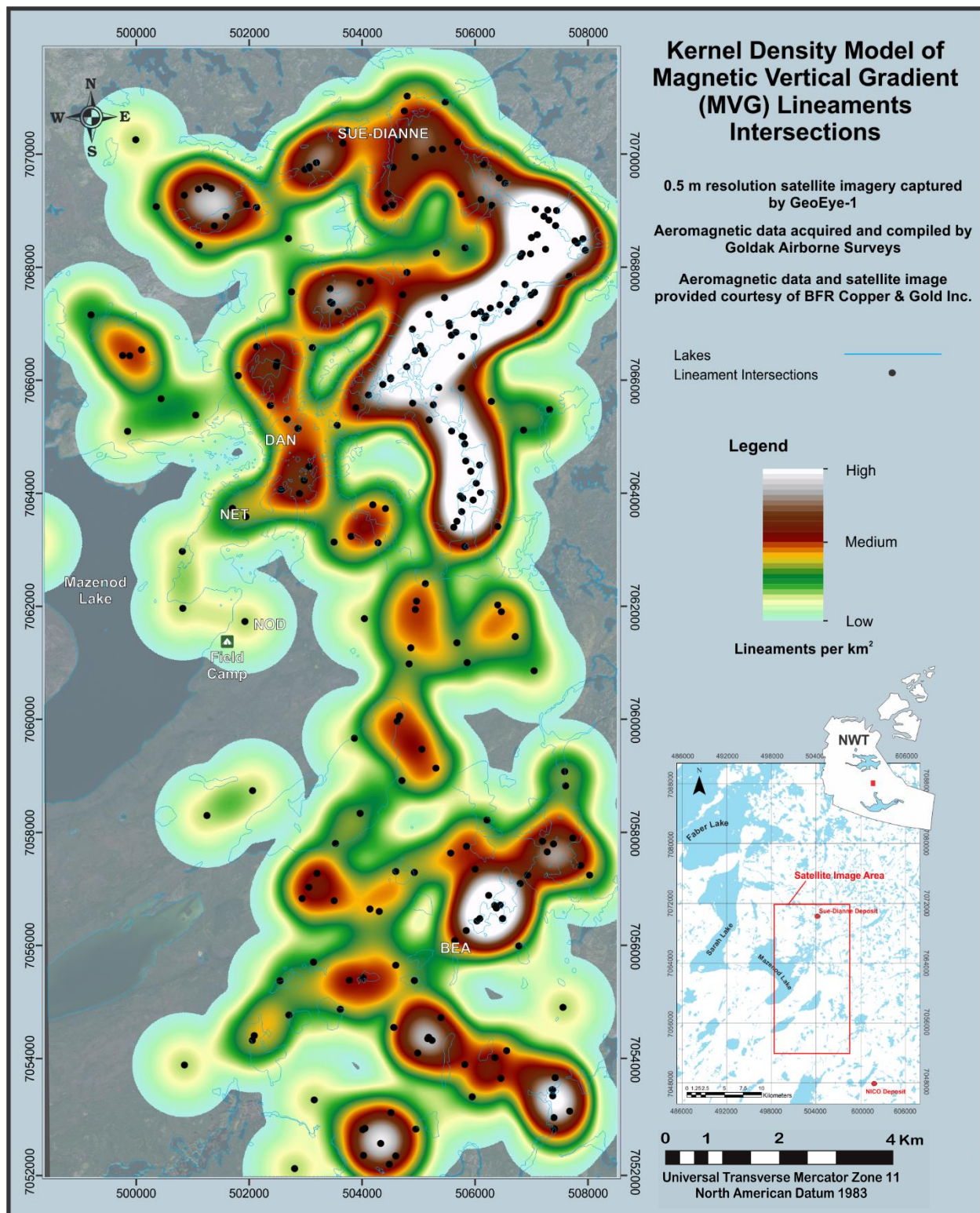


Fig. 26. Kernel density model showing the population density of lineament intersections per square kilometer, derived from the MVG lineament map.

Chapter VII: Geochemical Data Analysis

This chapter is dedicated to an analysis of lithogeochemical data. The geochemical data are from 906 grab samples collected in the Mazenod Lake area, covering an area ~36 km². The samples include 15 boulders, 3 quartz veins, 52 sedimentary rocks, 99 intrusive rocks, 724 volcanic rocks and 13 core samples (Fig. 27). All rocks collected are hydrothermally altered, with 13 of the samples selected as representative samples of lithology.

Saskatchewan Research Council (SRC) Geoanalytical Laboratories performed multi-element analysis of the samples. The geochemical analysis includes whole-rock and trace element analysis by lithium meta-borate fusion, inductively coupled plasma mass spectrometry (ICP-MS) and fire assay for Au. Fifty-nine elements were reported by the SRC, generating 53,336 geochemical data points, with 2D spatial control. Analytical parameters for the geochemical testing are available from SRC Geoanalytical Laboratories. Major elements are reported as weight percent oxide (wt.%), trace elements in parts per million (ppm) or parts per billion (ppb) and total iron is reported as Fe₂O₃. The geochemical data is included in a digital file accompanying this thesis (Mazenod Geochem Data.xls).

Whole-rock geochemical results of major and trace elements are presented qualitatively and quantitatively within this chapter. Geochemical discrimination diagrams are used to chemically classify rocks. This information is used to develop a two-dimensional chemical lithology map of the region that shows the distribution of rock types as discriminated by geochemistry. The mass balance method of lithogeochemical data analysis is used to calculate and graphically illustrate element gains and losses for several geochemical discriminations of

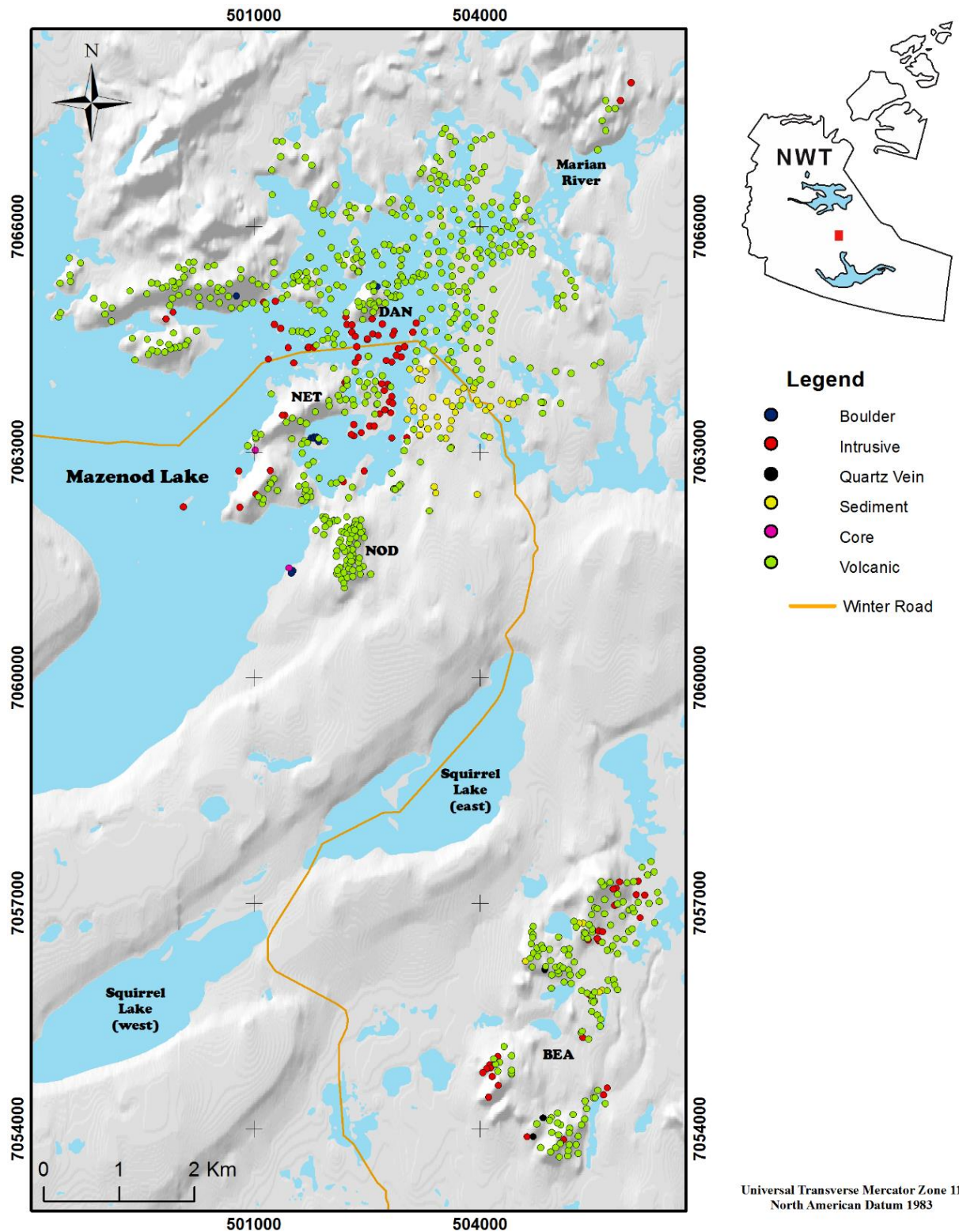


Fig. 27. Locations where geochemical samples were collected in the field at Mazenod Lake, NWT. Digital elevation data courtesy of the Ministry of Natural Resources.

hydrothermally altered and mineralized rocks. The results of mass balance calculations are used as a basis for the generation of diagnostic residual alteration indices (RAIs), which are interpolated and illustrated to show the spatial distribution of hydrothermal alteration intensity for several of the alteration types identified in the region.

Filtering Data and Handling Detection Limits

With any large geochemical dataset, it is important to organize, prioritize and prepare the data for statistical analysis. In this study, concern is for the igneous and sedimentary rocks originating from the Mazenod Lake region. The compositional data had to be filtered so that only those rocks that are involved in this analysis are present in the data. The remaining boulders, vein material, and core samples are not useful for characterizing lithology and/or hydrothermal alteration; consequently, they are not included in the following analyses.

In geochemical analyses, elements (such as Au) often have values below the detection limit. Despite the lack of accurate detection, these elements are still of interest for this study. To facilitate modelling, any element value below the detection limit is converted to half of its detection limit (Table 3). Any duplicate data within the lithogeochemical data is not applied in the following analyses. This anomalous data constitutes only a very minor portion of the geochemical data.

TABLE 3. Adjustments made to values in the geochemical data under the detection limit.

Detection limit	Converted value
<2	1
<1	0.5
<0.1	0.05
<0.01	0.005
<0.001	0.0005

Least Altered Representative Samples

In order to geochemically discriminate rock types and reveal mass changes in hydrothermally altered rocks, it is necessary to have a reference composition per rock type. This reference value is typically acquired from a parent (precursor) rock that represents the original composition (i.e. the rock remains unaltered). Field work and petrographic studies (Appendices 1 and 3) indicate there is no unaltered version of any of the rock types identified in the Mazenod Lake region. Despite the lack of unaltered rocks to choose from, there are several rock samples that have been affected by only a relatively minor amount of hydrothermal alteration. These ‘least altered’ samples are used as the best representation of each rock type in the following discrimination diagrams and mass balance analysis.

Least altered samples were selected based on their field descriptions and a visual inspection for most of the selected samples. Selected least altered rock types were then compared for similarities in whole-rock chemistry (with emphasis on major element oxides). Rocks with significant deviations from the average concentration of elements in a least altered rock were considered hydrothermally altered and not acceptable as a standard representation of a least-altered rock. Table 4 lists the samples selected as least altered representations of Mazenod lithology and their corresponding geochemical data. For rock types that have multiple least altered samples, an average of their whole-rock chemistry is used to represent a least altered rock. Some rock types have only a single least-altered sample. Mass balance calculations that include a single reference will have a greater potential for error than calculations that include an average of several least-altered samples.

TABLE 4: Selected least altered representatives of lithology

Least altered selection		Element concentrations												
Rock type		Al ₂ O ₃ wt. %	CaO wt. %	Fe ₂ O ₃ wt. %	MgO wt. %	MnO wt. %	P ₂ O ₅ wt. %	K ₂ O wt. %	Na ₂ O wt. %	TiO ₂ wt. %	SiO ₂ wt. %			
Andesite	Average ¹	15.93	3.74	5.85	2.13	0.14	0.11	4.21	3.13	0.61	61.67			
Basaltic Andesite	98156	17.3	7.45	8.82	4.25	0.1	0.08	2.3	2.82	0.68	54.2	1.6		
Dacite	98089	16.4	3.44	5.61	1.45	0.05	0.22	4.86	2.94	0.84	62.8	1.4		
Rhyodacite	Average ²	16	2.49	3.51	1.15	0.07	0.07	5.11	3	0.43	66.7	1.5		
Monzodiorite	97078	16.1	2.8	3.18	0.94	0.07	0.07	4.99	3.27	0.42	67.4	0.9		
Monzogranite	Average ³	12.3	0.19	1.2	0.21	0.02	0.01	7.48	1.65	0.1	76.25	0.55		
		Ag ppm	As ppm	Au ppb	Ba ppm	Be ppm	Bi ppm	Cd ppm	Ce ppm	Co ppm	Cr ppm	Cs ppm	Cu ppm	Dy ppm
Andesite	Average ¹	<0.1	6.8	3	820	2.1	0.3	<0.1	77	16.6	92	4.4	33.6	3.98
Basaltic Andesite	98156	<0.1	4.6	<2	248	2.1	0.3	<0.1	43	20.9	175	1.4	5	2.87
Dacite	98089	0.2	5.5	<2	867	2.6	0.1	0.2	106	10.1	73	2.4	18.2	5.47
Rhyodacite	Average ²	0.35	6.67	4	979	2.3	0.43	0.2	93	6.2	99.7	2.1	18.23	3.99
Monzodiorite	97078	<0.1	4.8	<2	908	2.4	0.3	0.2	88	5.2	129	1.6	9.6	3.78
Monzogranite	Average ³	0.41	0.88	1	235.5	2.7	0.23	<0.1	61	1.9	160.3	1.35	9.23	3.79
		Er ppm	Eu ppm	Ga ppm	Gd ppm	Ge ppm	Hf ppm	Hg ppm	Ho ppm	La ppm	Lu ppm	Mo ppm	Nb ppm	Nd ppm
Andesite	Average ¹	2.12	1.2	18.8	4.4	1.4	4.1	<0.1	0.99	39	0.3	1.5	9	29.9
Basaltic Andesite	98156	1.48	0.94	15.3	3.19	1.4	3.1	<0.1	0.66	21	0.2	1.3	5	19.2
Dacite	98089	2.66	1.76	19	6.17	1.5	7.6	<0.1	1.31	50	0.4	2.3	10	41
Rhyodacite	Average ²	2.12	1.35	17.73	4.53	1.33	5.60	0.23	0.95	49	0.37	1.9	9.7	33.17
Monzodiorite	97078	2.07	1.25	15.5	4.35	1.2	5.9	<0.1	0.88	46	0.4	1.5	10	31.4
Monzogranite	Average ³	2.18	0.36	13.03	3.55	1.38	3.75	<0.1	0.91	29.25	0.43	1	21.5	21.98

		Ni ppm	Pb ppm	Pr ppm	Rb ppm	Sb ppm	Sc ppm	Se ppm	Sm ppm	Sn ppm	Sr ppm	Ta ppm	Tb ppm	Te ppm
Andesite	Average ¹	13	12.3	9.06	209	4	13	<1	5.28	<0.1	195	1.82	0.7	<0.1
Basaltic Andesite	98156	39	5.7	5.13	146	1	23	<1	3.73	6.3	203	0.75	0.47	<0.1
Dacite	98089	10	17.2	12.1	176	5	11	<1	7.29	2.3	231	1.61	1	0.1
Rhyodacite	Average ²	19	21.13	10.14	194	1.3	7	0.67	5.26	1.28	206	1.6	0.7	<0.1
Monzodiorite	97078	39	1.03	0.74	<0.1	9.44	18.4	9.89	173	1	7	<1	5.26	9.3
Monzogranite	Average ³	7.75	10.33	6.92	298	0.75	1.25	0.5	4.19	0.86	38.75	4.49	0.61	0.06

		Th ppm	Tl ppm	Tm ppm	U ppm	V ppm	W ppm	Y ppm	Yb ppm	Zn ppm	Zr ppm
Andesite	Average ¹	21.4	<0.01	0.38	7.13	92	5	23.7	2.3	117	153
Basaltic Andesite	98156	9.48	<0.01	0.24	2.12	127	4	17.9	1.53	28	101
Dacite	98089	21.8	<0.01	0.51	6.69	57	6	29.7	2.8	42	257
Rhyodacite	Average ²	22.03	<0.01	0.39	5.98	38.3	24	23.1	2.33	46	195
Monzodiorite	97078	21.9	<0.01	0.36	6.22	34	7	21.9	2.28	49	167
Monzogranite	Average ³	43.83	0.01	0.43	11.62	3.75	2.75	23.28	2.84	10	67

¹Andesite least altered element concentrations averaged from samples 96259, 96423 and 96309.

²Rhyodacite least altered element concentrations averaged from samples 98138, 96372 and 96320.

³Monzogranite least altered element concentrations averaged from samples 96443, 96444, 97055, 98151.

Geochemical Classification

Volcanic rock samples are analyzed and classified in this study based on comparison of their chemical composition and the application of commonly used volcanic rock discrimination diagrams. Classification of rock samples by geochemistry constrains the origin of rocks in the Mazenod Lake area and is also useful for creating a baseline from which to calculate residual alteration indices (RAI), described later in this chapter. All geochemical rock classifications are complemented with field observations and petrographic analysis.

The Pearce (1996) volcanic rock trace element discrimination diagram is used to classify rock types in this study (Figure 28a and 28b). The advantage of this classification over other potential volcanic rock discrimination diagrams is that it uses elements that are known to be relatively immobile in the Mazenod Lake hydrothermal system (discussed in following text); consequently, rocks should plot in their correct composition field regardless of alteration. The diagrams show that volcanic rock samples from the Mazenod Lake region have predominantly intermediate to felsic chemical compositions. Some of the lithogeochemical data plotted in the composition diagrams show a borderline intermediate to felsic composition, also some samples originating from the same rock formations plot in both andesite and rhyodacite composition fields. For these instances, the rock formations are categorized based on the abundance of samples that plot within their respective composition fields. Based on the placement of the plotted chemistry data and hand specimen analysis, four rock types are identified, which include basaltic andesite, andesite, dacite and rhyodacite. Spatial distribution of the rock types recognized in the Mazenod Lake region is illustrated in Figure 29.

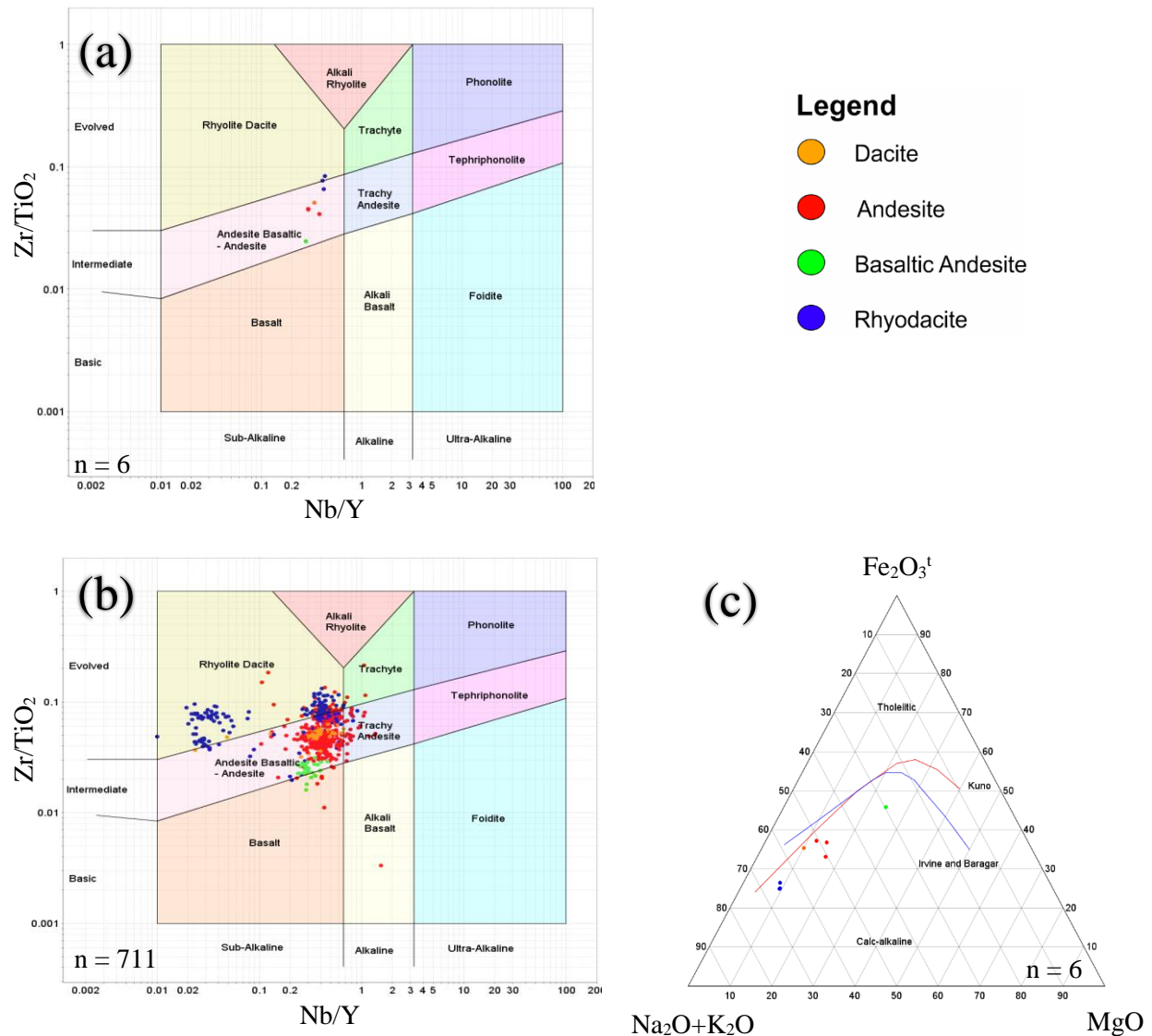


Fig. 28. (a) Least-altered representative samples plotted on a multivariate, immobile trace-element ratio volcanic rock discrimination diagram (Pearce, 1996). Samples are shown to have a variety of compositions that ranges from intermediate to felsic. Dacite classification based on petrographic observations of quartz phenocrysts. (b) Pearce (1996) volcanic rock discrimination diagram with all volcanic rock samples plotted. The diagram shows a similar, although greater spread to the geochemical data. Rocks within the same formation are grouped with their predominant composition field, irrespective of individual placement within the diagrams. (c) Least-altered volcanic rocks geochemical data plotted on the AFM tectonomagmatic discriminatory diagram. The plotted data collectively shows a fractionation trend that is consistent with the calc-alkaline magma series.

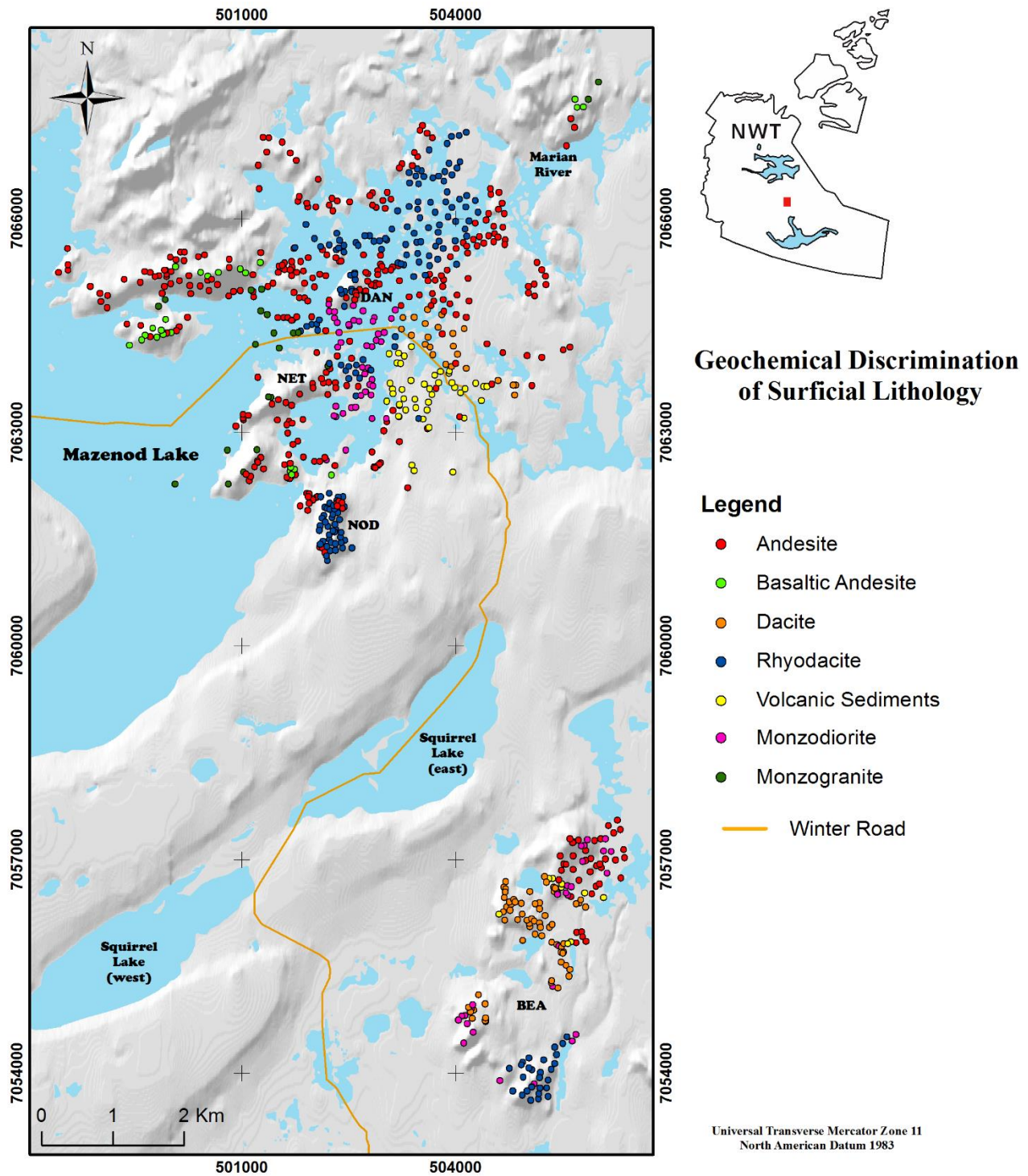


Fig. 29. Geochemical discrimination of rocks from the Mazenod Lake area. Digital elevation data courtesy of the Ministry of Natural Resources.

(a) Tectonomagmatic Classification

The $(\text{Na}_2\text{O} + \text{K}_2\text{O})$ vs Fe_2O_3^t vs MgO (AFM) igneous rock classification diagram is useful for constraining the tectonomagmatic origin of Mazenod Lake region rocks. In previous work several authors have classified rocks from the Mazenod Lake region as calc-alkaline (Gandhi, 1994; Gandhi et al., 2001; Skanderbeg, 2001; Kulla, 2004; Gandhi 2013). Evidence from this study supports this interpretation from previous work. Least-altered volcanic rock samples plotted on the AFM diagram (Fig. 28c) illustrate a fractionation trend that is consistent with the interpretation of a calc-alkaline magma series.

(b) Trace Element Discrimination of Granitic Rocks

The most typically used diagram to classify granitoid rocks based on their source region (and potentially tectonic setting) is from Pearce et al., (1984). This diagram uses composition fields which are defined by characteristic trace element abundances from known tectonic settings. Least-altered granitoid samples from the Mazenod Lake region plotted on the discrimination diagram lie within the fields for syn-collisional granites (Syn-COLG) and volcanic arc granites (VAG) (Fig. 30).

Element Mobility

Stanley and Madeisky (1994) define an immobile element as an element that is neither significantly added nor removed from a rock during metasomatism because of the elements low solubility in aqueous fluids. Typically recognized immobile elements usually include Al and High Field Strength Elements (HFSE) such as Ti, Zr, Hf, Nd, Y and/or Nb. These elements are often useful for classifying rock types and determining mass changes because their concentrations are not affected by hydrothermal additions and depletions. The ratios of immobile

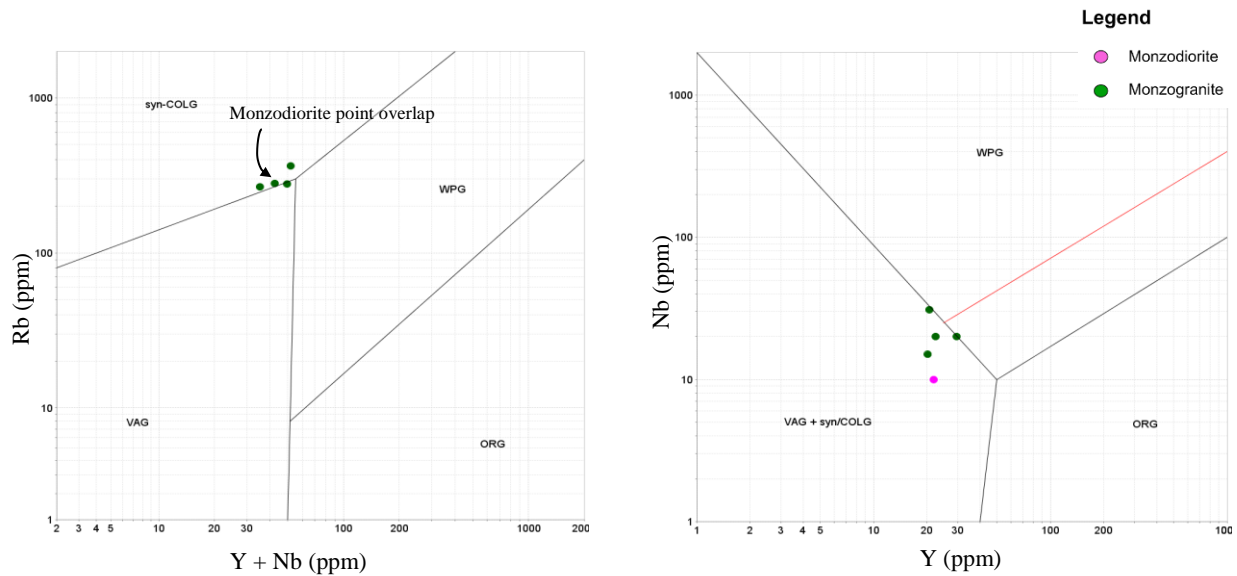


Fig. 30. Granite discrimination diagrams from Pearce et al. (1984). Selected samples plot in the fields for syn-collisional granites (Syn-COLG) and volcanic arc granites (VAG). The monzodiorite plots in the same location as a monzogranite on the left diagram (they overlap). Geochemical data for samples used as tectonic classifiers are listed in Table 5. The red line on the right hand diagram is the upper limit for some known ocean ridge granites (ORG). N=5.

elements for different rock types tend to plot in clusters on bivariate and multivariate diagrams.

Also, the immobile elements tend to plot along linear trends on binary diagrams that compare element concentration differences between unaltered and hydrothermally altered rocks.

There are several commonly used methods in related literature to determine immobile elements, including: using typical immobile elements, comparing correlation coefficients for element pairs, or observing a cluster of slope values of several element pairs then selecting an average from the selected slope values (MacLean and Kranidiotis, 1987; Cail and Cline, 2001; Grant, 2005). In this study, Zr and Hf were chosen as immobile elements. These elements are mainly associated with the mineral zircon, which is typically not affected by hydrothermal alteration. Aluminum is also recognized as an immobile element because it has been demonstrated as immobile in similar studies of IOCG hydrothermal systems (Montreuil et al., 2016) and has a moderately high correlation coefficient with Zr ($r=0.53$, $n=707$). For analytical

purposes, Al_2O_3 and Zr are preferentially used in the quantitative analysis of the geochemical data instead of Hf because the elements have a higher concentration within the rocks; consequently, they are less prone to error in the following examination.

Binary elemental plots can be used to analyze the mobility of elements in a hydrothermal system. The diagrams shown in Figure 31 compare elements that are known to be typically immobile against Zr. In general, there is a positive correlation and linear relationship between the typically recognized immobile elements and Zr. Although the significance of each relationship varies, the diagrams demonstrate that these elements have a relatively similar immobile behaviour in the altered volcanic rocks from the Mazenod hydrothermal system.

Binary diagrams shown in Figure 32 illustrates the relationship of several major elements to Zr. In general, samples that have lower concentrations of Zr have a greater variation in major element oxide content, but this may be due to analytical error arising from the low Zr values. Potassium concentrations ranges from almost 0 to 12.8 wt.%, and Na_2O from almost 0 to 9.7 wt.%. Compared to the average K_2O and Na_2O content of a typical unaltered calc-alkaline andesite (usually the concentrations are in the range of $\sim 3 \pm 0.5$ wt.%), the rocks from the Mazenod hydrothermal system demonstrate significant variation in these element concentrations. In contrast, P_2O_5 and SiO_2 have a relatively restricted variation in their concentration with respect to Zr, which indicates these elements are less mobile. The other major elements appear to be moderately (or selectively) mobile. There does not appear to be any correlation between rock type and degree of element mobility.

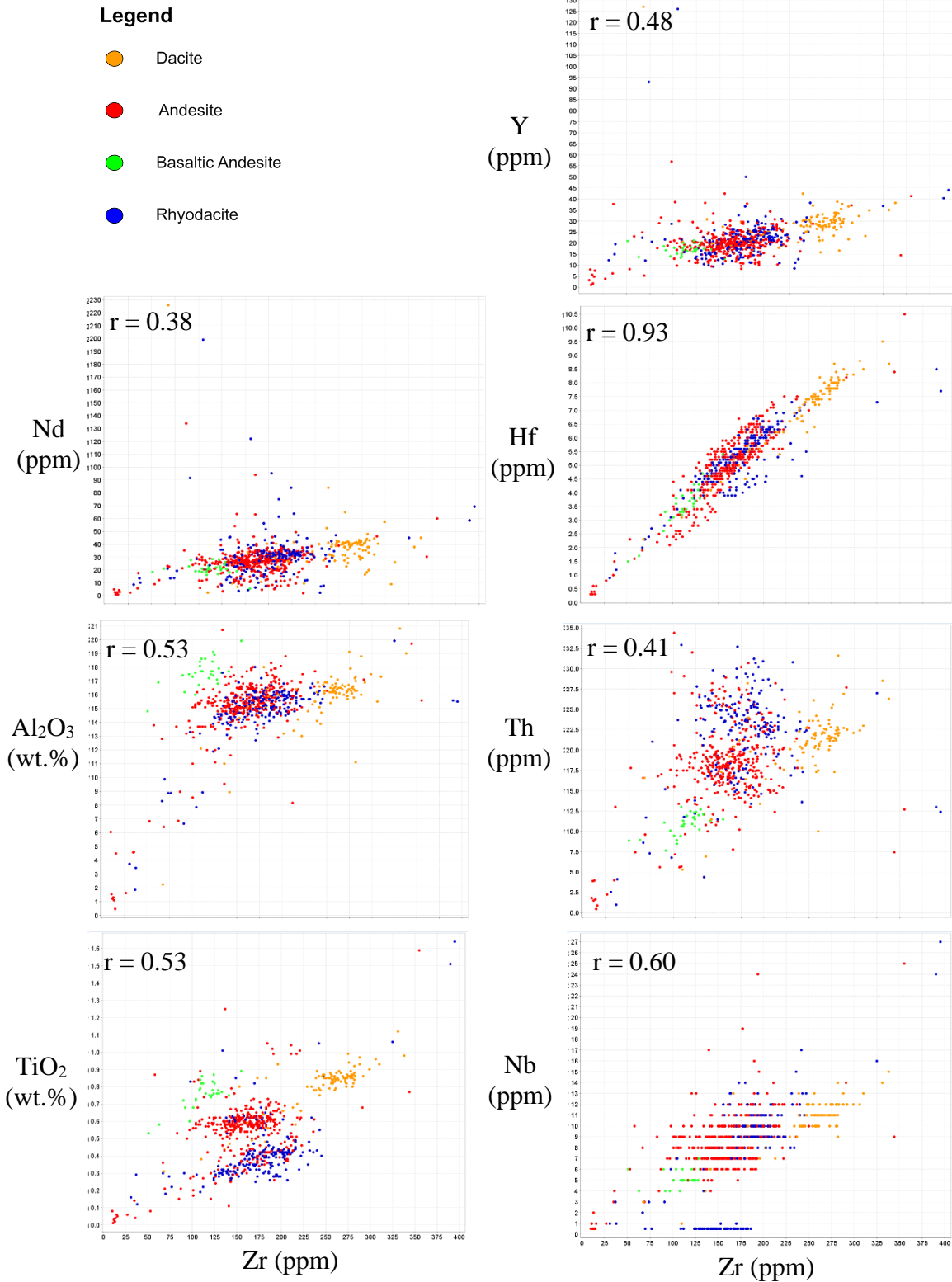


Fig. 31. Binary diagrams illustrating the relationship between elements that are typically immobile in hydrothermal systems ($n=707$). In general, The Zr-Hf plot is the most useful diagram for distinguishing unique rock formations and the Ti-Zr diagram for discriminating rock types. Several significant outliers have been removed to ease visual interpretation of the geochemical data.

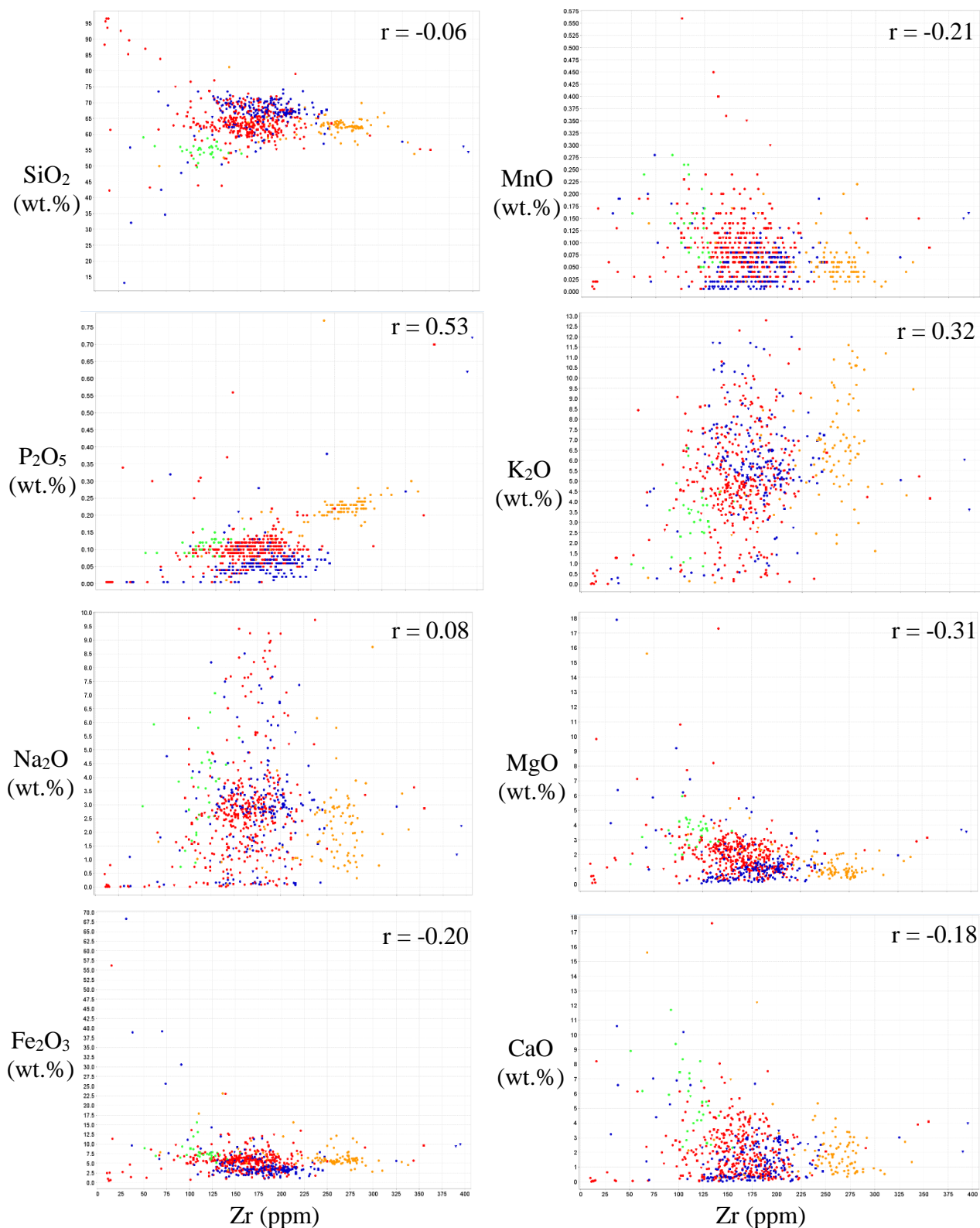


Fig. 32. Binary diagrams illustrating the relationship between major element oxides (wt. %) and Zr (ppm) ($n=707$). Elements that have a greater distribution in the vertical axis such as K₂O and Na₂O are the most mobile elements in the Mazenod hydrothermal system. Elements that do not have a significant vertical spread, such as SiO₂ and P₂O₅ are less mobile. Several significant outliers have been removed to ease visual interpretation of the geochemical data.

Mass Balance Analysis

There are several methods that can be used to evaluate chemical gains and losses that result from hydrothermal alteration (Gresens, 1967; Grant, 1986; MacLean and Barrett, 1993; Stanley and Madeisky, 1996). For this thesis, the isocon method developed by Grant (1986) is used to quantitatively assess chemical changes in the rocks. This is a simplified form of Gresens (1967) analytical approach for evaluating mass change. The isocon method also eliminates the need to apply complex mathematical methods in favor of a relatively simple graphical solution.

In the isocon method, elements of an altered rock (Y-axis) and elements from an unaltered rock (X-axis) are plotted in a binary diagram. A linear line is constructed through the origin and elements that are immobile. Consequently, the immobile elements lie upon a line of constant mass (the isocon, no mass change during hydrothermal alteration) within the binary diagram. The slope of the isocon defines whether the rock has experienced a net mass gain (addition) or loss (removal). If the slope of the isocon is >1 (i.e. $>45^\circ$) the rock has experienced a loss in mass, and if the slope is <1 (i.e. $<45^\circ$) the rock has gained in mass. Elements that are plotted above the isocon have gained in concentration and elements below have experienced depletion during alteration. The element concentration changes are quantified relative to the slope of the isocon. Equations used to determine concentration and mass changes are listed in Appendix 2 and resulting calculations for all the mass balance analysis completed for this study are listed in Appendix 5, Table 11. Figure 33 shows the spatial location of where the mass balance tested samples were originally collected and petrographic observations of the selected samples are discussed in Appendix 3, Table 10.

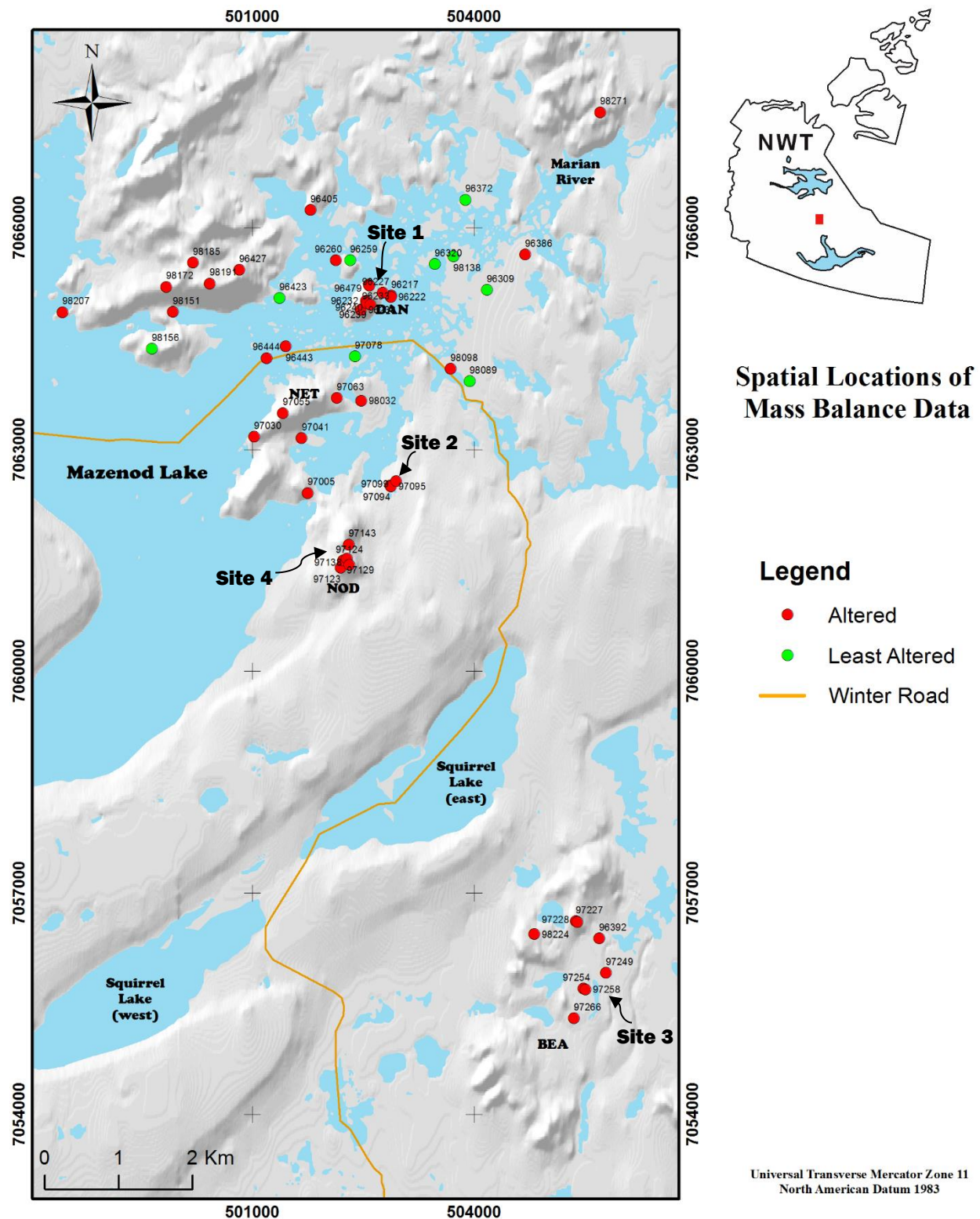


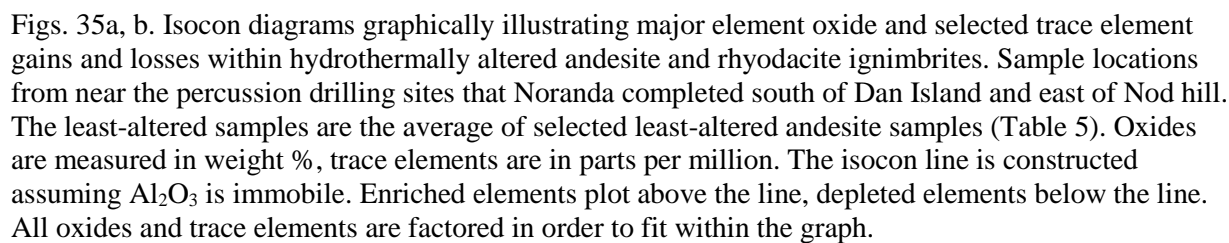
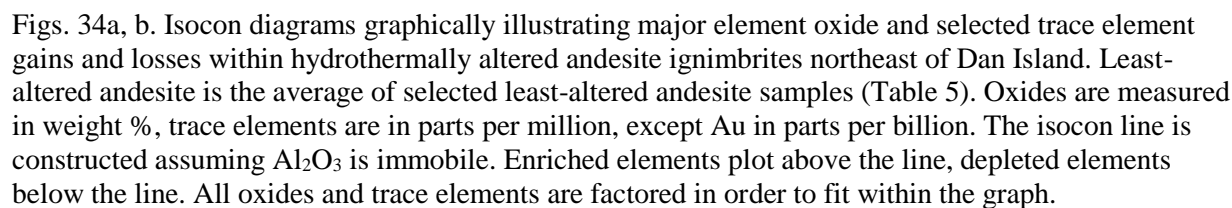
Fig. 33. Location map showing where lithogeochemical samples originated that have been mass balance analyzed for this thesis. Site locations reference the samples that are analyzed with the isocon diagrams. Digital elevation data courtesy of the Ministry of Natural Resources.

Isocons of Mineralized Samples

Eight isocon diagrams were constructed with the use of lithogeochemical data from selected mineralized samples and samples originating from locations of specific interest (Figs. 34 to 37). These analyzed samples contain varying but anomalous concentrations of Au, Cu, Bi, Co and W, from Dan Island, Nod Hill, the Bea area, and an isolated area to the east of Nod Hill. There are also visible sulphides and/or the oxidized mineral by-product of sulphides present in the hand samples. For the purposes of this analysis, Al_2O_3 is considered an immobile element in the mass balance testing.

(a) Site 1, Dan Island

The samples originating from Dan Island were collected from the same protolith and in relative proximity to each other (~15 m). Both of the samples analyzed are characterized by a moderate potassic alteration and the presence of sulphides. They show similar changes in element concentrations with both samples being significantly enriched in K_2O (avg. 154%) and Fe_2O_3 (avg. 74%) (Figs. 34a, b). These rocks have also been significantly depleted in CaO , Na_2O and MnO (avg. -73%, -52% and -45%). Major elements that are relatively conserved during alteration include SiO_2 , TiO_2 , and P_2O_5 (avg. 8%, -1% and -9%). Other significant concentration changes for both samples include the depletion of Zn, Sr and Cs (avg. -58%, -66% and -34%) as well as Bi, Ba and Rb enrichment (avg. 49,600%, 102% and 96%). No pattern of gains or losses are apparent for the REEs. Sample 96217 shows a relatively minor depletion in REE content, while the opposite is true for sample 96222. The trace element additions for sample 96217 occurred in the following decreasing order of percent change: Bi, As, Au, Co, Ag, Hg, Cu, W, Sn, Lu, Yb, Tm, Sb, Ba, Ni, Rb, Cr, Er, Cd, Y, Ho, Hf, U, Eu, Dy, V, Th, Te, Zr, Sc, Ga,



Tb. Trace element losses by increasing loss occurred for: Zn, Sr, Se, Mo, Cs, Tl, La, Pr, Nd, Ce, Pb, Ta, Gd, Be, Ge, Sm. For sample 96222 the additions that took place are: Bi, As, Au, Hg, Co, W, Te, Cu, Mo, Ni, Ba, Rb, Sb, Ce, Eu, La, Nd, Pr, Cr, Cd, Sm, Ga, Sn, Gd, Lu, Nb, Hf, Sc, U, Pb, Ge, V, Th, Tb. The losses of sample 96222 include: Sr, Tl, Zn, Y, Ho, Cs, Dy, Tm, Er, Ta, Be, Se, Zr, Yb. The two samples from Dan Island have a net mass increase of 12.21% and 10.65% respectively.

(b) Site 2, NE of Nod Hill

Two samples are mass balance analyzed from a location in moderate proximity to each other north-east of Nod Hill (~84 m) (Figs. 35a, b). These samples were collected from two unique andesite formations that have nearly equal distances from the contact that separates them. They are both characterized by a minor presence of sulphides (pyrite and chalcopyrite) and magnetite. Sample 97094 also contains veinlets of actinolite, and sample 97099 has a potassic alteration overprint. Both samples are enriched in Na₂O (avg. 177.98%) and depleted in K₂O, CaO and MnO (avg. -85%, -63% and -73%). The other major element oxides are relatively conserved, although Fe₂O₃ and MgO show variable minor gains and losses, and P₂O₅ in sample 97094 has an anomalous enrichment (44%). In sample 97094, trace element additions occurred in the following order of decreasing percent change: Cu, Bi, Hg, W, Au, Ag, As, Te, Sn, Pr, Ce, Nd, Sm, Cr, Tb, Gd, Dy, Lu, Er, Nb, Yb, Tm, Ho, Eu, Y, La, Hf, Be, Sb, U, Zr, Th, Ta and Ge. Elements that are shown to be immobile or have little change in concentration include Se, Ga and Co. Trace element losses occurred for Ni, Cd, Mo, Tl, Sc, Pb, V, Sr, Zn, Ba, Cs and Rb. In sample 97099, trace element additions include Cu, Au, Bi, Sn, As, Cr, Be, Nb, Hf, Yb, Dy and Nd. The mostly immobile elements include Y, Pr, Zr, Ag, Hg, U and Ni. Trace elements depleted from hydrothermal alteration include Cs, Zn, Rb, Ba, Sr, Pb, W, Sb, Co, Cd, La, V, Mo, Th, Se,

Ce and Ta. There was a net mass gain of 16.28% (Fig. 35) and net mass loss of 4.02% (Fig. 36) for the two samples, respectively.

(c) Site 3, Bea Area

Element gains and losses for the mineralized samples collected from the Bea area are illustrated in Figures 36a, b. The two samples have a different protolith and are not from an area near each other (~400 m apart), but have been described as having been similarly altered with hematite, magnetite, quartz and minor sulphide hydrothermal minerals. Sample 97258 experienced a significant enrichment in Fe₂O₃ and MgO (217% and 20%) as well as depletion in Na₂O and CaO (-62% and -68%). Trace element gains arranged in order from greatest enrichment include W, Hg, Sn, Co, Mo, As, Bi, Ni, Cu, Cr, U, V, Au and Se. Elements that have been conserved include Al₂O₃, TiO₂, Th, Zr, Hf, Sb and Ta. Trace elements depleted in order of percent depletion includes Zn, La, Ce, Pr, Nd, Cs, Ag, Pb, Be, Sr, Cd, Dy and Rb. In sample 97249, most of the major elements are relatively conserved. There are only comparatively minor gains in P₂O₅, K₂O, SiO₂, TiO₂ and CaO (38%, 26%, 26%, 13% and 11%). Major elements significantly depleted include MnO and MgO (-83% and -31%) along with minor depletions of Fe₂O₃ and Na₂O (-11% and -9%). Trace element gains in order of enrichment include Ag, Cu, Au, Hg, Sn, W, Bi, U, Rb, Nb, Cr, Ta, As, Be, Co, Th, Ni, Hf and Zr. Trace element depletions include Mo, Zn, Se, V, Sb, Ba, La, Pr, Ce, Y, Nd, Dy, Cd, Yb, Sr and Cs. Both samples gained in mass, 22.39% (Fig. 37) and 17.16% (Fig. 38) respectively.

(d) Site 4, Nod Hill

Illustrated in Figures 37a and b are the isocon diagrams for samples collected from Nod Hill. The two samples were collected approximately 277 m apart from each other in the central

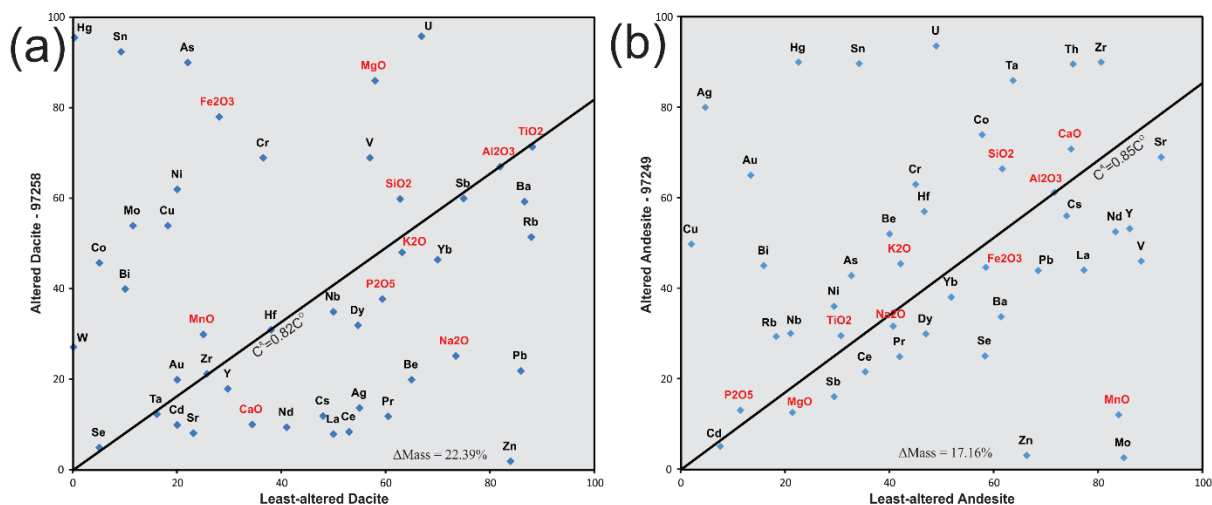


Fig. 36a, b. Isocon diagrams graphically illustrating major element oxide and selected trace element gains and losses within hydrothermally altered andesite and dacite ignimbrites located in the Bea area. Least-altered andesite is the average of selected least-altered andesite samples (Table 5). Oxides are measured in weight %, trace elements are in parts per million. The isocon line is constructed assuming Al_2O_3 is immobile. Enriched elements plot above the line, depleted elements below the line. All oxides and trace elements are factored in order to fit within the graph.

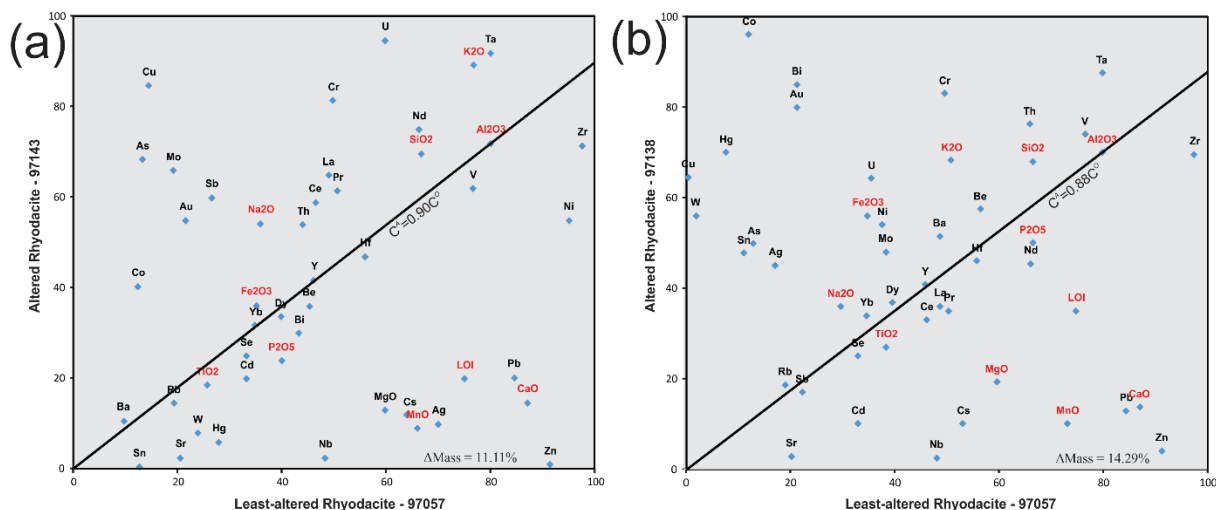


Fig. 37a, b. Isocon diagrams graphically illustrating major element oxide and selected trace element gains and losses within hydrothermally altered rhyodacite ignimbrites located at Nod hill. Oxides are measured in weight %, trace elements are in parts per million. The isocon line is constructed assuming Al_2O_3 is immobile. Enriched elements plot above the line, depleted elements below the line. All oxides and trace elements are factored in order to fit within the graph.

and southern portion of Nod Hill respectively. They are both characterized by a moderate potassic alteration and are comprised of a minor amount of sulphides (pyrite and chalcopyrite) and magnetite. Both samples have been moderately enriched in K_2O , Na_2O , Fe_2O_3 and SiO_2 (avg. 41%, 52%, 48% and 16%) and have been depleted in MnO , CaO , TiO_2 , P_2O_5 and MgO (avg. -85%, -82%, -20%, -24% and -70%). The two samples have many similarities in their trace element enrichments and depletions. The REEs are variable, but have comparatively minor enrichments and depletions. Both samples have gains in concentrations for Cu, As, Mo, Au, Cr, Co, Ta, U and Th. Trace elements commonly depleted include Zn, Pb, Nb, Cd, Zr, Hf and Sr. Both samples have gained in mass, 11.11% and 14.29%, respectively.

Quantitatively Assessing Hydrothermal Alteration

In this subsection of the thesis, different types of hydrothermal alteration are distinguished by their own distinct chemical signatures. This information is crucial for development of alteration indices, which quantifies the intensity of each alteration type throughout the study region based on the unique chemical signature.

Enrichment-depletion diagrams are used to graphically demonstrate relative concentration changes (mobility) of major and trace elements (Rollison, 1993). These diagrams display multiple samples from different rocks in a similar arrangement to ease visual interpretation. The x-axis of the diagram is adjusted such that it is equivalent to the isocon line, with the assumption that Al_2O_3 is an immobile element. The bars parallel to the y-axis display the relative percent change of chemical composition for a corresponding element listed at the base of the x-axis. The maximum amount of percent change displayed on the diagram is 350%; however, the actual amount of change can exceed this limit. Mass balance formulas used to calculate percentage changes in element abundance are listed in Appendix 2. Petrographic

descriptions and classifications for each analyzed sample are listed in Appendix 3, Table 10.

Reported averages in this section are in percent element concentration change.

Samples selected to classify alteration were chosen based on a visual interpretation or by a review of sample descriptions completed by geologists from BFR Copper & Gold. Most of the samples chosen are classified as intensely altered of a certain alteration type and a few as moderately altered. Samples were also preferentially selected for replacement-type alteration as opposed to vein filling; however, several of the chosen samples do contain veins which have some impact on results and following interpretations. Many of the selected samples analyzed by this method have only one visible type of alteration affecting the rock although there are several samples that have minor, yet discernible different alteration effects. As mentioned in Chapter 5, there are regional, pervasive and early alkali alteration effects (predominantly potassic alteration) to the rocks in the Mazenod Lake region that likely impact both K_2O and Na_2O concentration gains and losses in many, if not all the samples mass balance analyzed.

(a) Magnetite \pm Actinolite (MA) Alteration

Figure 38 illustrates the percent gains and losses in major and trace elements for selected samples that contain MA (magnetite \pm actinolite) alteration. Consistently depleted major element oxides for these samples include MgO and MnO (avg. -47% and -41%). The main distinct pattern in Na_2O and K_2O mobility is the relatively opposite trends of enrichment and depletion. In samples enriched with Na_2O , they are also depleted in K_2O and vice versa. Conserved major elements include SiO_2 and TiO_2 (avg. 5% and 1%). Calcium and iron oxide have a similar correlation of their concentration changes but are variably enriched or depleted.

Percent changes in major and trace element concentrations

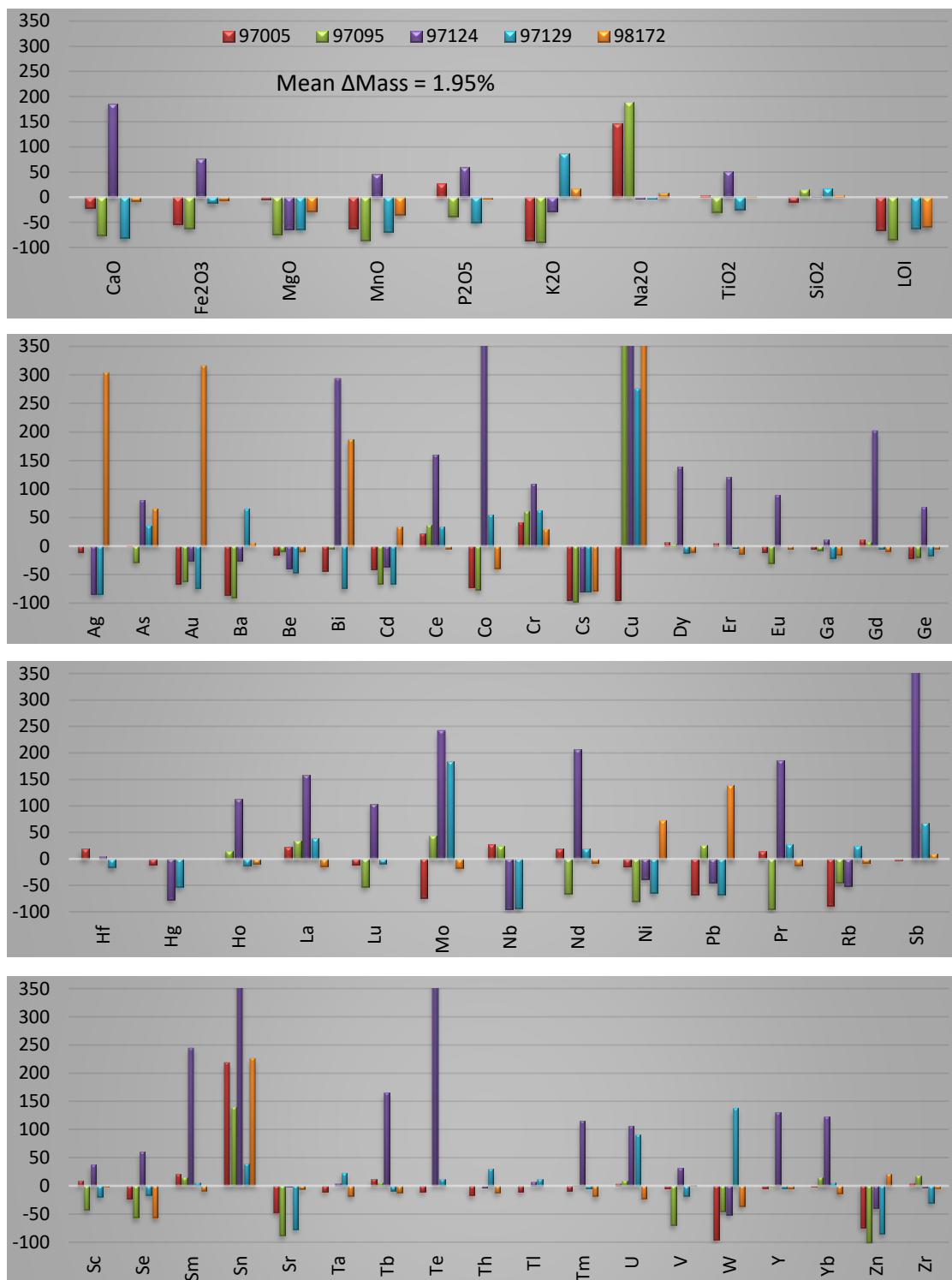


Fig. 38. Graphical illustration of calculated concentration changes for samples that have been magnetite-actinolite (MA) altered. Aluminum is not listed, as it was used as a conserved element for mass balance calculations. Absolute value results listed in Appendix 5, Table 11.

The higher amount of CaO enrichment in sample 97124 (186%) is probably influenced by the minor presence of epidote observed in the sample. The trace elements typically enriched include Sn, As, Cr and Ce. Trace elements depleted most often include Cs, Zn, Sr, Cd and Be. Conserved trace elements include Zr, Hf, Tl, Ta and the HREEs. The rest of the trace elements have variable minor to moderate trends in element gains and losses. Mass changes are variable for each of the analyzed samples but shows an average gain of 1.95%.

(b) Potassic Alteration

Potassic altered samples are enriched in K₂O (avg. 131%) and generally depleted in Na₂O, CaO, MgO and MnO (avg. -46%, -93%, -72% and -81%) (Fig. 39). Comparatively conserved elements include Fe₂O₃, TiO₂ and SiO₂ (avg. -7%, -20% and 20%), whereas P₂O₅ is variably enriched or depleted. Trace elements that have relatively constant enrichments include Ba, Cr, Rb, Te, Th and U. Trace elements that are commonly depleted in these altered samples include Be, HREEs, Mo, Nb, Nd, Ni, Pb, Sc, Sr, and Zn. Most of the remaining trace elements show minor to moderate enrichment and depletion, with the exception of the immobile element Zr. The mean mass change for the potassic altered samples is a gain of 12.58%.

(c) Tourmaline Alteration

Metasomatic rocks with abundant tourmaline exhibit a substantial range in element mobility (Fig. 40). Samples representative of tourmaline alteration are mostly enriched in K₂O (avg. 71%). Major elements oxides that have comparatively minor gains in concentration includes SiO₂ and Fe₂O₃ (avg. 37% and 28%). Typically depleted elements include Na₂O, CaO, MnO and usually MgO (avg. -70%, -88%, -85%, and -16%, respectively). The only relatively conserved major element oxides include TiO₂ (avg. 8.82%). In contrast, P₂O₅ has a large variance, with both gains and losses. Trace elements usually added to the tourmaline

Percent changes in major and trace element concentrations

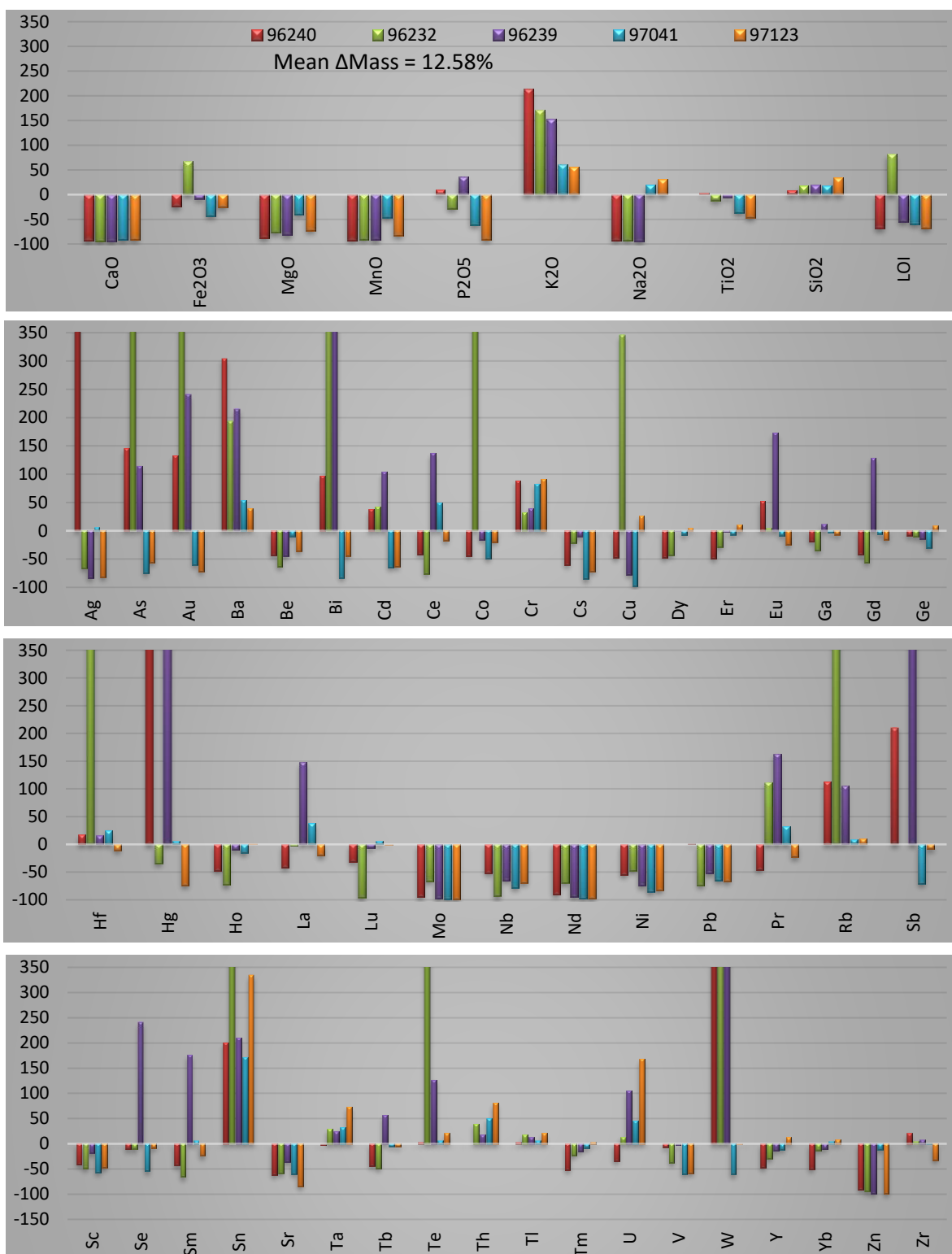


Fig. 39. Graphical illustration of calculated concentration changes for samples that have been potassic altered. Aluminum is not listed, as it was used as a conserved element for mass balance calculations. Absolute value results listed in Appendix 5, Table11.

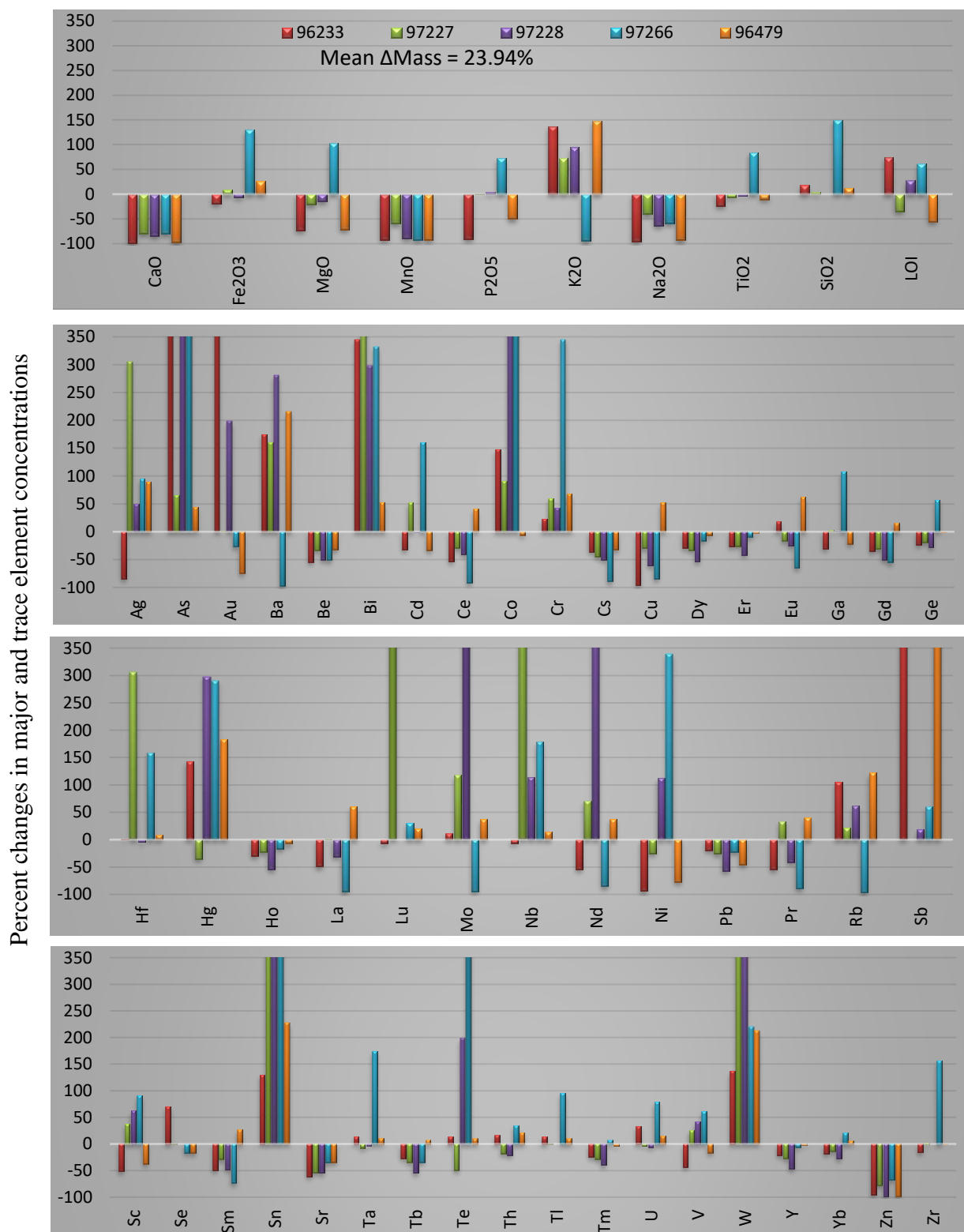


Fig. 40. Graphical illustration of calculated concentration changes for samples that have been tourmaline altered. Aluminum is not listed, as it was used as a conserved element for mass balance calculations. Absolute value results listed in Appendix 5, Table 11.

altered samples include Ag, As, Ba, Bi, Co, Cr, Hg, Mo, Rb, Sb, and W. Those elements mostly depleted include Be, Ce, Cu, Pb, Cs, REEs, Sr and Zn. Trace elements that have the least concentration changes include Zr, U, Th, Se, Ta and Tl. The rest of the elements have no identifiable trend. The average change in mass is a gain of 23.94%.

(d) Propylitic Alteration

Figure 41 illustrates the percent concentration changes for several propylitic metasomatized samples. These samples contain abundant epidote and often contain chlorite and carbonate alteration minerals. Changes are generally minor and there is very little consistency in the pattern of gains and losses of major element oxides, other than that SiO₂ remains mostly unchanged. Trace elements usually added to the rocks due to alteration include Bi, REEs, Cu, Sb and Sr. The only trace elements usually removed during alteration includes Au, Ni and Cs. Trace elements that are mostly conserved despite alteration include Ag, Ga, Hf, Nb, Sc, Te, Th, Tl, Y and Zr. The remaining elements are variably enriched or depleted. The average mass change for these samples is a gain of 1.14%.

(e) Hematite Alteration

Figure 42 shows the percent concentration changes of several hematite altered samples. Sample 97063 contains abundant vein material and is therefore excluded in the following discussion and listed average concentration changes. Hematite altered samples are predominantly enriched in Fe₂O₃ (avg. 266%). Most samples have also been enriched in MgO, MnO and lesser K₂O (avg. 116%, 90%, and 63%), while Na₂O is consistently depleted (avg. -78%). Major elements are generally depleted include CaO and P₂O₅. Comparatively conserved during alteration are TiO₂ and SiO₂ (avg. -21% and 15%). The trace elements usually enriched include

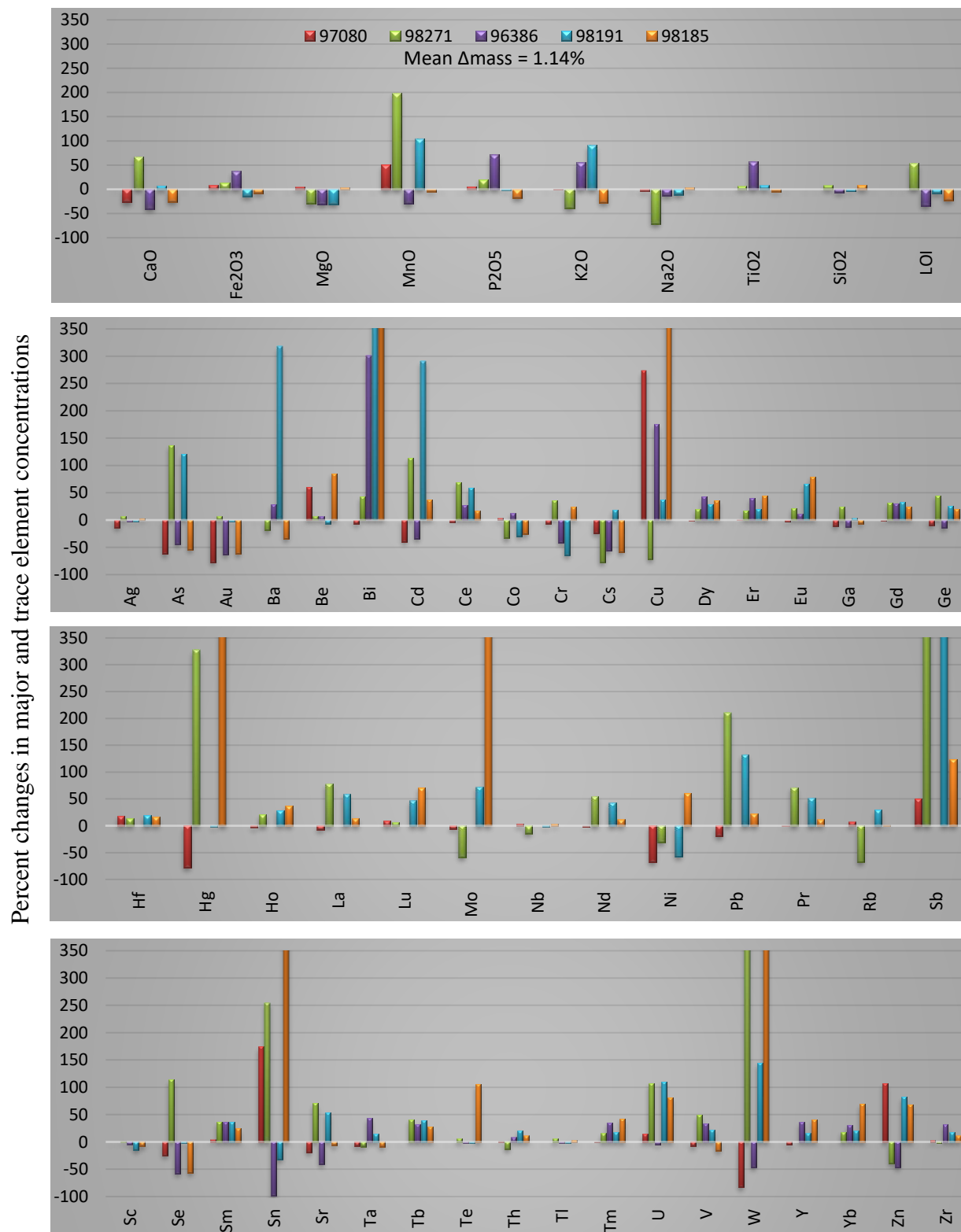


Fig. 41. Graphical illustration of calculated concentration changes for samples that have been propylitic altered. Aluminum is not listed, as it was used as a conserved element for mass balance calculations. Absolute value results listed in Appendix 5, Table 11.

Percent changes in major and trace element concentrations

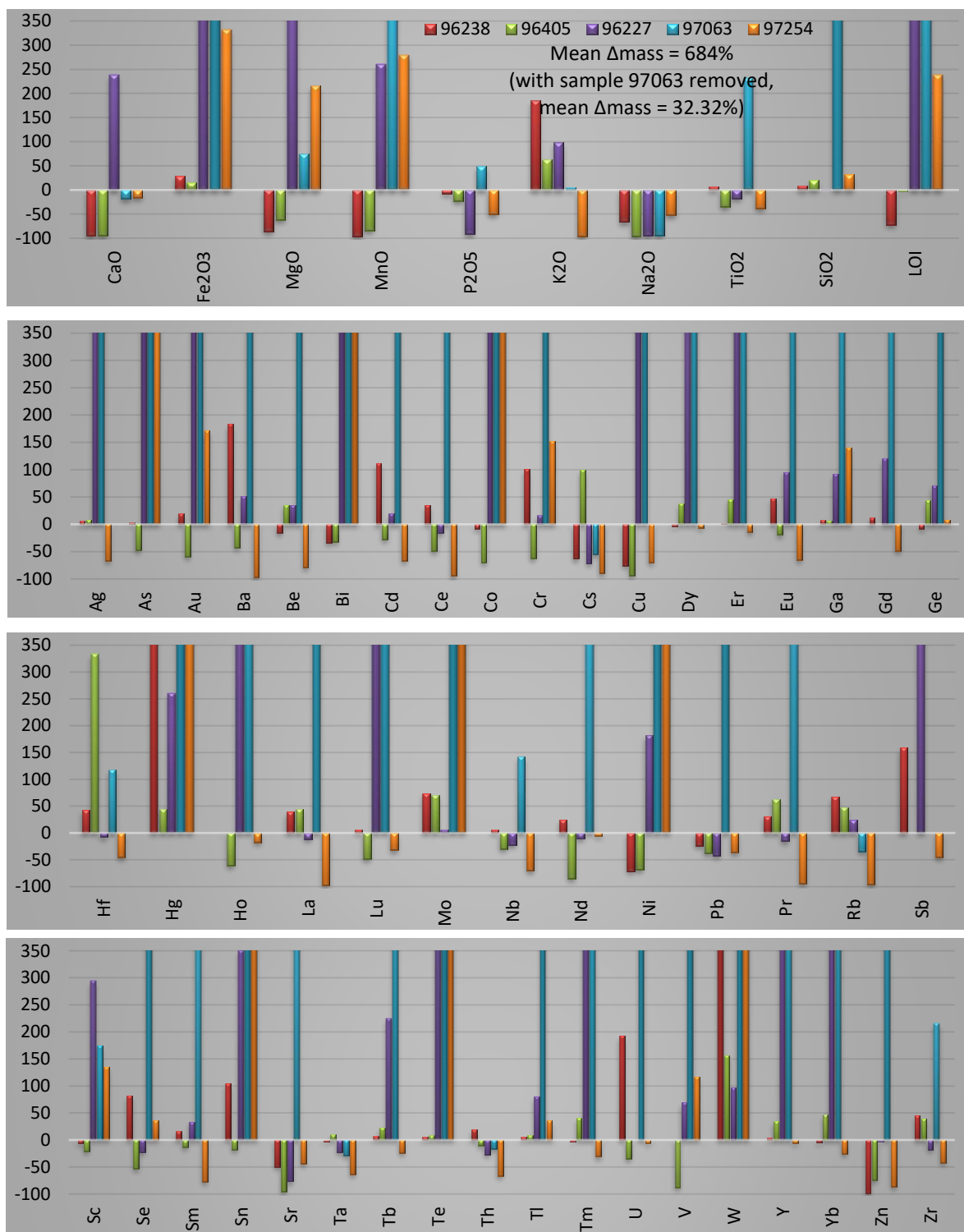


Fig. 42. Graphical illustration of calculated concentration changes for samples that have been hematite altered. Aluminum is not listed, as it was used as a conserved element for mass balance calculations. Absolute value results listed in Appendix 5, Table 11.

Hg, Cr, Ga, Ge, Sn, Te, Tl, and W. Those trace elements typically depleted include Cs, Pb, Sr, Th and Zn. Trace elements that remain comparatively unchanged from alteration include Th and Ta. The remaining elements are variably enriched or depleted. Mass change for these samples is variable, although they all have increased in mass from the hydrothermal alteration. The average mass gain (not including sample 97063) is 32.32%

(f) Silicification

Most of the silicified samples have gained significant SiO_2 (avg. 736%) (Fig. 43). The major element oxides removed from the host rocks usually include CaO and Na_2O (avg. -55% and -50%) and in lesser amounts TiO_2 and P_2O_5 (avg. -22% and -20%). The other major elements have variable trends in their gains or losses. Trace elements usually gained in the selected silicified samples include Ag, As, Au, Bi, Cu, Hg, Mo, Nb, Nd and Te. The trace elements typically lost in these samples include Eu and Sr. Relatively conserved trace elements include Hf, Ta, Th, U, W, Zr and most REEs. The remaining elements are variably enriched or depleted.

Alteration Indices

The final geochemical analysis is the development and testing of alteration indices (AIs) and residual alteration indices (RAIs) using techniques originally developed by Ishikawa (1974) and Mumin (1988), respectively. The AI is useful for quantifying relative intensity of alteration within a specified rock type of uniform chemical composition and determining chemical alteration patterns that are not manifest as changes in mineralogy. Each AI represents an alteration type and/or element enrichment that is scaled in relative intensity based on the concentration of elements added and removed from the rock. Alteration indices are calculated using the following

Percent changes in major and trace element concentrations

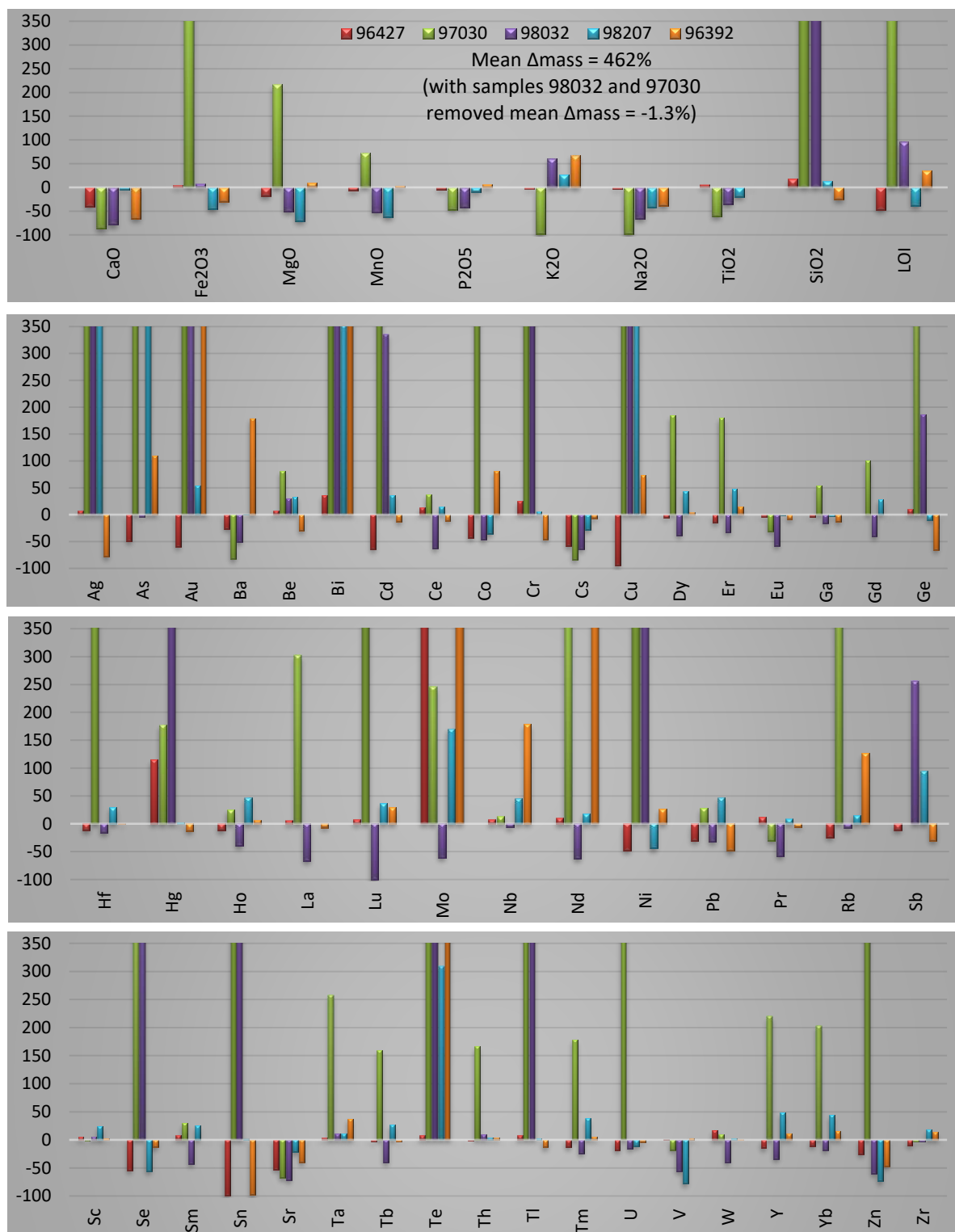


Fig. 43. Graphical illustration of calculated concentration changes for samples that have been silicified. Aluminum is not listed, as it was used as a conserved element for mass balance calculations. Absolute value results listed in Appendix 5, Table 11.

general equation:

$$(1) \quad \text{Alteration Index (AI)} = \left(\frac{\text{Sum of Elements added during alteration}}{\text{Sum of Elements subtracted (or conserved) and added during alteration}} \right) \times 100\%$$

The RAI calculation is a method for removing the effect of different host rock compositions on the alteration index (Mumin, 1988). It allows comparison between rocks of different initial composition and sets the measured alteration intensity scale from 0% – 100% for all samples analyzed. Intensity of alteration is measured from 0% (no detectable alteration) to 100% (the maximum possible alteration effect according to a particular AI). To remove the effect of variable host rock composition on the AI, a base index (BI) is subtracted. The BI is the alteration index applied to the least altered rock version of each geochemically distinct rock type (Table 5). The range of the index is constrained by dividing the AI-BI by 100 minus BI. For clarity in plotting and interpretation, any result of the RAI that is below zero is converted to a zero value since there is no ‘negative’ alteration. The equation is as follows:

$$(2) \quad RAI = \frac{AI - BI}{100 - BI} \times 100\%$$

For developing the AI formulae, preference in choosing variables is given to the major element oxides. These are the most abundant elements within rocks and so best reflect hydrothermal alteration. Only those rocks that have a least altered representation (listed in Table 4) are analyzed in this method. Table 5 lists the unique alteration types and the RAI formula that have been applied to them.

The calculated results are shown as bubble plots and as interpolated surfaces (contoured) overlaid on a map of the Mazenod Lake area in Figures 44 to 55. The simple kriging method within ArcMap software is used to construct the contoured maps. This method is an advanced

TABLE 5. Residual Alteration Indices (RAIs) applied to the Mazenod Lake region.

Residual Alteration Index	Element Ratios	Alteration Process	Figures	Source
Sodium Enrichment	$[\text{Na}_2\text{O}/(\text{Na}_2\text{O}+\text{Al}_2\text{O}_3)]$	Na_2O enrichment, Al_2O_3 conserved	44 & 45	
Iron Enrichment	$[\text{Fe}_2\text{O}_3/(\text{Fe}_2\text{O}_3+\text{Al}_2\text{O}_3)]$	Fe_2O_3 enrichment, Al_2O_3 conserved	46 & 47	
Ca-Fe Enrichment	$[(\text{CaO}+\text{Fe}_2\text{O}_3)/(\text{CaO}+\text{Fe}_2\text{O}_3+\text{K}_2\text{O})]$	Addition of CaO and Fe_2O_3 as magnetite-actinolite and/or chlorite-epidote-carbonate as well as depletion of K_2O from replacement of feldspars	48 & 49	
Potassic I	$[\text{K}_2\text{O}/(\text{K}_2\text{O}+\text{Na}_2\text{O}+\text{MgO}+\text{MnO}+\text{CaO})]$	Addition of K_2O as K-feldspar, depletion of Na_2O , CaO , MgO and MnO from replacement of ferromagnesium and Na-rich feldspars	50 & 51	
Potassic II	$[\text{K}_2\text{O}/(\text{K}_2\text{O}+\text{Na}_2\text{O})]$	Addition of K_2O as K-feldspar, depletion of Na_2O from replacement of Na-rich feldspars	52 & 53	Sericite Index from Saeki & Date (1980)
Silica Enrichment	$[\text{SiO}_2/(\text{SiO}_2+\text{Al}_2\text{O}_3)]$	SiO_2 enrichment, Al_2O_3 conserved	54 & 55	

geostatistical procedure that calculates values between known quantities and creates a two-dimensional prediction surface (map). The predicted values that the kriging algorithm calculates are a weighted average, based on modeling of a semivariogram graph. A complete explanation of kriging methodology is beyond the scope of this thesis. For an overview of the process involved in creating surfaces using the kriging technique, it is recommended to see the ArcGIS help file, available online at: <http://desktop.arcgis.com/en/arcmap/10.3/guide-books/extensions/geostatistical-analyst/understanding-how-to-create-surfaces-using-geostatistical-techniques.htm>. Kriging parameters used to customize the surfaces are included in the metadata accompanying the digital map files. Since the contours of the RAIs in some cases

correlate with mineralogy in outcrops, to a rough degree they can be corroborated by field observations to determine relative accuracy of the RAI.

Only those alteration types that have predictable geochemical enrichment and/or depletion patterns are used to calculate RAIs. For example, tourmaline alteration has no consistent enrichment or depletion pattern (other than potentially B-enrichment, which is not included in the geochemical analysis package). Consequently, no effective RAI could be constructed for identifying areas and intensity of tourmaline alteration.

Residual Alteration Indices

(a) Sodium Enrichment Index

The sodium AI is defined by the equation $\text{Na}_2\text{O}/(\text{Na}_2\text{O}+\text{Al}_2\text{O}_3)$. Highest percent values of the sodic RAI have the highest amount of Na_2O enrichment (Figs. 44 and 45). These maps represent a gauge of the intensity of Na_2O gains throughout the Mazenod Lake region, with the assumption that Al_2O_3 is immobile during hydrothermal alteration. Despite the small degree of sodium enrichment, the RAI plots indicate that there are previously unrecognized sodic alteration zones at the north end of Nod Hill and at the south end of the Bea area. Other more isolated zones of Na-enrichment are spread throughout the area.

(b) Iron Alteration Index

Iron enrichment RAI is an indication of the extent of the intensity of iron enrichment relative to the immobile element aluminum (Figs. 46 and 47). The AI is defined by the equation $\text{Fe}_2\text{O}_3/(\text{Fe}_2\text{O}_3+\text{Al}_2\text{O}_3)$. It is included in this thesis because iron is a major metal typically associated with IOCG-type deposits and systems (Hitzman et al., 1992). The iron enrichment

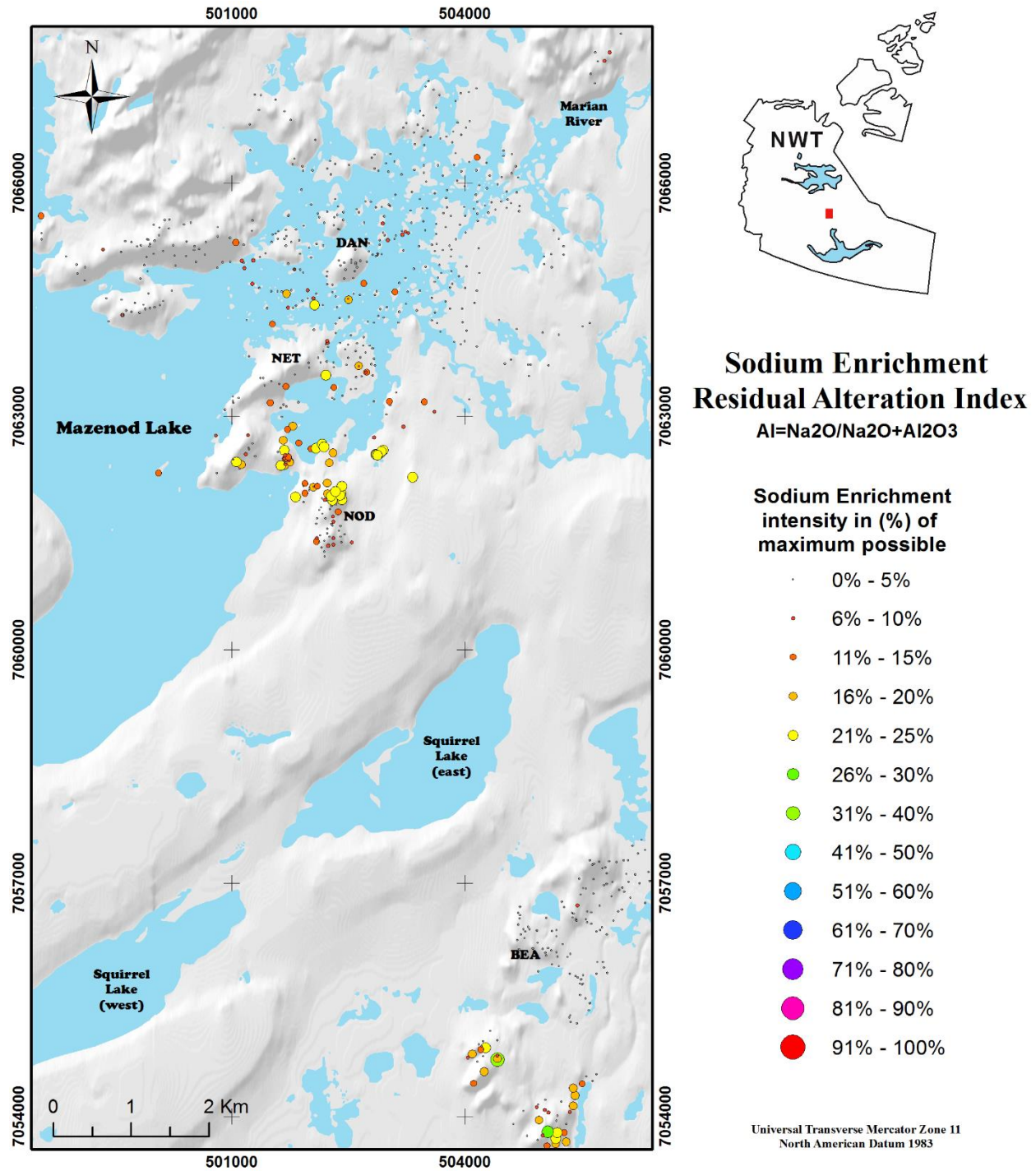


Fig. 44. Bubble plot map that illustrates the distribution of sodium enrichment intensity (in %). Gradient in color and size of points indicates changes in the amount of sodium enrichment relative to the immobile element aluminum. Digital elevation data courtesy of the Ministry of Natural Resources.

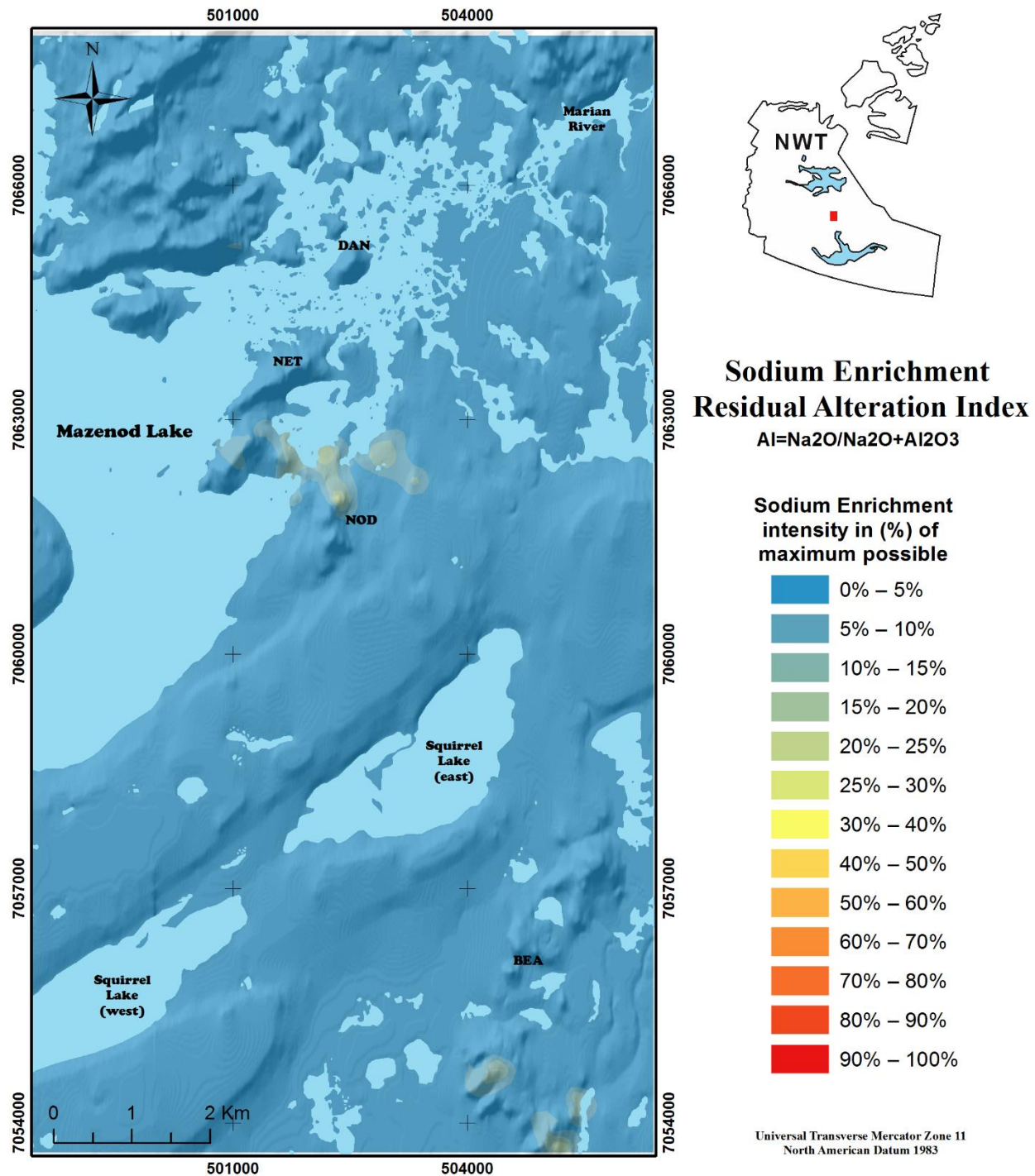


Fig. 45. Interpolated prediction surface that illustrates the distribution of sodium enrichment intensity (in %). Contours show a gradient of the amount of sodium enrichment relative to the immobile element aluminum. Digital elevation data courtesy of the Ministry of Natural Resources.

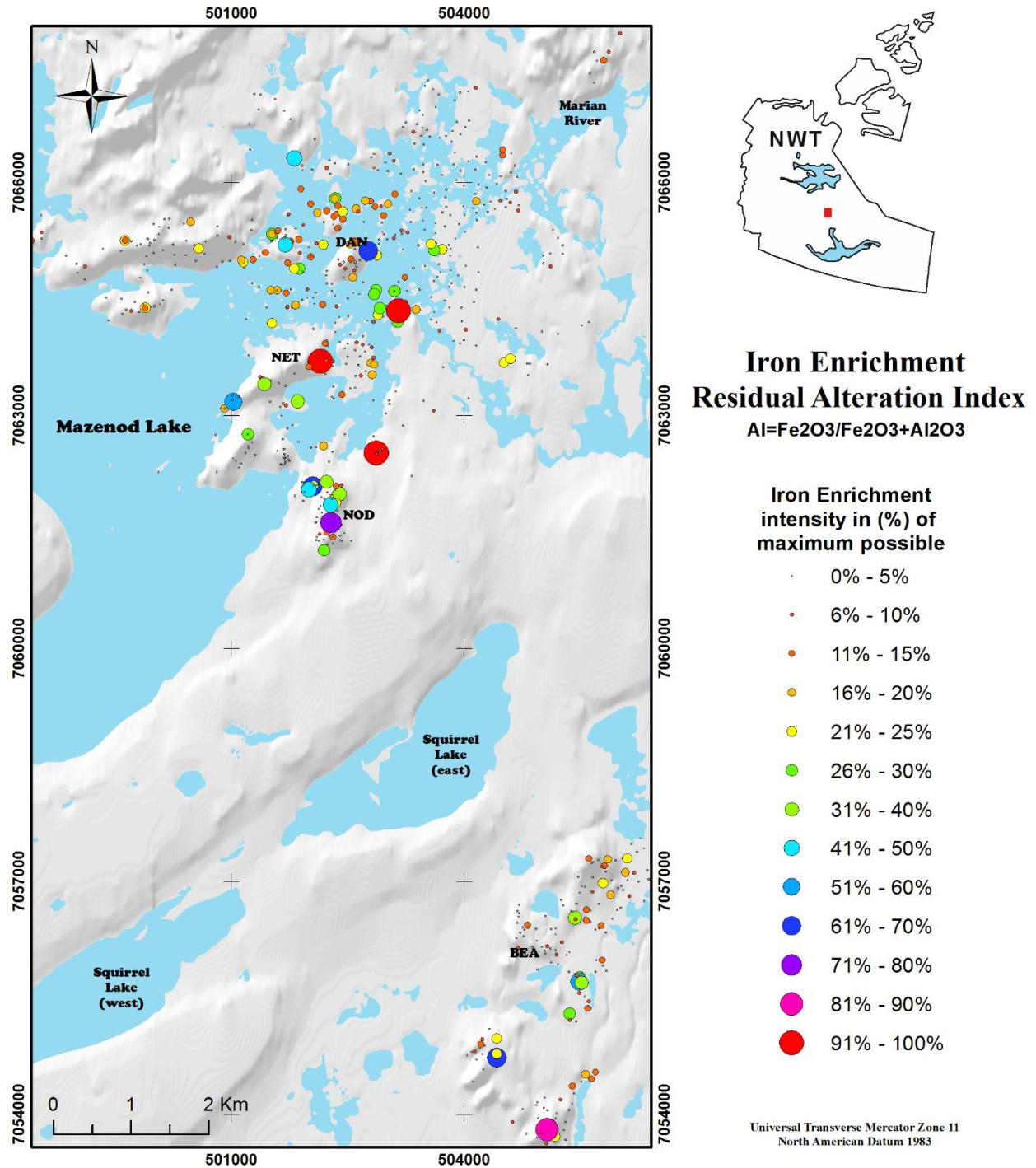


Fig. 46. Bubble plot map that illustrates the distribution of iron enrichment intensity (in %). Gradient in color and size of points indicates changes in the amount of iron enrichment relative to the immobile element aluminum. Digital elevation data courtesy of the Ministry of Natural Resources.

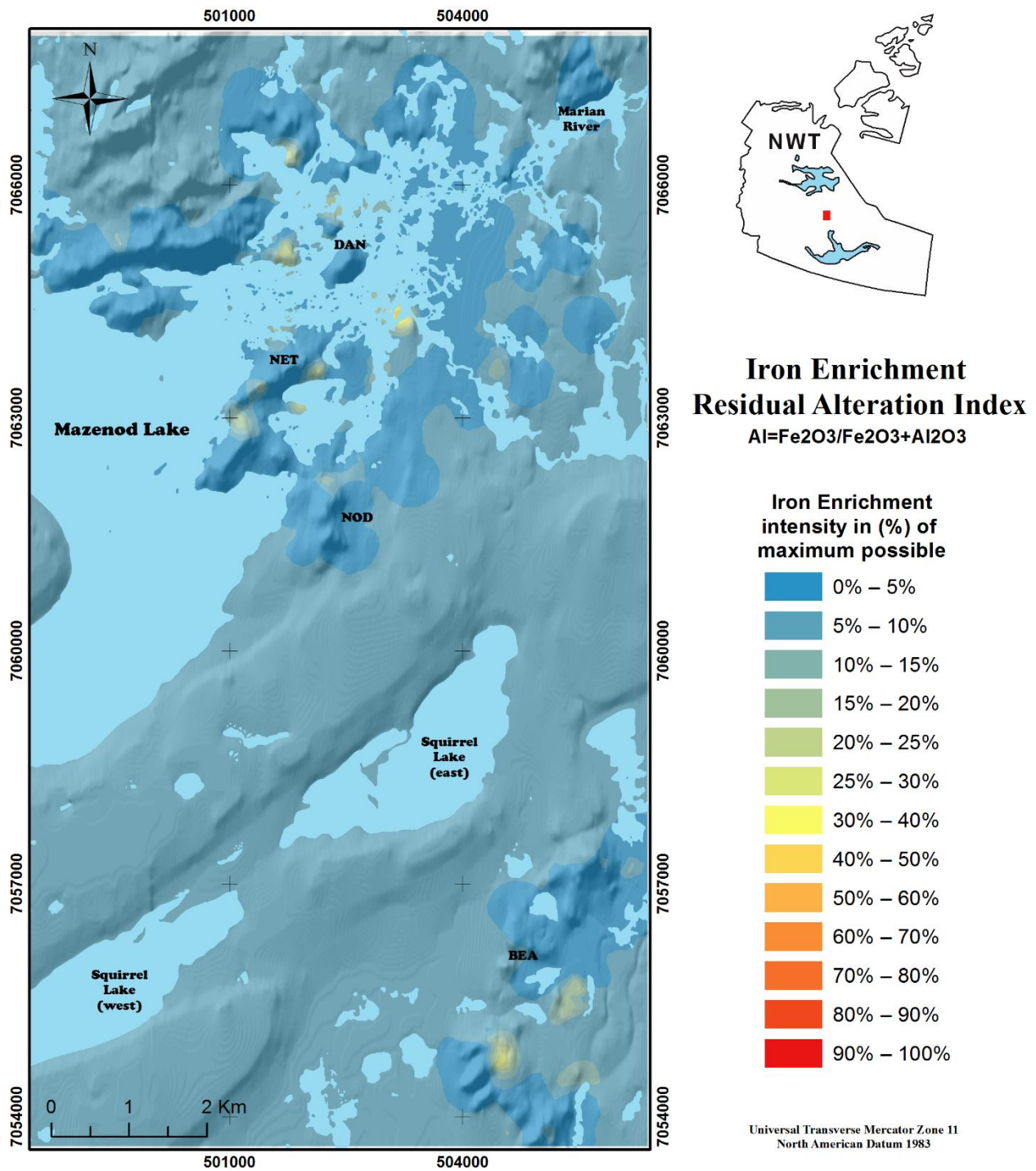


Fig. 47. Interpolated prediction surface that illustrates the distribution of iron enrichment intensity (in %). Contours show a gradient of the amount of iron enrichment relative to the immobile element aluminum. Digital elevation data courtesy of the Ministry of Natural Resources.

RAI maps show many individual and local groupings with Fe-enrichment. There is a distinct zone of iron enrichment surrounding Dan Island (particularly in the NW and SE) and locally at Nod Hill. In the Bea area, there are subtler anomalies that are mostly grouped close together. These observations tend to be coincident with areas noted in the field with relatively abundant hematite and/or magnetite alteration minerals. There are also a few areas with outcrops that contain moderate amounts of these minerals and show little or no enrichment on the RAI maps, which indicates this magnetite is not a result of hydrothermal alteration (such as the magnetite-bearing dacite ignimbrite). These RAI maps are an indication of the regional influence of iron enrichment across the Mazenod Lake region.

(c) Ca-Fe Alteration Index

The MA RAI (Figs. 48 and 49) scales the intensity of calcium and iron enrichment as well as potassium depletion. This is intended to coincide with the alteration process that involves replacement of host rock minerals (mostly feldspars) by magnetite and actinolite. However, in general, the high values of MA RAI index maps are an indication of the relative abundance and distribution of iron plus calcium-rich minerals, which can include actinolite, magnetite, chlorite, epidote and carbonate. The AI is represented by the equation $[(\text{Fe}_2\text{O}_3 + \text{CaO}) / (\text{Fe}_2\text{O}_3 + \text{CaO} + \text{K}_2\text{O})]$. High MA RAI values (>61%) mostly correlate with rock samples that contain actinolite \pm magnetite; however, the mid-range values (<61% - 10%) are quite often associated with epidote altered samples and even some tourmaline altered samples. The very highest MA RAI values can be linked directly to actinolite cemented hydrothermal breccias, such as at the northern end of Nod Hill. There are a few exceptions, including the far

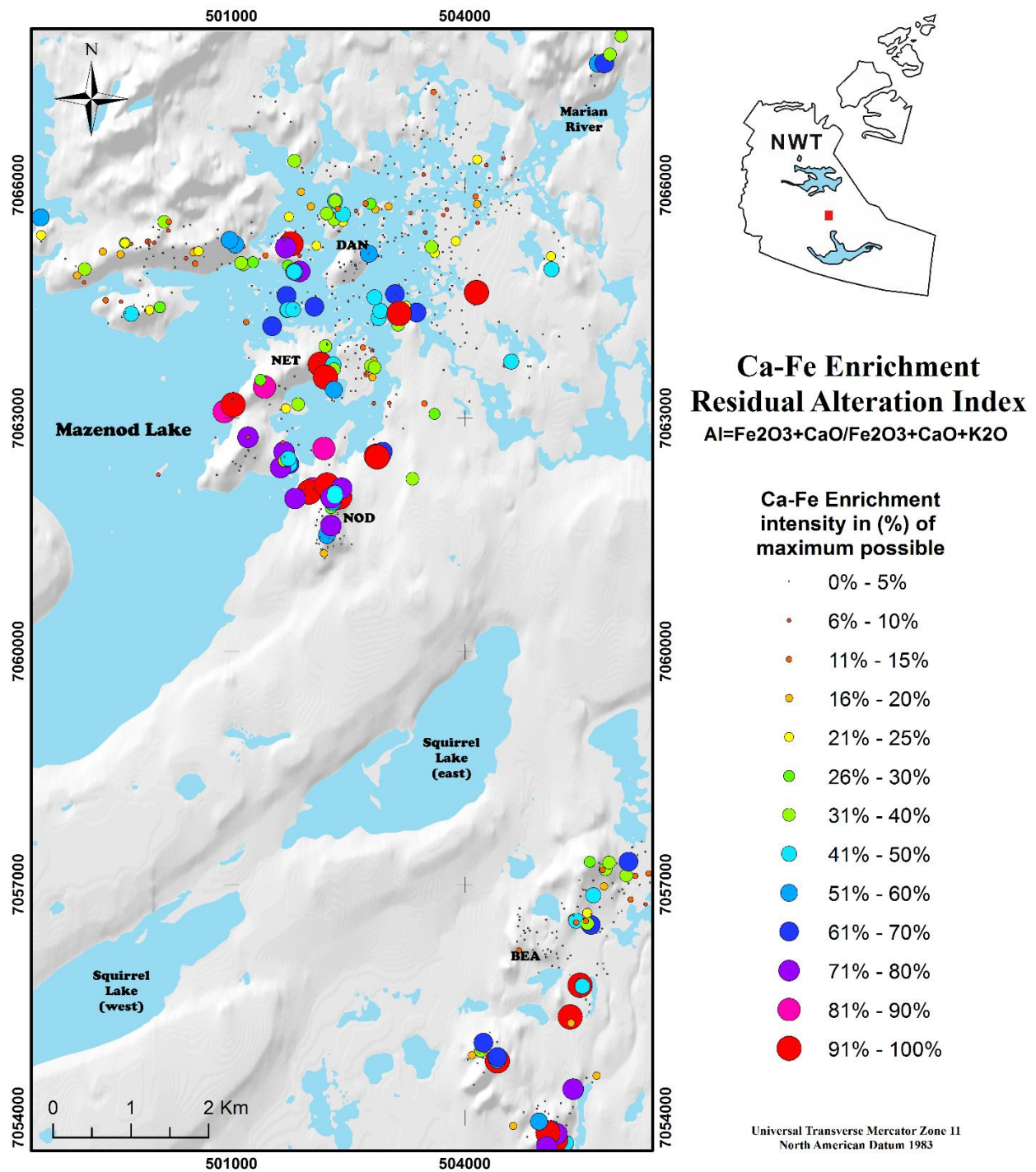


Fig. 48. Bubble plot map that illustrates the distribution of Ca-Fe enrichment intensity (in %). Gradient in color and size of points indicates changes in the amount of iron and calcium enrichment as well as potassium depletion. Digital elevation data courtesy of the Ministry of Natural Resources.

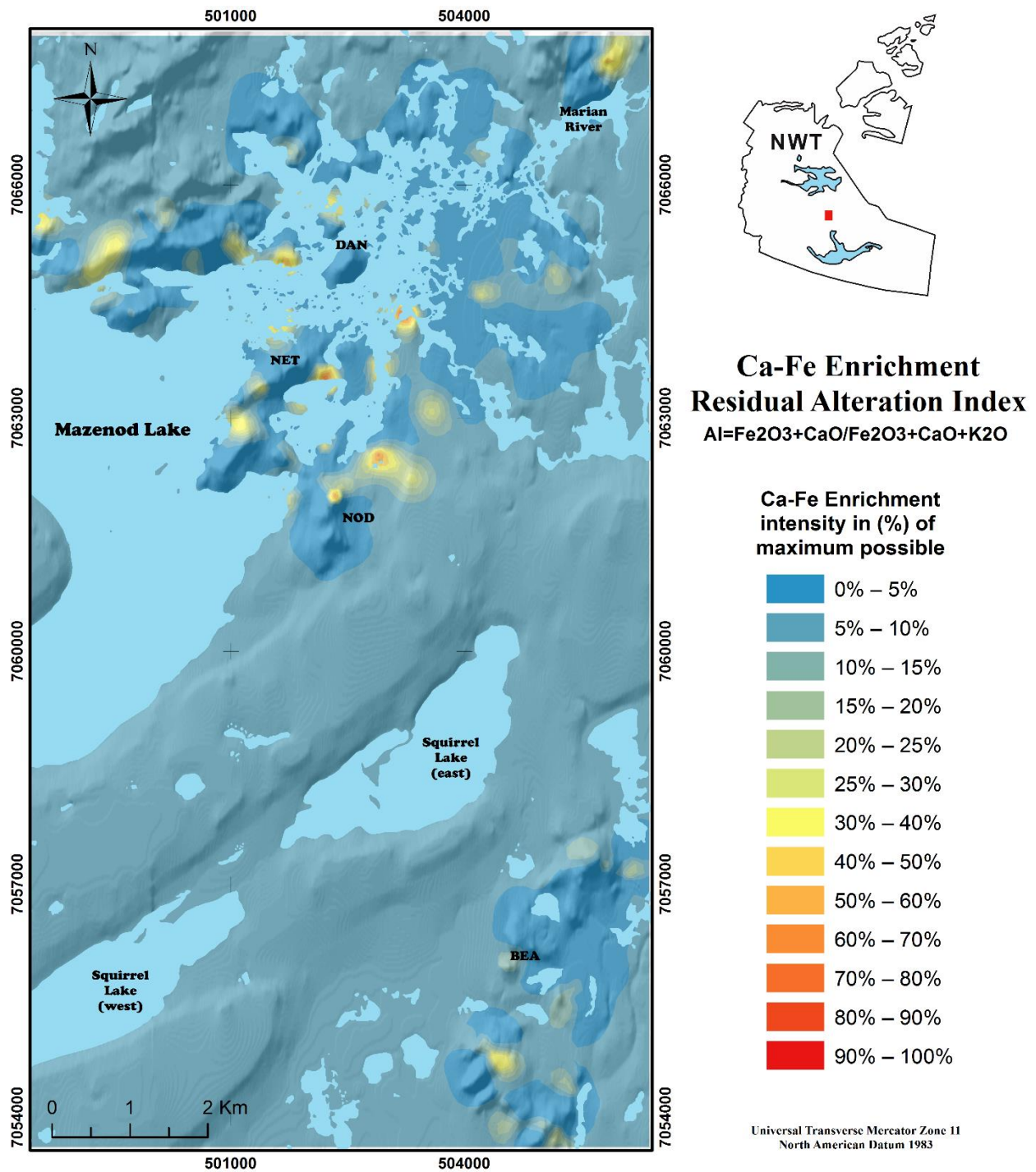


Fig. 49. Interpolated prediction surface that illustrates the distribution of Ca-Fe enrichment intensity (in %). Contours show a gradient for the amount of iron and calcium enrichment as well as potassium depletion. Digital elevation data courtesy of the Ministry of Natural Resources.

north eastern and western portions of the contour map. At these locations, higher intensity contours overlap with areas noted to contain abundant epidote alteration minerals. Contextual field observations are necessary to differentiate between zones containing the different alteration minerals.

(d) Potassic Alteration Indices

Two potassium RAI $K_2O/(K_2O+Na_2O)$ and $K_2O/(K_2O+Na_2O+CaO+MgO+MnO)$ are plotted in Figures 50 to 53. The former RAI is a simple test for intensity of potassium enrichment and sodium depletion, typically associated with crystallization of K-feldspar and replacement of plagioclase (Benevides et al., 2008). Similarly, the latter potassic RAI tests for the same result, but in addition include the effects of the removal of calcium, magnesium and manganese, due to the replacement of ferromagnesium minerals by K-feldspar as well. The highest values of this index may correlate with feldspar-like K-altered rocks.

The potassic indices indicate the most widespread and intense hydrothermal alteration of any index plotted. This matches field observations noted in Chapter 5 that suggested potassic alteration is near ubiquitous in the study area. The highest values are located near the center and highest elevated part of Dan Island, in proximity to the NE-oriented Kemaz fault. Another distinctive grouping of higher potassic RAIs values occurs at Nod Hill and in the central Bea area. These three distinctive potassic RAI anomalies also correspond with the intersections of known faults.

Size of the K-alteration halos surrounding the highest potassic RAI values show that the alteration can extend for several kilometers away from the potential foci of hydrothermal alteration. The K-alteration plots demonstrate the spatially extensive area affected by hydrothermal alteration.

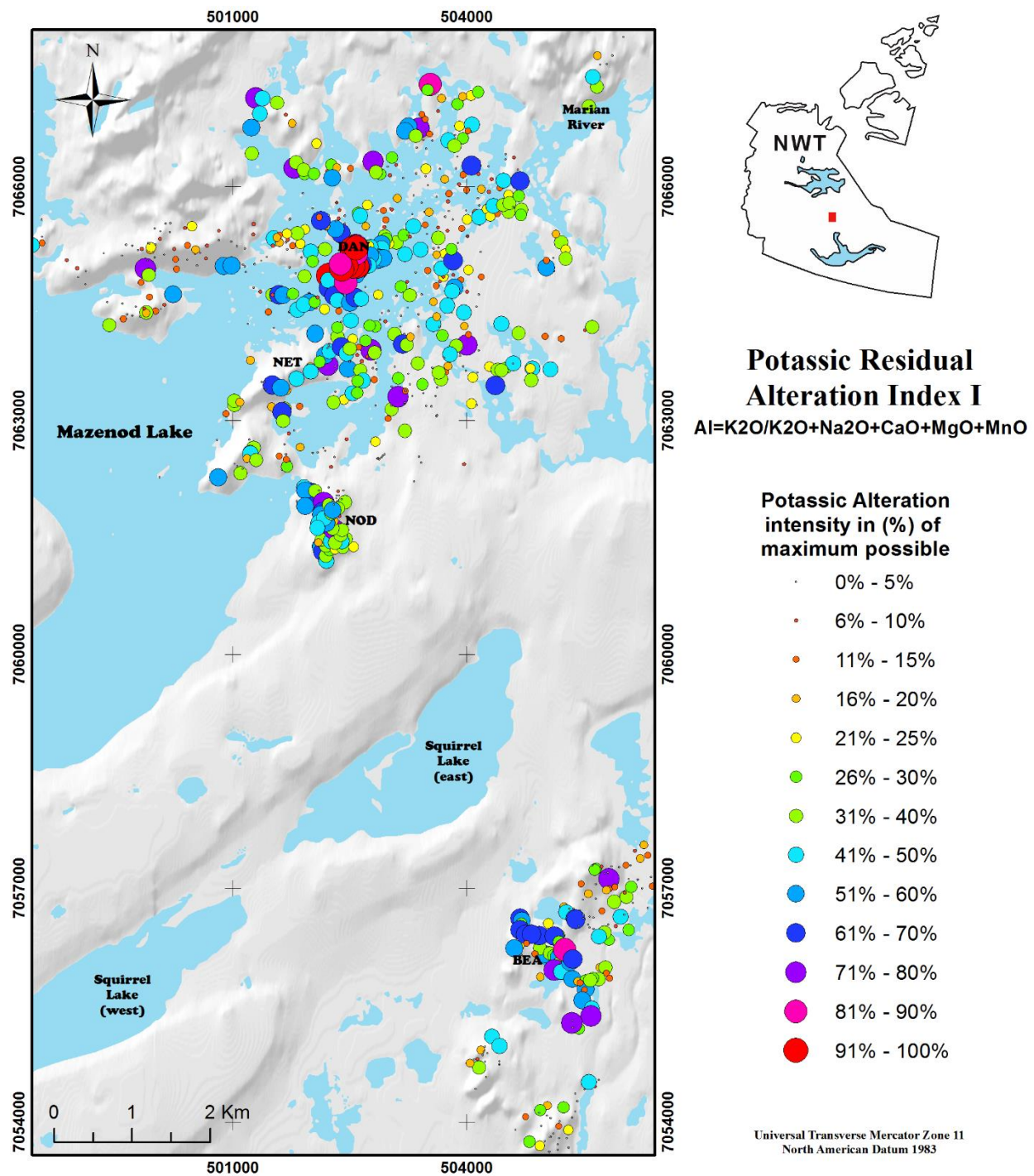


Fig. 50. Bubble plot map that illustrates the distribution of potassic alteration intensity (in %). Gradient in color and size of points indicates changes in the amount of potassic enrichment as well as sodium, calcium, magnesium and manganese depletion. Digital elevation data courtesy of the Ministry of Natural Resources.

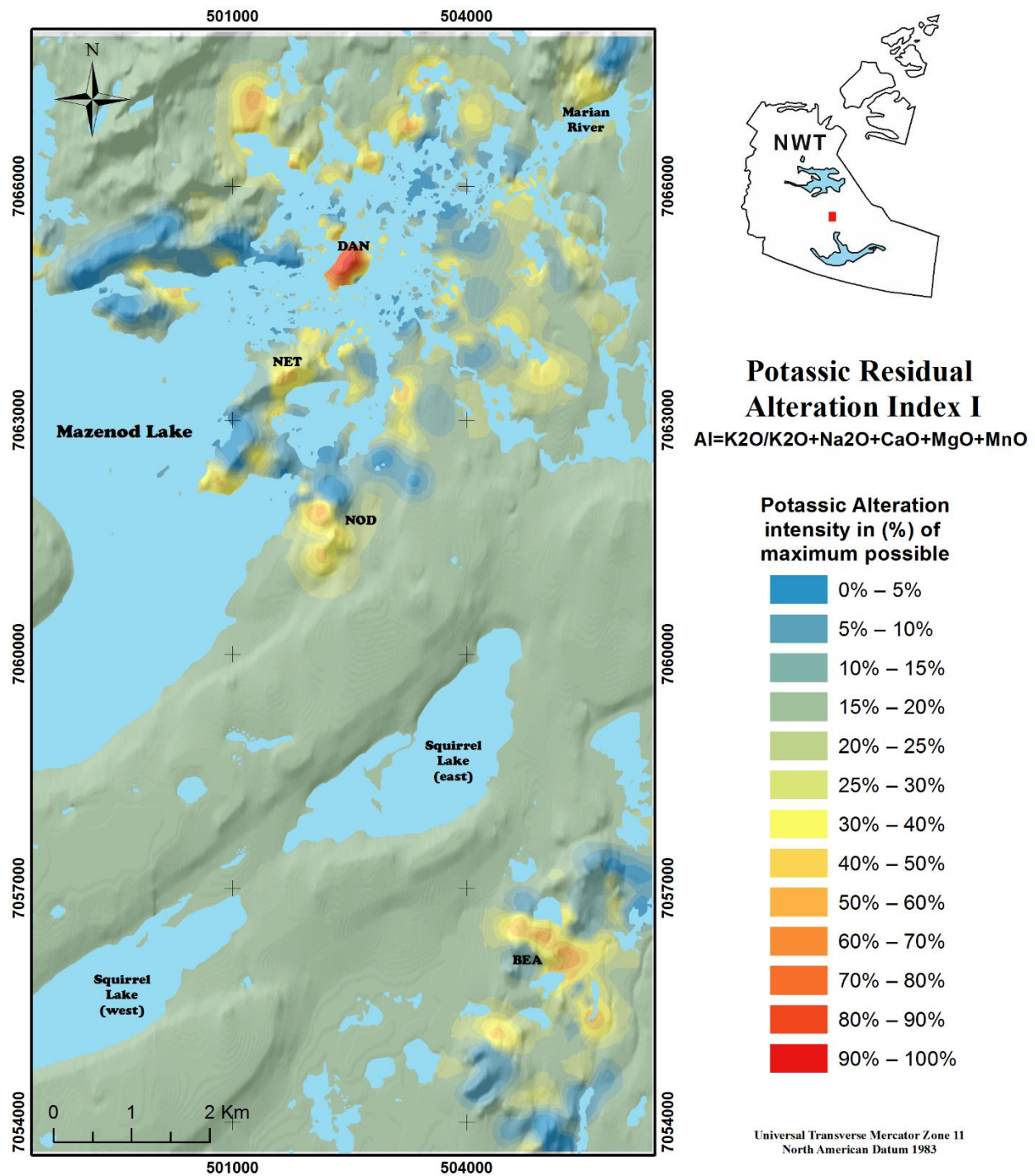


Fig. 51. Interpolated prediction surface that illustrates the distribution of potassium alteration intensity (in %). Contours show a gradient for the amount of potassic enrichment as well as sodium, calcium, magnesium and manganese depletion. Digital elevation data courtesy of the Ministry of Natural Resources.

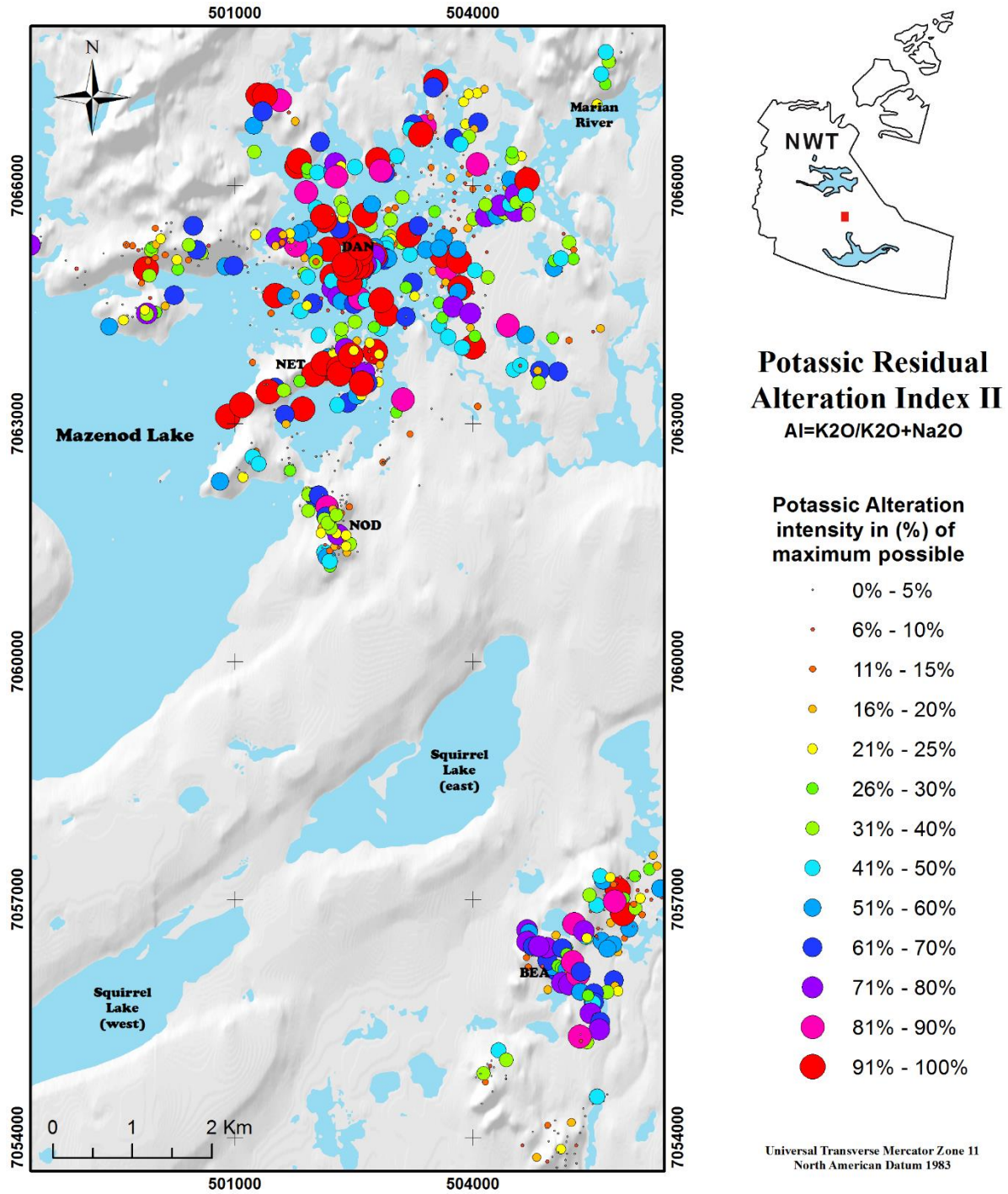


Fig. 52. Bubble plot map that illustrates the distribution of potassic alteration intensity (in %). Gradient in color and size of points indicates changes in the amount of potassic enrichment and sodium depletion. Digital elevation data courtesy of the Ministry of Natural Resources.

(c) Silica Alteration Index

The silica enrichment RAI maps characterize the spatial extent of silica enrichment intensity (i.e. silicification), with the assumption that aluminum is immobile during the alteration (Figs. 54 and 55). Equation for the silica AI is $\text{SiO}_2/(\text{SiO}_2+\text{Al}_2\text{O}_3)$. There are several giant quartz-vein-silicification complexes present in the Mazenod Lake area, which represent an extreme form of silica enrichment. These are largely vein complexes recorded during mapping, so they are excluded from the RAI analysis.

Mid to high range silica RAI values (41% and greater) mostly coincide with field observations of silicification. These high value anomalies have surrounding lower silica enrichment RAI values (usually 15% or less), which do not match areas visually observed to contain silicification. This indicates that silica alteration extends further than what can be observed directly in outcrops and that the contours of the silica RAI represent a gradation of silica alteration intensity.

In the vicinity of Mazenod Lake, there is a subtle silica RAI anomaly at Dan Hill (slightly higher values in the rhyodacite). Along Net Ridge, there are several high silica RAI anomalies, which are in accord with field observations of silicification along the Marian River fault at that location (in the volcanic rocks), and are in spatial proximity to a giant quartz-vein complex. Silica RAI values are also subtly higher across most of Nod Hill, with highest values in the northern portion of the hill. These values correlate with actinolite-quartz \pm magnetite veins and breccia. The potassic RAI contours are arranged comparatively similarly within the extent of Nod Hill. At the Bea area the silica and potassic RAI values instead have an almost inverse relationship. High silica RAI values mostly correspond with low potassic RAI values at the same coordinates in the Bea area. Many of the other regional high silica RAI anomalies are relatively

isolated as compared to the previously mentioned locations. Most of these anomalies are proximal to locally recognized faults and/or hydrothermal breccias.

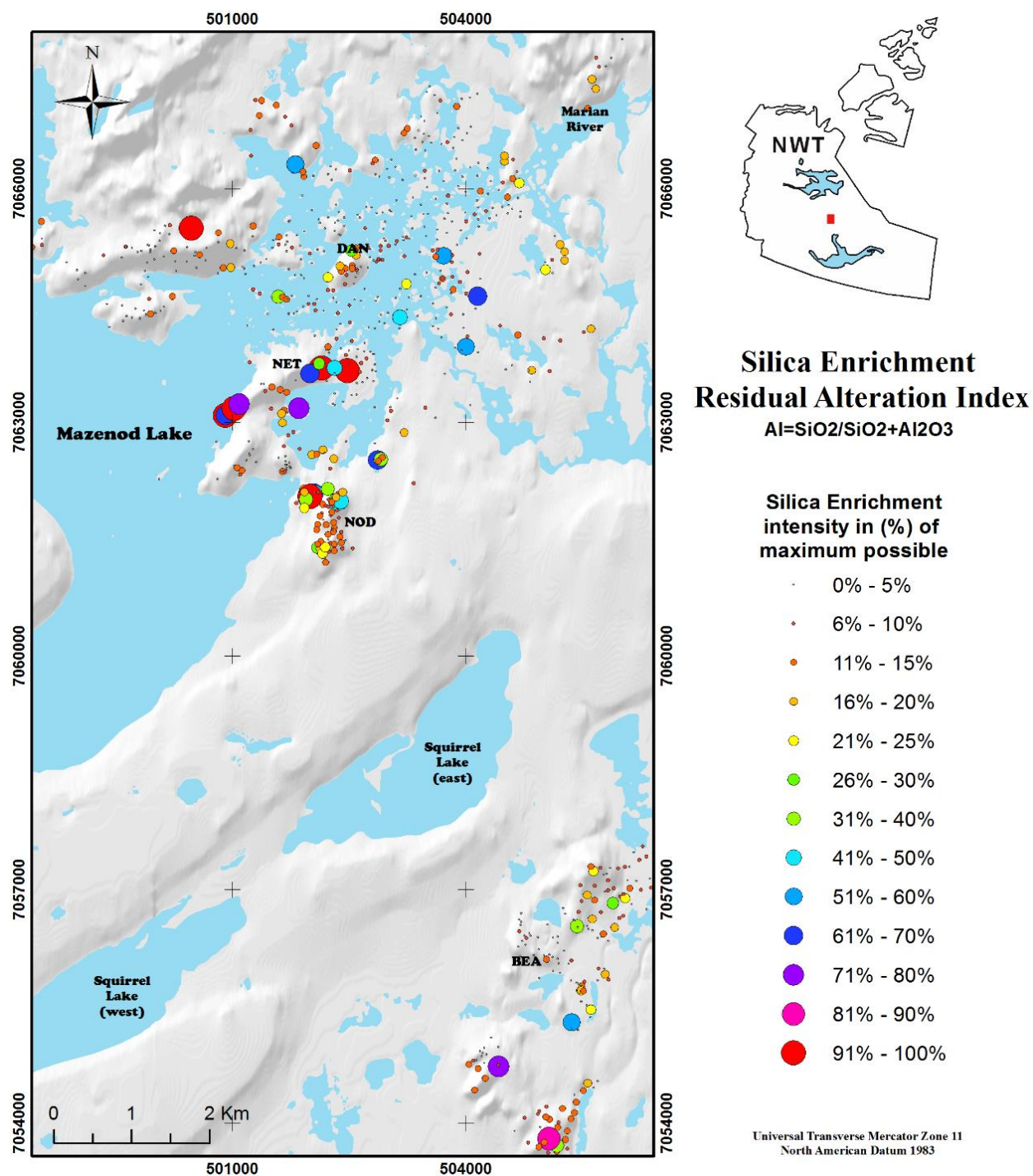


Fig. 54. Bubble plot map that illustrates the distribution of silica enrichment intensity (in %). Gradient in color and size of points are intended to indicate changes in the amount of silica enrichment relative to the immobile element aluminum. Digital elevation data courtesy of the Ministry of Natural Resources.

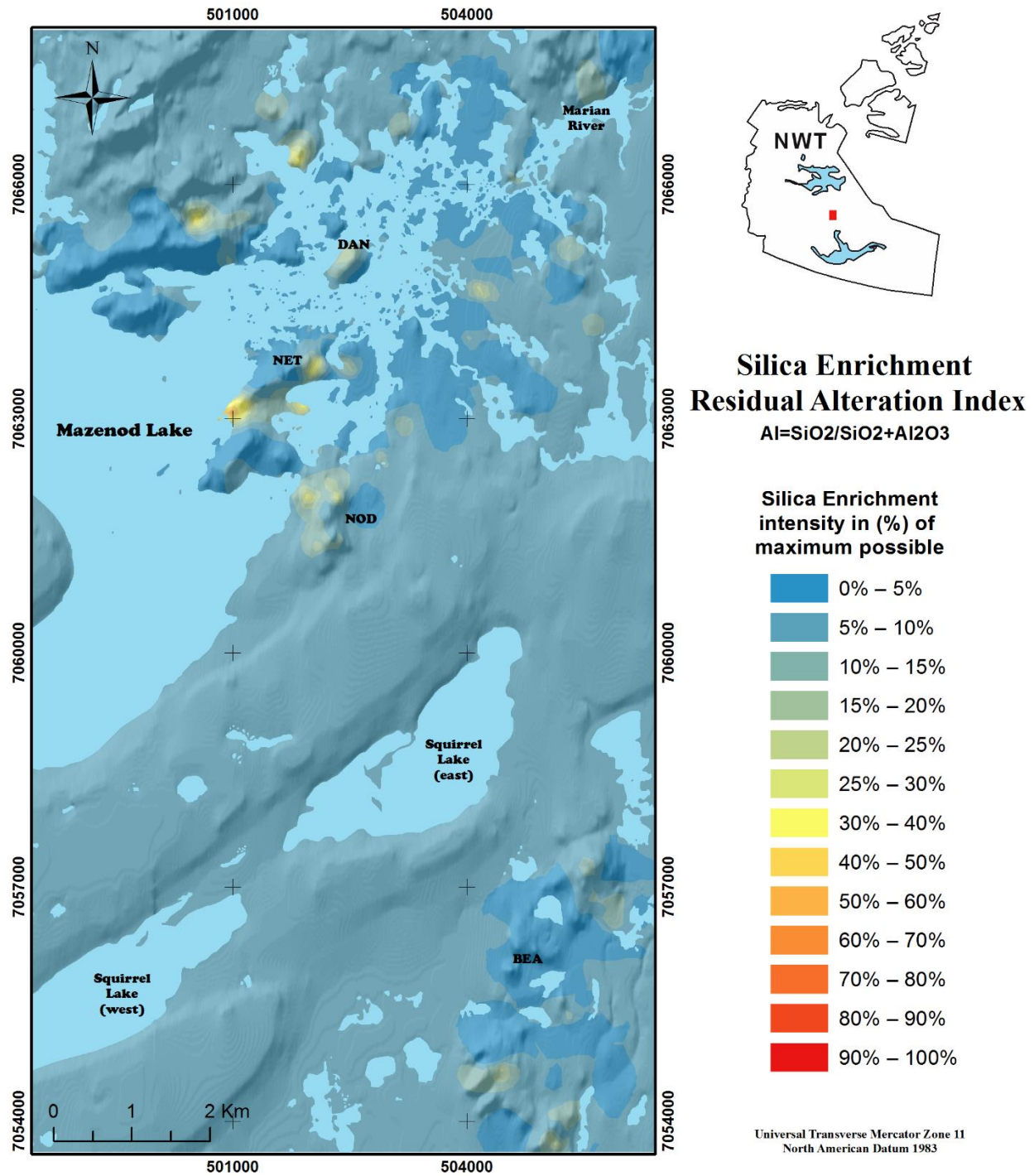


Fig. 55. Interpolated prediction surface that illustrates the distribution of silica enrichment intensity (in %). Contours show a gradient for the amount of silica enrichment relative to the immobile element aluminum. Digital elevation data courtesy of the Ministry of Natural Resources.

Chapter VIII: Discussion

The Mazenod Lake region is underlain by early Proterozoic volcanic, sedimentary and intrusive rocks, with younger Phanerozoic sedimentary rocks occupying part of the central and western portion of the study area. The study area is dominated by volcanic rocks that are mostly pyroclastic flows (ignimbrites), typical of stratovolcanic terrains. Least hydrothermally altered versions of these volcanic rocks are usually dark grey, massive, undeformed and often eutaxitic. Textures of the volcanic rocks include porphyritic, intergranular, inequigranular, seriate, trachytic, corroded, and/or poikilitic types. The typical ignimbrites are crystal tuff, but the volcanoclastic facies comprise tuffs, lapilli, ash, and pyroclastic breccias (Fisher, 1966). Each volcanic rock formation varies slightly in mineral composition and vol. %, but usually contains phenocrysts of potassium feldspar, plagioclase, biotite, quartz, pyroxene, and/or amphiboles. The chemical classifications indicate they are calc-alkaline intermediate to felsic volcanic rocks.

The intrusive rocks are chemically similar to the volcanic rocks. They include deep-seated and near surface expressions, such as the Marian River monzogranite batholith and a monzodiorite intrusion, respectively. These plutonic rocks constrain and/or intrude into the volcanic belt. The intrusive rocks have typically an orange-red hue at weathered surface, with textures that are medium to coarse grained and feldspar-phyric. Intrusive dykes cross-cut the volcanic belt, are spatially intermittent and generally are oriented sub-parallel to NE-trending en echelon faults.

Volcanic sediments predominantly comprised of reworked volcanic tephra and other lithic fragments unconformably lie above most volcanic rock formations. Various facies of the sedimentary rocks include well-preserved beds of claystones, sandstones and conglomerates. A separate sequence of much younger Paleozoic era marine transgression sediments is discordant and unconformably overlies all the other rocks in the region.

Stratigraphy

Exposed stratigraphy at and around Mazenod Lake portrays a succession of Paleoproterozoic volcanic events that comprise several intermediate to felsic ignimbrite flows. Local igneous rocks belong to the Faber Group, a subdivision of the McTavish Supergroup (Gandhi et al., 2001; Hildebrand et al., 2010). Volcanism commenced ca. 1873 Ma and lasted for a period of approximately 7 million years (Gandhi and van Breemen, 2005; Montreuil et al., 2016). Locally, extrusive events commenced with the emplacement of the Mazenod Lake assemblage and sequentially continued with the eruption, deposition and consolidation of the Bea Lake, Squirrel Lake, Lou Lake and Dianne Lake assemblages. During periods of volcanic dormancy autochthonous sedimentary material was deposited and unconformably separated the volcanic assemblages (Gandhi et al., 2001). Synchronous with the volcanic events a porphyritic monzodiorite intruded and was emplaced in the region (Figs. 8-10). This intrusion is a likely source intrusion for the region, and is presently mostly exposed along the southeastern shoreline of Mazenod Lake and near Dan Island. The monzodiorite is interpreted to be an early expression of the deep-seated Marian River Batholith monzogranite and/or the Sarah Lake granite. The deep-seated plutonic rocks have been dated at 1866 – 1863 Ma (Gandhi et al., 2001).

After volcanic activity, during the Paleozoic era, a layer of sedimentary strata was unconformably deposited over large sections of volcano-plutonic rocks within the Mazenod Lake

area and the rest of the GBMZ (Hildebrand and Bowring, 1984; Hoffman, 1987; Gandhi et al., 2001).

Structure

The geotectonic framework of the Mazenod Lake region is characterized by several sets of subparallel linear and curvilinear faults and deformation zones. In Chapter 6, many of the aforementioned structural features have been shown to form lineaments well-defined on satellite, aeromagnetic and digital elevation images. A visual inspection of the lineaments reveals a complex strike-slip fault system. Numerous structures visibly intersect, segment, dislocate and distort each other in an intricate arrangement, that at least in part reflects the spherical geometry of the Earth.

The dominant regional structures are evident on the satellite, aeromagnetic and digital elevation images shown in Chapter 6 (Figs. 16 to 19 and 55a). They are also visible at outcrop scale as faults, fractures and vein systems (Fig. 55b). The NE-trending faults are the most frequently visible structures, although NW and NNE-trending faults are not uncommon. The

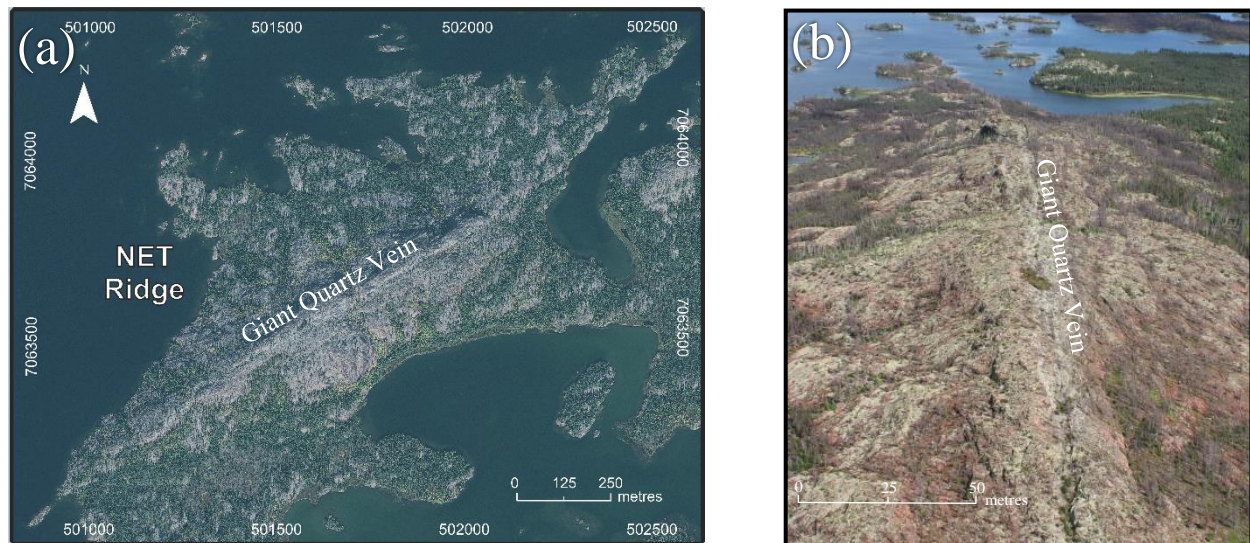


Fig. 56a, b. Satellite image on the left and aerial photograph on the right showing the Net Ridge giant quartz vein, which is a continuation of the right lateral offset Marian River Fault. In proximity to the fault there are large quartz stockworks, an abundance of fractures and intense silica and potassic alteration.

NW-oriented faults are more easily identifiable in the Bea area on the satellite and magnetic vertical gradient (MVG) aeromagnetic images (Figs. 21 and 23). There are also breaks in the supracrustal rocks that orient in many other directions; however, there are no significant patterns that can be established from these subordinate structures. They are relatively inconsequential when compared to the large quantity of recognized primary structures and most are likely a secondary consequence of primary tectonic features. An illustration of an interpretation of major faults and their movements is shown in Figure 56.

The general trend of the observable major faults within the Mazenod Lake region is to the NE (average orientation $\sim 050^\circ$) (See rose diagrams that illustrate fault and/or lineament orientations in Chapter 6, Figs. 19, 21 and 23). These are right-laterally displaced faults that are subparallel to regionally significant transcurrent faults that occur throughout the GBMZ (Hildebrand et al., 1986; Gandhi et al., 2001; Mumin et al., 2014; Hayward and Corriveau, 2014; Ootes et al., 2015). Along with less recognizable left-lateral offset NW-trending faults (average orientation $\sim 340^\circ$) they form a conjugate system of steeply dipping faults (e.g. $\sim 75^\circ$ NW dip of the Dianne Lake fault; Mumin et al., 2010). These fault sets are part of a regional conjugate fault set that displaces and segments most of the GBMZ (Hoffman, 1980; Hildebrand et al., 1986; Mitchell et al., 2010; Hayward and Corriveau, 2014). The NW-oriented faults often separate stratigraphy along unconformities. A third significant set of right-lateral offset faults orients to the NNE (average orientation $\sim 020^\circ$). Analysis of satellite and aeromagnetic images, as well as measurements taken directly in the field show that each of these major crustal breaks are oblique strike-slip faults, with a near-vertical dip at surface, and horizontal displacements up to ~ 1.5 km. A summary of the faults in the Mazenod Lake region and their estimated horizontal offset are shown in Table 6 and Figure 57.

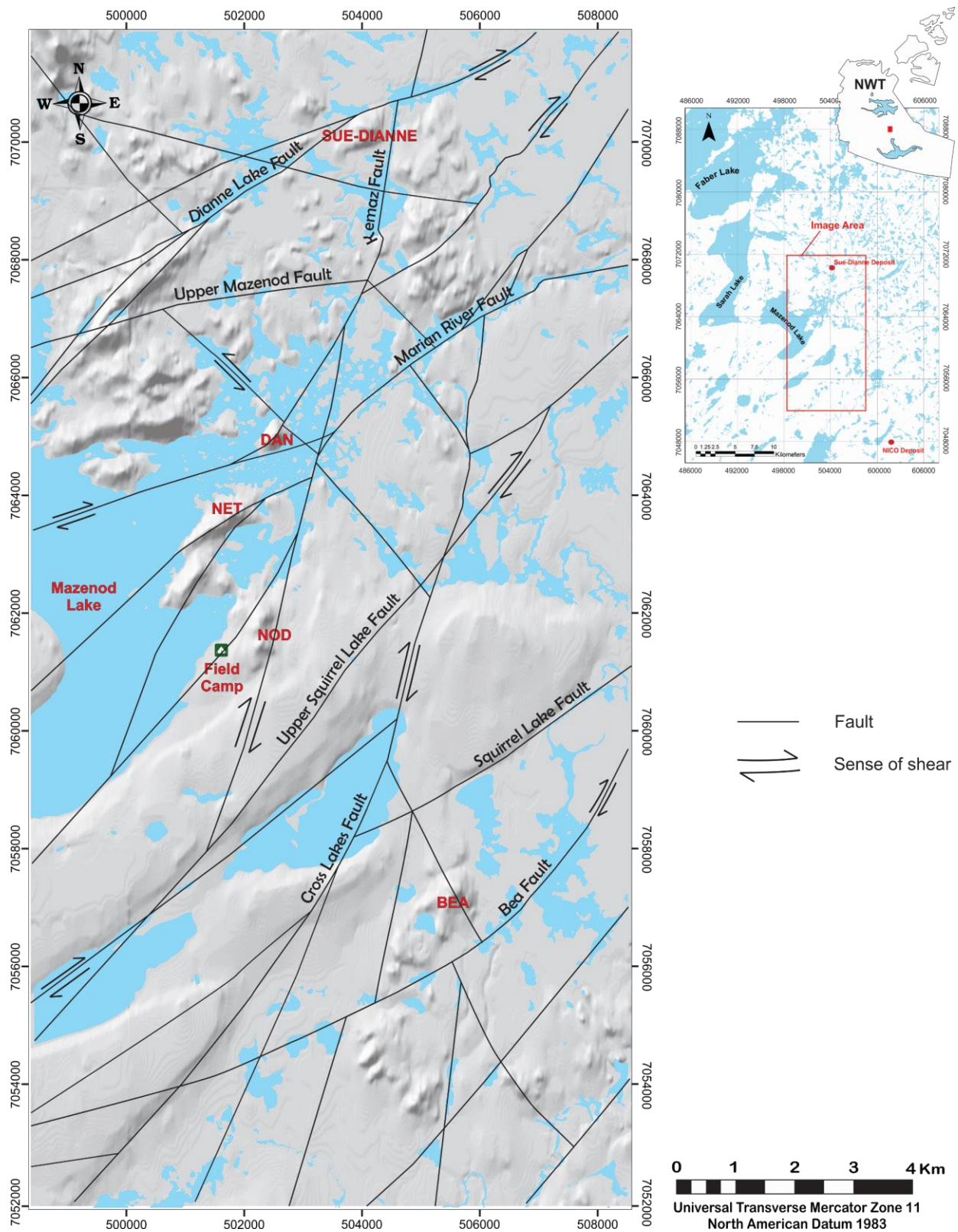


Fig. 57. Interpretation of major structures in the Mazenod Lake region. Digital elevation data courtesy of the Ministry of Natural Resources.

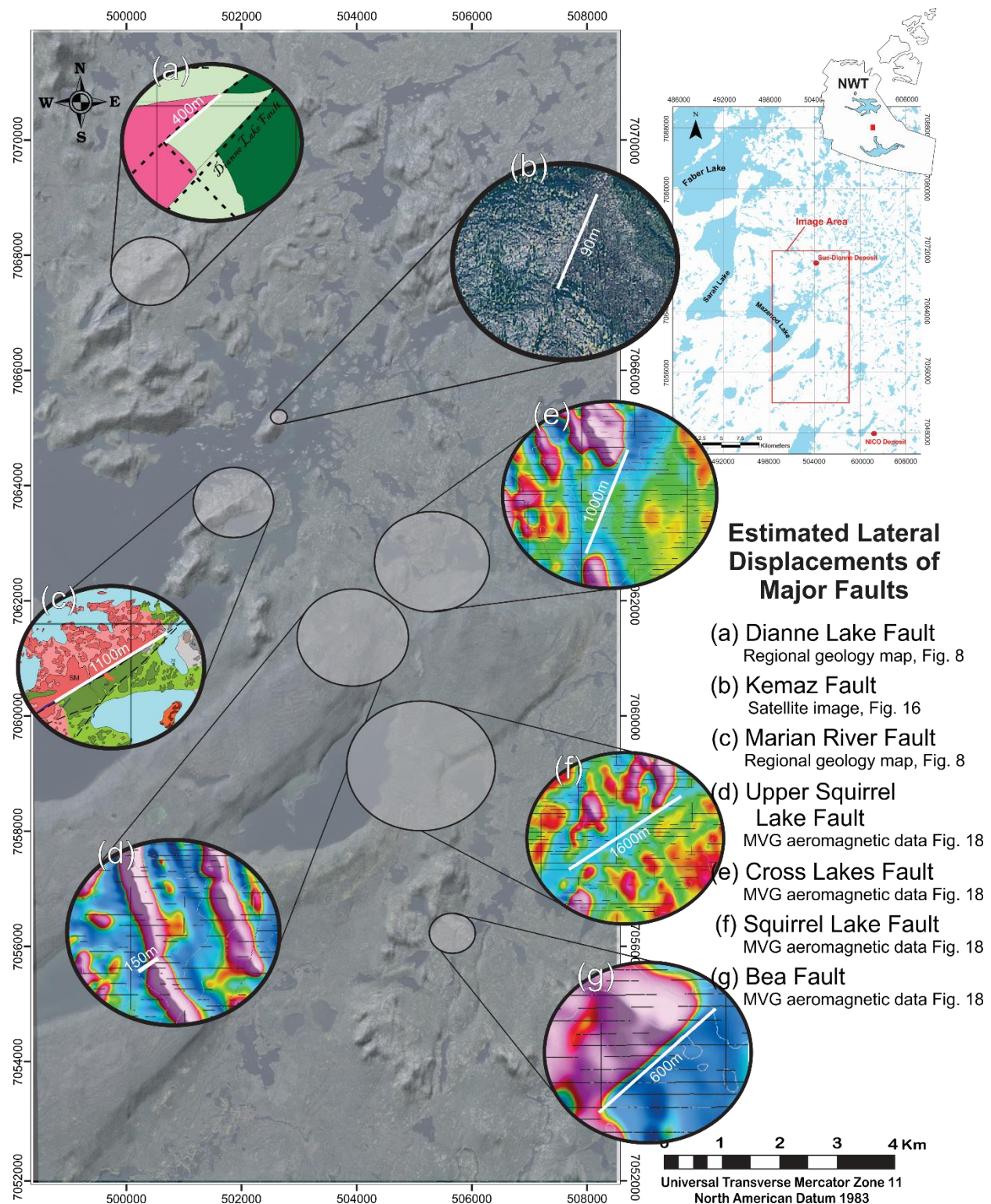


Fig. 58. Estimated horizontal offset of major strike-slip faults within the Mazenod Lake region. Measurements are estimated from a combination of structural field mapping, magnetic vertical gradient data (MVG) offsets and satellite image observations. Digital elevation data courtesy of the Ministry of Natural Resources.

TABLE 6. Dominant faults in the Mazenod Lake region and their estimated horizontal offset

Fault Name	Estimated Lateral Displacement ¹
Dianne Lake Fault	400 m?
Marian River Fault	1100 m
Upper Squirrel Lake Fault	150 m
Squirrel Lake Fault	1500 m
Bea Fault	650 m
Kemaz Fault	90 m
Cross Lakes Fault	1000 m

¹Estimates based on field mapping, aeromagnetic data, and satellite image measurements (Fig. 57).

A complete chronologic sequence of tectonic activity is difficult to determine for the study area. Many of the faults of different orientations appear to offset each other. Despite the difficulty, a general interpretation of age relationships can be substantiated from the analysis of local structures and their spatial relationships. For instance, the hydrothermal alteration tends to be focused along major structural corridors. This implies that the alteration hosting structures were essentially coeval and/or pre-date the alteration and volcanic activity in the region. Additional evidence for the similar timing relationship is demonstrated by structural breccias and stockworks that are re-cemented with hydrothermal minerals. Further displacement of the lithology and hydrothermal alteration that cannot itself be directly linked to volcanic or hydrothermal activity is evidence that tectonic activity continued past periods of volcanism and alteration that is now exposed at surface. Prior to emplacement of the volcanic assemblages (Faber Group volcanism) the recognized system of major faults is likely to have already been in place. If this hypothesis is true, the present tectonic framework could be a result of re-activation of prevailing structures.

An indication of the component of dip-slip movement along the Kemaz oblique-slip fault can be interpreted from the differences in lithology between bounding faults. At Dan Island, the Kemaz fault separates a rhyodacite from an andesite (west and east sides respectively).

Assuming the stratigraphy has been correctly interpreted, the west flank of the Kemaz fault is probably the down-dropped block. The eastern side of the Kemaz fault (up-thrown block) would experience erosion to a deeper level, because the amount of exposure is greater. Eventually, older lithology would be uncovered on the up-thrown side. This suggests that at Dan Island the Kemaz fault has a component of reverse type oblique-slip faulting. Camier (2002) made a similar interpretation for the Kemaz fault at the Sue-Dianne deposit.

The magnetic vertical gradient (MVG) data define three main areas that are characterized by distinct and mostly unique magnetic lineament patterns (Fig. 58). These are tectonic blocks segmented by major en echelon NE-oriented faults (strong magnetic discontinuities), that have a similar dextral shear sense, but are disproportionally rotated and horizontally displaced. The major tectonic blocks are identified here as the Mazenod, Squirrel and Bea tectonic blocks.

There is also a characteristic pattern of lineament orientations that distinctly separates the volcanic belt and intense hydrothermal alteration from the surrounding intrusive rocks. The plutonic rocks magnetic lineaments are predominantly oriented to the NE, essentially parallel to the regional transcurrent faults. Within the volcanic belt, lineaments are mostly parallel to NW-trending structures and lithology. Unlike the NNE and NE oriented structures, there is no apparent evidence on the satellite image, geophysical data or digital elevation data that indicates NW-trending structures were active after volcanism. This suggests that the belt-parallel structures and associated alteration were tied exclusively to the period of GBMZ volcanism.

Vertical axis clockwise rotation of the Mazenod tectonic block is revealed by the disparate orientation of lithology at the flanks of the segmenting Marian River fault (Figs. 8 and 9). There is an approximately 130° dihedral angle (angle between two planes) between the orientation of the Dianne Lake assemblage and the orientation of the Lou, Squirrel and Bea Lake

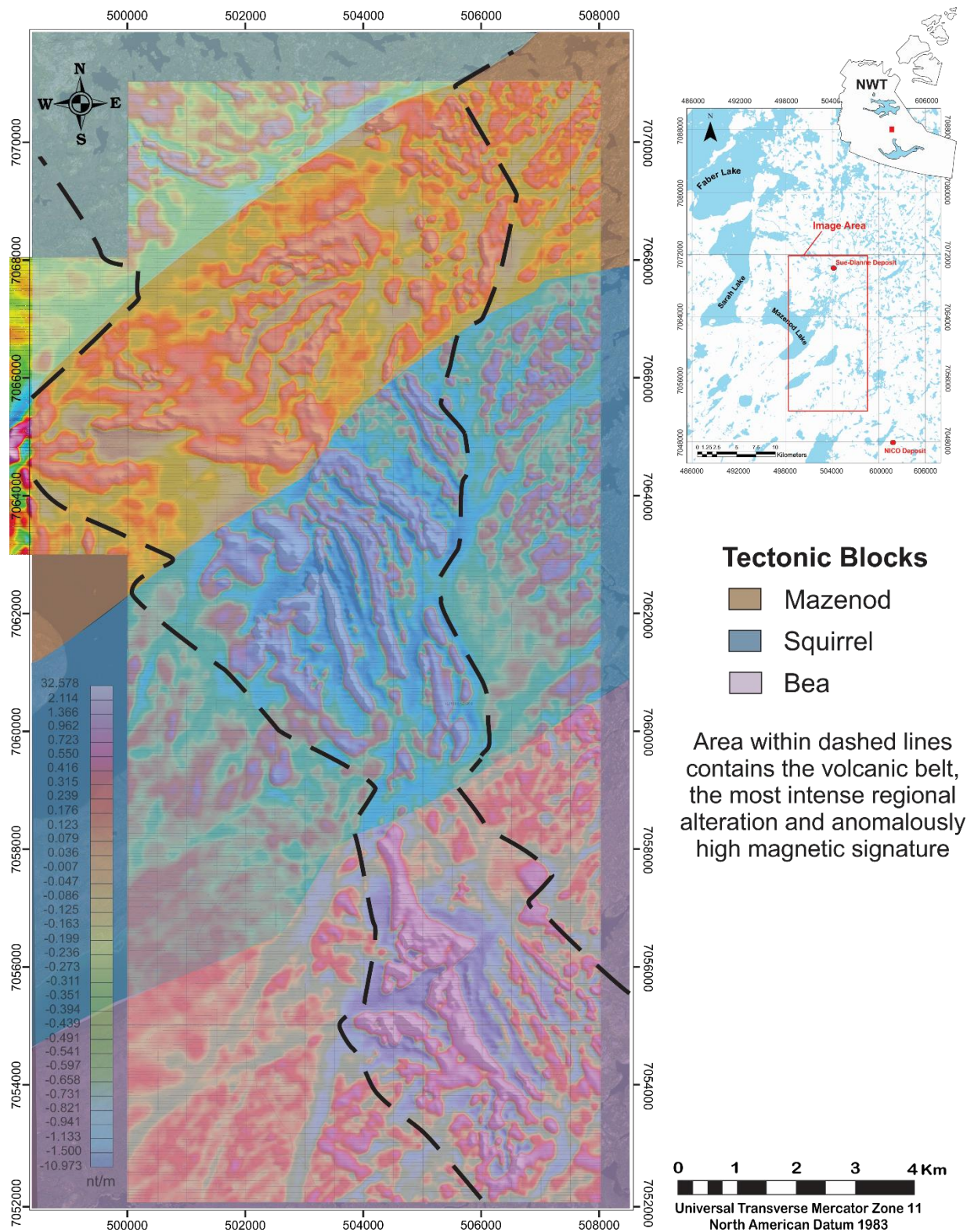


Fig. 59. Tectonic blocks are separated by transcurrent right lateral faults. Area within dashed lines contains the volcanic belt. Magnetic vertical gradient (MVG) overlay of a satellite image of the Mazenod Lake area.

assemblages, where the lithology is separated. The separation in lithology orientation was unlikely to have developed during volcanism. More likely, post-volcanic disruptions caused the shifting and rotation.

Left-stepping or bends along right-lateral offset transcurrent faults typically indicate dextral transpression and an E-W shortening of the lithosphere along a fault. There is an obvious example of this transpression along the Marian River fault, near Dan Island. South of the island a left shifting kink in the right-lateral strike-slip fault links an oblique orientation of the fault that continues through Net Ridge (Fig. 56). En echelon NE oriented faults correspondingly bend or step at a similar longitude. The bend along the transcurrent faults is also readily apparent in compilations of GBMZ geophysical data (Hayward et al., 2014).

The aeromagnetic data and geology also shows evidence of extensional characteristics along NE-oriented structures. In the Bea area a significant magnetic-low lineament correlates with a large diorite dyke, that fills in part of the Bea Fault. This large dyke, and several other NE-oriented dykes and vein structures in the Bea area indicate a stretching direction between $\sim 296^\circ$ to 336° (assuming no significant rotation of the tectonic block), that has up to 150 m local extension (Fig. 11). Total extension across the region is difficult to estimate, but must accommodate fault, vein and fracture infill (e.g. Marian River and Dianne Lake fault giant quartz vein systems) as well as various other intrusions such as the monzodiorite (c.f. Mumin et al., 2010; 2014).

Major faults in the Mazenod Lake region have a distinctly recognizable association to hydrothermal alteration, that is characteristic of the entire region. Throughout the study area, an abundance of fractures, faults and structural breccias are cemented with hydrothermal minerals. At Dan Island and Nod Hill, recognizable faults are in vicinity to the most intense hydrothermal

alteration. The hydrothermal alteration appears to be related to all the major and many secondary faults, regardless of orientation. It should be commented that the relationship of NW-oriented structures to alteration is more ambiguous than other primary structures. Typically, the major structures are spatially affiliated with silica and/or potassic alteration, but regionally all the other alteration types identified at surface have a spatial correlation with local structures. The NE and NNE oriented structures are associated with the most intense hydrothermal alteration regionally, including at Dan Island, Net Ridge, Nod Hill, along the Dianne Lake fault and close to the Bea area (Mumin et al., 2010). These observations support evidence that the fault zones provided permeable pathways for a greater concentration of hydrothermal fluids, which then fluxed throughout the supracrustal rocks. The genetic association of structural breccias, faults and hydrothermal alteration places a clear constraint on relative timing for hydrothermal alteration and tectonic activity, which appear to have been essentially coeval. Notwithstanding the above, major structures (e.g. NE-oriented faults) were clearly also active post-GBMZ volcanism.

Hydrothermal Alteration

The geochemical analysis documents the effects of widespread metasomatism throughout the Mazenod Lake area. Nine distinct alteration types have been distinguished. They are characterized by unique mineral assemblages, spatial zonation and unique geochemical signatures. The alteration types include sodic, magnetite \pm actinolite (MA), silication, potassic, tourmaline, hematite, phyllic, propylitic and silica alteration.

Based on the detailed mapping, petrography and geochemical analysis performed for this study, an interpretation of the local hydrothermal alteration zoning can be established. There is a distinct pattern to the occurrence of alteration types and minerals, that repeats across the Mazenod Lake region, irrespective of local geology. The spatial arrangement of alteration types

in general follows the sequence proposed by Richards and Mumin (2013b) (Fig. 4) (c.f. Hitzman et al., 1992; Mumin et al., 2010; Corriveau et al., 2007). Higher temperature, neutral pH forming hydrothermal alteration types are typically transitioned to lower temperature, more acidic pH forming alteration types in the following order: sodic, magnetite \pm actinolite (MA), potassic, tourmaline, hematite, phyllic, propylitic and silica alteration. Exceptions exist, but in such instances the out of place alteration may be related to separate overlapping hydrothermal cells or multiple hydrothermal alteration events/pulses. Silication is not included in the zoning model because it is not visible at surface, and is a consequence of primary rock composition rather than zoning.

Mass balance testing has shown that diverse elemental exchanges accompany mineral transformations during alteration in a series of distinct stages. For several of the alteration types, there are surprisingly inconsistent element exchanges despite similar macroscopic hydrothermal alteration. This indicates there may be unrecognized alteration in analyzed samples that is invisible to the naked eye, which results in spurious gains and losses for certain elements in the mass balance analysis. See Table 7 for a complete summary of typical element mobility patterns associated with most of the alteration types found in the Mazenod Lake region.

Graphical analysis shown in binary plots (Figs. 30 and 31) and mass balance diagrams (Figs. 34-42) indicate that Al, Ti, Zr and Hf are the most consistent and reliable immobile elements in the suite of hydrothermally altered rocks from the Mazenod Lake area. Although some alteration types show higher variations for gains and losses of Ti, Zr and Hf as compared to Al, the mobility of these elements are more consistently similar than other typically immobile element pairs. The most inconsistent immobile element exchanges take place during hematite

TABLE 7. Element mobility associated with most common Mazenod Lake region hydrothermal alteration types¹

Alteration Type	Typical Mineral Assemblages	Immobile Elements	Mobile Elements			
			Major Element Oxides		Trace Elements	
			Enriched	Depleted	Enriched	Depleted
Sodic ²	Albite ± Magnetite	Al ₂ O ₃ , TiO ₂ , Ta, Zr, Hf	Na ₂ O	K ₂ O, CaO, MnO	Cr, Sn, Bi, As	Rb, Zn, Cs, Sr, Mo
MA	Magnetite ± Actinolite	Al ₂ O ₃ , TiO ₂ , SiO ₂ , Zr, Hf, Tl, Ta, HREEs	Na ₂ O	K ₂ O, MgO, MnO	Sn, As, Cr, Ce	Cs, Zn, Sr, Cd, Be
Potassic	K-feldspar ± Biotite ± Magnetite	Al ₂ O ₃ , Fe ₂ O ₃ , TiO ₂ , SiO ₂ , Zr	K ₂ O	Na ₂ O, CaO, MgO, MnO	Ba, Cr, Rb, Te, Th, U	Be, HREEs, Mo, Nb, Nd, Ni, Pb, Sc, Sr, Zn
Tourmaline	Tourmaline ± Quartz	Al ₂ O ₃ , TiO ₂ , Zr, U, Th, Se, Ta, Tl	K ₂ O, SiO ₂ , Fe ₂ O ₃	Na ₂ O, CaO, MnO, MgO	Ag, As, Ba, Bi, Co, Cr, Hg, Mo, Rb, Sb, W	Be, Ce, Cu, Pb, Cs, REEs, Sr, Zn
Hematite	Hematite ± Quartz	Al ₂ O ₃ , TiO ₂ , SiO ₂ , Th, Ta	Fe ₂ O ₃ , MgO, MnO, K ₂ O	Na ₂ O, CaO, P ₂ O ₅	Hg, Cr, Ga, Ge, Sn, Te, Tl, W	Cs, Pb, Sr, Th, Zn
Propylitic	Epidote ± Chlorite ± Carbonate ± Quartz	Al ₂ O ₃ , SiO ₂ , Ag, Ga, Hf, Nb, Sc, Te, Th, Tl, Y, Zr	MnO, P ₂ O ₅	MgO, Na ₂ O	Bi, REEs, Cu, Sb, Sr	Au, Ni, Cs
Silicification	Quartz	Al ₂ O ₃ , Hf, Ta, Th, U, W, Zr, REEs	SiO ₂	CaO, Na ₂ O, TiO ₂ , P ₂ O ₅	Ag, As, Au, Bi, Cu, Hg, Mo, Nb, Nd, Te	Eu, Sr

¹Several of the samples have been altered by an early-stage potassic alteration, which can impact the major element oxides as spurious K₂O enrichment and Na₂O depletion for the alteration types listed in this table.

²Sodic alteration element exchanges based on the results of isocon mass balance tests of sodium enriched samples shown in Figs. 35a, b.

alteration. This discrepancy indicates that in conditions which favor hematite alteration, the typically immobile elements are more soluble in hydrothermal fluids.

The eight main types of alteration (visible at surface) that have been documented within the Mazenod Lake region are summarized below in relative order from high-temperature proximal types to the more distant, low-temperature alteration:

(a) Sodic Alteration

Analysis of Na-enriched rock samples show that concurrent to Na gains, K, Ca and Mn are also leached from the rocks. This exchange of elements leads to the formation of secondary albite. It is difficult to accurately identify the extent of sodic alteration, because it was not identified in the field, although suspected. Despite the uncertainty of field data, analysis of sodium enrichment residual alteration index (RAI) maps outlines sodic altered areas. These sodic alteration zones extend north of Nod Hill and exist at the south end of the Bea area (Figs. 43 and 44). The Na may have been originally derived from a nearby cooling and crystallizing magma, such as the monzodiorite south of Dan Island.

(b) Magnetite \pm Actinolite (MA) Alteration

For MA-altered rocks, magnetite \pm actinolite \pm quartz is the preferentially formed minerals. Mass balance testing shows MA-altered samples have mostly insignificant differences in element exchanges from Na-enriched samples, other than a lack of Ca leaching. Since the mass balance analysis has shown there is no observed significant hydrothermal enrichment of Fe and Ca during magnetite \pm actinolite alteration (Fig. 38), the wall rock must have had the necessary abundance of Fe and Ca to crystallize the minerals. In spite of this observation, the Ca-Fe enrichment RAI maps (which emphasize rocks enriched in Fe and Ca, Figs. 41 and 42) fairly accurately correlate with regional MA alteration zones.

Investigations by other researchers of similar alteration often suggest there is hydrothermal Ca-Fe enrichment during MA alteration (e.g. Montreuil et al., 2016). The MA-altered samples mass balance analyzed in this project did not show this enrichment apart from sample 97124. The reason for the discrepancy in the geochemistry data may be related to sample bias or misidentification of alteration in field notes. The data may also be skewed by the presence of vein or breccia infill minerals in the samples.

(c) Potassic Alteration

Field observations and potassic RAI maps (Figs. 49 – 52) have shown how spatially extensive potassic alteration is within the Mazenod Lake area. Mass balance analysis shows that previously leached and/or magmatic derived K was deposited as K-feldspar \pm biotite in potassic altered samples. During this process, Na, Ca, Mg and Mn were leached from the altered rock. Where this alteration is most intense, the host rock is converted to near monomineralic K-feldspar. Dan Island is an obvious regional strong K-alteration anomaly. There also appears to be increasingly intense potassic alteration in the central Bea area near the Bea Fault, which alludes to a similar anomaly in the area.

(d) Tourmaline Alteration

Tourmaline alteration shows a similar element mobility pattern to potassic alteration. This is due to mass balance tested samples that comprise superimposed secondary tourmaline on previously potassic altered rocks. Since the tourmaline altered samples analyzed for this study are known to contain spurious element exchanges, it is difficult to accurately remark on the alteration process. Most research in similar settings suggest that the formation of tourmaline alteration is linked to acidic, boron-bearing hydrothermal fluids reacting with country rock (Henry and Dutrow, 1996). Temperature conditions are mostly not considered as a controlling

factor for tourmaline alteration because of the wide temperature forming range. Like the other main alteration types, secondary tourmaline is widespread, although the occurrence is sporadic with local zones of intense alteration.

(e) Hematite Alteration

Hematite alteration occurs in two distinctly different forms, either as microscopic-sized particles of hematite in K-feldspar or as veins and stockworks of hematite \pm quartz. It is an interesting observation that there is no evidence of significant Fe having been leached during any of the other alterations, yet is significantly enriched during hematite alteration. The discrepancy indicates that most of the Fe must have been transported by hydrothermal fluids from a source other than previously leached wall rocks. The monzodiorite intrusion exposed near Dan Island is one possible candidate as a magmatic source of iron.

(f) Phyllic Alteration

Phyllic alteration within the Mazenod hydrothermal system predominantly involves the conversion of feldspar to sericite \pm quartz. The pyrite that is typically linked with phyllic alteration is characteristically minimal or often absent. This is possibly due to a lack of the ligand sulphur, which is necessary to form pyrite. Richards and Mumin (2013a, b) discuss the apparent S-poor content associated with similar magmatic hydrothermal IOCG systems, that may explain the relative scarcity of sulphide minerals associated with this alteration. There is also field evidence in localized areas of weathered out sulphides in the near-surface rocks, which partially accounts for the relative scarcity of sulphides. Generally, phyllic alteration is considered to be caused by a mild increase in acidity of hydrothermal fluids (Pirajno, 2009). This facilitates the conversion of feldspars to white mica (sericite). Primary textures are typically preserved in this type of alteration (c.f. Mumin et al., 2010). Although this alteration is widespread in the study

area, it is usually not obvious in outcrops. It is only through petrographic analysis that the pervasive extent is revealed.

(g) Propylitic Alteration

Propylitic alteration is one of the more extensive alteration types within the Mazenod hydrothermal system. This alteration produces secondary epidote \pm chlorite \pm carbonate \pm quartz, that occur together or less often independently. The propylitic alteration is usually not intense, but there are areas of significant epidote alteration, including cemented hydrothermal breccias southwest of Dan Island. Mass balance analysis shows that these altered rocks have generally been enriched with Mn and P, whereas Mg and Na are leached. The enriched elements likely originated from previously leached wall rocks and/or a magmatic derived source.

(h) Silicification

This is another common alteration in the Mazenod Lake region. Silicification preferentially occurs along and in proximity to major faults, such as the Marian River and Dianne Lake faults. During silicification, Si is enriched in the country rock, while Ca, Na, Ti and P are depleted. Where space is available the alteration results in extensive quartz veins, stocks, breccia bodies and/or replacement of local host rocks. The spatial relationship and superposition of silica alteration over other alteration types implies the alteration is a late-stage retrograde phase.

Residual Alteration Indices (RAIs)

The residual alteration index (RAI) maps are useful at illustrating distribution and intensity of the various alteration types. By extension, the maps can also illustrate the progressive migration of hydrothermal fluids through host rocks. The highest RAI values are generally

located near significant permeable conduits that hydrothermal fluids used to penetrate the surrounding country rock. Spatially separate areas that have distinct high RAI values are an indication that there are several uniquely developed local hydrothermal cells within the Mazenod Lake region. This essentially means there are several significant subsurface sources in the Mazenod Lake region.

Areas containing high RAI values are characterized by an abundance of secondary hydrothermal minerals. Around Mazenod Lake, the most apparent foci of alteration intensity appear in several instances surrounding, along or adjacent to major faults, relatively close to the monzodiorite intrusion. At and surrounding Mazenod Lake the field observations and RAI maps

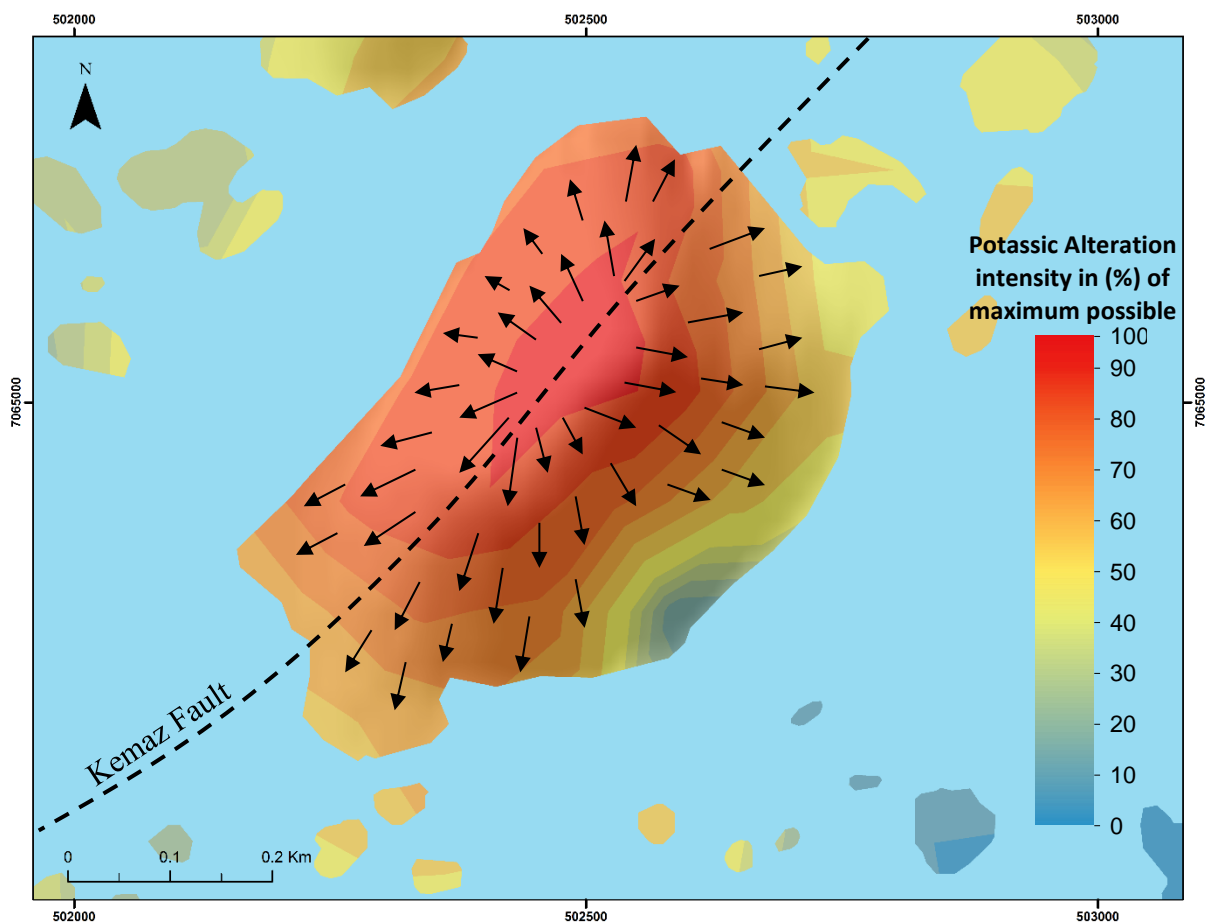


Fig. 60. A close-up illustration of the potassic RAI I contours overlain on Dan Island. Arrows indicate an estimation of the hydrothermal fluid migration directions from the permeable conduit- Kemaz Fault and into the supracrustal rocks. In reality, the migration of fluids would involve a vertical component.

coincide with a foci of alteration intensity at central Dan Island (Fig. 59) and in the northern portion of Nod Hill (Figs. 49 and 50). In the Bea area, the foci of most intense alteration are spatially difficult to delineate from the RAI maps because the lithogeochemical sampling does not cover the entire area. Despite the lack of uniform sampling, local gradational changes in hydrothermal alteration intensity can be used to interpret an approximate vector towards the most intense alteration. For instance, in the center of the Bea area, potassic RAI values increase continually to the southern edge of the sampled area (Figs. 44 and 46). The highest of these values are adjacent to where the Bea Fault is interpreted to cross-cut the region. This increasing trend of RAI values indicates that either the most intense potassic alteration is at the southern limit of the sampled area or the intensity increases further south. A similar interpretation can be made with the sodium enrichment index (Fig. 43). Sodium RAI values subtly increase towards the southern edge of the mapped/sampled area, and could potentially continue to increase further south outside of the study area.

Mineralization

As discussed in Chapter 5, there are several occurrences and varieties of mineralization that have been identified across the Mazenod Lake region. Instances of Cu, Mo, Co, U, Fe and LREE-bearing minerals have been observed, mostly in relatively small localized areas and usually not in significant quantities. Chalcopyrite (CuFeS_2) is the most common of these minerals by far, but is generally irregularly dispersed. Local concentrations of chalcopyrite typically are associated with alteration and/or structural disruptions and is often visible at surface within oxidized (gossan) areas. Trace Cu-bearing minerals occur locally with most of the recognized alteration types. Based on the spatial relationships of local mineral concentrations,

hydrothermal alteration and faulting, their ages are considered to be broadly contemporaneous with each other and Great Bear magmatism.

Implications for Exploration

A spatial comparison of the RAI values (Figs. 43 to 54) to concentrations of elements that are commonly associated with IOCG-type deposits (indicator elements: Ag, As, Au, Bi, Co, Cu, Hg, La, Mo, W, U; Figs. 62 to 72) show there is a relationship between hydrothermal alteration intensity and indicator elements. For example, clusters of higher concentrations of indicator elements tend to overlap with mid to higher potassic RAI contours (Figs. 45 and 47). Also, clusters of low concentrations of indicator elements occur preferentially in most zones of intense Ca-Fe enrichment (which correlates with intense MA alteration, Figs. 41 and 42). This relationship is most obvious at the north end of Nod Hill. Not surprisingly, areas that are comprised of higher RAI values that spatially correlate with higher concentrations of indicator elements are also located along or adjacent to major strike-slip faults. The most significant examples of areas containing these coincident features are at Dan Island adjacent to a splay of the Kemaz Fault, Nod Hill along the Kemaz Fault and in the central Bea area along the Bea Fault. Consequently, these coincident features are suggested as potential targets for additional mineral exploration work.

An obvious global implication for this study is that the types of RAIs developed for the Mazenod Lake hydrothermal system may be effective for delineating alteration types and hydrothermal fluid migration in other IOCG hydrothermal systems. This is conditional on the availability of an extensive geochemical database.

Chapter IX: Conclusions

The broad goal of this investigation was to improve the general understanding of the genesis of the large magmatic hydrothermal iron-oxide copper gold (MH-IOCG) system at Mazenod Lake, NWT. Within this general objective, an emphasis of the investigation was placed on analyzing the geology, structure and geochemistry. The following list describes several of the more important conclusions made in this thesis:

1. 1:2000 scale geologic mapping at and surrounding Mazenod Lake revealed fourteen unique relatively undeformed volcanic formations that make up the Faber Group volcanic assemblages. These volcanic rocks are a series of sub-parallel pyroclastic ignimbrite flows. Textural varieties range from ash, crystal and lapilli tuffs to pyroclastic breccias. In-situ formed volcanic sediments unconformably separate many of the volcanic assemblages, with the exception of the Squirrel Lake volcanic assemblage. A subvolcanic monzodiorite intrusion that is a possible cause for alteration and mineralization exists in the central area of Mazenod Lake, located between Nod Hill and Dan Island. Enclosing the Faber Group volcanic and subvolcanic rocks is the genetically linked Marian River granitoid batholith to the east and Sarah Lake monzogranite to the west. Overlying the aforementioned geology in the western third of the area are Paleozoic sedimentary strata.
2. Geochemical analysis of the Mazenod Lake area examines a near-horizontal slice through a volcanic system, controlled by the current depth of erosion and outcrop exposure. The spatially controlled geochemical data reveal patterns linked to unique characteristics of lithology and hydrothermal alteration.
3. Chemical discrimination of the Mazenod Lake area lithology has shown that the volcanic rocks are compositionally mostly andesite, but also include basaltic andesite, dacite and

rhyodacite. Chemical tectonomagmatic discrimination of the least-altered rocks shows these rocks have a calc-alkaline character. Granite discrimination diagrams support an interpretation that the least-altered granitoid rocks formed in a syn-collisional and volcanic arc tectonic setting.

4. The Mazenod Lake region structural framework is characterized by mostly brittle strike-slip tectonics. There are several sets of en echelon oblique strike-slip faults that intersect, segment and displace the local lithology. Faults have three main directional trends that orient mostly N50°E, N30°W and N20°E. The NE and NW oriented faults are interpreted to be a conjugate pair, part of the regional GBMZ faulting. The NNE faults may have been a result of transferring stress between differentially displaced NE oriented en echelon faults.
5. Density analysis of lineaments and their intersections spatially evaluates areas of greatest strain. Zones of concentrated deformation include the Sue-Dianne deposit, Dan Island, the central Bea area and an area NE of the Sue-Dianne deposit within the Marian River batholith. The areas which have significantly dense quantities of lineaments and lineament intersections tend to occur in close proximity to intersections of major faults, and in at least three out of the four anomalous zones, areas of minor concentrations of mineralization. However, the lineament density analysis is strongly biased towards areas with a high density of outcrop exposure.
6. Three main tectonic blocks have been recognized in the Mazenod Lake region. They are characterized by similar patterns of lineaments that were derived from remotely sensed images. Defining the tectonic blocks emphasizes the differential deformation the region has experienced. While each tectonic block has a dextral shear sense, the amount of

horizontal shift and rotation is unique for every block. In the northern part of the region, the Mazenod tectonic block appears to have been rotated about a vertical axis, significantly more than the southern Squirrel and Bea tectonic blocks.

7. Hydrothermal alteration is pervasive within the Mazenod Lake region, with no truly completely unaltered rocks visible at surface. Prevailing alteration includes the proximal high-temperature alteration types, sodic, MA (magnetite \pm actinolite) to the more distal intermediate and lower-temperature alteration types potassic (K-feldspar \pm biotite), tourmaline, hematite, phyllic (quartz, sericite \pm pyrite), propylitic (epidote \pm chlorite \pm carbonate \pm sericite \pm quartz), and silicification. Silication-type in the form of skarn metasomatism (clinopyroxene-garnet-magnetite) has also been identified, although because the alteration was not recognized at surface it was not included in the geochemical analysis. These various alteration types occur locally as replacements, stockworks, veins and hydrothermal breccias. In general, paragenesis of the alteration minerals follows the zoning model of proximal to distal alteration assemblages (Richards and Mumin, 2013b).
8. The Mazenod hydrothermal system is believed to be a magmatic-hydrothermal type IOCG system that was driven by the intrusion of a monzodiorite pluton(s) into mostly andesitic volcanic rocks. This system is characterized by pervasive alteration, predominantly potassic, but includes all the common types of an IOCG system. There are several local hydrothermal cells that exist as part of the regional Mazenod hydrothermal system. Each cell visibly has gradational changes in alteration intensity. They also have overlapping alteration halos which locally obfuscate the established zoning model.

Unique hydrothermal cells are revealed on the RAI maps, which demonstrates their areal extent and systematic gradational change of alteration intensity.

9. Evaluation of elemental exchanges involved in the hydrothermal alteration process shows there is a pattern to the alteration processes. Early and hotter reactions involve the enrichment of country rock with Na and a simultaneous leaching of K, Mg, Ca and Mn leading to the formation of hydrothermal albite. As the fluid is convected throughout the hydrothermal system, changing physico-chemical conditions and hydrothermal fluid chemistry resulted in varying element substitutions and crystallization of different minerals. During magnetite \pm actinolite alteration, Ca was no longer leached. With potassic alteration, K is enriched, while Na, Mg, Mn and Ca are depleted. Hematite alteration is associated with an Fe enrichment. The Fe likely originated from a source other than previously leached wall rocks, because there is little evidence of any alteration causing significant Fe leaching with the exception of intense albitization not observed in surface rocks at Mazenod, but known to occur elsewhere in the GBMZ (Mumin et al., 2010). In propylitic alteration, Mn and P are enriched in country rock, while Mg and Na are leached. Silicification then involved an enrichment of Si in country rock and leaching of Ca, Na, Ti and P.
10. Several residual alteration indices (RAIs) have been developed and interpolated that have potential exploration applications. These RAIs have been shown as useful for delineating various hydrothermal alteration types, showing possible migratory paths for the hydrothermal fluids and locating hydrothermal centres.
11. Analysis of the geology, structure and geochemistry of the Mazenod Lake region reveals hydrothermal centres. Dan Island, Nod Hill and the central Bea area are the most evident

centers of hydrothermal activity. These locations all contain intense alteration, are cross-cut by regionally disruptive faults, have evidence of mineralization, and contain greater concentrations of indicator elements than the surrounding areas.

12. Exploration of the Mazenod Lake region is still in the preliminary stages and economic mineralization remains to be discovered. While there is additional ground work that could be completed to reveal unexplored geology, expand upon the geochemical or geophysical database, in order to successfully diagnose potential economic mineralization, a full exploration drilling program is recommended. On the basis of this thesis, hydrothermal centers located at Dan Island, Nod Hill and in the central Bea area are considered primary targets for additional exploration activity.

References

- Baker, T., 1998, Alteration, mineralization, and fluid evolution at the Eloise Cu-Au deposit, Cloncurry District, northwest Queensland, Australia: *Economic Geology*, v. 93, p. 1213-1236.
- Barton, M.D., 2014, 13.20 - Iron Oxide(-Cu-Au-REE-P-Ag-U-Co) Systems, *in* Holland, H.D. and Turekian, K.K., eds., *Treatise on Geochemistry (Second Edition)*: Oxford, Elsevier, p. 515.
- Barton, M.D. and Johnson, D.A., 1996, Evaporitic-source model for igneous-related Fe-oxide-(REE-Cu-Au-U) mineralization: *Geology*, v. 24, p. 259-262.
- Barton, M.D. and Johnson, D.A., 2000, Alternative brine sources for Fe-oxide (-Cu-Au) systems: Implications for hydrothermal alteration and metals, *in* Porter, T.M., ed., *Hydrothermal iron oxide copper-gold and related deposits: A global perspective*: Adelaide, Australia, Australian Mineral Foundation, p. 43-60.
- Barton, M.D. and Johnson, D.A., 2004, Footprints of Fe-oxide (-Cu-Au) systems: *University of Western Australia Special Publication*, v. 33, p. 112-116.
- Bender, K., 2013, Project Description, Technical report for BFR Copper & Gold Inc.
- BHP Billiton, 2015, *Resourcing global growth Annual Report 2015*.
- Bowring, S.A., 1985: U-Pb zircon geochronology of early Proterozoic Wopmay orogen, NWT Canada: an example of rapid crustal evolution.

- Bowring, S.A. and Grotzinger, J.P., 1992, Implications of new chronostratigraphy for tectonic evolution of Wopmay Orogen, northwest Canadian Shield: *American Journal of Science*, v. 292, p. 1-20.
- Burgess, H., Gowans, R.M., Hennessey, B.T., Lattanzi, C.R. and Puritch, E., 2014, Technical report on the feasibility study for the NICO gold-cobalt-bismuth-copper project Northwest Territories, Canada: Toronto, Ontario, Micon International Limited, 385 p.
- Canada digital elevation data. cdem_hillshade_141025_142529. Ottawa, ON: Natural Resources Canada, 2016.
- Cail, T.L. and Cline, J.S., 2001, Alteration associated with gold deposition at the Getchell Carlin-type gold deposit, North-central Nevada: *Economic Geology*, v. 96, p. 1343-1359.
- Camier, John, 2002, The Sue-Dianne Proterozoic Fe-oxide Cu-Ag-Au breccia complex, Northwest Territories, Canada: M.Sc. thesis, University of Western Ontario, p. 210.
- Clowes, R.M., 1997, LITHOPROBE Phase V Proposal - Evolution of a continent revealed: LITHOPROBE Secretariat, The University of British Columbia, Vancouver, B.C., p. 292.
- Coles, R., Haines, G. and Hannaford, W., 1976, Large scale magnetic anomalies over western Canada and the Arctic: a discussion: *Canadian Journal of Earth Sciences*, v. 13, p. 790-802.
- Collins, A.C., 2010, Mineralogy and Geochemistry of Tourmaline in Contrasting Hydrothermal Systems: Copiapó Area, Northern Chile: M.Sc. thesis, University of Arizona, p. 225

- Corriveau, L., Ootes, L., Mumin, H., Jackson, V., Bennett, V., Cremer, J., Rivard, B., McMartin, I. and Beaudoin, G., 2007, Alteration vectoring to IOCG (U) deposits in frontier volcano-plutonic terrains, Canada: Proceedings of Exploration, Proceedings, p. 1171-1177.
- Corriveau, L., Mumin, A.H. and Setterfield, T., 2010, IOCG environments in Canada: Characteristics and geological vectors to ore and challenges, *in* Porter, T.M., ed., Hydrothermal iron oxide copper-gold and related deposits: A global perspective: PGC Publishing, Adelaide, v.4, p. 311-343.
- Davidson, G.J., Paterson, H., Meffre, S. and Berry, R.F., 2007, Characteristics and origin of the Oak Dam East breccia-hosted, iron oxide Cu-U-(Au) deposit: Olympic Dam region, Gawler craton, South Australia: Economic Geology, v. 102, p. 1471-1498.
- de Hoog, J., Mason, P. and van Bergen, M.J., 2001, Sulfur and chalcophile elements in subduction zones: constraints from a laser ablation ICP-MS study of melt inclusions from Galunggung Volcano, Indonesia: Geochimica et Cosmochimica Acta, v. 65, p. 3147-3164.
- de Jong, G., Rotherham, J., Phillips, G.N. and Williams, P.J., 1997, Mobility of rare-earth elements and copper during shear-zone-related retrograde metamorphism: Geologie en Mijnbouw, v. 76, p. 311-319.
- Environment Canada, 2015, Gameti Airport Climate Data, Canada.
- Fisher, R.V., 1966, Rocks composed of volcanic fragments and their classification, Earth Sci. Reviews 1, no. 4, p. 287-298.

Fisher, L. and Kendrick, M., 2008, Metamorphic fluid origins in the Osborne Fe oxide–Cu–Au deposit, Australia: evidence from noble gases and halogens: *Mineralium Deposita*, v. 43, p. 483-497.

Fortune Minerals Limited, November, 19, 2009, Fortune Minerals Limited - News Release (<http://www.fortuneminerals.com/news/press-releases/press-release-details/2009/FortuneMineralsLimited-NewsRelease1121270/default.aspx>).

Gabrielsen, R.H., Braathen, A., Dehls, J., Roberts, D., 2002, Tectonic lineaments of Norway: *Norsk Geolisk Tidsskrift*, Scandinavian University Press, v. 82, p. 153-174.

Galkin, V., 2010, Complex structural study of the West Red Lake Area, Northwestern Ontario, Canada, Toronto: unpublished report, p. 133

Gandhi, S.S., 1994, Geological setting and genetic aspects of mineral occurrences in the southern Great Bear magmatic zone, Northwest Territories: *In Studies of Rare-Metal Deposits in the Northwest Territories*, (ed.) W.D. Sinclair and D.G. Richardson: Geological Survey of Canada, Bulletin 475, p. 63-96

Gandhi, S.S., 2003, An overview of the Fe oxide-Cu-Au deposits and related deposit types, CIM Montreal 2003 Mining Industry Conference and Exhibition, Canadian Institute of Mining, Technical Paper, CD-ROM.

Gandhi, S.S., 2013, Report on the Geological and Mineral Occurrence Map of the Mazenod Lake-Lou Lake Area, Northwest Territories: Geological Survey of Canada, Open File 7546, 44 p.

- Gandhi, S.S. and Breemen, O.V., 2005, SHRIMP U-Pb geochronology of detrital zircons from the Treasure Lake Group new evidence for Paleoproterozoic collisional tectonics in the southern Hottah terrane, northwestern Canadian Shield: Canadian Journal of Earth Sciences, v. 42, p. 833-845.
- Gandhi, S.S., Prasad, N. and Charbonneau, B.W., 1996, Geological and geophysical signatures of a large polymetallic exploration target at Lou Lake, southern Great Bear magmatic zone, Northwest Territories; In Current Research 1996-E: Geological Survey of Canada, p. 147-158.
- Gandhi, S.S., Mortensen, J., Prasad, N. and Breemen, O.V., 2001, Magmatic evolution of the southern Great Bear continental arc, northwestern Canadian Shield: Geochronological constraints: Canadian Journal of Earth Sciences, v. 38, p. 767-785.
- Gandhi, S.S., Montreuil, J. -F. and Corriveau, L., 2014, Geology and mineral occurrences, Mazenod Lake-Lou Lake area, Northwest Territories, Geological Survey of Canada, Canadian Geoscience Map 148 (preliminary): Northwest Territories Geoscience Office, Open Report 2013-004, scale 1:50 000. doi: 10.4095/292918.
- Goad, R.E., Mumin, H.A., Duke, N.A., Neale, K.L., Mulligan, D.L. and Camier, J.W., 2000, The NICO and Sue-Dianne Proterozoic, iron oxide-hosted, polymetallic deposits, Northwest Territories; application of the Olympic Dam model in exploration: Exploration and Mining Geology, v. 9, p. 123-140.
- Grant, J.A., 1986, The Isocon Diagram = A simple solution to Gresens' equation for metasomatic alteration: Economic Geology, v. 81, p. 1976-1982.

- Grant, J.A., 2005, Isocon analysis: a brief review of the method and applications: *Physics and Chemistry of the Earth, Parts A/B/C*, v. 30, p. 97-1004.
- Gresens, R.L., 1967, Composition-volume relationships in metasomatism: *Chemical Geology*, v. 2, p. 47-55.
- Groves, D.I. and Vielreicher, N.M., 2001, The Phalabowra (Palabora) carbonatite-hosted magnetite-copper sulfide deposit, South Africa: An end-member of the iron oxide-copper-gold-rare earth element deposit group?: *Mineralium Deposita*, v. 36, p. 189-194.
- Hamilton, M.S., 2013, Mineralogy and Hydrothermal Alteration in the Mazenod Lake IOCG System, Northwest Territories: B.Sc. honours thesis, Brandon University, 271 pp.
- Hauck, S.A., 1990, Petrogenesis and tectonic setting of middle Proterozoic iron oxide-rich ore deposits: An ore deposit model for Olympic Dam-type mineralization: U.S. Geological Survey Bulletin B-1932, p. 4-39.
- Haynes, D.W., 2000, Iron oxide copper(-gold) deposits: Their position in the ore deposit spectrum and modes of origin, *in* Porter, T.M., ed., *Hydrothermal iron oxide copper-gold & related deposits: A global perspective*, v. 1: Adelaide, Australian Mineral Foundation, p. 71-90.
- Haynes, D.W., Cross, K.C., Bills, R.T. and Reed, M.H., 1995, Olympic Dam ore genesis; a fluid-mixing model: *Economic Geology*, v. 90, p. 281-307.

Hayward, N. and Corriveau, L., 2014, Fault reconstructions using aeromagnetic data in the Great Bear magmatic zone, Northwest Territories, Canada: *Canadian Journal of Earth Sciences*, v. 51, p. 1-16.

Hayward, N. and Skirrow, R.G., 2010, Geodynamic setting and controls on iron oxide Cu-Au (\pm U) Ore in the Gawler Craton, South Australia, *in* Porter T.M., ed. *Hydrothermal Iron Oxide Copper-Gold and Related Deposits: A Global Perspective-Advances in the Understanding of IOCG Deposits*: PGC Publishing, Adelaide, v. 3, p. 119-146

Henry, D.J. and Dutrow, B.L., 1996, Metamorphic tourmaline and its petrologic applications: *Reviews in Mineralogy*, 33, 503-557.

Hetu, R.J., Homan, P.B., Charbonneau, B.W., Prasad, N., Gandhi, S.S., 1994, Airborne geophysical survey, Mazenod Lake, NWT: Geological Survey of Canada, Open file 2806, doi: 10.4095/183817.

Hildebrand, R.S., 1982, A continental volcanic arc of early Proterozoic age at Great Bear Lake, Northwest Territories: PhD thesis, Memorial University of Newfoundland, p. 237.

Hildebrand, R.S. and Bowring, S., 1988, Geology of parts of the Calder River map area, central Wopmay orogen, District of Mackenzie: *Current Research, Part C*, Geological Survey of Canada, Paper, p. 199-205.

Hildebrand, R., Annesley, I., Bardoux, M., Davis, W., Heon, D. and Reichenbach, I., 1984, Geology of the early Proterozoic rocks in parts of the Leith Peninsula map area, district of Mackenzie: Geological Survey of Canada, Paper 84-01A, p. 217-221.

Hildebrand, R.S., Hoffman, P.F. and Bowring, S.A., 1987, Tectono-magmatic evolution of the 1.9-Ga Great Bear magmatic zone, Wopmay Orogen, northwestern Canada: *Journal of Volcanology and Geothermal Research*, v. 32, p. 99-118.

Hildebrand, R., Bowring, S. and Housh, T., 1990, The medial zone of Wopmay orogen, District of Mackenzie: Current research, part C. Geological Survey of Canada, Paper, p. 167-176.

Hildebrand, R.S., Hoffman, P.F. and Bowring, S.A., 2010, The Calderian orogeny in Wopmay orogen (1.9 Ga), northwestern Canadian Shield: *Geological Society of America Bulletin*, v. 122, p. 794-814.

Hildebrand, R.S., Hoffman, P.F., Housh, T. and Bowring, S.A., 2010, The nature of volcano-plutonic relations and the shapes of epizonal plutons of continental arcs as revealed in the Great Bear magmatic zone, northwestern Canada: *Geosphere*, v. 6, p. 812-839.

Hitzman, M.W., 2000, Iron oxide Cu-Au deposits: What, where, when, and why? *in* Porter, T.M. ed., *Hydrothermal Iron Oxide Copper-Gold & Related Deposits: A global perspective*: Adelaide, Australian Mineral Foundation, v. 1, p. 201-218.

Hitzman, M.W., Oreskes, N. and Einaudi, M.T., 1992, Geological characteristics and tectonic setting of Proterozoic iron oxide (Cu-U-Au-REE) deposits: *Precambrian Research*, v. 58, p. 241-287.

Hobbs, W.H., 1904, Lineaments of the Atlantic border region: *Geological Society of America Bulletin*, v. 15, p. 483-506.

- Hoffman, P.F., 1980, Wopmay orogen: a Wilson Cycle of early Proterozoic age in the northwest of the Canadian Shield. In: *The Continental Crust and its Mineral Resources*. Edited by D.W. Strangway, Geological Association of Canada, Special Paper, v. 20, p. 523-549.
- Hoffman, P.F., 1987, Continental transform tectonics: Great Slave Lake shear zone (ca. 1.9 Ga), northwest Canada: *Geology*, v. 15, p. 785-788.
- Hoffman, P.F. and Bowring, S.A., 1984, Short-lived 1.9 Ga continental margin and its destruction, Wopmay orogen, northwest Canada: *Geology*, v. 12, p. 68-72.
- Hoffman, P.F. and Hall, L., 1993, *Geology, Slave Craton and environs, District of Mackenzie, Northwest Territories*: Geological Survey of Canada, Open File 2559, 1 sheet.
- Hoffman, P.F., Bowring, S.A., Buchwaldt, R. and Hildebrand, R.S., 2011, Birthdate for the Coronation paleocean: age of initial rifting in the Wopmay Orogen, Canada.: *Canadian Journal of Earth Sciences*, v. 48, p. 281-293.
- Hunt, J., Baker, T. and Thorkelson, D., 2007, A review of iron oxide copper-gold deposits, with focus on the Wernecke Breccias, Yukon, Canada, as an example of a non-magmatic end member and implications for IOCG genesis and classification: *Exploration and Mining Geology*, v. 16, p. 209-232.
- Ishikawa, Y., Sawaguchi, S., and Iwaya, H.M., 1976, Delineation of prospecting targets for Kuroku deposits based on modes of volcanism of underlying dacite and alteration haloes: *Mining Geology*, p. 105-117.

Indian and Northern Affairs, 2003, Land Claims and Self-Government Agreement among the Tlicho and the government of the Northwest Territories and the government of Canada, Canada.

Kendrick, M., Honda, M., Gillen, D., Baker, T. and Phillips, D., 2008, New constraints on regional brecciation in the Wernecke Mountains, Canada, from He, Ne, Ar, Kr, Xe, Cl, Br and I in fluid inclusions: *Chemical Geology*, v. 255, p. 33-46.

Kulla, G., 2004, Diamond Drilling Report on the Mazenod Property SQU 1-4, SQU 6-7, SQU10-11, & JAZ 1 Claims Northwest Territories, Phelps Dodge Corporation of Canada Limited.

Lord, C.S., 1942, Snare River, District of Mackenzie, Northwest Territories, Geological Survey of Canada, Map 690A, scale 1:63:360.

MacLean, W.H. and Barrett, T.J., 1993, Lithogeochemical techniques using immobile elements: *Journal of Geochemical Exploration*, v. 48, p. 109-133.

MacLean, W.H. and Kranidiotis, P., 1987, Immobile elements as monitors of mass transfer in hydrothermal alteration; Phelps Dodge massive sulfide deposit, Matagami, Quebec: *Economic Geology*, v. 82, p. 951-962.

Mark, G., Oliver, N.H. and Williams, P.J., 2006, Mineralogical and chemical evolution of the Ernest Henry Fe oxide–Cu–Au ore system, Cloncurry district, northwest Queensland, Australia: *Mineralium Deposita*, v. 40, p. 769-801.

Marschik, R. and Fontboté, L., 2001, The Candelaria-Punta del Cobre iron oxide Cu-Au (-Zn-Ag) deposits, Chile: *Economic Geology*, v. 96, p. 1799-1826.

- Menard, J., 1995, Relationship between altered pyroxene diorite and the magnetite mineralization in the Chilean Iron Belt, with emphasis on the El Algarrobo iron deposits (Atacama region, Chile): *Mineralium Deposita*, v. 30, p. 268-274.
- McGlynn, J.C., 1979, Turni Lake, District of Mackenzie, Geological Survey of Canada, Map 1230A, scale: 63,360.
- Mitchell, R.N., Hoffman, P.F., Evans, D.A.D., 2010, Coronation loop resurrected: Oscillatory apparent polar wander of Orosirian (2.05-1.8 Ga) paleomagnetic poles from Slave craton: *Precambrian Research*, v.179, p. 121-134.
- Montreuil, J.-F., Corriveau, L. and Grunsky, E.C., 2013, Compositional data analysis of hydrothermal alteration in IOCG systems, Great Bear magmatic zone, Canada: to each alteration type its own geochemical signature: *Geological Society of London*, v. 16.
- Montreuil, J. -F., Potter, E.G., Corriveau, L., Davis, W.J., 2016, Element mobility patterns in magnetite-group IOCG systems: The Fab IOCG system, Northwest Territories, Canada: *Ore Geology Reviews*, v. 72, p. 562-584.
- Mumin, A., 1988, Tectonic and structural controls on massive sulfide deposition in the south Sturgeon Lake volcanic pile, northwestern Ontario and hydrothermally altered rocks associated with the Lyon Lake Arcean volcanogenic massive sulfide ore deposits, Sturgeon Lake: unpublished M.Sc. thesis, University of Toronto.
- Mumin, H. and Richards, J.P., 2012, Subduction-modified lithosphere as a source for a spectrum of distal-to post-subduction magmatic-hydrothermal Cu-Au-Mo-Fe deposits: Porphyries to

IOCGs, Geological Society of America, Charlotte, North Carolina, 2012, Annual Meeting, Abstracts with Programs, Paper no. 213-6 (online).

Mumin, H. and Richards, J.P., 2013, Evolution of magmatic-hydrothermal ore systems in response to secular changes in sulphur, oxygen, biospheric processes and geothermal gradients from the Archean to the present: GAC-MAC, Winnipeg, Manitoba, 2013, Annual Meeting, Program with Abstracts, p. 149.

Mumin, A.H., Corriveau, L., Somarin, A. and Ootes, L., 2007, Iron oxide copper-gold-type polymetallic mineralization in the Contact Lake belt, Great Bear magmatic zone, Northwest Territories, Canada: Exploration and Mining Geology, v. 16, p. 187-208.

Mumin, A.H., Somarin, A., Jones, B., Corriveau, L., Ootes, L. and Camier, J., 2010, The IOCG-porphyry-epithermal continuum in the Great Bear magmatic zone, Northwest Territories, Canada: Exploring for iron oxide copper-gold deposits: Canada and global analogues. Geological Association of Canada, Short Course Notes, v. 20, p. 59-78.

Mumin, A.H., Phillips, A., Katsuragi, C.J., Mumin, A., and Ivanov, G., 2014, Geotectonic interpretation of the Echo Bay stratovolcano complex, northern Great Bear magmatic zone, NWT, Canada: Northwest Territories Geoscience Office, NWT Open File 2013-01, p. 25.

O'leary, D.W., Friedman, J.D., Pohn, H.A., 1976, Lineament, linear, lineation: some proposed new standards for old terms: Geological Society of America Bulletin, v. 87, p. 1463-1469.

Oliver N.H.S., Cleverley, G.M., Pollard, P.J., Bin Fu, Marshall, L.J., Rubenach, M.J., Williams, P.J., Baker, T., 2004, Modeling the Role of Sodic Alteration in the Genesis of Iron Oxide-

Copper-Gold Deposits, Eastern Mount Isa Block, Australia: *Economic Geology*, v. 99, p. 1145-1176.

Oliver N.H.S., Butera, K.M., Rubenach, M.J., Marshall, L.J., Cleverley, J.S., Mark, G., Tullemans, F., Esser, D., 2008, The protracted hydrothermal evolution of the Mount Isa Eastern Succession: A review and tectonic implications: *Precambrian Research*, v. 163, p. 108-130.

Ootes, L., Davis, W.J., Jackson, V.A., van Breemen, O. and Corfu, F., 2015, Chronostratigraphy of the Hottah terrane and Great Bear magmatic zone of Wopmay Orogen, Canada, and exploration of a terrane translation model: *Canadian Journal of Earth Sciences*, v. 52, p. 1062-1092.

Oreskes, N. and Einaudi, M.T., 1992, Origin of hydrothermal fluids at Olympic Dam; preliminary results from fluid inclusions and stable isotopes: *Economic Geology*, v. 87, p. 64-90.

Perreault, S. and Lafrance, B., 2015, Kwyjibo, a REE-enriched iron oxides-copper-gold (IOCG) deposit, Grenville Province, Québec: Symposium on critical and strategic materials. *British Columbia Geological Survey Paper, Proceedings*, p. 139.

Pearce, J.A., Harris, N.B.W. and Tindle, A.G., 1984, Trace element discrimination diagrams for the tectonic interpretation of granitic rocks: *Journal of Petrology*, v. 25, p. 956-983.

- Pearce, J.A., 1996, A user's guide to basalt discrimination diagrams: Trace element geochemistry of volcanic rocks: applications for massive sulphide exploration: Geological Association of Canada, Short Course Notes, v. 12, p. 113.
- Pirajno, F., 2009, Hydrothermal Processes and Mineral Systems, Springer Science & Business Media, 1250 p.
- Pollard, P.J., 2000, Evidence of a magmatic fluid and metal source for Fe-oxide Cu-Au mineralization: Australian Mineral Foundation, p. 27-41.
- Pollard, P.J., 2006, An intrusion-related origin for Cu–Au mineralization in iron oxide–copper–gold (IOCG) provinces: Mineralium Deposita, v. 41, p. 179-187.
- Porter, T.M., 2000, Hydrothermal iron oxide copper-gold and related deposits: A global perspective: Adelaide, Australian Mineral Foundation, p. 349.
- Prouteau, G. and Scaillet, B., 2013, Experimental constraints on sulphur behaviour in subduction zones: Implications for TTG and adakite production and the global sulphur cycle since the Archean: Journal of Petrology, p. 183-213.
- Reeve, J.S., Cross, C.C., Smith, R.N., Oreskes, N., 1990, Olympic Dam copper-uranium-gold-silver deposit, *In* Hughes, F.E. (ed.) Geology of the Mineral Deposits of Australia and Papua New Guinea: Australasian Institute of Mining and Metallurgy Monograph, v. 14, p. 1009-1035.

- Requia, K. and Fontboté, L., 2000, The Salobo iron oxide copper-gold deposit, Carajás, northern Brazil, *in* Porter T.M., ed., Hydrothermal iron oxide copper–gold and related deposits: A global perspective. Adelaide, Australian Mineral Foundation, p. 225-236.
- Richards, J.P., 2000, Lineaments revisited: Society of Economic Geologists Newsletter, n.42, p. 14-20.
- Richards, J.P., 2009, Postsubduction porphyry Cu-Au and epithermal Au deposits: Products of remelting of subduction-modified lithosphere: *Geology*, v. 37, p. 247-250.
- Richards, J.P. and Mumin, A.H., 2013a, Magmatic-hydrothermal processes within an evolving Earth: Iron oxide-copper-gold and porphyry Cu±Mo±Au deposits: *Geology*, v. 41, p. 767-770.
- Richards, J.P. and Mumin, A.H., 2013b, Lithospheric fertilization and mineralization by arc magmas: Genetic links and secular differences between porphyry copper ± molybdenum ± gold and magmatic-hydrothermal iron oxide copper-gold deposits: Society of Economic Geologists, Special Publication, v. 17, p. 277-299.
- Rollinson, H.R., 1993, Using geochemical data: evaluation, presentation, interpretation: Routledge.
- Saeki, Y. and Date, J., 1980, Computer application to the alteration data of the footwall dacite lava at the Ezuri Kuroku deposits, Akita Prefecture: *Mining Geology*, v. 30, p. 241-250
- Schottenfeld, M.T., 2012, Structural analysis and reconstruction of the southern end of the Pumpkin Hollow deposit, Yerington District, Nevada, University of Arizona.

- Sillitoe, R.H., 2003, Iron oxide-copper-gold deposits: an Andean view: *Mineralium Deposita*, v. 38, p. 787-812.
- Sillitoe, R.H., 2010, Porphyry Copper Systems: *Economic Geology*, v.105, p. 3-41
- Silverman, B.W., 1986, Density estimation for statistics and data analysis: CRC press, v. 26.
- Skanderbeg, B., 2001, Report on Geological Reconnaissance, Prospecting, Lithogeochemical and Soil Sampling, and Prospect Evaluation of the Mazenod Lake Property, Technical report for Phelps Dodge Corporation of Canada Limited.
- Skirrow, R., 2010, “Hematite-group” IOCG + U ore systems: Tectonic setting, hydrothermal characteristics, and Cu-Au and U mineralizing processes. Geological Association Canada, Short Course Notes, v. 20, p. 39-59.
- Skirrow, R.G., Bastrakov, E.N., Barovich, K., Fraser, G.L., Creaser, R.A., Fanning, C.M., Raymond, O.L. and Davidson, G.J., 2007, Timing of iron oxide Cu-Au-(U) hydrothermal activity and Nd isotope constraints on metal sources in the Gawler craton, South Australia: *Economic Geology*, v. 102, p. 1441-1470.
- Somarin, A.K. and Mumin, A.H., 2013, P–T composition and evolution of paleofluids in the Paleoproterozoic Mag Hill IOCG system, Contact Lake belt, Northwest Territories, Canada: *Mineralium Deposita*, v. 49, p. 199-215.
- Soto-Pinto, C., Arellano-Baeza, A., Sánchez, G., 2013: A new code for automatic detection and analysis of the lineament patterns for geophysical and geological purposes (ADALGEO): *Computers & Geosciences*, v. 57, p. 93-103.

Stanley, C.R and Madeisky, H.E., 1994, Lithogeochemical Exploration for Hydrothermal Ore Deposits Using Pearce Element Ratio Analysis, *In* Lentz, D.R., ed., Alteration and Alteration Processes associated with Ore-forming Systems: Geological Association of Canada, Short Course Notes, v. 11, p. 193-211.

Stanley, C.R. and Madeisky, H.E., 1996, Lithogeochemical exploration for metasomatic zones associated with hydrothermal mineral deposits using Pearce Element Ratio Analysis: Short Course Notes on Pearce Element Ratio Analysis.

Ullrich, T.D., Clark, A. and Kyser, T., 2001, The Candelaria Cu–Au deposit, III Región, Chile: product of long-term mixing of magmatic-hydrothermal and evaporite-sourced fluids: GSA Annual Meeting, Boston, Abstracts with Programs, p A-3.

Wallace, P.J. and Edmonds, M., 2011, The sulfur budget in magmas: evidence from melt inclusions, submarine glasses, and volcanic gas emissions: *Reviews in Mineralogy and Geochemistry*, v. 73, p. 215-246.

Wenner D.B. and Taylor H.P. Jr., 1987, Oxygen and hydrogen isotope studies of a Precambrian granite-rhyolite terrane, St. Francois Mountains, southeastern Missouri: *Geological Society of America Bulletin* 87, p. 444-460.

Williams, P.J., 1994, Iron mobility during synmetamorphic alteration in the Selwyn Range area, NW Queensland; implications for the origin of ironstone-hosted Au-Cu deposits: *Mineralium Deposita*, v.29, p. 250-260.

Williams, P.J., 2010, Classifying IOCG deposits: Exploring for iron oxide copper–gold deposits: Canada and global analogues. Geological Association of Canada, Short Course Notes, v. 20, p. 11-19.

Williams, P.J. and Skirrow, R.G., 2000, Overview of iron oxide–copper–gold deposits in the Curnamona Province and Cloncurry district (Eastern Mount Isa Block), Australia, *in* Porter, T.M., ed., Hydrothermal iron oxide copper-gold and related deposits: A global perspective, p. 105-122.

Williams, P.J., Dong, G., Ryan, C.G., Pollard, P.J., Rotherham, J.F., Mernagh, T.P. and Chapman, L.H., 2001, Geochemistry of hypersaline fluid inclusions from the Starra (Fe oxide)-Au-Cu deposit, Cloncurry District, Queensland: Economic Geology, v. 96, p. 875-883.

Williams, P.J., Barton, M.D., Johnson, D.A., Fontboté, L., De Haller, A., Mark, G., Oliver, N.H. and Marschik, R., 2005, Iron oxide copper-gold deposits: Geology, space-time distribution, and possible modes of origin: Economic Geology, p. 371-405.

Williams, P.J., Kendrick, M.A. and Xavier, R.P., 2010, Sources of ore fluid components in IOCG deposits.

Appendix I: Petrographic Analysis

Thin sections were cut from 6 samples that represent several rock types, alteration types and uniquely mineralized samples. Sample 98197 was also analyzed using the scanning electron microprobe (SEM). Each sample was photographed and cut into thin sections using Brandon University's lapidary facilities. Several of these sections were polished for reflected light microscopy analysis. Samples were individually examined in transmitted and/or reflected light to determine petrography of each sample. Analysis was performed using A Nikon Eclipse E600 POL microscope in the Laboratory for Applied Research in Resource Geology at Brandon University. Texturally interesting features or mineral anomalies were photographed using an attached Canon Rebel T4i EOS 650D. Petrography, mineralogy and descriptions are summarized in Table 10.

Sample 98197 was carbon coated to a thickness of 15 nm and analyzed using a JEOL JSM-639OLV/GS SEM, equipped with an Oxford Instruments INCA x0act Energy Dispersive Spectrometer (EDS) X-ray detector. Operating conditions include a 20kV accelerating voltage for 30-s count times using Inca Energy software and the XPP correction scheme developed by Pouchou and Pichoir (1990). Semi-quantitative analysis was collected (normalized to 100%) and standardized to the Oxford INCA default settings. Microprobe images and associated tables follow the thin section petrographic report. The SEM analysis was performed for the purposes of potentially identifying minerals associated with anomalous geochemically reported tungsten content.

TABLE 8. Hand sample and thin section analysis of selected rocks.

Sample		96224	97078	98021
Analysis ¹		Reflected & Transmitted Light	Transmitted Light	Transmitted Light
Rock Type ²		Andesite (A3)	Monzodiorite (MD)	Rhyodacite (R3)
Thin Section Figures 61a-h		(a), (b)	(c)	(d)
Hand Sample Description		Slightly gossaneous and stained with malachite andesite ignimbrite. Trace sulphides visible, most likely chalcopyrite and lesser pyrite. Fragmentals range from 1 - 5 mm, with quartz making up the larger proportions. Veins of magnetite present making up ~2-3%. ~2% has bright red plagioclase phenocrysts, from hematite in crystal structure	Relatively unaltered in appearance monzodiorite subvolcanic intrusion. Contains ~30% inequigranular plagioclase phenocrysts ~2% of which are poikilitic (black <0.01 mm inclusions?). Sausseritization of plagioclase. Contains ~ 5% biotite phenocrysts, trace K-feldspar	Somewhat bleached appearance containing ~5-10% very sausseritized subhedral plagioclase phenocrysts and 2-3% quartz phenocrysts, both ~1-2 mm diameter. Also contains ~1% mafic minerals, probably biotite and ~1% of an unknown bleached white tabular trachytic mineral
Primary Minerals	Plagioclase	~15% - Phenocrysts ~30% has been replaced with sericite. Often fractured and commonly has resorption textures. About half appear fragmental (shard-like) and the rest are euhedral phenocrysts	~25% - Inequigranular phenocrysts mostly euhedral with common resorption and crystal zoning textures	Only relict shapes. Completely replaced with very fine-grained cross-hatched pattern of sericite
	Quartz	~5% - Commonly has resorption textures with embayments	~2-3% - 1% of phenocrysts up to 1 mm and is seriate within groundmass. Commonly has resorption textures	~5-7% quartz phenocrysts up to 2-3 mm. Most are fractured with fractures filled with sericite

	Groundmass	~45% - Sericitized, appears to be mostly composed of plagioclase	~70% - Appears to be predominantly (but unknown %) plagioclase with lesser quartz	Appears to be predominantly (but unknown %) plagioclase with lesser quartz
Characterizing & Accessory Minerals	Biotite	Mostly relict minerals replaced by chlorite and calcite	2-3% - Phenocrysts ~1-2 mm on average. Oikocrysts with ~1% magnetite within the biotite. Associated with a chlorite replacement	Predominantly replaced by chlorite
	Titanite	-	Trace - Associated with biotite phenocrysts	-
Hydrothermal Minerals	Epidote	Trace - Associated with chlorite	-	-
	Titanite	-	-	-
	Calcite	~1% - Associated with chlorite and epidote as veins and pseudomorphic replacement	-	-
	Chlorite	~3% - Chlorite veins and pseudomorphic replacement of biotite. Associated with trace quartz and greater calcite and epidote	~1% - Hydrothermal replacement of biotite phenocrysts	~2% - Hydrothermal replacement of biotite phenocrysts

Apatite	Trace - Chadacrysts within plagioclase	-	-
Sericite	~5% - Replacement of the feldspar phenocrysts and groundmass	Approximately 10% of the plagioclase phenocrysts have been replaced with a very fine-grained sericitic alteration product. The sericite does not affect the groundmass	~70% - Veins and pseudomorphic replacement of feldspars. All of the feldspars are completely converted to sericite, only relict shapes
Quartz	Trace - <1 mm diameter veins	-	Trace - associated with sericitic replacement of feldspars and sericite veins
Magnetite	~2% - Chadacrysts within chlorite. Ilmenite exsolution within the magnetite	Chadacrysts within biotite and chlorite.	Chadacrysts within biotite and chlorite.
Hematite	Trace - Associated with magnetite	-	-
Sulphides	~1% - Pyrite and chalcopyrite. Probably multiple crystallization phases but pyrite definitely encloses magnetite indicating an earlier crystallization phase of magnetite. Like the magnetite, forms within veins of chlorite	-	-

Sample Analysis* Rock Type** Thin Section Figures 61a-h		98089 Transmitted Light Dacite (D1) (e)	98157 Reflected & Transmitted Light Basaltic Andesite (BA1) (f)	98197 Transmitted Light Andesite (A3) (g), (h)
Hand Sample Description		Relatively unaltered in appearance dacite ignimbrite. Strongly magnetic. Containing approximately 20%, 1-4 mm subhedral - euhedral plagioclase phenocrysts in a light grey slightly siliceous looking matrix	Rock has a high specific gravity. Contains very metallic red looking hematite (almost looks like sphalerite). Contains veins of mm-scale epidote surrounded by red staining (probably more hematite). Weathered surface has pink staining reminiscent of cobalt bloom. Few k-feldspar veins, not as many and smaller than the epidote veins	Malachite stained on weathered surface, fresh surface has trace barely visible sulphides (chalcopyrite?). Reddish hue to rock and veins of black material that pervades it
Primary Minerals	Plagioclase	~20% - Mostly euhedral and predominantly (~80%) sericitized. ~15% replaced with epidote and ~1% with calcite	~20% - Cut sample is mostly vein material, but groundmass appears to be predominantly plagioclase that is often perthitic.	Phenocrysts completely replaced with very fine-grained sericite
	Quartz	-	-	-
	Groundmass	Appears to be composed of micron and smaller sized plagioclase	Appears to be plagioclase	Appears to be plagioclase

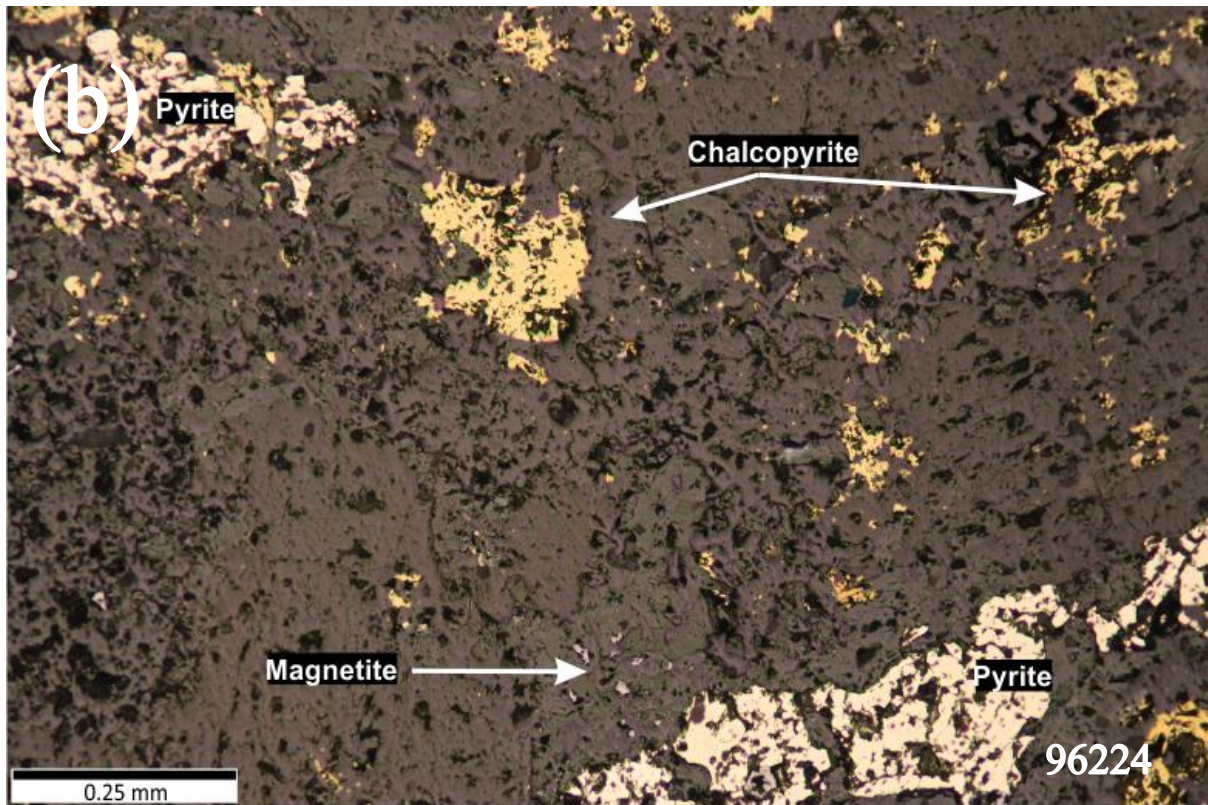
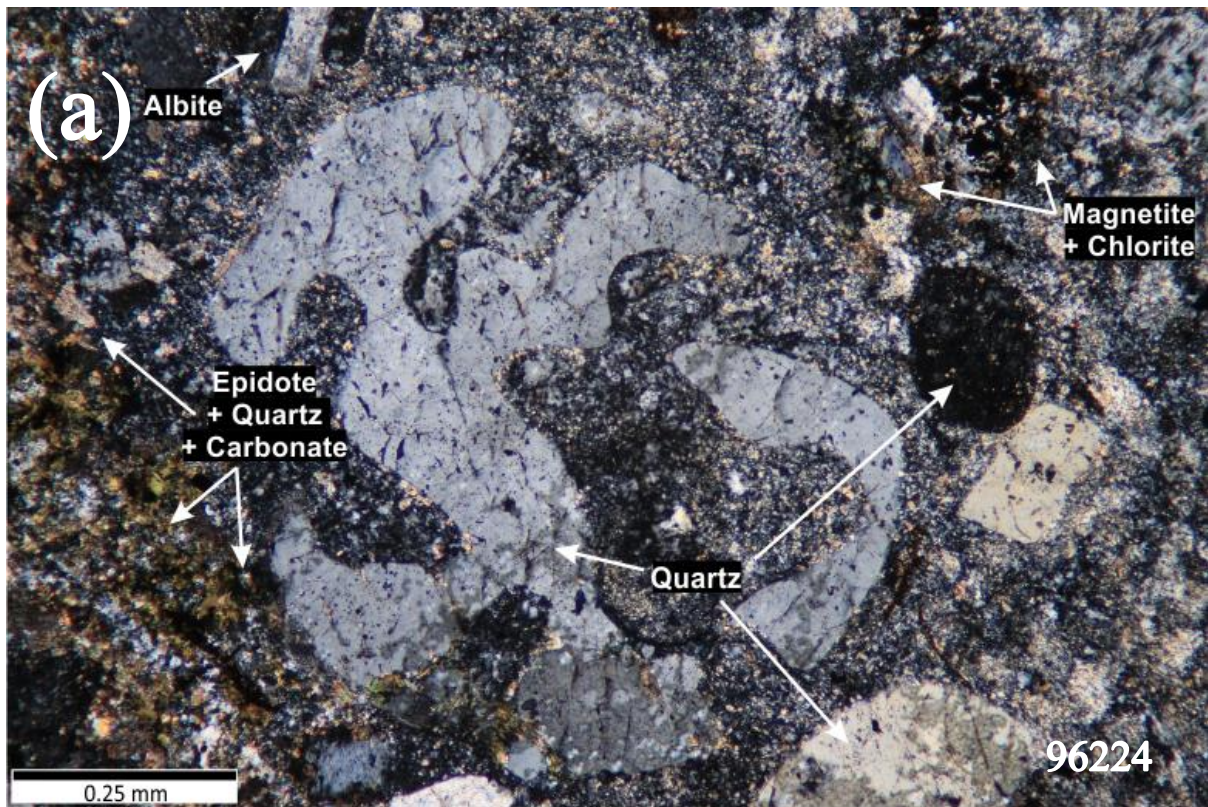
Characterizing & Accessory Minerals	Biotite	Trace - Mostly relict biotite, replaced with epidote, chlorite and/or magnetite	-	-
	Titanite	-	-	-
Hydrothermal Minerals	Epidote	~2% - Predominantly replacing groundmass and on the periphery of plagioclase phenocrysts. Micron-scale veins disseminated throughout. ~15% associated with chlorite veins	~70% - Thin section is predominantly from an epidote vein ~1.2 cm in diameter. Mostly very fine-grained but a few >1 mm crystals near a quartz vein	Trace - Associated with chlorite
	Titanite	Trace - Epidote veins and replacement commonly form around titanite crystals	-	Trace - Associated with chlorite
	Calcite	Trace - Veins within plagioclase phenocrysts. Earlier phase alteration than the sericite replacement (sericite forms around calcite veins)	-	-

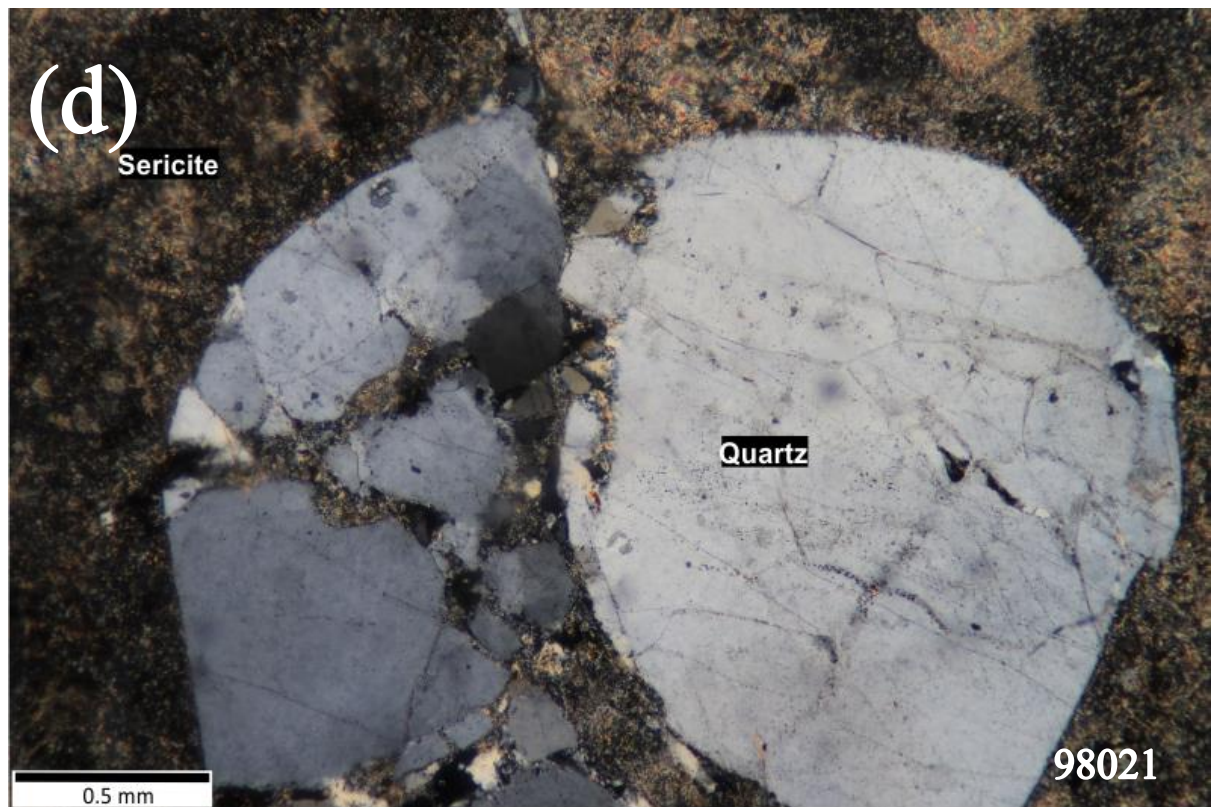
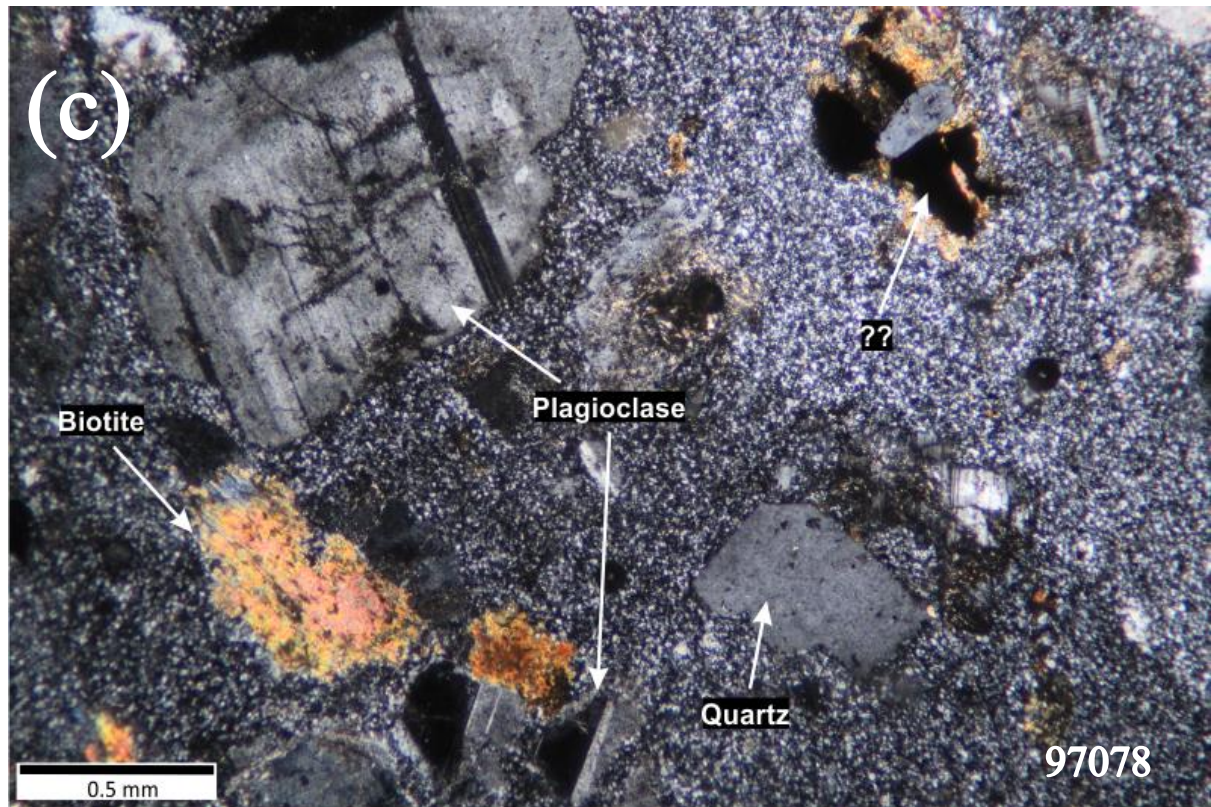
Chlorite	~2% - Occurs predominantly in groundmass as ~0.001 mm veinlets associated with magnetite and quartz	Trace - Associated with epidote	~20% - Veins of chlorite that cross-cut and follow pre-existing quartz veins. In local zones replacing feldspars and sericite
Apatite	-	-	-
Sericite	~15% - Has replaced ~60% of the plagioclase phenocrysts. Trace association with carbonate.	Trace - in phenocrysts and groundmass	~50% - Complete replacement of plagioclase phenocrysts
Quartz	Trace - Hydrothermal quartz associated with micron-scale actinolite veins	Vein of quartz is earlier alteration product than the epidote. Chilled margin surrounding the quartz vein	~5% - <0.01 - 1 mm veins of quartz. It is offset and cross-cut by larger epidote veins
Magnetite	~10% - Disseminated and poikilitic throughout groundmass euhedral magnetite from < micron to 0.1 mm. Concentrated magnetite crystals are associated with chlorite veinlets	Trace - few euhedral phenocrysts within a quartz vein - earlier phase of alteration than quartz vein?	Trace - Disseminated in groundmass

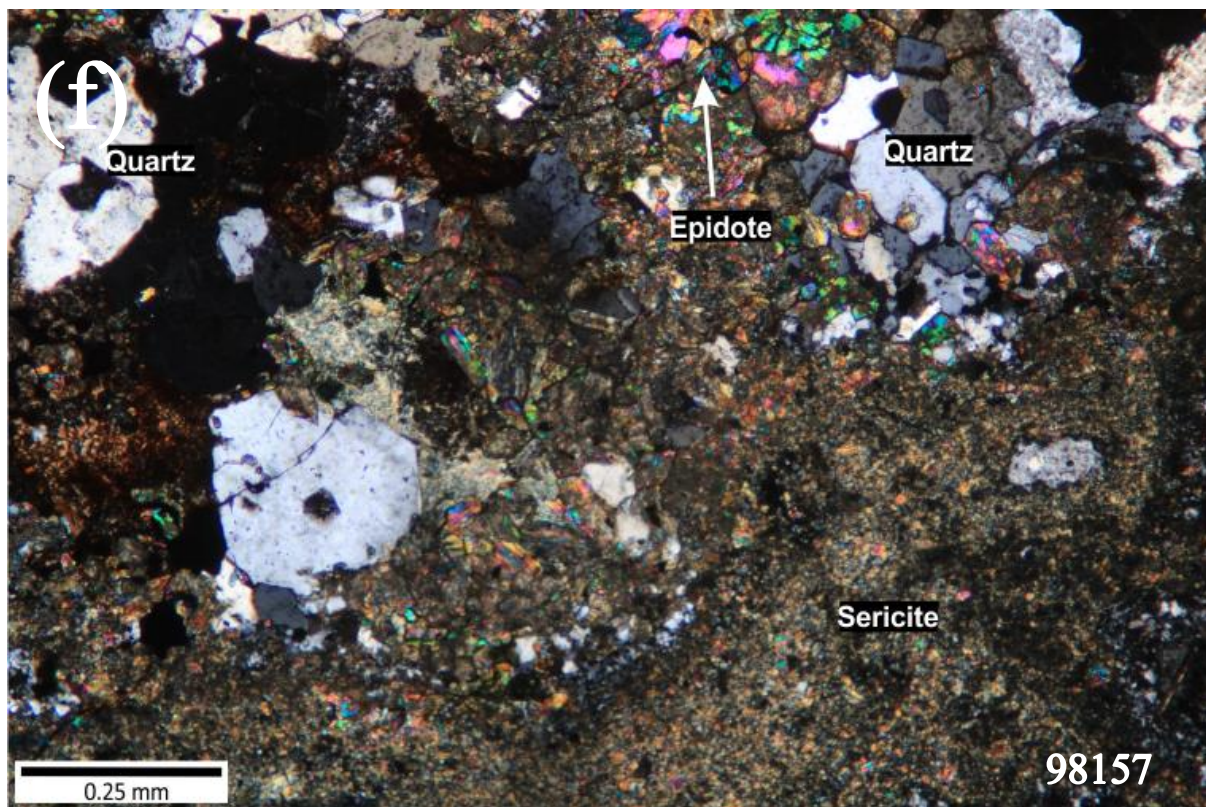
Hematite	-	~5% of the plagioclase phenocrysts have a brownish-siderite appearance. Likely due to hematite being within the crystal structure of the plagioclase. Veins of hematite cross-cut the epidote	~1% Within crystal structure of feldspars and few <0.01 mm euhedral crystals
Sulphides	Trace unknown sulphide (possibly chalcopyrite)	-	?

¹Sulphides and other typical opaque minerals only capable of being identified in reflected light microscopy.

²See North Mazenod map for comparable rock type classifications.







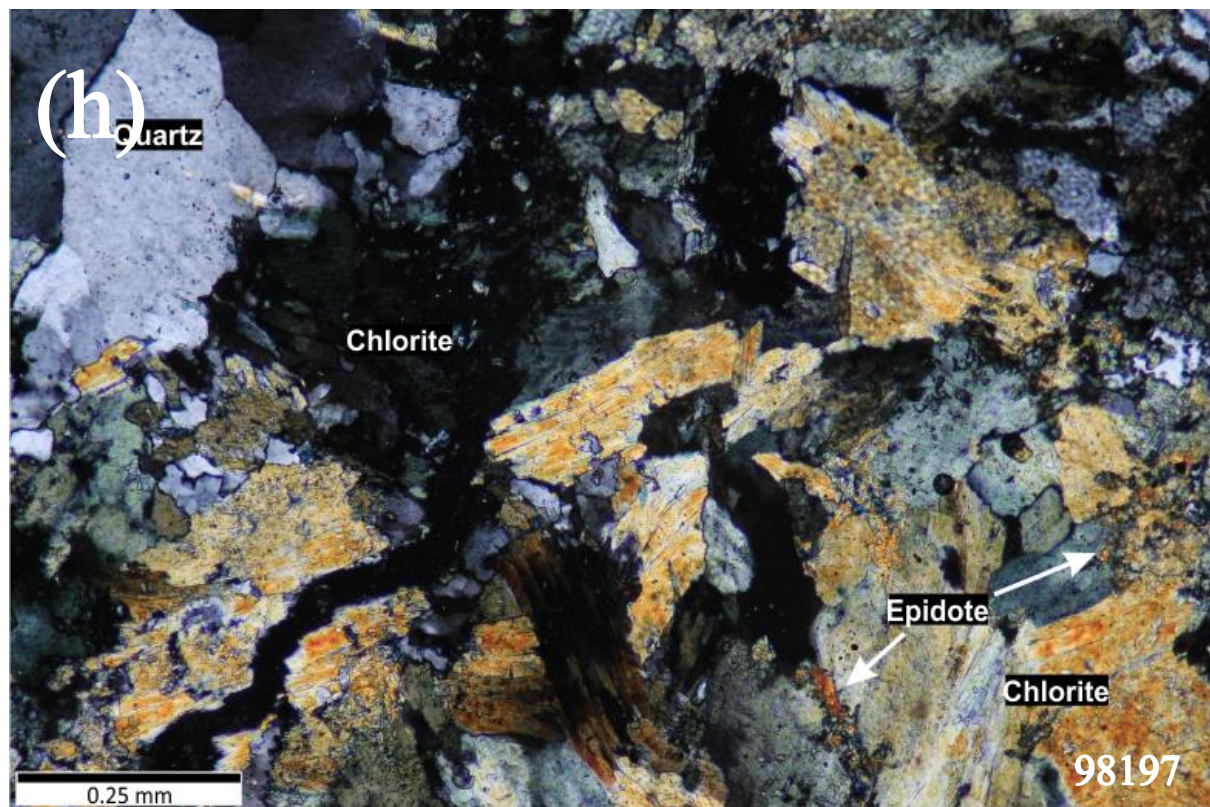
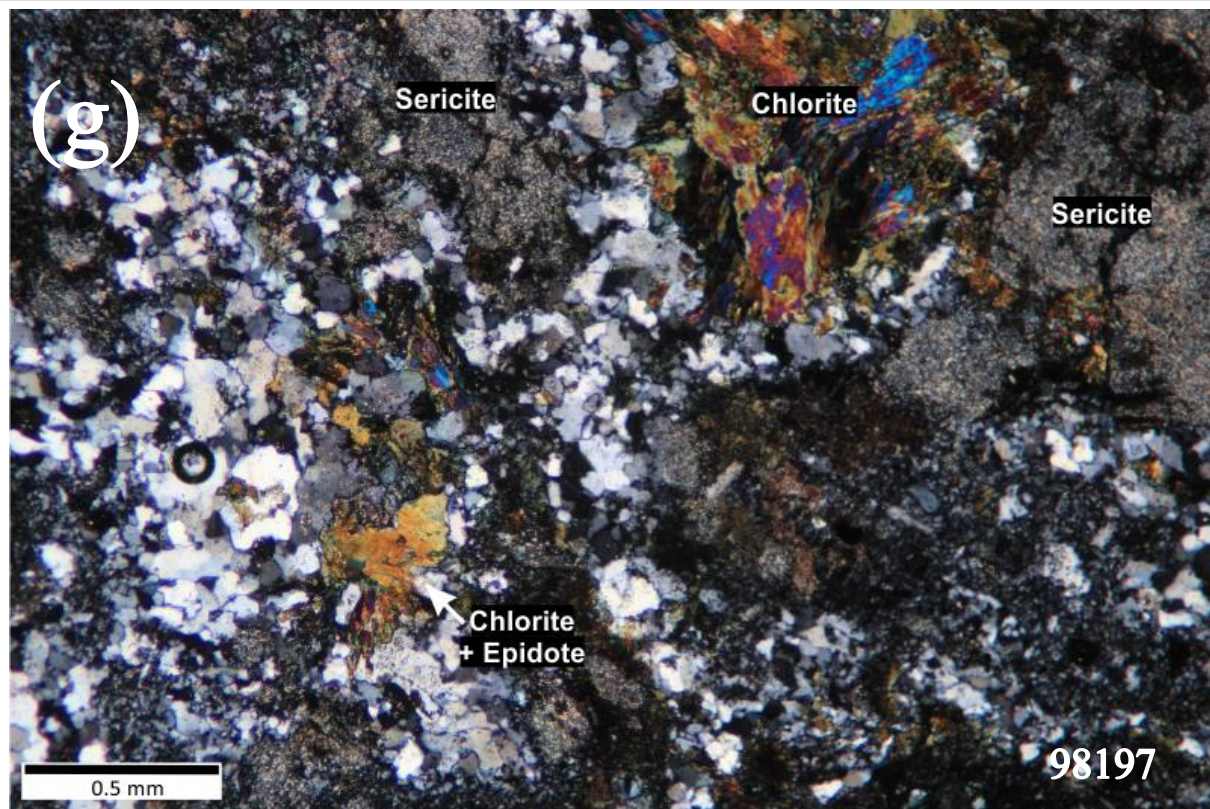


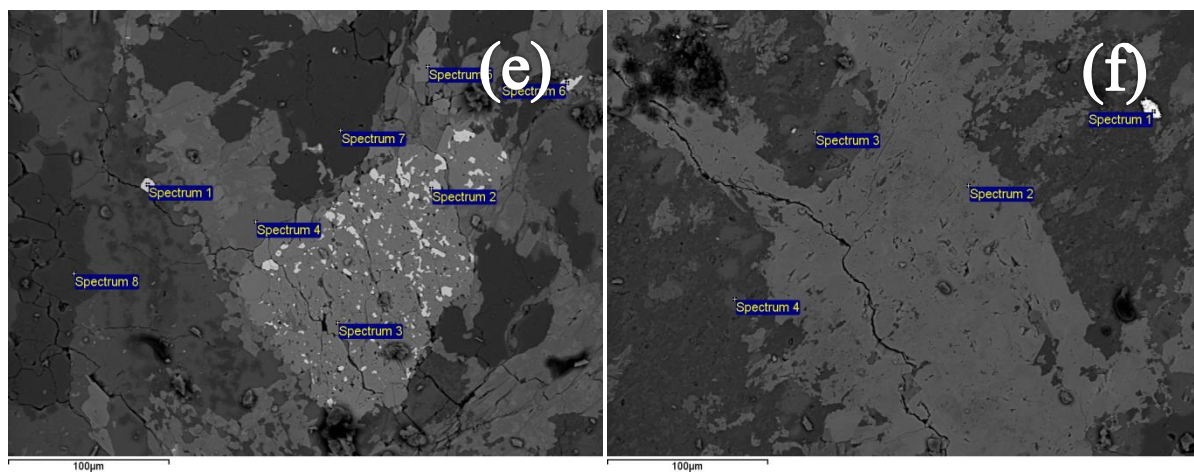
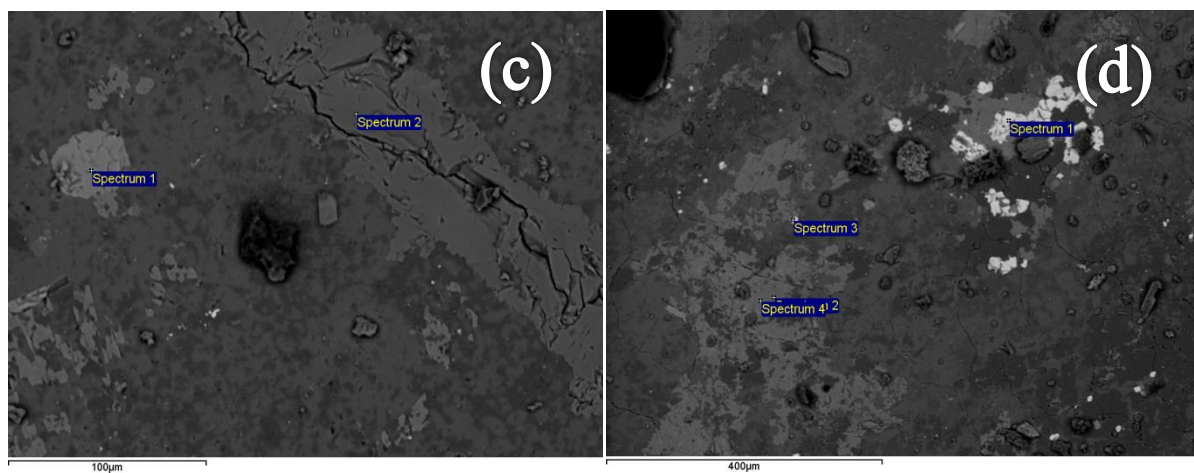
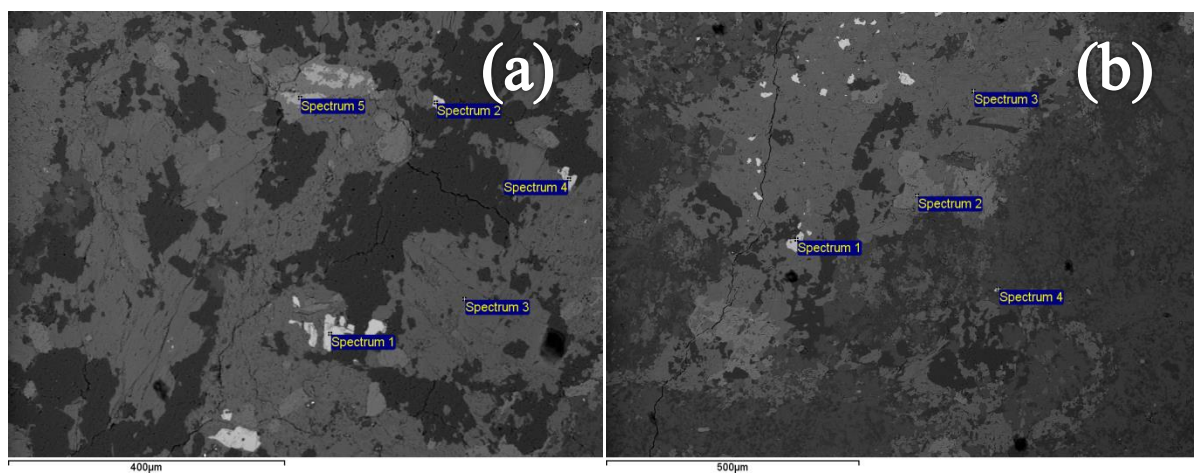
TABLE 9. SEM analysis of sample 98197

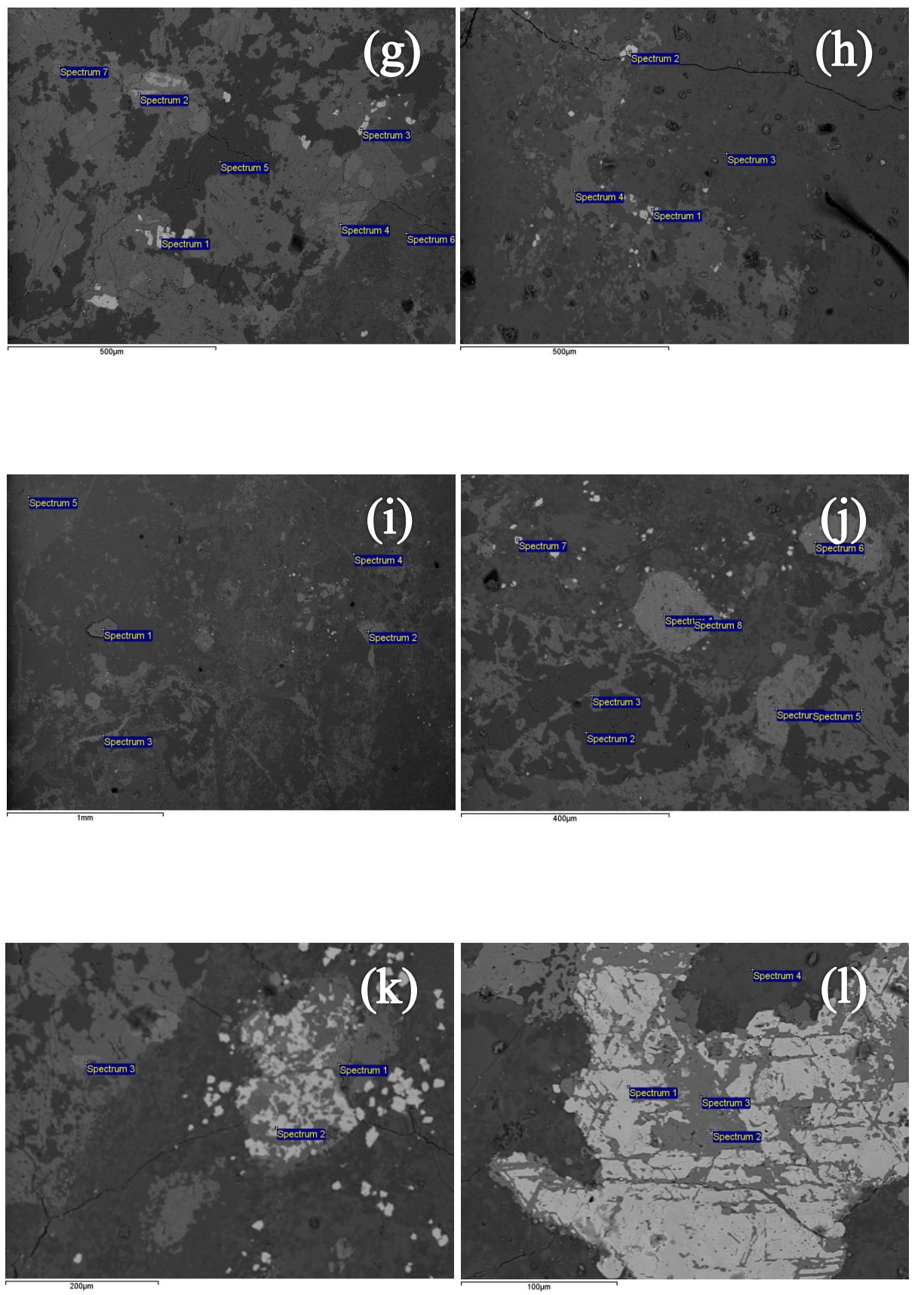
Elements (wt.%)	O	F	Na	Mg	Al	Si	P	Cl	K	Ca	Ti	Cr	Mn	V	Fe	Cu	W	Zn	Zr	Total
Site (a)																				
Spectrum 1	32.72														67.28					100
Spectrum 2	32.03					0.96									67.01					100
Spectrum 3	48.23		0.59	7.04	3.16	21.58			0.3	7.48			0.41		11.21					100
Spectrum 4	31.89					0.69									67.41					100
Spectrum 5	47.31					1.13				2.09	25.52		0.29		23.67					100
Site (b)																				
Spectrum 1	36.2											0.27			63.53					100
Spectrum 2	46.73	1.41			1.14	13.91				17.6	18.49				0.72					100
Spectrum 3	47.15		0.63	5.85	4.18	20.7		0.27	0.78	7.51			0.37		12.56					100
Spectrum 4	48.75				4.95	20.21			6.8										19.29	100
Site (c)																				
Spectrum 1	39.65	5.78					19.2	0.28		34.01							1.08			100
Spectrum 2	50.66			1.5	12.93	17.38				14.47			0.4		2.66					100
Site (d)																				
Spectrum 1	31.33					0.96									67.7					100
Spectrum 2	48.1		0.33	7.06	2.6	21.78		0.2	0.4	7.68			0.55		11.3					100
Spectrum 3	32.8			0.61		1.42									65.17					100
Spectrum 4	47.65			6.73	2.69	22			0.56	7.77			0.54		12.05					100
Site (e)																				
Spectrum 1	35.62														64.38					100
Spectrum 2	36.83					0.84				1.53	1.77				59.03					100
Spectrum 3	48.31				0.99	13.56				17.63	18.29				1.21					100
Spectrum 4	48.28		0.47	7.02	3.17	21.84			0.4	7.64			0.36		10.82					100

Elements (wt.%)	O	F	Na	Mg	Al	Si	P	Cl	K	Ca	Ti	Cr	Mn	V	Fe	Cu	W	Zn	Zr	Total
Spectrum 5	48.31				0.95	14.01				17.42	18.15				1.16					100
Spectrum 6	33.88					0.54		0.28		0.22					65.09					100
Spectrum 7	56.82					43.18														100
Spectrum 8	56.35					43.65														100
Site (f)																				
Spectrum 1	15.32			1.04	2.18	5.43			0.15	0.3					0.69	68.56		6.34		100
Spectrum 2	48.75				11.61	17.35			0.32	14.29			0.25		7.44					100
Spectrum 3	51.87		0.35		8.53	28.35			10.9											100
Spectrum 4	50.33				8.64	28.52			12.52											100
Site (g)																				
Spectrum 1	33.87														66.13					100
Spectrum 2	47.78									0.5	27.78				23.94					100
Spectrum 3	35.65														64.35					100
Spectrum 4	48.26				0.99	13.61				17.85	18.51				0.79					100
Spectrum 5	56.48					43.52														100
Spectrum 6	51.32				9	28.75			10.93											100
Spectrum 7	43.18	5.25					18.5			33.07										100
Site (h)																				
Spectrum 1	31.92					0.63									67.45					100
Spectrum 2	39.39			2.64	0.76	7.36				4.51					45.34					100
Spectrum 3	48.74		0.43		8.45	31.11			11.27											100
Spectrum 4	35.9			5.37	4.45	19.07			0.59	6.81					27.81					100
Site (i)																				
Spectrum 1	53.38			6.15	7.18	15.83			2.64	0.97	1.21		0.37		12.27					100
Spectrum 2	52.12				1.23	13.01				15.78	16.68				1.17					100

Elements (wt.%)	O	F	Na	Mg	Al	Si	P	Cl	K	Ca	Ti	Cr	Mn	V	Fe	Cu	W	Zn	Zr	Total
Spectrum 3	51.88			2.62	1.33	17.8				12.05	9.9				4.43					100
Spectrum 4	51.22		5.14		9.79	29.25			4.01	0.59										100
Spectrum 5	52.36				5.94	33.13			6.89	1.68										100
Site (j)																				
Spectrum 1	46.96				0.88	14.04				18.04	19.4				0.67					100
Spectrum 2	54.94					45.06														100
Spectrum 3	50.71		0.49	6.61	3.09	20.98			0.31	6.9			0.42		10.49					100
Spectrum 4	48.66				1.12	13.45				17	18.47				1.3					100
Spectrum 5	44.27		0.31	6.87	2.26	24.09			0.32	8.44			0.63		12.8					100
Spectrum 6	47.26				0.93	13.96				17.9	19.15				0.81					100
Spectrum 7	32.7														67.3					100
Spectrum 8	45.49		0.55	7.02	2.83	22.47			0.47	8.01			0.66		12.5					100
Site (k)																				
Spectrum 1	47.76				0.9	15.38				16.74	17.92				1.29					100
Spectrum 2	30.94					1.29		0.49							67.28					100
Spectrum 3	50.07			0.51	0.99	13.59				14.85	18.63				1.37					100
Site (l)																				
Spectrum 1	39.42													0.22	60.36					100
Spectrum 2	41.13					1.14				0.76	0.93				56.04					100
Spectrum 3	50.76				0.75	12.5				14.5	16.06				5.44					100
Spectrum 4	50.61				8.99	28.35			12.05											100
Site (m)																				
Spectrum 1	44.61		0.58		2.18	14.47				18.54	18.65				0.96					100
Spectrum 2	17.59					1.18									81.24					100
Spectrum 3	51.67		5.1		9.75	27.68			4.07	1.13					0.59					100

Elements (wt.%)	O	F	Na	Mg	Al	Si	P	Cl	K	Ca	Ti	Cr	Mn	V	Fe	Cu	W	Zn	Zr	Total
Site (n)																				
Spectrum 1	44.61		0.58		2.18	14.47				18.54	18.65				0.96					100
Spectrum 2	17.59					1.18									81.24					100
Spectrum 3	51.67		5.1		9.75	27.68			4.07	1.13					0.59					100
Apatite with a minor W content																				





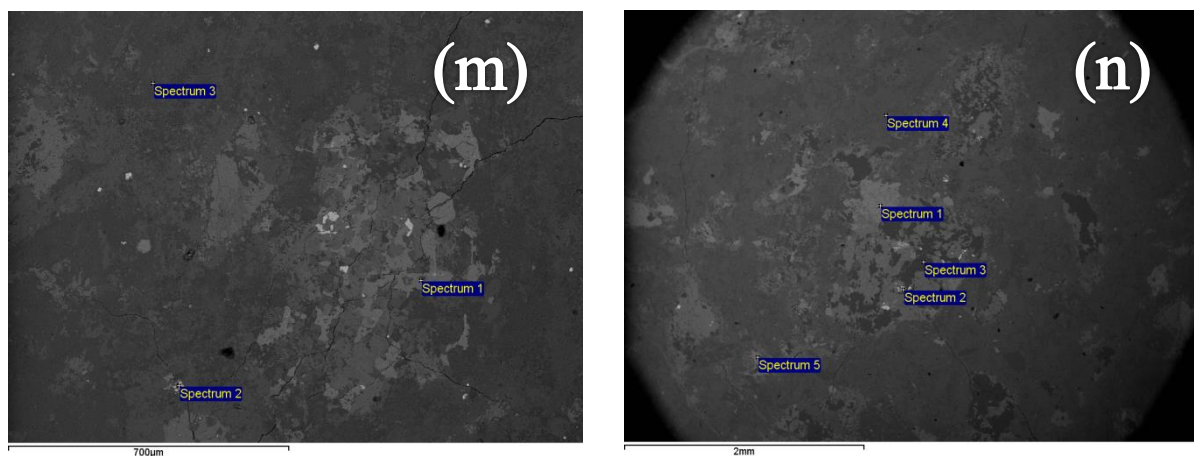


Fig 62a-n. Backscattered electron microprobe images of selected sites in sample 98197. See Table 11 for spectrum assay results.

Appendix II: Formulas

Formula derived from mass balance analysis and isocon diagrams (Grant, 1986):

Equation of the isocon line:

$$C^A = \left(\frac{m^O}{m^A} \right) C^O$$

Percent elemental change:

$$\Delta C_i \% = \left\{ \left[\frac{\frac{C_i^A}{C_i^O}}{\frac{m^A}{m^O}} \right] - 1 \right\} * 100\%$$

Change in mass:

$$\Delta M \% = \left[\left(\frac{m^O}{m^A} \right) - 1 \right] * 100\%$$

Where: C^A = Concentration of component altered sample

C^O = Concentration of component of least-altered sample

m^A = Concentration of immobile element in the altered sample (usually Al_2O_3)

m^O = Concentration of immobile element in the least-altered sample (usually Al_2O_3)

C_i = Concentration of component i

C_i^A = Concentration of component i in altered rock

C_i^O = Concentration of component i in least-altered rock

Appendix III: Sample Descriptions

TABLE 10. Sample descriptions amalgamated from sample booklet data, field notes and later observations for those samples undergone mass balance analysis in this study.

Sample ID	Easting	Northing	Host Rock	Alteration Classification	Description
96217	502880	7065083	Andesite	Mineralized	Fractured and mildly potassic altered crystal tuff with actinolite, magnetite and chlorite? Contains vein with pyrite chalcopyrite and arsinides? Erythrite and malachite present
96222	502875	7065066	Andesite	Mineralized	Potassic altered with minor weathered sulphides along fracture
96227	502765	7065118	Andesite	Hematite + Potassic	Potassium altered fracture zone, 5% specular hematite. Vuggy weathered
96232	502540	7065013	Rhyodacite	Potassic	Felsite with disseminated sulphides, slightly magnetic
96233	502577	7065232	Rhyodacite	Tourmaline	Strongly potassic altered rock with tourmaline crackle breccia and phyllic overprint along with minor disseminated pyrite
96238	502465	7064891	Andesite	Hematite	Potassic altered crackle breccia rock cemented with hematite
96239	502542	7064976	Rhyodacite	Potassic	Felsite with hematite veins and slightly magnetic. Sulphide boxwork structures/pits
96240	502594	7064962	Andesite	Potassic	Brecciated strongly potassic altered rock
96259	502321	7065561	Andesite	Least Altered	Porphyritic andesite feldspar crystal tuff. 15-20% 1-3 mm plagioclase phenocrysts, 2-3% up to 1 cm plagioclase phenocrysts in a dark grey matrix. Trace pyroxene and carbonate along a fracture

96260	502129	7065560	Andesite	Carbonate	Minor carbonate veining in a weakly potassic altered lapilli tuff. Minor weathered out sulphides along fracturing
96309	504174	7065162	Andesite	Least Altered	Least altered feldspar-quartz crystal tuff
96386	504696	7065636	Basaltic Andesite	Epidote	Epidote altered associated with up to 1% euhedral pyrite. Hosted in a crystal tuff
96392	505694	7056379	Dacite	Silicification + Potassic + Magnetite	Strongly potassic altered and silicified. Also contains magnetite veins up to 3 cm thick
96397	505495	7056659	Dacite	Propylitic	Brecciated and bedded ash tuff cemented with epidote that is associated with a minor amount of sulphides
96405	501787	7066243	Rhyodacite	Hematite	Fine-grained with pervasive hematite staining and veining with a structurally fractured zone
96423	501367	7065050	Andesite	Least Altered	Crystal tuff with a very fine-grained dark matrix. Contains ~15% 0.5-3 mm feldspar phenocrysts. Trace alteration minerals of K-feldspar, epidote and magnetite noted in fractures
96427	500824	7065429	Dacite	Silicification	Strong alteration, Pervasive k-feldspar and quartz, moderate to strong potassic alteration, Lapilli appears silicified (dark v.f.g colour). Fine epidote veins and clots, but not nearly as abundant as previously, rock has pervasive weak to moderate magnetism
96443	501453	7064395	Monzogranite	Least Altered	Coarse-grained granitoid

96444	501191	7064237	Monzogranite	Least Altered	Medium-grained granitoid
96479	502581	7065216	Rhyodacite	Tourmaline + Silica + Potassic	Crystal tuff altered to felsite. Stockwork of fine mm-scale tourmaline-quartz veins
97005	501749	7062411	Andesite	MA	Crystal tuff containing actinolite crystals 2-5mm, pink-red-purple matrix. Med-fine-grained
97030	501021	7063174	Rhyodacite	Silicification	Sample acquired from near uranium exploration trench. Quartz breccia hosted within a crystal tuff
97041	501667	7063150	Rhyodacite	Potassic	Strongly potassic altered and quartz-rich in phenocrysts. Trace magnetite. Fine cherty ash matrix. 2-3% mafic grains.
97055	501407	7063494	Monzogranite	Least Altered	Fine-grained granitoid. 1-2 mm crystals of quartz and feldspar. 25-30% quartz, 20% plagioclase, 3-4% biotite and 45-50% K-feldspar. Sucrosic texture with a pink fresh surface
97057	501224	7063776	Rhyodacite	Least Altered	Phenocrysts of feldspar, quartz and biotite, possibly a lapilli tuff. Aphanitic light grey matrix material. Contains minor amount of amphiboles and biotite
97063	502143	7063695	Rhyodacite	Hematite + Quartz	Crystal Tuff hosting massive quartz-hematite rich vein. Sample is mostly hematite
97078	502387	7064262	Monzodiorite	Least Altered	Massive dark grey, with crystalline grains of biotite and feldspar up to 4 mm
97094	502864	7062516	Rhyodacite	Mineralized	Vuggy quartz vein + actinolite + pyrite + chalcopyrite in a crystal tuff

97095	502875	7062501	Rhyodacite	MA	Structural breccia containing actinolite and magnetite which are associated with trace chalcopryrite and 1% or greater pyrite. Silicification occurring at the outer edge of the actinolite veins. Contains several <1 mm veins of magnetite that are cross-cut by the actinolite veins
97099	502944	7062571	Andesite	Mineralized	Moderate to strongly potassic altered with 1 mm phenocrysts of pink-red-grey K-feldspars and <1% mafic minerals. Fine to medium grained, weakly magnetic and may contains some hematite
97123	502192	7061400	Rhyodacite	Potassic	Strongly potassic altered tuff with traces of pyrite and magnetite. Almost a felsite. Sugary/cherty texture.
97124	502226	7061496	Andesite	MA	Magnetite breccia with associated epidote and disseminated sulphides
97129	502278	7061524	Rhyodacite	MA	Crystal tuff with hydrothermal magnetite and sulphides from the top of Nod Hill
97138	502315	7061428	Rhyodacite	Mineralized	Magnetite crackle breccia with minor pyrite, chalcopryrite and malachite
97143	502300	7061713	Rhyodacite	Mineralized	Crystal tuff with magnetite and sulphides in veins. Moderate potassic alteration

97227	505382	7056684	Dacite	Tourmaline	Rock that has 'red rock' alteration of hematite and k-feldspar. Stockwork veins > 1 cm wide of tourmaline pervade this rock. Central in some of the veins is quartz veins
97228	505396	7056604	Dacite	Tourmaline	Tourmaline veined and brecciated. Sulphides (pyrite) associated with the tourmaline veins. <0.1 mm scale veins of K-feldspar. Host rock is bright red, from suspected hematite and k-feldspar alteration
97249	505789	7055914	Andesite	Mineralized	Crystal tuff containing chalcopyrite associated with magnetite
97254	505483	7055703	Dacite	Hematite + Quartz	Hematite quartz cemented breccia containing trace sulphides. Rock is heavily weathered.
97258	505509	7055692	Andesite	Mineralized, Tourmaline	Tourmaline breccia with minor hematite and sulphides
97266	505355	7055298	Andesite	Tourmaline	Tourmaline quartz breccia containing trace pyrite
98024	503196	7064111	Volcanic Sediments	Least Altered	Thin bedded sediment. No visible alteration
98032	502473	7063661	Rhyodacite	Silicification	Vuggy quartz vein that has association with hematite
98089	503944	7063923	Dacite	Least Altered	Lapilli tuff. Outcrop surrounding least altered piece contained minor epidote alteration

98098	503684	7064094	Dacite	Carbonate	Ash tuff with minor carbonate
98151	499921	7064864	Monzogranite	Least Altered	Whitish-pink, no visible alteration. Rock contains ~60% quartz crystals and 20% K-feldspar and plagioclase makes up the rest. ~1% mafic minerals, biotite?
98156	499638	7064361	Basaltic Andesite	Least Altered	Greyish ash tuff, no visible alteration effect. Up to 5% 1-3 mm feldspars
98172	499830	706520	Andesite	MA	Strongly potassic altered rock with abundant clots of actinolite-magnetite
98185	500195	7065530	Andesite	Epidote	Crystal tuff, strong epidote, trace - pyrite, chalcopyrite and malachite
98191	500419	7065247	Basaltic Andesite	Epidote	Crystal tuff containing actinolite, epidote breccia. Weakly potassic altered
98207	498424	7064858	Andesite	Silicification	Silicified crystal tuff. Contains ~3% pyrite
98244	505529	7054416	Andesite	Carbonate	Crystal tuff with epidote and magnetite veining plus trace sulphide. Outcrop was brecciated with dolomite or a ferrocarbonate
98271	505710	7067564	Basaltic Andesite	Epidote	Ash tuff containing an epidote breccia associated with lesser actinolite. Almost an epidotite

Appendix IV: Common Indicator Element Concentrations

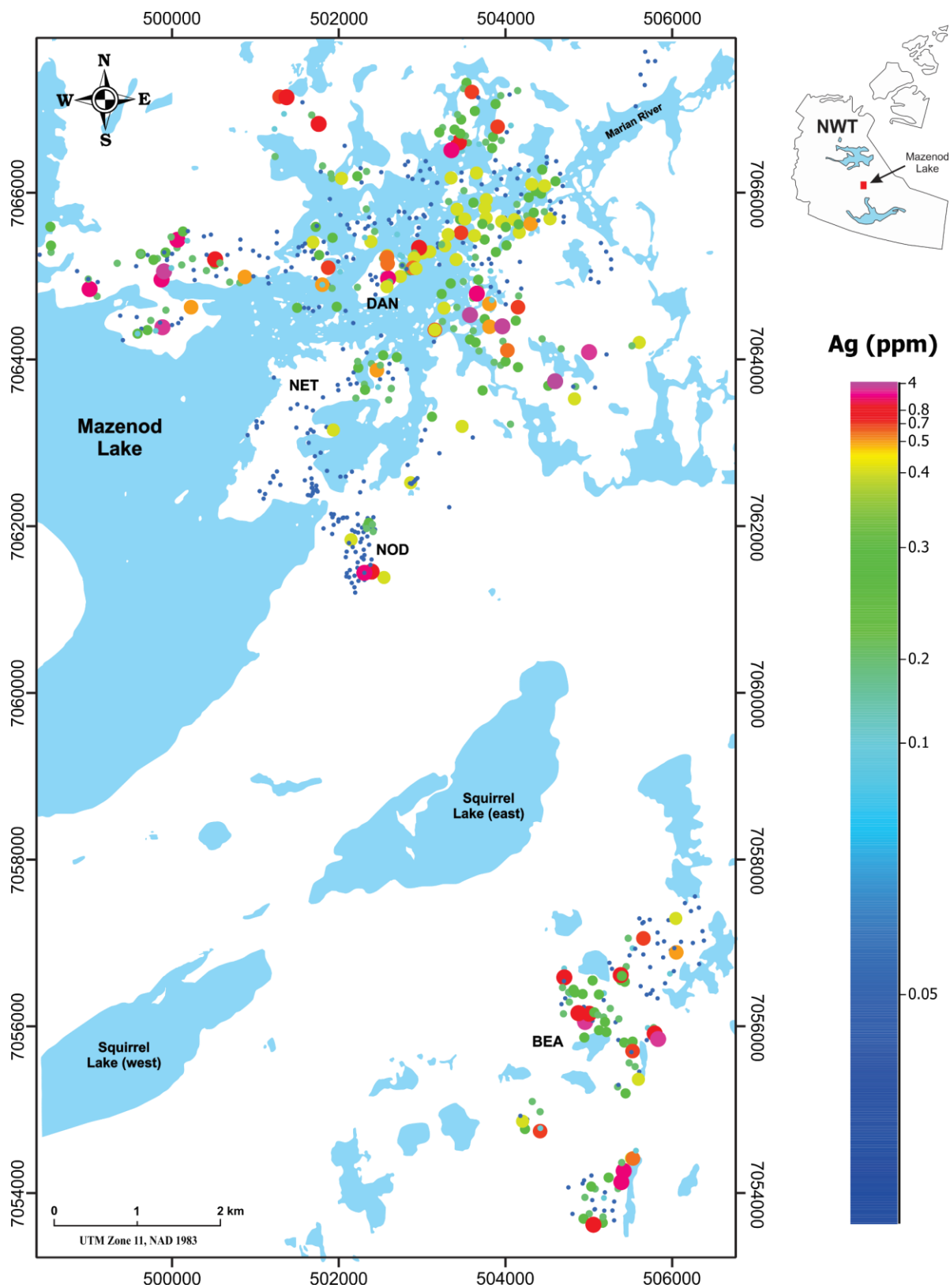


Fig. 63. Distribution of silver concentrations in the Mazenod Lake region.

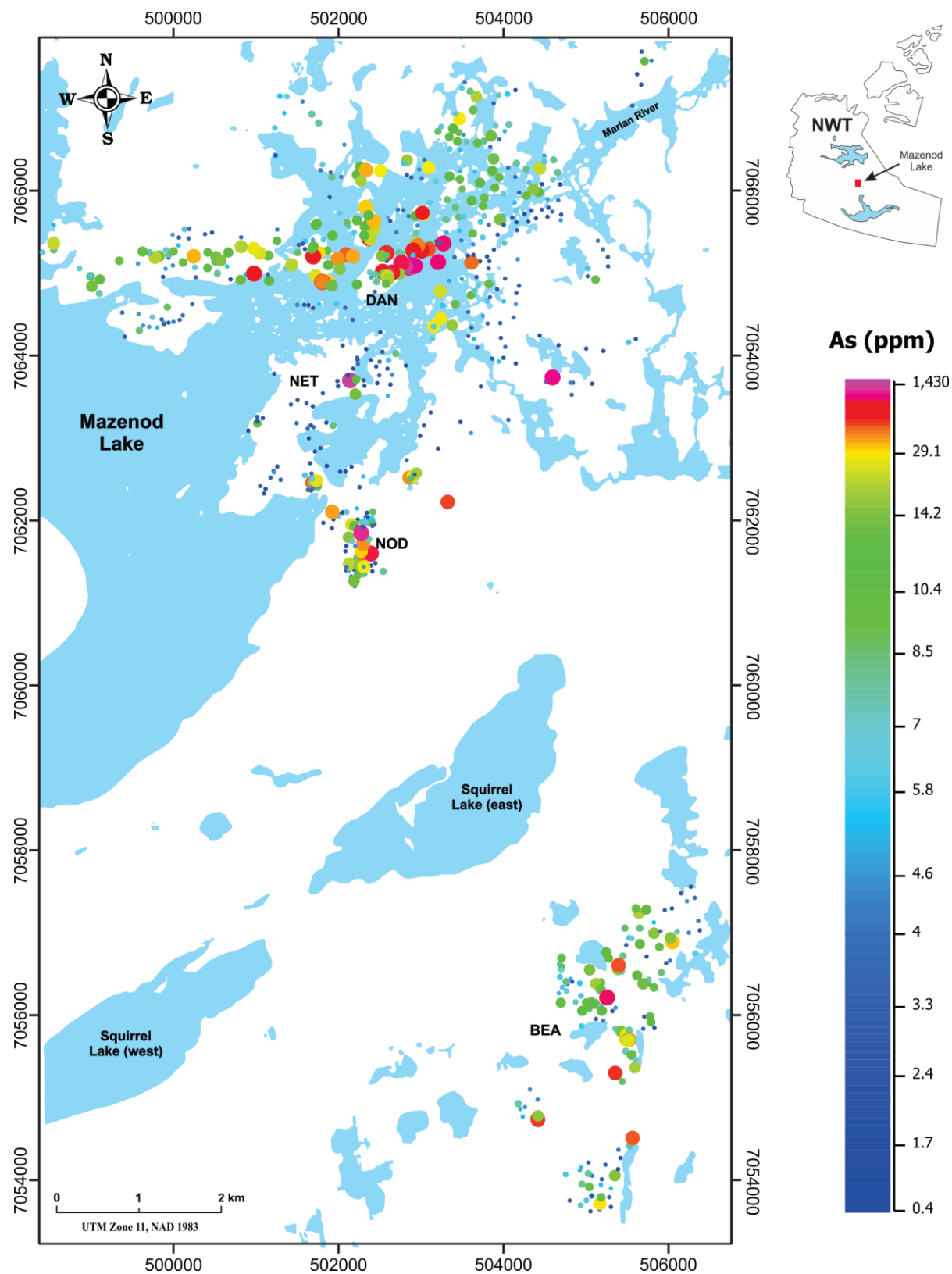


Fig. 64. Distribution of arsenic concentrations in the Mazenod Lake region.

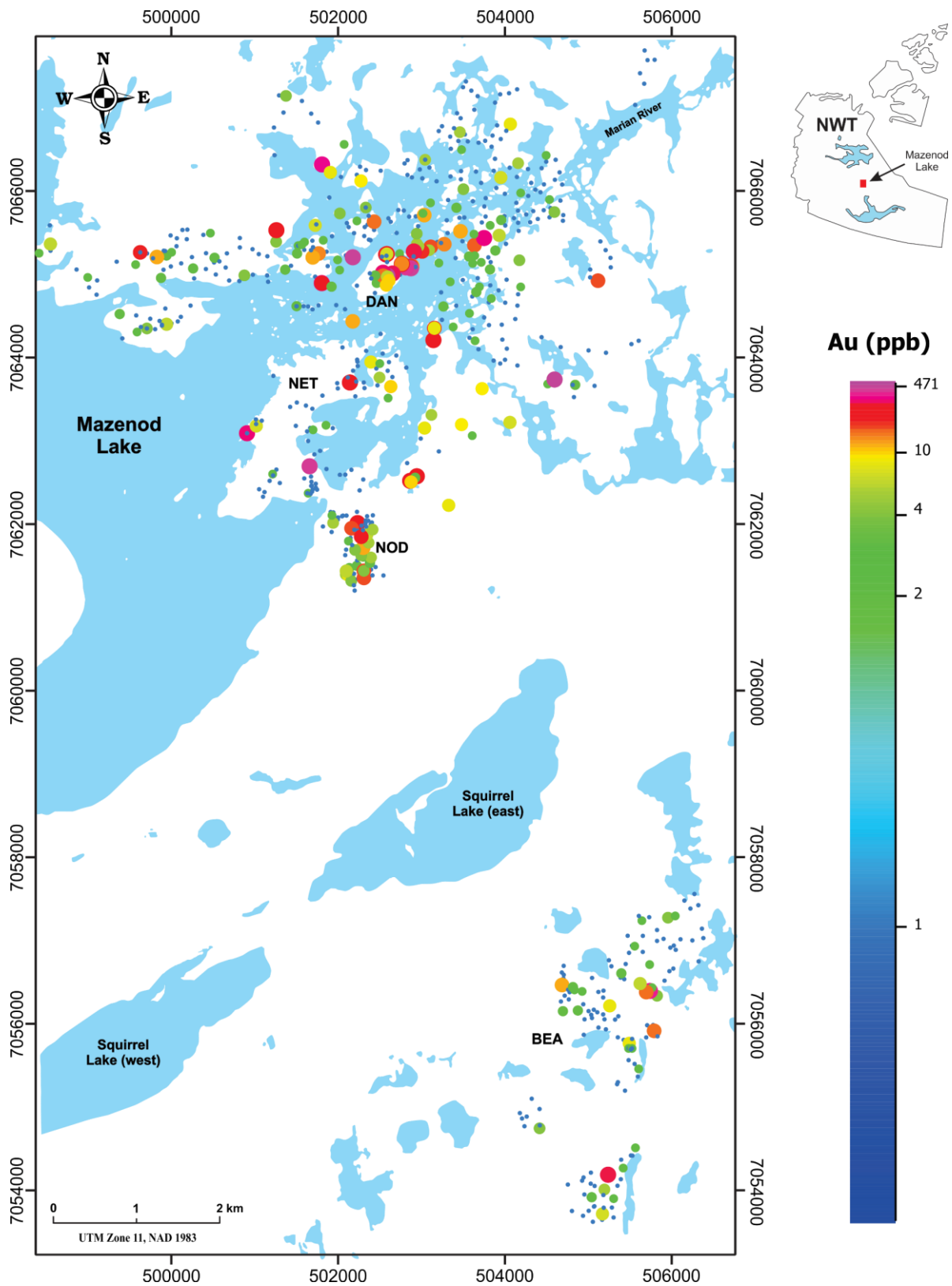


Fig. 65. Distribution of gold concentrations in the Mazenod Lake region.

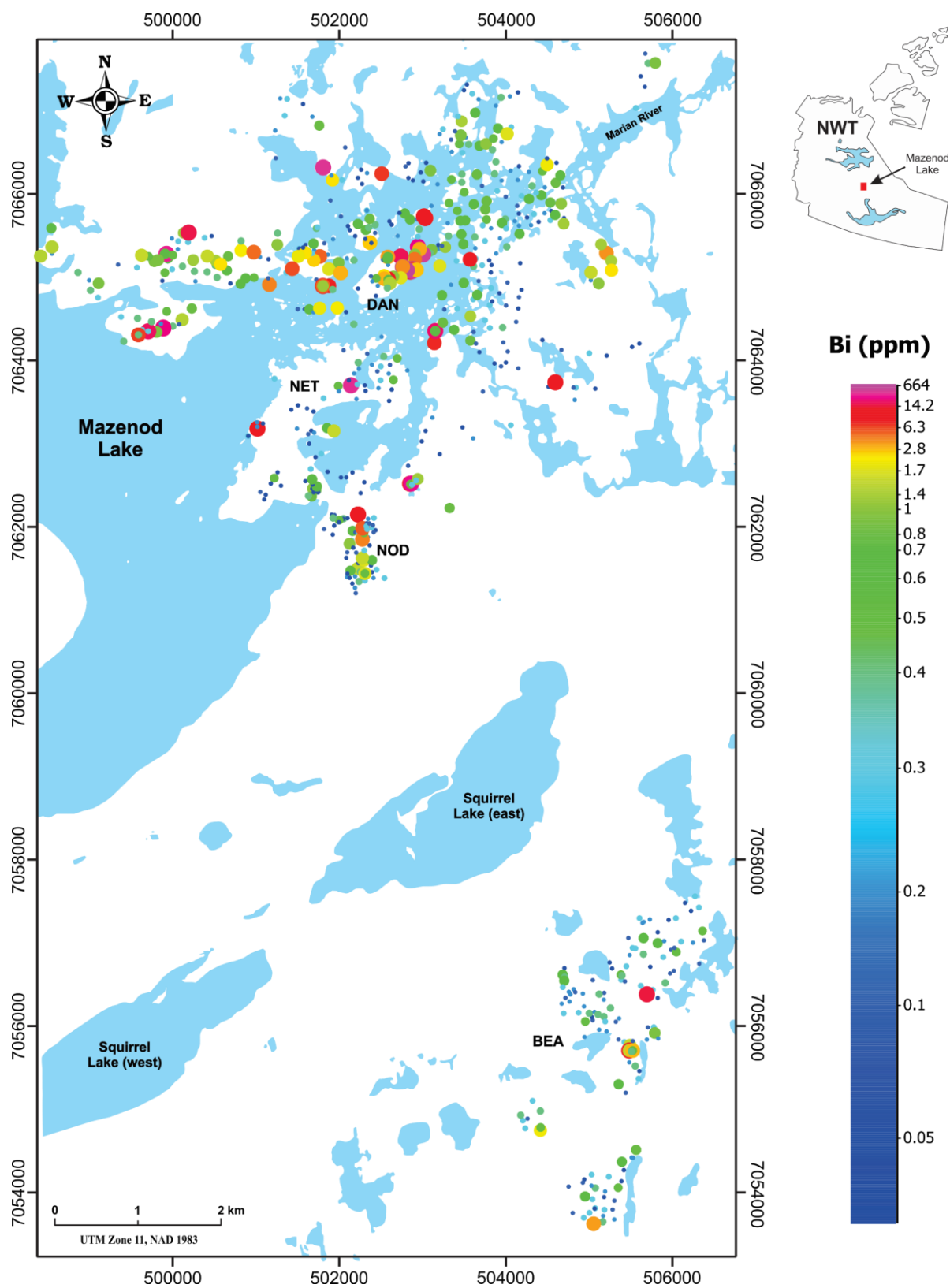


Fig. 66. Distribution of bismuth concentrations in the Mazenod Lake region.

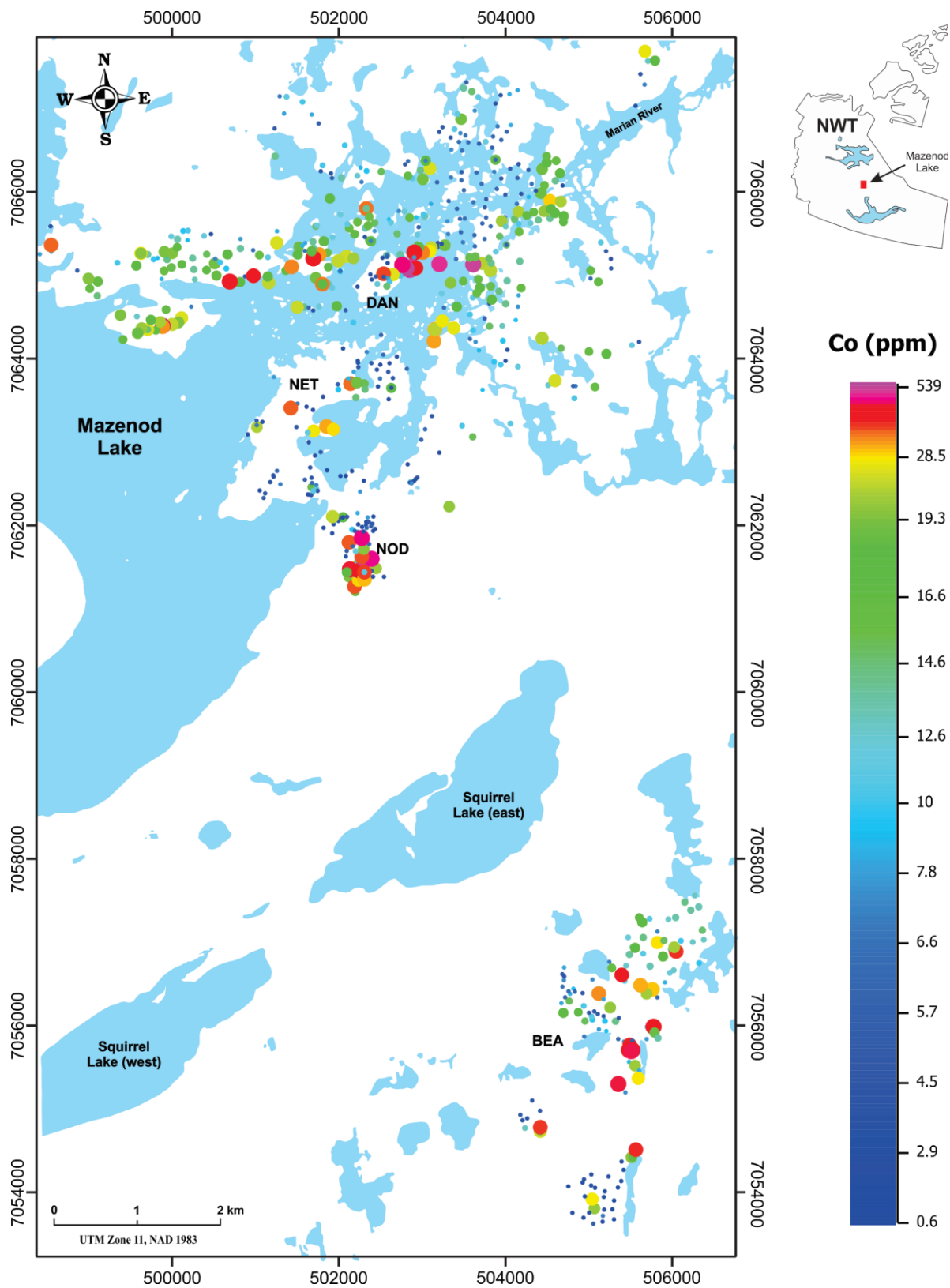


Fig. 67. Distribution of cobalt concentrations in the Mazenod Lake region.

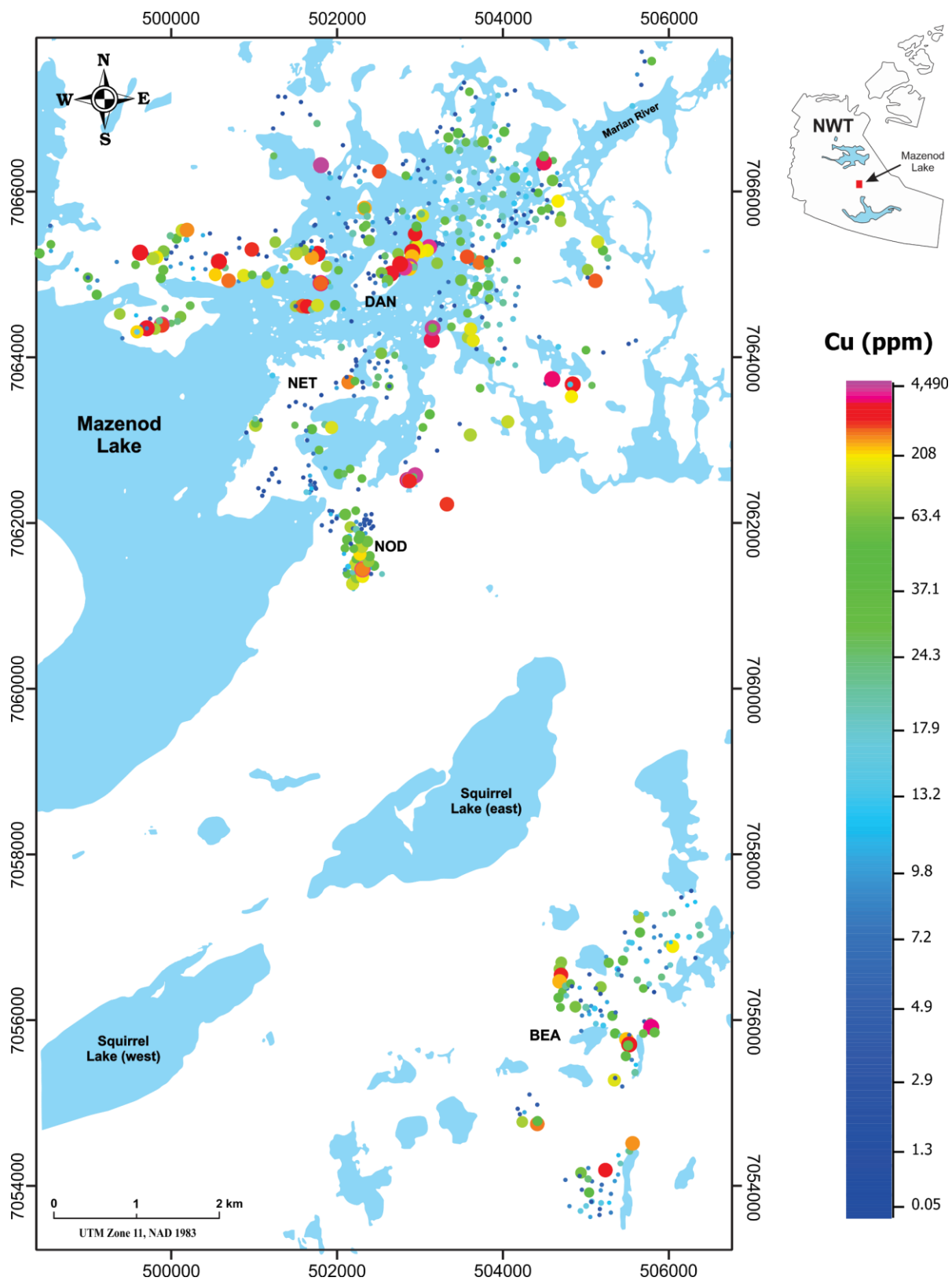


Fig. 68. Distribution of copper concentrations in the Mazenod Lake region.

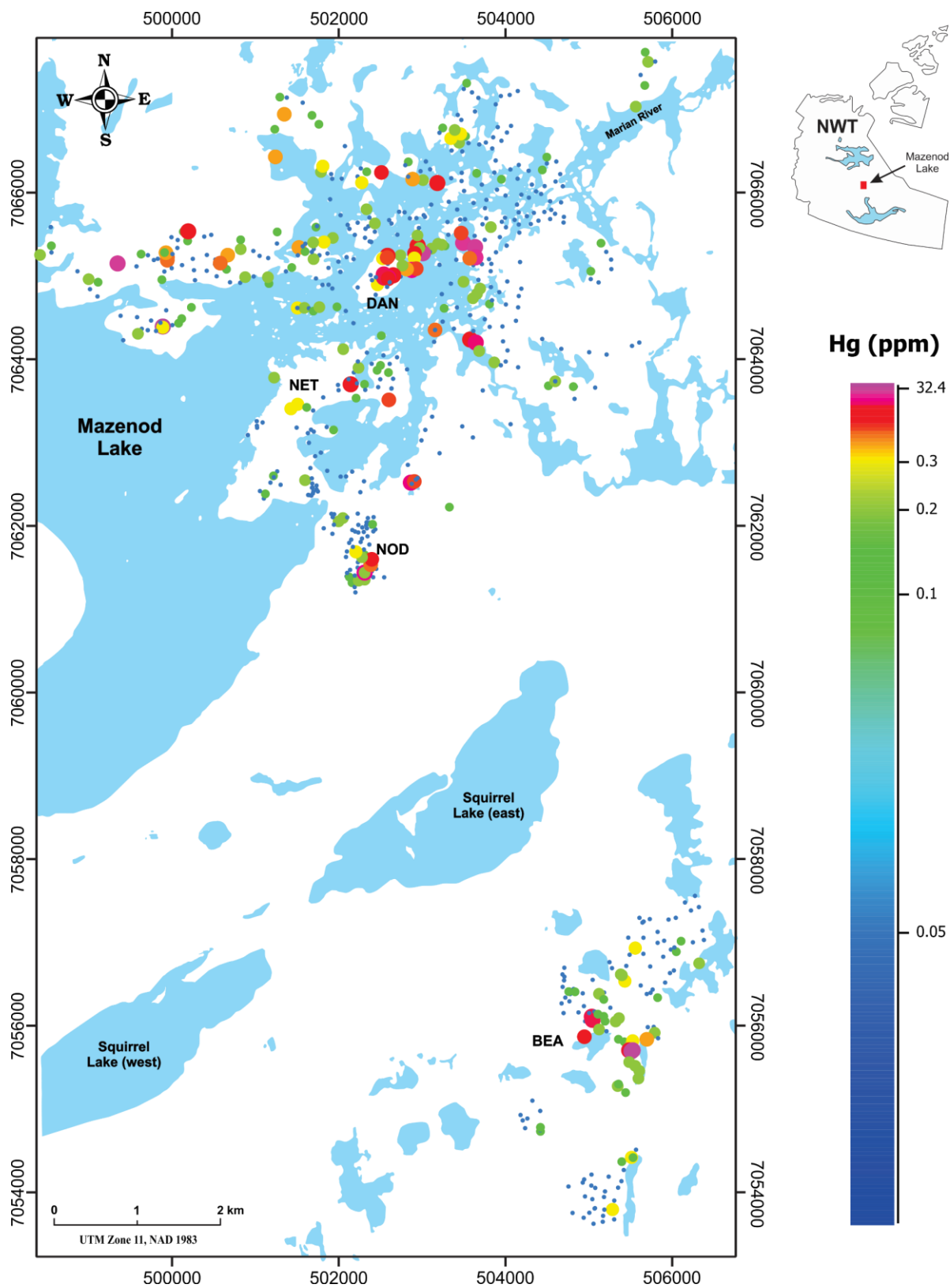


Fig. 69. Distribution of mercury concentrations in the Mazenod Lake region.

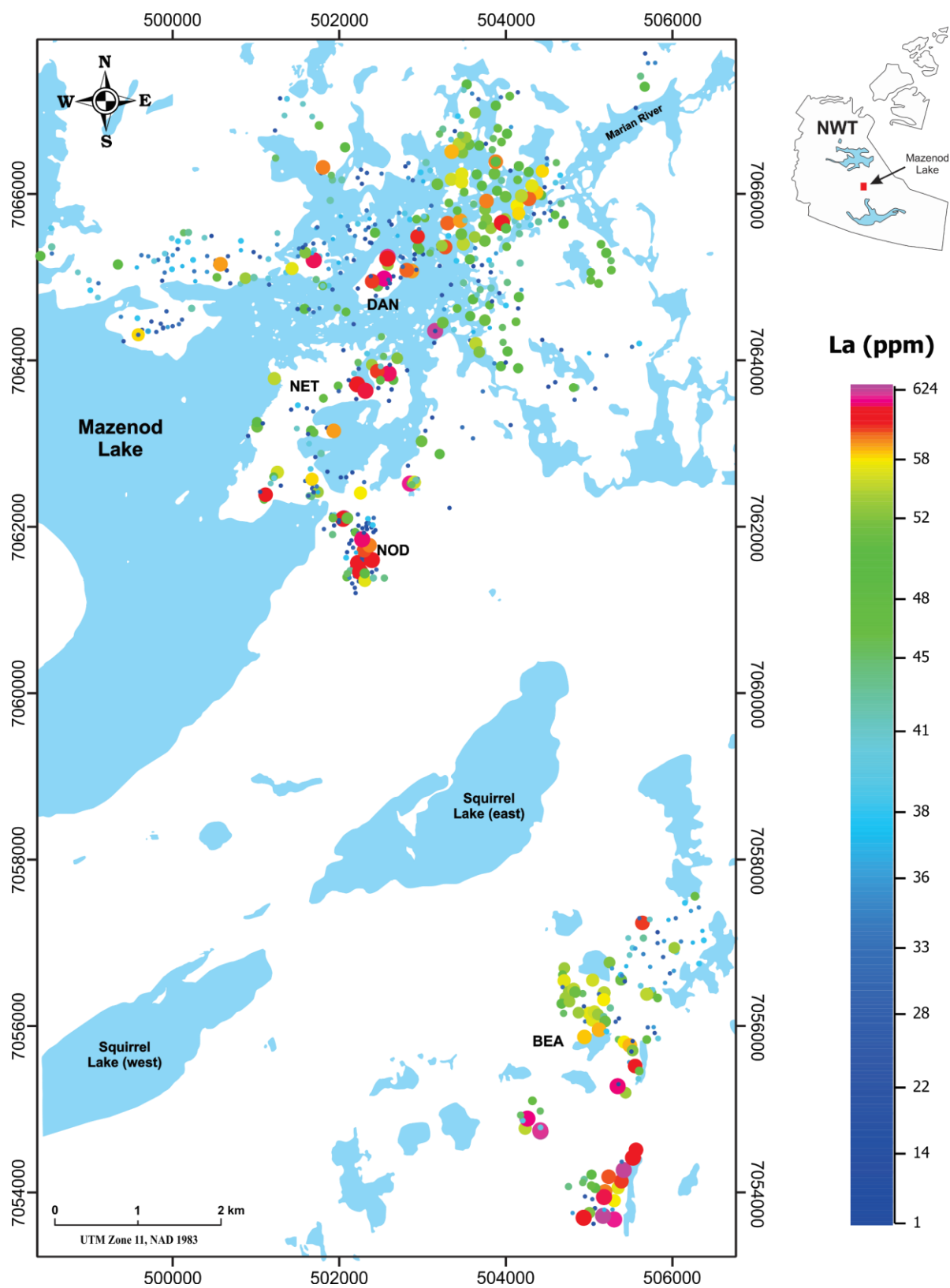


Fig. 70. Distribution of lanthanum concentrations in the Mazenod Lake region.

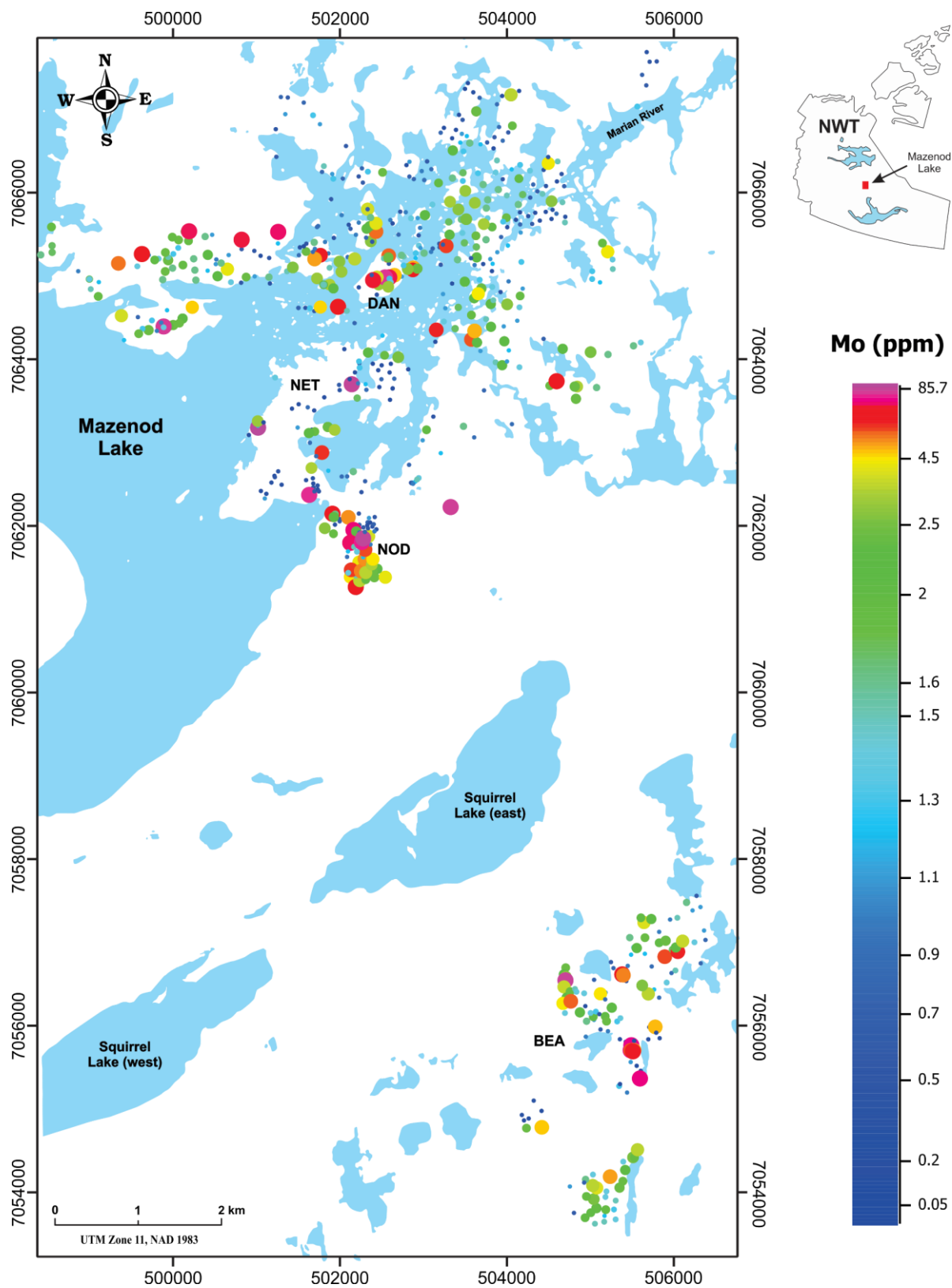


Fig. 71. Distribution of molybdenum concentrations in the Mazenod Lake region.

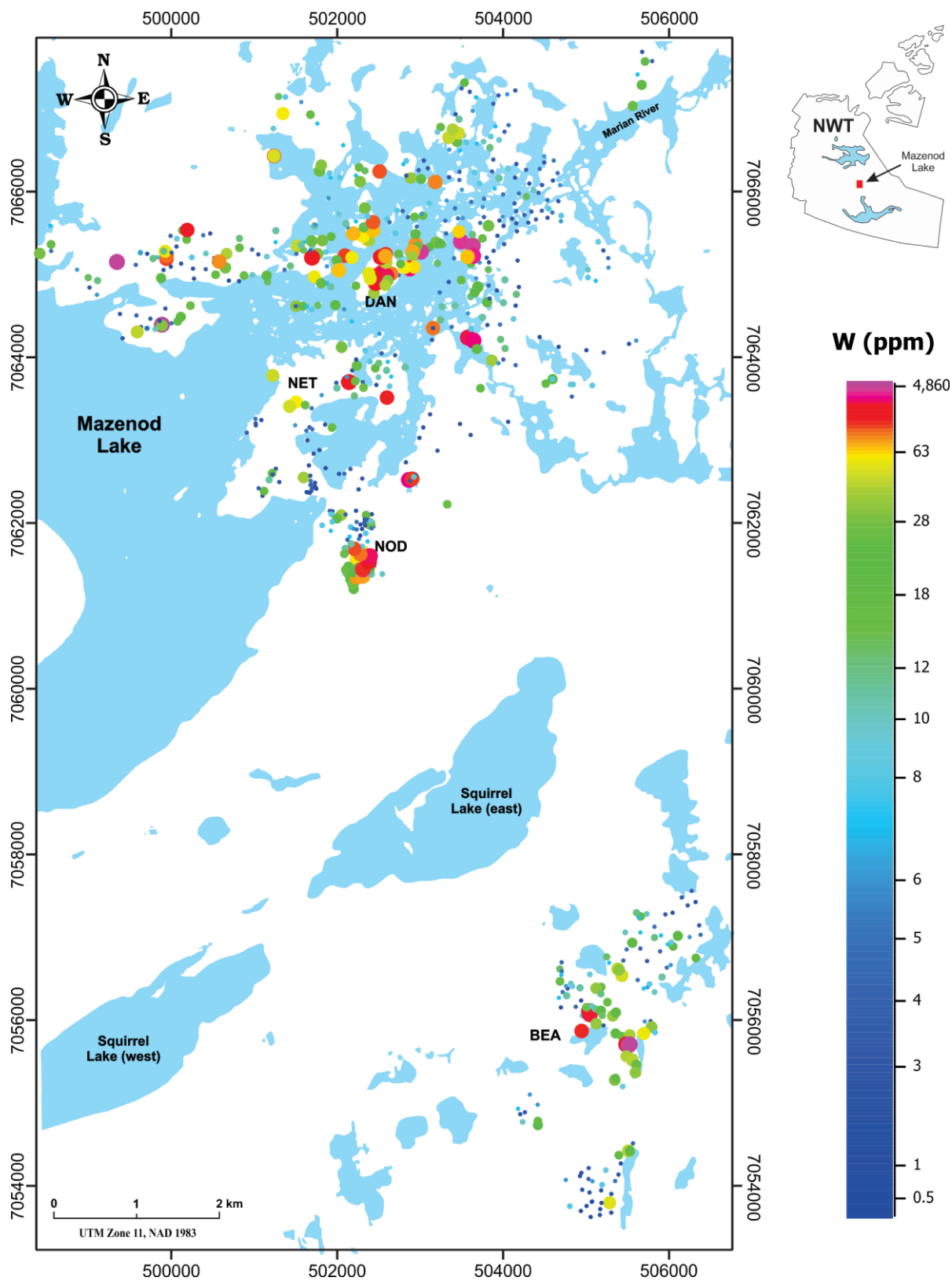


Fig. 72. Distribution of tungsten concentrations in the Mazenod Lake region.

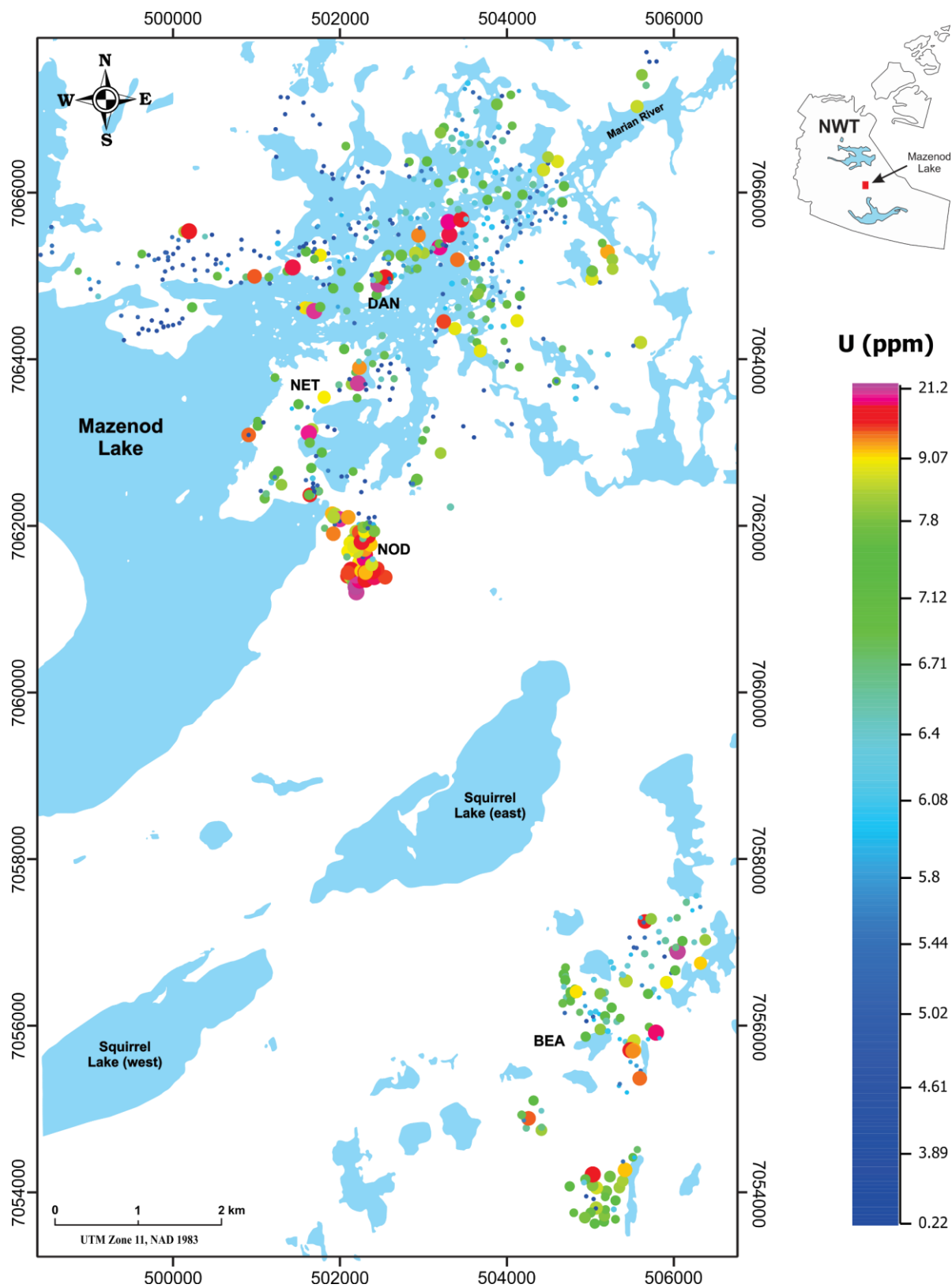


Fig. 73. Distribution of uranium concentrations in the Mazenod Lake region.

Appendix V: Mass Balance Data

TABLE 11. Results of Mass-Balance Calculations

Average Least Altered Andesite		96217		96222		96227	
Elements	Least altered C_i^0	Altered C_i	% Gain or Loss $\Delta C_i\%$	Altered C_i	% Gain or Loss $\Delta C_i\%$	Altered C_i	% Gain or Loss $\Delta C_i\%$
Au (ppb)	2.67	77	3135.24%	147	5990.59%	29	1852.85%
Ag (ppm)	0.05	0.4	797.46%	0.05	10.63%	0.2	619.19%
As	8.17	698	9484.31%	1430	19262.76%	219	4719.52%
Ba	767.67	1210	76.82%	1570	126.24%	645	51.07%
Be	2	1.6	-10.25%	1.7	-5.97%	1.5	34.85%
Bi	0.32	172	60198.42%	113	38964.45%	664	372978.44%
Cd	0.15	0.2	49.58%	0.2	47.50%	0.1	19.86%
Ce	70.67	48	-23.80%	114	78.45%	33	-16.04%
Co	14.53	395	2949.71%	480	3554.51%	143	1669.51%
Cr	90	135	68.27%	122	49.96%	58	15.87%
Cs	3.7	1.8	-45.42%	2.6	-22.26%	0.6	-70.84%
Cu	31.43	229	717.37%	216	660.26%	329	1782.06%
Dy	3.61	3.82	18.71%	2.68	-17.87%	9.59	377.63%
Er	1.94	2.64	52.66%	1.5	-14.47%	8.17	657.19%
Eu	1.23	1.32	20.39%	1.95	75.38%	1.34	95.88%
Ga	17.23	16	4.17%	19.4	24.56%	18.4	92.01%
Gd	4.21	3.33	-11.27%	4.58	20.35%	5.14	119.51%
Ge	1.37	1.1	-9.93%	1.3	4.97%	1.3	70.61%
Hf	4.67	5.2	24.91%	4.6	8.97%	2.4	-7.60%
Hg	0.05	0.4	797.46%	2	4325.00%	0.1	259.59%
Ho	0.87	1.04	34.10%	0.59	-24.98%	3.21	563.39%
La	38.67	24	-30.38%	61	74.51%	19	-11.66%
Lu	0.3	0.8	199.15%	0.3	10.63%	1.6	858.92%
Mo	1.7	0.8	-47.21%	7.7	401.07%	1	5.76%
Nb	7	7	12.18%	7	10.63%	3	-22.94%
Nd	27.8	18.8	-24.14%	41.5	65.14%	13.8	-10.75%
Ni	14.67	23	75.88%	35	163.93%	23	181.89%
Pb	12.46	8.85	-20.32%	12	6.54%	4.04	-41.70%
Pr	8.39	5.37	-28.20%	12.3	62.18%	3.94	-15.57%
Rb	178	279	75.84%	346	115.04%	123	24.24%
Sb	3.67	6	83.41%	6	80.86%	11	438.90%
Sc	12.33	12	9.18%	12	7.66%	27	293.72%
Se	1.17	0.5	-52.06%	1	-5.45%	0.5	-23.16%
Sm	4.84	3.92	-9.14%	6.41	46.51%	3.59	33.36%
Sn	3.72	11.1	234.74%	4.1	21.93%	9.3	349.49%
Sr	184.33	61	-62.88%	51	-69.39%	24	-76.59%
Ta	1.42	1.09	-13.89%	1.11	-13.53%	0.61	-22.76%
Tb	0.65	0.6	3.55%	0.59	0.41%	1.18	226.40%
Te	0.05	0.05	12.18%	0.5	1006.25%	0.2	619.19%
Th	17.97	18.1	12.99%	16.4	0.96%	7.3	-26.96%
Tl	0.01	0.005	-43.91%	0.005	-44.69%	0.005	-10.10%
Tm	0.35	0.58	85.90%	0.26	-17.82%	1.58	711.65%
U	6.02	6.64	23.74%	5.82	6.95%	3.35	0.05%
V	88.33	89	13.03%	82	2.70%	83	68.95%
W	11	48	389.53%	216	2072.27%	12	96.14%
Y	21.53	26.3	37.04%	14	-28.07%	93	676.64%
Yb	2.07	4.3	133.04%	1.85	-1.13%	9.97	765.98%
Zn	66.33	15	-74.63%	36	-39.96%	36	-2.42%
Zr	161.33	161	11.95%	143	-1.94%	74	-17.53%
Al ₂ O ₃ (wt.%)	15.93	14.2	0.00%	14.4	0.00%	8.86	0.00%
CaO	3.74	1.26	-62.21%	0.54	-84.03%	7.03	237.96%
Fe ₂ O ₃	5.85	7.73	48.24%	10.5	98.56%	25.6	686.80%
MgO	2.13	2	5.34%	2.07	7.51%	5.87	395.50%
MnO	0.14	0.07	-43.91%	0.07	-44.69%	0.28	259.59%
P ₂ O ₅	0.11	0.08	-18.41%	0.09	-9.49%	0.005	-91.83%
K ₂ O	4.21	9.61	156.08%	9.54	150.68%	4.64	98.16%
Na ₂ O	3.13	1.27	-54.48%	1.43	-49.46%	0.09	-94.83%
TiO ₂	0.61	0.54	-0.69%	0.55	-0.26%	0.28	-17.47%
SiO ₂	61.67	60.3	9.69%	57.1	2.43%	34.6	0.88%
LOI	2.67	2.8	17.65%	3.7	53.30%	12.7	755.21%

Mass change

12.18%

10.63%

79.80%

Average Least Altered Andesite		96238		96240		96260	
Elements	Least altered C_i^0	Altered C_i	% Gain or Loss $\Delta C_i\%$	Altered C_i	% Gain or Loss $\Delta C_i\%$	Altered C_i	% Gain or Loss $\Delta C_i\%$
Au (ppb)	2.67	13	450.08%	6	132.45%	1	-63.84%
Ag (ppm)	0.05	0.05	12.98%	0.9	1761.95%	0.05	-3.45%
As	8.17	12.6	74.24%	19.4	145.63%	6.1	-27.92%
Ba	767.67	2720	300.30%	3000	304.24%	1100	38.34%
Be	2	1.1	-37.86%	1.1	-43.11%	1.6	-22.76%
Bi	0.32	2.9	923.87%	0.6	93.95%	0.05	-84.91%
Cd	0.15	0.3	125.96%	0.2	37.92%	0.2	28.73%
Ce	70.67	194	210.14%	40	-41.45%	47	-35.79%
Co	14.53	4.6	-64.23%	7.7	-45.18%	15.8	4.98%
Cr	90	123	54.40%	164	88.49%	86	-7.75%
Cs	3.7	1.7	-48.09%	1.4	-60.86%	2.6	-32.16%
Cu	31.43	3.6	-87.06%	15.8	-48.00%	0.05	-99.85%
Dy	3.61	3.48	8.91%	1.83	-47.56%	3.66	-2.12%
Er	1.94	1.82	5.99%	0.95	-49.35%	1.87	-6.94%
Eu	1.23	3.24	197.60%	1.82	53.06%	1.29	1.25%
Ga	17.23	17.4	14.09%	13.5	-18.95%	17.4	-2.50%
Gd	4.21	9.1	144.21%	2.34	-42.51%	4.38	0.44%
Ge	1.37	1	-17.53%	1.2	-9.39%	1.5	5.71%
Hf	4.67	5.7	37.90%	5.3	17.40%	5.3	9.57%
Hg	0.05	1.2	2611.49%	0.7	1348.18%	0.05	-3.45%
Ho	0.87	0.75	-2.60%	0.44	-47.68%	0.85	-5.67%
La	38.67	107	212.61%	22	-41.15%	22	-45.07%
Lu	0.3	0.3	12.98%	0.2	-31.04%	0.3	-3.45%
Mo	1.7	44.5	2857.38%	1.3	-20.90%	0.7	-60.25%
Nb	7	8	29.12%	8	18.22%	8	10.34%
Nd	27.8	75	204.80%	15	-44.19%	20.7	-28.11%
Ni	14.67	0.5	-96.15%	3	-78.85%	23	51.37%
Pb	12.46	8.79	-20.30%	12.2	1.28%	3.87	-70.01%
Pr	8.39	23.5	216.45%	4.38	-46.00%	5.82	-33.03%
Rb	178	350	122.15%	366	112.69%	189	2.51%
Sb	3.67	10	207.84%	11	210.04%	3	-21.08%
Sc	12.33	5	-54.19%	7	-41.27%	13	1.79%
Se	1.17	2	93.13%	1	-11.59%	1	-17.48%
Sm	4.84	12.8	198.79%	2.66	-43.15%	4.44	-11.43%
Sn	3.72	3.5	6.30%	10.8	200.31%	2.8	-27.33%
Sr	184.33	116	-28.90%	67	-62.40%	54	-71.72%
Ta	1.42	1.76	40.03%	1.34	-2.39%	1.24	-15.69%
Tb	0.65	0.96	66.86%	0.35	-44.30%	0.7	3.97%
Te	0.05	0.1	125.96%	0.05	3.44%	0.05	-3.45%
Th	17.97	22.9	43.97%	17.4	0.16%	15.5	-16.72%
Tl	0.01	0.005	-43.51%	0.005	-48.28%	0.005	-51.73%
Tm	0.35	0.29	-6.39%	0.16	-52.71%	0.29	-20.01%
U	6.02	10.8	102.69%	3.81	-34.53%	4.98	-20.13%
V	88.33	33	-57.79%	80	-6.31%	92	0.56%
W	11	244	2406.07%	194	1724.33%	6	-47.34%
Y	21.53	17.5	-8.17%	11	-47.15%	22.5	0.90%
Yb	2.07	1.84	0.43%	1	-50.03%	1.88	-12.32%
Zn	66.33	0.5	-99.15%	6	-90.64%	33	-51.97%
Zr	161.33	186	30.26%	188	20.54%	184	10.11%
Al ₂ O ₃ (wt.%)	15.93	14.1	0.00%	15.4	0.00%	16.5	0.00%
CaO	3.74	0.1	-96.98%	0.22	-93.92%	0.34	-91.22%
Fe ₂ O ₃	5.85	2.82	-45.54%	4.25	-24.85%	5.81	-4.11%
MgO	2.13	0.18	-90.45%	0.25	-87.86%	2.24	1.53%
MnO	0.14	0.005	-95.97%	0.01	-92.61%	0.07	-51.73%
P ₂ O ₅	0.11	0.08	-17.83%	0.12	12.85%	0.14	22.88%
K ₂ O	4.21	11.4	205.93%	12.8	214.50%	8.58	96.76%
Na ₂ O	3.13	0.13	-95.31%	0.22	-92.73%	0.35	-89.20%
TiO ₂	0.61	0.36	-33.32%	0.61	3.44%	0.63	-0.29%
SiO ₂	61.67	70	28.24%	65.1	9.19%	62.6	-2.00%
LOI	2.67	0.6	-74.61%	0.8	-69.01%	2.7	-2.37%

Mass change

12.98%

3.44%

-3.45%

Average Least Altered Andesite							
				96386		96405	
						96427	
Elements	Least altered C _i ⁰	Altered C _i	% Gain or Loss ΔC _i %	Altered C _i	% Gain or Loss ΔC _i %	Altered C _i	% Gain or Loss ΔC _i %
Au (ppb)	2.67	1	-63.40%	1	-59.41%	1	-59.69%
Ag (ppm)	0.05	0.05	-2.27%	0.05	8.37%	0.05	7.64%
As	8.17	4.7	-43.78%	4	-46.94%	3.8	-49.94%
Ba	767.67	1010	28.58%	407	-42.55%	521	-26.95%
Be	2	2.2	7.50%	2.5	35.46%	2	7.64%
Bi	0.32	1.3	297.03%	0.2	-32.27%	0.4	34.54%
Cd	0.15	0.1	-34.85%	0.1	-27.76%	0.05	-64.12%
Ce	70.67	92	27.23%	33	-49.40%	74	12.71%
Co	14.53	16.7	12.33%	4.1	-69.42%	7.7	-42.96%
Cr	90	54	-41.36%	31	-62.67%	104	24.38%
Cs	3.7	1.7	-55.10%	6.8	99.16%	1.4	-59.27%
Cu	31.43	88.6	175.50%	1.6	-94.48%	1.4	-95.21%
Dy	3.61	5.27	42.67%	4.59	37.79%	3.17	-5.48%
Er	1.94	2.78	40.05%	2.61	45.79%	1.55	-14.00%
Eu	1.23	1.4	11.24%	0.92	-18.94%	1.1	-3.74%
Ga	17.23	15.4	-12.65%	16.8	5.66%	15.3	-4.42%
Gd	4.21	5.6	30.00%	3.88	-0.13%	3.91	-0.03%
Ge	1.37	1.2	-14.40%	1.8	42.38%	1.4	9.99%
Hf	4.67	5.6	17.19%	6.3	46.19%	3.8	-12.42%
Hg	0.05	0.05	-2.27%	0.2	333.47%	0.1	115.27%
Ho	0.87	1.26	41.54%	1.16	44.49%	0.71	-12.16%
La	38.67	49	23.84%	14	-60.77%	38	5.77%
Lu	0.3	0.4	30.31%	0.4	44.49%	0.3	7.64%
Mo	1.7	1.5	-13.77%	0.8	-49.00%	13.9	780.08%
Nb	7	12	67.54%	11	70.29%	7	7.64%
Nd	27.8	37.5	31.83%	18.1	-29.44%	28.5	10.35%
Ni	14.67	4	-73.35%	2	-85.23%	7	-48.64%
Pb	12.46	10.7	-16.07%	3.68	-67.99%	8.03	-30.63%
Pr	8.39	11.2	30.46%	4.84	-37.49%	8.73	12.00%
Rb	178	243	33.42%	268	63.16%	124	-25.02%
Sb	3.67	4	6.52%	5	47.64%	3	-12.01%
Sc	12.33	12	-4.89%	9	-20.90%	12	4.75%
Se	1.17	0.5	-58.24%	0.5	-53.69%	0.5	-54.00%
Sm	4.84	6.72	35.69%	3.88	-13.13%	4.89	8.75%
Sn	3.72	0.05	-98.69%	2.8	-18.43%	0.05	-98.55%
Sr	184.33	111	-41.15%	8	-95.30%	81	-52.70%
Ta	1.42	2.07	42.47%	1.44	9.89%	1.36	3.09%
Tb	0.65	0.88	32.31%	0.74	23.37%	0.59	-2.30%
Te	0.05	0.05	-2.27%	0.05	8.37%	0.05	7.64%
Th	17.97	20	8.77%	14.9	-10.15%	16.5	-1.17%
Tl	0.01	0.005	-51.13%	0.005	-45.82%	0.005	-46.18%
Tm	0.35	0.48	34.03%	0.45	39.33%	0.28	-13.89%
U	6.02	5.88	-4.54%	3.62	-34.84%	4.57	-18.29%
V	88.33	120	32.77%	10	-87.73%	83	1.14%
W	11	6	-46.69%	26	156.14%	12	17.42%
Y	21.53	30	36.18%	26.7	34.39%	17	-15.01%
Yb	2.07	2.77	30.78%	2.81	47.11%	1.72	-10.56%
Zn	66.33	36	-46.96%	16	-73.86%	46	-25.35%
Zr	161.33	217	31.45%	207	39.04%	135	-9.93%
Al ₂ O ₃ (wt.%)	15.93	16.3	0.00%	14.7	0.00%	14.8	0.00%
CaO	3.74	2.26	-40.94%	0.2	-94.20%	2.08	-40.14%
Fe ₂ O ₃	5.85	8.24	37.66%	6.2	14.85%	5.69	4.69%
MgO	2.13	1.48	-32.09%	0.76	-61.33%	1.63	-17.63%
MnO	0.14	0.1	-30.19%	0.02	-84.52%	0.12	-7.74%
P ₂ O ₅	0.11	0.2	77.69%	0.08	-21.19%	0.1	-2.15%
K ₂ O	4.21	6.74	56.46%	6.37	63.97%	3.82	-2.34%
Na ₂ O	3.13	2.76	-13.82%	0.1	-96.54%	2.82	-3.03%
TiO ₂	0.61	0.99	58.61%	0.37	-34.27%	0.6	5.87%
SiO ₂	61.67	58.5	-7.29%	68	19.49%	67.2	17.29%
LOI	2.67	1.8	-34.11%	2.4	-2.59%	1.3	-47.59%

Mass change

-2.27%

8.37%

7.64%

Average Least Altered Andesite				97005		97030		97041	
Elements	Least altered C _i ⁰	Altered C _i	% Gain or Loss ΔC _i %	Altered C _i	% Gain or Loss ΔC _i %	Altered C _i	% Gain or Loss ΔC _i %	Altered C _i	% Gain or Loss ΔC _i %
Au (ppb)	2.67	1	-66.48%	7	3063.94%	1	-60.22%		
Ag (ppm)	0.05	0.05	-10.51%	0.05	1106.82%	0.05	6.20%		
As	8.17	9.2	0.78%	10.2	1406.68%	1.9	-75.30%		
Ba	767.67	120	-86.01%	11	-82.71%	1110	53.56%		
Be	2	1.9	-14.98%	0.3	81.02%	1.7	-9.73%		
Bi	0.32	0.2	-44.07%	9.3	34973.15%	0.05	-83.41%		
Cd	0.15	0.1	-40.34%	0.3	2313.64%	0.05	-64.60%		
Ce	70.67	96	21.57%	8	36.61%	99	48.77%		
Co	14.53	4.6	-71.67%	21.5	1685.73%	6.9	-49.57%		
Cr	90	143	42.20%	205	2648.86%	155	82.90%		
Cs	3.7	0.2	-95.16%	0.05	-83.69%	0.5	-85.65%		
Cu	31.43	1.9	-94.59%	101	3778.10%	0.5	-98.31%		
Dy	3.61	4.31	6.85%	0.85	184.15%	3.16	-7.04%		
Er	1.94	2.27	4.72%	0.45	179.93%	1.69	-7.49%		
Eu	1.23	1.24	-9.78%	0.07	-31.32%	1.06	-8.48%		
Ga	17.23	18.3	-4.95%	2.2	54.09%	15.6	-3.85%		
Gd	4.21	5.2	10.54%	0.7	100.66%	3.7	-6.67%		
Ge	1.37	1.2	-21.61%	0.7	516.62%	0.9	-30.23%		
Hf	4.67	6.2	18.81%	0.6	55.05%	5.5	25.07%		
Hg	0.05	0.05	-10.51%	0.05	1106.82%	0.05	6.20%		
Ho	0.87	0.98	0.81%	0.2	177.43%	0.69	-15.77%		
La	38.67	53	22.66%	4	24.83%	50	37.32%		
Lu	0.3	0.3	-10.51%	0.1	302.27%	0.3	6.20%		
Mo	1.7	0.5	-73.68%	85.7	60737.83%	0.3	-81.26%		
Nb	7	10	27.85%	2	244.81%	10	51.71%		
Nd	27.8	36.8	18.47%	2.6	12.87%	32.4	23.77%		
Ni	14.67	14	-14.59%	6	393.59%	14	1.35%		
Pb	12.46	4.62	-66.82%	49.1	4655.60%	4.12	-64.88%		
Pr	8.39	10.7	14.13%	0.89	28.02%	10.5	32.91%		
Rb	178	24.2	-87.83%	10.2	-30.85%	182	8.59%		
Sb	3.67	4	-2.46%	2	557.67%	1	-71.06%		
Sc	12.33	15	8.87%	1	-2.12%	5	-56.93%		
Se	1.17	1	-23.51%	0.5	415.73%	0.5	-54.62%		
Sm	4.84	6.53	20.74%	0.52	29.66%	4.85	6.42%		
Sn	3.72	13.2	217.56%	5.4	1651.83%	9.5	171.21%		
Sr	184.33	108	-47.56%	5	-67.26%	70	-59.67%		
Ta	1.42	1.42	-10.51%	0.42	256.95%	1.76	31.63%		
Tb	0.65	0.82	12.90%	0.14	159.93%	0.58	-5.24%		
Te	0.05	0.05	-10.51%	0.05	1106.82%	0.05	6.20%		
Th	17.97	16.7	-16.83%	3.96	165.94%	25.4	50.11%		
Tl	0.01	0.005	-55.25%	0.005	503.41%	0.005	-46.90%		
Tm	0.35	0.35	-10.51%	0.08	175.84%	0.3	-8.97%		
U	6.02	6.98	3.77%	3.93	687.84%	8.21	44.83%		
V	88.33	94	-4.76%	6	-18.02%	33	-60.32%		
W	11	0.5	-95.93%	1	9.71%	4	-61.38%		
Y	21.53	23.1	-3.98%	5.69	218.94%	17.8	-12.20%		
Yb	2.07	2.28	-1.43%	0.52	203.16%	2.04	4.66%		
Zn	66.33	19	-74.36%	99	1701.22%	55	-11.94%		
Zr	161.33	188	4.29%	13	-2.75%	154	1.37%		
Al ₂ O ₃ (wt.%)	15.93	17.8	0.00%	1.32	0.00%	15	0.00%		
CaO	3.74	3.29	-21.27%	0.04	-87.09%	0.28	-92.05%		
Fe ₂ O ₃	5.85	3.03	-53.65%	2.6	436.36%	3.12	-43.36%		
MgO	2.13	2.27	-4.62%	0.56	217.29%	1.19	-40.67%		
MnO	0.14	0.06	-61.65%	0.02	72.40%	0.07	-46.90%		
P ₂ O ₅	0.11	0.16	30.17%	0.005	-45.14%	0.04	-61.38%		
K ₂ O	4.21	0.68	-85.54%	0.005	-98.57%	6.4	61.44%		
Na ₂ O	3.13	8.61	146.18%	0.005	-98.07%	3.54	20.11%		
TiO ₂	0.61	0.71	4.17%	0.02	-60.43%	0.36	-37.32%		
SiO ₂	61.67	62.1	-9.88%	93.6	1731.66%	68.5	17.96%		
LOI	2.67	1	-66.48%	1.5	577.99%	1	-60.22%		

Mass change

-10.51%

1106.82%

6.20%

Average Least Altered Andesite		97063		97094		97095	
Elements	Least altered C_i^0	Altered C_i	% Gain or Loss $\Delta C_i\%$	Altered C_i	% Gain or Loss $\Delta C_i\%$	Altered C_i	% Gain or Loss $\Delta C_i\%$
Au (ppb)	2.67	29	36713.29%	38	1554.88%	1	-62.24%
Ag (ppm)	0.05	0.05	3289.36%	0.4	830.22%	0.05	0.82%
As	8.17	685	284075.37%	34.2	386.74%	5.8	-28.42%
Ba	767.67	534	2257.68%	70	-89.40%	77	-89.89%
Be	2	2.1	3458.83%	2.2	27.91%	1.8	-9.26%
Bi	0.32	42.3	447931.25%	31.7	11418.73%	0.3	-5.48%
Cd	0.15	0.1	2159.57%	0.1	-22.48%	0.05	-66.39%
Ce	70.67	25	1099.01%	118	94.15%	96	36.96%
Co	14.53	39.3	9067.37%	11.7	-6.37%	3.3	-77.10%
Cr	90	197	7318.94%	144	86.04%	144	61.32%
Cs	3.7	0.05	-54.20%	0.3	-90.57%	0.1	-97.28%
Cu	31.43	265	28477.18%	4490	16511.05%	201	544.78%
Dy	3.61	0.92	763.77%	4.98	60.40%	3.7	3.34%
Er	1.94	0.46	703.66%	2.5	49.84%	1.94	0.82%
Eu	1.23	0.36	892.01%	1.52	43.69%	0.86	-29.51%
Ga	17.23	3.9	667.18%	14.7	-0.80%	15.9	-6.96%
Gd	4.21	0.94	656.77%	6.26	72.90%	4.48	7.29%
Ge	1.37	2.1	5095.37%	1.3	10.34%	1.1	-19.05%
Hf	4.67	0.3	117.73%	5.4	34.45%	6.5	40.33%
Hg	0.05	0.9	60908.51%	1.8	4085.99%	0.05	0.82%
Ho	0.87	0.22	757.08%	1.09	45.68%	0.86	-0.34%
La	38.67	20	1652.97%	47	41.32%	44	14.72%
Lu	0.3	0.1	1029.79%	0.4	55.04%	0.4	34.43%
Mo	1.7	60.6	120720.78%	1.1	-24.76%	0.8	-52.55%
Nb	7	0.5	142.10%	9	49.50%	10	44.03%
Nd	27.8	4.4	436.45%	46	92.40%	34	23.31%
Ni	14.67	39	8910.57%	10	-20.74%	5	-65.64%
Pb	12.46	22.9	6129.24%	5.17	-51.75%	2.45	-80.18%
Pr	8.39	1.66	570.60%	14.2	96.80%	10.5	26.18%
Rb	178	3.4	-35.26%	14.3	-90.66%	9.3	-94.73%
Sb	3.67	12	10982.38%	4	26.73%	2	-45.06%
Sc	12.33	1	174.89%	6	-43.42%	7	-42.76%
Se	1.17	0.5	1348.45%	1	-0.62%	0.5	-56.91%
Sm	4.84	0.7	390.20%	7.84	88.35%	5.51	14.78%
Sn	3.72	7.1	6368.94%	11.2	250.08%	8.8	138.51%
Sr	184.33	26	378.07%	25	-84.23%	21	-88.51%
Ta	1.42	0.03	-28.39%	1.36	11.36%	1.41	0.11%
Tb	0.65	0.15	682.16%	0.97	73.52%	0.68	5.48%
Te	0.05	3.7	250712.77%	0.2	365.11%	0.05	0.82%
Th	17.97	0.44	-17.01%	17.5	13.24%	17.9	0.43%
Tl	0.01	0.005	1594.68%	0.005	-41.86%	0.005	-49.59%
Tm	0.35	0.08	674.71%	0.44	46.18%	0.35	0.82%
U	6.02	8.04	4426.66%	6.3	21.69%	6.54	9.53%
V	88.33	138	5195.28%	32	-57.88%	26	-70.32%
W	11	152	46734.82%	296	3028.92%	6	-45.01%
Y	21.53	4.81	657.21%	26.5	43.12%	21.2	-0.72%
Yb	2.07	0.54	784.18%	2.64	48.30%	2.36	14.95%
Zn	66.33	23	1075.26%	8	-85.98%	0.5	-99.24%
Zr	161.33	15	215.13%	159	14.60%	189	18.12%
Al ₂ O ₃ (wt.%)	15.93	0.47	0.00%	13.7	0.00%	15.8	0.00%
CaO	3.74	0.09	-18.44%	1.26	-60.83%	0.9	-75.74%
Fe ₂ O ₃	5.85	56.2	32461.05%	5.04	0.18%	2.22	-61.74%
MgO	2.13	0.11	75.04%	1.15	-37.22%	0.54	-74.44%
MnO	0.14	0.02	384.19%	0.04	-66.78%	0.02	-85.60%
P ₂ O ₅	0.11	0.005	54.06%	0.14	47.99%	0.07	-35.84%
K ₂ O	4.21	0.13	4.66%	0.59	-83.70%	0.43	-89.70%
Na ₂ O	3.13	0.005	-94.59%	7.33	172.30%	8.98	189.26%
TiO ₂	0.61	0.06	233.38%	0.38	-27.56%	0.43	-28.93%
SiO ₂	61.67	42.3	2224.79%	68.9	29.91%	70	14.44%
LOI	2.67	0.6	661.65%	1.6	-30.32%	0.4	-84.90%

Mass change

3289.36%

16.28%

0.82%

Average Least Altered Andesite				97099				97249				97254			
Elements	Least altered C_i^0		Altered C_i	% Gain or Loss $\Delta C_i\%$		Altered C_i	% Gain or Loss $\Delta C_i\%$		Altered C_i	% Gain or Loss $\Delta C_i\%$		Altered C_i	% Gain or Loss $\Delta C_i\%$		
Au (ppb)	2.67		28	906.36%		13	470.31%		2	-1.38%					
Ag (ppm)	0.05		0.05	-4.04%		0.8	1774.12%		0.05	31.65%					
As	8.17		16.7	96.16%		10.7	53.40%		20.2	225.51%					
Ba	767.67		69	-91.37%		421	-35.76%		19	-96.74%					
Be	2		2.7	29.55%		2.6	52.27%		0.4	-73.67%					
Bi	0.32		1.2	259.86%		0.9	229.43%		8.6	3438.17%					
Cd	0.15		0.05	-68.01%		0.1	-21.91%		0.05	-56.12%					
Ce	70.67		66	-10.38%		43	-28.73%		4	-92.55%					
Co	14.53		4.8	-68.30%		18.8	51.55%		94.1	752.62%					
Cr	90		137	46.08%		126	63.99%		136	98.94%					
Cs	3.7		0.2	-94.81%		2.8	-11.36%		0.2	-92.88%					
Cu	31.43		1810	5426.39%		974	3529.87%		4.1	-82.83%					
Dy	3.61		4.12	9.52%		2.3	-25.37%		3.79	38.22%					
Er	1.94		2.19	8.33%		1.4	-15.47%		1.68	14.01%					
Eu	1.23		0.87	-32.12%		0.93	-11.44%		0.46	-50.76%					
Ga	17.23		16.8	-6.43%		13	-11.62%		33.6	156.73%					
Gd	4.21		4.53	3.26%		2.44	-32.11%		2.32	-27.45%					
Ge	1.37		1.3	-8.94%		1	-14.50%		1.2	15.32%					
Hf	4.67		5.7	17.13%		5.7	42.97%		3.1	-12.61%					
Hg	0.05		0.05	-4.04%		0.2	368.53%		0.3	689.92%					
Ho	0.87		0.98	8.10%		0.53	-28.64%		0.8	21.06%					
La	38.67		23	-42.92%		22	-33.36%		1	-96.60%					
Lu	0.3		0.4	27.95%		0.2	-21.91%		0.2	-12.23%					
Mo	1.7		1.4	-20.97%		0.05	-96.55%		29.6	2192.31%					
Nb	7		9	23.38%		10	67.33%		1	-81.19%					
Nd	27.8		31	7.01%		17.5	-26.27%		2.5	-88.16%					
Ni	14.67		16	4.66%		18	43.72%		72	546.15%					
Pb	12.46		3.16	-75.66%		7.98	-24.98%		8.03	-15.15%					
Pr	8.39		8.88	1.57%		4.97	-30.61%		0.53	-91.68%					
Rb	178		11.5	-93.80%		290	90.83%		4.2	-96.89%					
Sb	3.67		1	-73.85%		2	-36.17%		2	-28.25%					
Sc	12.33		13	1.18%		9	-14.50%		19	102.87%					
Se	1.17		1	-17.98%		0.5	-49.94%		0.5	-43.74%					
Sm	4.84		5.48	8.65%		2.87	-30.54%		1.21	-67.09%					
Sn	3.72		8.2	111.53%		11.2	252.66%		18.1	540.57%					
Sr	184.33		26	-86.46%		138	-12.31%		95	-32.15%					
Ta	1.42		1.33	-10.12%		1.91	57.55%		0.43	-60.13%					
Tb	0.65		0.73	7.77%		0.38	-31.52%		0.56	13.42%					
Te	0.05		0.05	-4.04%		0.1	134.26%		2.4	6219.34%					
Th	17.97		15.3	-18.29%		22.4	46.01%		5.31	-61.10%					
Tl	0.01		0.005	-52.02%		0.005	-41.43%		0.005	-34.17%					
Tm	0.35		0.38	4.19%		0.22	-26.37%		0.26	-2.20%					
U	6.02		5.87	-6.43%		11.7	127.65%		4.67	2.13%					
V	88.33		58	-36.99%		46	-39.00%		91	35.63%					
W	11		3	-73.83%		32	240.75%		39	366.77%					
Y	21.53		22.8	1.62%		13.3	-27.64%		20.7	26.58%					
Yb	2.07		2.48	14.97%		1.52	-13.99%		1.53	-2.69%					
Zn	66.33		4	-94.21%		3	-94.70%		4	-92.06%					
Zr	161.33		167	-0.66%		180	30.69%		110	-10.23%					
Al ₂ O ₃ (wt.%)	15.93		16.6	0.00%		13.6	0.00%		12.1	0.00%					
CaO	3.74		1.38	-64.59%		3.54	10.87%		2.13	-25.02%					
Fe ₂ O ₃	5.85		3.91	-35.86%		4.46	-10.70%		17.9	302.84%					
MgO	2.13		1.38	-37.83%		1.25	-31.26%		3.38	108.91%					
MnO	0.14		0.03	-79.44%		0.02	-83.27%		0.14	31.65%					
P ₂ O ₅	0.11		0.12	4.69%		0.13	38.43%		0.08	-4.25%					
K ₂ O	4.21		0.63	-85.64%		4.54	26.31%		0.14	-95.62%					
Na ₂ O	3.13		9.25	183.60%		2.43	-9.06%		1.02	-57.10%					
TiO ₂	0.61		0.5	-21.34%		0.59	13.29%		0.38	-17.99%					
SiO ₂	61.67		65.1	1.30%		66.4	26.12%		61	30.22%					
LOI	2.67		1.1	-60.46%		2.5	9.67%		3.5	72.58%					

Mass change

-4.04%

17.13%

31.65%

Average Least Altered Andesite				97266	98032	98172	
Elements	Least altered C_i^0	Altered C_i	% Gain or Loss $\Delta C_i\%$	Altered C_i	% Gain or Loss $\Delta C_i\%$	Altered C_i	% Gain or Loss $\Delta C_i\%$
Au (ppb)	2.67	1	-26.88%	1	389.04%	11	315.37%
Ag (ppm)	0.05	0.05	95.22%	0.1	2511.48%	0.2	303.29%
As	8.17	52.6	1156.87%	0.6	-4.11%	13.4	65.36%
Ba	767.67	11	-97.20%	29	-50.67%	798	4.81%
Be	2	0.5	-51.19%	0.2	30.57%	1.8	-9.26%
Bi	0.32	0.7	327.05%	0.2	716.09%	0.9	183.56%
Cd	0.15	0.2	160.29%	0.05	335.25%	0.2	34.43%
Ce	70.67	3	-91.71%	2	-63.05%	67	-4.41%
Co	14.53	91.3	1126.68%	0.6	-46.08%	8.8	-38.94%
Cr	90	205	344.67%	254	3585.08%	115	28.83%
Cs	3.7	0.2	-89.45%	0.1	-64.71%	0.8	-78.20%
Cu	31.43	2.5	-84.47%	25.3	951.07%	150	381.18%
Dy	3.61	1.55	-16.18%	0.17	-38.51%	3.22	-10.07%
Er	1.94	0.9	-9.43%	0.1	-32.69%	1.67	-13.21%
Eu	1.23	0.22	-65.08%	0.04	-57.54%	1.16	-4.92%
Ga	17.23	18.3	107.34%	1.1	-16.64%	14.4	-15.74%
Gd	4.21	0.96	-55.48%	0.19	-41.07%	3.83	-8.28%
Ge	1.37	1.1	56.75%	0.3	185.93%	1.3	-4.33%
Hf	4.67	6.2	159.18%	0.3	-16.12%	4.6	-0.69%
Hg	0.05	0.1	290.44%	0.05	1205.74%	0.05	0.82%
Ho	0.87	0.37	-16.98%	0.04	-39.97%	0.78	-9.61%
La	38.67	1	-94.95%	1	-66.23%	33	-13.96%
Lu	0.3	0.2	30.15%	0	-100.00%	0.3	0.82%
Mo	1.7	0.05	-94.26%	0.05	-61.60%	1.4	-16.97%
Nb	7	10	178.89%	0.5	-6.73%	7	0.82%
Nd	27.8	2.1	-85.25%	0.8	-62.42%	25.4	-7.88%
Ni	14.67	33	339.15%	14	1146.10%	25	71.82%
Pb	12.46	4.96	-22.29%	0.654	-31.46%	29.5	138.71%
Pr	8.39	0.45	-89.53%	0.27	-57.98%	7.31	-12.16%
Rb	178	3.8	-95.83%	12.6	-7.57%	162	-8.24%
Sb	3.67	3	59.58%	1	255.79%	4	9.89%
Sc	12.33	12	90.00%	1	5.90%	12	-1.88%
Se	1.17	0.5	-16.57%	0.5	458.01%	0.5	-56.91%
Sm	4.84	0.65	-73.78%	0.21	-43.35%	4.34	-9.59%
Sn	3.72	17	792.14%	2.3	707.31%	12	225.23%
Sr	184.33	61	-35.40%	4	-71.67%	171	-6.47%
Ta	1.42	1.99	173.58%	0.12	10.34%	1.14	-19.06%
Tb	0.65	0.22	-33.93%	0.03	-39.74%	0.57	-11.59%
Te	0.05	1.8	6927.94%	0.1	2511.48%	0.05	0.82%
Th	17.97	12.4	34.71%	1.51	9.72%	15.7	-11.91%
Tl	0.01	0.005	-2.39%	0.005	552.87%	0.005	-49.59%
Tm	0.35	0.19	5.98%	0.02	-25.39%	0.28	-19.34%
U	6.02	5.52	79.01%	0.39	-15.41%	4.62	-22.62%
V	88.33	73	61.34%	3	-55.65%	89	1.59%
W	11	18	219.45%	0.5	-40.65%	7	-35.84%
Y	21.53	10.3	-6.61%	1.09	-33.89%	20.4	-4.47%
Yb	2.07	1.28	20.72%	0.13	-18.00%	1.77	-13.79%
Zn	66.33	11	-67.63%	2	-60.63%	80	21.60%
Zr	161.33	212	156.53%	12	-2.88%	154	-3.76%
Al ₂ O ₃ (wt.%)	15.93	8.16	0.00%	1.22	0.00%	15.8	0.00%
CaO	3.74	0.39	-79.64%	0.06	-79.05%	3.45	-7.00%
Fe ₂ O ₃	5.85	6.88	129.59%	0.48	7.14%	5.49	-5.38%
MgO	2.13	2.22	103.47%	0.08	-50.96%	1.5	-29.00%
MnO	0.14	0.005	-93.03%	0.005	-53.37%	0.09	-35.19%
P ₂ O ₅	0.11	0.1	77.47%	0.005	-40.65%	0.11	0.82%
K ₂ O	4.21	0.11	-94.90%	0.52	61.28%	4.86	16.39%
Na ₂ O	3.13	0.66	-58.84%	0.08	-66.63%	3.38	8.88%
TiO ₂	0.61	0.58	85.62%	0.03	-35.78%	0.62	2.48%
SiO ₂	61.67	79	150.08%	96.5	1943.19%	63.3	3.49%
LOI	2.67	2.2	60.86%	0.4	95.62%	1.1	-58.46%

Mass change

95.22%

1205.74%

0.82%

Average Least Altered Andesite		98185		98207	
Elements	Least altered C_i^0	Altered C_i	% Gain or Loss $\Delta C_i\%$	Altered C_i	% Gain or Loss $\Delta C_i\%$
Au (ppb)	2.67	1	-61.51%	4	52.98%
Ag (ppm)	0.05	0.05	2.77%	0.3	512.69%
As	8.17	3.6	-54.71%	81.2	914.90%
Ba	767.67	486	-34.94%	762	1.36%
Be	2	3.6	84.99%	2.6	32.75%
Bi	0.32	15.6	4910.24%	1.4	346.75%
Cd	0.15	0.2	37.03%	0.2	36.15%
Ce	70.67	80	16.34%	79	14.15%
Co	14.53	10.4	-26.44%	9.2	-35.34%
Cr	90	108	23.33%	93	5.52%
Cs	3.7	1.5	-58.33%	2.6	-28.24%
Cu	31.43	262	756.72%	143	364.60%
Dy	3.61	4.76	35.51%	5.06	43.13%
Er	1.94	2.73	44.63%	2.8	47.38%
Eu	1.23	2.15	79.65%	1.19	-1.21%
Ga	17.23	15.6	-6.95%	16.4	-2.80%
Gd	4.21	5.1	24.50%	5.25	27.34%
Ge	1.37	1.6	20.03%	1.2	-10.56%
Hf	4.67	5.3	16.64%	5.9	29.01%
Hg	0.05	0.8	1544.39%	0.05	2.12%
Ho	0.87	1.16	37.03%	1.25	46.72%
La	38.67	43	14.28%	38	0.35%
Lu	0.3	0.5	71.29%	0.4	36.15%
Mo	1.7	15.2	818.92%	4.5	170.31%
Nb	7	7	2.77%	10	45.88%
Nd	27.8	30.1	11.28%	32.2	18.28%
Ni	14.67	23	61.13%	8	-44.31%
Pb	12.46	14.8	22.08%	17.9	46.70%
Pr	8.39	9.09	11.35%	8.93	8.69%
Rb	178	177	2.20%	201	15.31%
Sb	3.67	8	124.03%	7	94.77%
Sc	12.33	11	-8.31%	15	24.23%
Se	1.17	0.5	-56.08%	0.5	-56.36%
Sm	4.84	5.88	24.86%	5.9	24.48%
Sn	3.72	140	3767.85%	3.7	1.57%
Sr	184.33	167	-6.89%	141	-21.89%
Ta	1.42	1.25	-9.53%	1.54	10.74%
Tb	0.65	0.81	28.07%	0.81	27.25%
Te	0.05	0.1	105.55%	0.2	308.46%
Th	17.97	19.4	10.95%	18.4	4.56%
Tl	0.01	0.005	-48.61%	0.005	-48.94%
Tm	0.35	0.48	40.95%	0.47	37.13%
U	6.02	10.6	80.96%	5.21	-11.62%
V	88.33	72	-16.23%	19	-78.03%
W	11	113	955.77%	11	2.12%
Y	21.53	29.5	40.82%	31.1	47.51%
Yb	2.07	3.42	69.80%	2.93	44.54%
Zn	66.33	108	67.34%	17	-73.83%
Zr	161.33	175	11.48%	187	18.36%
Al ₂ O ₃ (wt.%)	15.93	15.5	0.00%	15.6	0.00%
CaO	3.74	2.71	-25.53%	3.49	-4.71%
Fe ₂ O ₃	5.85	5.22	-8.29%	3.08	-46.24%
MgO	2.13	2.15	3.74%	0.61	-70.76%
MnO	0.14	0.13	-4.57%	0.05	-63.53%
P ₂ O ₅	0.11	0.09	-15.91%	0.1	-7.17%
K ₂ O	4.21	2.96	-27.74%	5.24	27.10%
Na ₂ O	3.13	3.16	3.76%	1.77	-42.25%
TiO ₂	0.61	0.57	-3.97%	0.48	-19.65%
SiO ₂	61.67	65.3	8.82%	68.4	13.26%
LOI	2.67	2	-23.02%	1.6	-38.81%

Mass change

2.77%

2.12%

Least Altered Basaltic Andesite			98191	98271		
Elements	Least altered C _i ⁰	Altered C _i	% Gain or Loss ΔC _i %	Altered C _i	% Gain or Loss ΔC _i %	
Au (ppb)	1	1	-2.26%	1	6.79%	
Ag (ppm)	0.05	0.05	-2.26%	0.05	6.79%	
As	4.6	10.4	120.98%	10.2	136.80%	
Ba	248	1060	317.76%	188	-19.05%	
Be	2.1	2	-6.91%	2.1	6.79%	
Bi	0.3	1.6	421.28%	0.4	42.39%	
Cd	0.05	0.2	290.96%	0.1	113.58%	
Ce	43	70	59.11%	68	68.88%	
Co	20.9	15.1	-29.38%	13	-33.58%	
Cr	175	63	-64.81%	223	36.08%	
Cs	1.4	1.7	18.68%	0.3	-77.12%	
Cu	5	7	36.84%	1.3	-72.23%	
Dy	2.87	3.78	28.73%	3.22	19.81%	
Er	1.48	1.82	20.19%	1.63	17.61%	
Eu	0.94	1.6	66.37%	1.07	21.56%	
Ga	15.3	16.2	3.49%	17.8	24.24%	
Gd	3.19	4.32	32.36%	3.92	31.23%	
Ge	1.4	1.8	25.67%	1.9	44.93%	
Hf	3.1	3.8	19.81%	3.3	13.68%	
Hg	0.05	0.05	-2.26%	0.2	327.16%	
Ho	0.66	0.87	28.84%	0.75	21.35%	
La	21	34	58.25%	35	77.98%	
Lu	0.2	0.3	46.61%	0.2	6.79%	
Mo	1.3	2.3	72.92%	0.5	-58.93%	
Nb	5	5	-2.26%	4	-14.57%	
Nd	19.2	28.2	43.56%	27.9	55.18%	
Ni	39	17	-57.40%	25	-31.54%	
Pb	5.7	13.6	133.20%	16.6	211.00%	
Pr	5.13	7.94	51.28%	8.23	71.32%	
Rb	146	193	29.20%	43.5	-68.18%	
Sb	1	9	779.66%	7	647.53%	
Sc	23	20	-15.01%	22	2.15%	
Se	0.5	0.5	-2.26%	1	113.58%	
Sm	3.73	5.18	35.74%	4.79	37.14%	
Sn	6.3	4.4	-31.74%	20.9	254.27%	
Sr	203	318	53.11%	324	70.44%	
Ta	0.75	0.88	14.68%	0.64	-8.87%	
Tb	0.47	0.67	39.33%	0.62	40.87%	
Te	0.05	0.05	-2.26%	0.05	6.79%	
Th	9.48	11.7	20.63%	7.64	-13.94%	
Tl	0.005	0.005	-2.26%	0.005	6.79%	
Tm	0.24	0.29	18.10%	0.26	15.69%	
U	2.12	4.56	110.23%	4.12	107.54%	
V	127	159	22.37%	177	48.83%	
W	4	10	144.35%	19	407.25%	
Y	17.9	21.2	15.76%	16.8	0.23%	
Yb	1.53	1.88	20.10%	1.69	17.96%	
Zn	28	52	81.52%	16	-38.98%	
Zr	101	122	18.06%	92	-2.73%	
Al ₂ O ₃ (wt.%)	17.3	17.7	0.00%	16.2	0.00%	
CaO	7.45	8.21	7.71%	11.7	67.71%	
Fe ₂ O ₃	8.82	7.65	-15.23%	9.38	13.57%	
MgO	4.25	2.99	-31.24%	2.78	-30.15%	
MnO	0.1	0.21	105.25%	0.28	199.01%	
P ₂ O ₅	0.08	0.08	-2.26%	0.09	20.14%	
K ₂ O	2.3	4.5	91.23%	1.3	-39.64%	
Na ₂ O	2.82	2.55	-11.62%	0.74	-71.98%	
TiO ₂	0.68	0.75	7.80%	0.68	6.79%	
SiO ₂	54.2	53.8	-2.98%	54.7	7.78%	
LOI	1.6	1.5	-8.37%	2.3	53.51%	

Mass change

-2.26%

6.79%

Elements	Least Altered Dacite	96392		97227		97228	
	Least altered C _i ⁰	Altered C _i	% Gain or Loss ΔC _i %	Altered C _i	% Gain or Loss ΔC _i %	Altered C _i	% Gain or Loss ΔC _i %
Au (ppb)	1	13	1022.11%	1	1.23%	3	198.18%
Ag (ppm)	0.2	0.05	-78.42%	0.8	304.94%	0.3	49.09%
As	5.5	13.3	108.73%	9	65.66%	47.1	751.17%
Ba	867	2800	178.76%	2230	160.38%	3320	280.61%
Be	2.6	2.1	-30.28%	1.7	-33.81%	1.3	-50.30%
Bi	0.1	14.2	12156.84%	0.5	406.17%	0.4	297.58%
Cd	0.2	0.2	-13.68%	0.3	51.85%	0.2	-0.61%
Ce	106	108	-12.06%	74	-29.33%	63	-40.93%
Co	10.1	21.2	81.18%	19	90.44%	63.6	525.89%
Cr	73	46	-45.61%	115	59.48%	105	42.96%
Cs	2.4	2.6	-6.49%	1.3	-45.16%	1.2	-50.30%
Cu	18.2	36.5	73.11%	12.6	-29.91%	7.2	-60.68%
Dy	5.47	6.58	3.83%	3.6	-33.37%	2.57	-53.30%
Er	2.66	3.53	14.55%	1.95	-25.79%	1.56	-41.71%
Eu	1.76	1.86	-8.78%	1.45	-16.60%	1.32	-25.45%
Ga	19	19	-13.68%	19.2	2.30%	19.5	2.01%
Gd	6.17	7.12	-0.39%	4.2	-31.09%	3.08	-50.38%
Ge	1.5	0.6	-65.47%	1.2	-19.01%	1.1	-27.11%
Hf	7.6	8.7	-1.19%	7.5	-0.10%	7.4	-3.22%
Hg	0.05	0.05	-13.68%	0.2	304.94%	0.2	297.58%
Ho	1.31	1.62	6.74%	0.84	-35.09%	0.61	-53.72%
La	50	54	-6.78%	38	-23.06%	35	-30.42%
Lu	0.4	0.6	29.47%	0.4	1.23%	0.4	-0.61%
Mo	2.3	3.1	16.34%	10.6	366.56%	6	159.29%
Nb	10	15	29.47%	10	1.23%	10	-0.61%
Nd	41	45.2	-4.84%	29.1	-28.15%	22.8	-44.73%
Ni	10	13	12.21%	15	51.85%	19	88.85%
Pb	17.2	10.2	-48.81%	12.7	-25.25%	7.42	-57.12%
Pr	12.1	13.2	-5.84%	8.85	-25.96%	7.17	-41.10%
Rb	176	462	126.58%	232	33.45%	286	61.52%
Sb	5	4	-30.95%	6	21.48%	6	19.27%
Sc	11	13	2.01%	15	38.05%	18	62.64%
Se	0.5	0.5	-13.68%	0.5	1.23%	0.5	-0.61%
Sm	7.29	8.44	-0.07%	5.11	-29.04%	3.84	-47.64%
Sn	2.3	0.05	-98.12%	15.5	582.23%	17.1	638.97%
Sr	231	159	-40.59%	106	-53.55%	105	-54.82%
Ta	1.61	2.56	37.25%	1.47	-7.57%	1.56	-3.69%
Tb	1	1.13	-2.46%	0.65	-34.20%	0.46	-54.28%
Te	0.1	11.4	9740.00%	0.05	-49.38%	0.3	198.18%
Th	21.8	26.3	4.13%	17.5	-18.73%	17.3	-21.12%
Tl	0.005	0.005	-13.68%	0.005	1.23%	0.005	-0.61%
Tm	0.51	0.62	4.93%	0.36	-28.54%	0.31	-39.58%
U	6.69	7.42	-4.27%	6.38	-3.46%	6.32	-6.10%
V	57	68	2.97%	71	26.10%	81	41.24%
W	6	7	0.70%	40	574.90%	32	430.10%
Y	29.7	38.2	11.02%	21.4	-27.06%	15.9	-46.79%
Yb	2.8	3.76	15.91%	2.4	-13.23%	2.04	-27.58%
Zn	42	26	-46.57%	9	-78.31%	0.5	-98.82%
Zr	257	338	13.52%	260	2.42%	258	-0.22%
Al ₂ O ₃ (wt.%)	16.4	19	0.00%	16.2	0.00%	16.5	0.00%
CaO	3.44	1.35	-66.13%	0.68	-79.99%	0.53	-84.69%
Fe ₂ O ₃	5.61	4.57	-29.69%	6.03	8.81%	5.27	-6.63%
MgO	1.45	1.84	9.53%	1.13	-21.11%	1.24	-15.00%
MnO	0.05	0.06	3.58%	0.02	-59.51%	0.005	-90.06%
P ₂ O ₅	0.22	0.27	5.93%	0.22	1.23%	0.23	3.91%
K ₂ O	4.86	9.46	68.01%	8.28	72.47%	9.53	94.90%
Na ₂ O	2.94	2.1	-38.35%	1.72	-40.77%	1.07	-63.83%
TiO ₂	0.84	0.98	0.70%	0.78	-6.00%	0.82	-2.97%
SiO ₂	62.8	53.8	-26.05%	64.4	3.81%	63.3	0.19%
LOI	1.4	2.2	35.64%	0.9	-34.92%	1.8	27.79%

Mass change

-13.68%

1.23%

-0.61%

Elements	Least Altered Dacite			97258			98098		
	Least altered C _i ⁰	Altered C _i	% Gain or Loss ΔC _i %	Altered C _i	% Gain or Loss ΔC _i %		Altered C _i	% Gain or Loss ΔC _i %	
Au (ppb)	1	1	22.39%	1	0.00%		1	0.00%	
Ag (ppm)	0.2	0.05	-69.40%	0.2	0.00%		0.2	0.00%	
As	5.5	22.5	400.68%	3.1	-43.64%		3.1	-43.64%	
Ba	867	593	-16.29%	1450	67.24%		1450	67.24%	
Be	2.6	0.8	-62.34%	1.8	-30.77%		1.8	-30.77%	
Bi	0.1	0.4	389.55%	0.05	-50.00%		0.05	-50.00%	
Cd	0.2	0.1	-38.81%	0.2	0.00%		0.2	0.00%	
Ce	106	17	-80.37%	107	0.94%		107	0.94%	
Co	10.1	91.6	1009.97%	8.8	-12.87%		8.8	-12.87%	
Cr	73	138	131.36%	123	68.49%		123	68.49%	
Cs	2.4	0.6	-69.40%	2	-16.67%		2	-16.67%	
Cu	18.2	54	263.13%	1.3	-92.86%		1.3	-92.86%	
Dy	5.47	3.2	-28.40%	4.31	-21.21%		4.31	-21.21%	
Er	2.66	1.66	-23.62%	2.44	-8.27%		2.44	-8.27%	
Eu	1.76	0.77	-46.46%	1.88	6.82%		1.88	6.82%	
Ga	19	28.7	84.87%	15.2	-20.00%		15.2	-20.00%	
Gd	6.17	2.69	-46.64%	5.18	-16.05%		5.18	-16.05%	
Ge	1.5	1.4	14.23%	1.1	-26.67%		1.1	-26.67%	
Hf	7.6	6.2	-0.16%	5.5	-27.63%		5.5	-27.63%	
Hg	0.05	19.1	46652.24%	0.2	300.00%		0.2	300.00%	
Ho	1.31	0.75	-29.93%	1.09	-16.79%		1.09	-16.79%	
La	50	8	-80.42%	52	4.00%		52	4.00%	
Lu	0.4	0.3	-8.21%	0.4	0.00%		0.4	0.00%	
Mo	2.3	10.8	474.69%	1.1	-52.17%		1.1	-52.17%	
Nb	10	7	-14.33%	10	0.00%		10	0.00%	
Nd	41	9.5	-71.64%	40.5	-1.22%		40.5	-1.22%	
Ni	10	31	279.40%	23	130.00%		23	130.00%	
Pb	17.2	4.39	-68.76%	5.58	-67.56%		5.58	-67.56%	
Pr	12.1	2.38	-75.93%	12.2	0.83%		12.2	0.83%	
Rb	176	103	-28.38%	304	72.73%		304	72.73%	
Sb	5	4	-2.09%	6	20.00%		6	20.00%	
Sc	11	11	22.39%	22	100.00%		22	100.00%	
Se	0.5	0.5	22.39%	0.5	0.00%		0.5	0.00%	
Sm	7.29	2.46	-58.70%	7.22	-0.96%		7.22	-0.96%	
Sn	2.3	23.1	1129.20%	4.3	86.96%		4.3	86.96%	
Sr	231	82	-56.55%	82	-64.50%		82	-64.50%	
Ta	1.61	1.24	-5.74%	1.94	20.50%		1.94	20.50%	
Tb	1	0.5	-38.81%	0.76	-24.00%		0.76	-24.00%	
Te	0.1	0.4	389.55%	0.05	-50.00%		0.05	-50.00%	
Th	21.8	18.3	2.74%	24	10.09%		24	10.09%	
Tl	0.005	0.005	22.39%	0.005	0.00%		0.005	0.00%	
Tm	0.51	0.3	-28.01%	0.47	-7.84%		0.47	-7.84%	
U	6.69	9.58	75.26%	8.66	29.45%		8.66	29.45%	
V	57	69	48.15%	150	163.16%		150	163.16%	
W	6	2720	55382.59%	23	283.33%		23	283.33%	
Y	29.7	18	-25.83%	25.2	-15.15%		25.2	-15.15%	
Yb	2.8	1.86	-18.70%	2.63	-6.07%		2.63	-6.07%	
Zn	42	1	-97.09%	40	-4.76%		40	-4.76%	
Zr	257	213	1.43%	183	-28.79%		183	-28.79%	
Al ₂ O ₃ (wt.%)	16.4	13.4	0.00%	16.4	0.00%		16.4	0.00%	
CaO	3.44	1.01	-64.07%	1.56	-54.65%		1.56	-54.65%	
Fe ₂ O ₃	5.61	15.6	240.33%	7.2	28.34%		7.2	28.34%	
MgO	1.45	2.15	81.47%	2.39	64.83%		2.39	64.83%	
MnO	0.05	0.06	46.87%	0.07	40.00%		0.07	40.00%	
P ₂ O ₅	0.22	0.14	-22.12%	0.21	-4.55%		0.21	-4.55%	
K ₂ O	4.86	3.7	-6.82%	7.23	48.77%		7.23	48.77%	
Na ₂ O	2.94	1.01	-57.96%	2.11	-28.23%		2.11	-28.23%	
TiO ₂	0.84	0.68	-0.92%	0.85	1.19%		0.85	1.19%	
SiO ₂	62.8	59.9	16.74%	58.7	-6.53%		58.7	-6.53%	
LOI	1.4	2	74.84%	3.2	128.57%		3.2	128.57%	

Mass change

22.39%

0.00%

Average Least Altered Rhyodacite			96232		96233		96239	
Elements	Least altered C _i ⁰	Altered C _i	% Gain or Loss ΔC _i %	Altered C _i	% Gain or Loss ΔC _i %	Altered C _i	% Gain or Loss ΔC _i %	
Au (ppb)	4	46	1262.96%	3	-20.53%	6	55.84%	
Ag (ppm)	0.35	0.1	-66.14%	0.05	-84.86%	0.9	167.16%	
As	6.67	104	1747.96%	8	27.09%	19.4	202.19%	
Ba	979	2420	192.97%	2060	122.96%	3000	218.37%	
Be	2.3	0.7	-63.93%	1.6	-26.29%	1.1	-50.31%	
Bi	0.43	2.3	533.94%	0.2	-50.72%	0.6	44.97%	
Cd	0.2	0.2	18.52%	0.3	58.94%	0.2	3.90%	
Ce	93	19	-75.79%	90	2.54%	40	-55.31%	
Co	6.2	47.9	815.65%	12.6	115.34%	7.7	29.03%	
Cr	99.7	111	31.95%	171	81.74%	164	70.90%	
Cs	2.1	1.4	-20.99%	1.3	-34.41%	1.4	-30.74%	
Cu	18.23	68.3	344.04%	7.3	-57.57%	15.8	-9.95%	
Dy	3.99	1.91	-43.27%	3.29	-12.63%	1.83	-52.35%	
Er	2.12	1.28	-28.33%	1.87	-6.39%	0.95	-53.37%	
Eu	1.35	1.19	4.47%	1.72	35.00%	1.82	40.07%	
Ga	17.73	9.7	-35.17%	17.6	5.16%	13.5	-20.91%	
Gd	4.53	1.7	-55.49%	4.46	4.40%	2.34	-46.29%	
Ge	1.33	1	-11.11%	1.2	-4.64%	1.2	-6.49%	
Hf	5.60	6.1	29.10%	6.3	19.21%	5.3	-1.67%	
Hg	0.23	1.3	560.32%	0.3	36.23%	0.7	211.69%	
Ho	0.95	0.52	-35.13%	0.82	-8.54%	0.44	-51.88%	
La	49	11	-73.39%	51	10.29%	22	-53.35%	
Lu	0.37	0.3	-3.03%	0.3	-13.31%	0.2	-43.33%	
Mo	1.9	0.8	-50.10%	2.8	56.15%	1.3	-28.91%	
Nb	9.7	9	9.97%	7	-23.53%	8	-14.31%	
Nd	33.17	7.5	-73.20%	32.9	5.11%	15	-53.01%	
Ni	19	5	-68.81%	4	-77.69%	3	-83.60%	
Pb	21.13	9.27	-48.00%	8.99	-54.92%	12.2	-40.01%	
Pr	10.14	2.26	-73.58%	10.4	8.68%	4.38	-55.12%	
Rb	194	345	110.77%	282	54.02%	366	96.01%	
Sb	1.3	9	720.51%	9	633.57%	11	779.12%	
Sc	7	3	-49.21%	11	66.51%	7	3.90%	
Se	0.67	0.5	-11.55%	2	216.30%	1	55.07%	
Sm	5.26	1.51	-65.98%	5.31	6.97%	2.66	-47.46%	
Sn	1.28	9.5	779.63%	7.2	496.03%	10.8	776.62%	
Sr	206	72	-58.58%	87	-55.25%	67	-66.21%	
Ta	1.6	1.74	28.89%	1.3	-13.91%	1.34	-12.99%	
Tb	0.7	0.3	-49.21%	0.66	-0.09%	0.35	-48.05%	
Te	0.05	0.4	848.15%	0.05	5.96%	0.05	3.90%	
Th	22.03	25.9	39.34%	20.3	-2.36%	17.4	-17.94%	
Tl	0.005	0.005	18.52%	0.005	5.96%	0.005	3.90%	
Tm	0.39	0.25	-24.03%	0.32	-13.06%	0.16	-57.38%	
U	5.98	5.75	13.96%	16.7	195.91%	3.81	-33.81%	
V	38.3	20	-38.11%	83	129.63%	80	117.02%	
W	24	126	522.22%	150	562.25%	194	739.83%	
Y	23.1	13.6	-30.22%	21.2	-2.76%	11	-50.53%	
Yb	2.33	1.71	-13.02%	1.88	-14.50%	1	-55.41%	
Zn	46	2	-94.85%	0.5	-98.85%	6	-86.45%	
Zr	195	172	4.54%	222	20.63%	188	0.17%	
Al ₂ O ₃ (wt.%)	16	13.5	0.00%	15.1	0.00%	15.4	0.00%	
CaO	2.49	0.11	-94.76%	0.16	-93.19%	0.22	-90.82%	
Fe ₂ O ₃	3.51	4.95	67.14%	7.11	114.64%	4.25	25.80%	
MgO	1.15	0.22	-77.33%	0.29	-73.28%	0.25	-77.41%	
MnO	0.07	0.005	-91.53%	0.005	-92.43%	0.01	-85.16%	
P ₂ O ₅	0.07	0.04	-32.28%	0.1	51.37%	0.12	78.11%	
K ₂ O	5.11	11.7	171.36%	11.4	136.39%	12.8	160.25%	
Na ₂ O	3	0.19	-92.49%	0.99	-65.03%	0.22	-92.38%	
TiO ₂	0.43	0.32	-11.80%	0.62	52.78%	0.61	47.39%	
SiO ₂	66.7	66.6	18.34%	63.3	0.56%	65.1	1.40%	
LOI	1.5	2.3	81.73%	0.7	-50.55%	0.8	-44.59%	

Mass change

18.52%

5.96%

3.90%

Average Least Altered Rhyodacite			96479		97080		97123			
Elements	Least altered C _i ⁰		Altered C _i	% Gain or Loss ΔC _i %		Altered C _i	% Gain or Loss ΔC _i %		Altered C _i	% Gain or Loss ΔC _i %
Au (ppb)	4		1	-72.41%		1	-74.84%		1	-69.70%
Ag (ppm)	0.35		0.6	89.16%		0.3	-13.75%		0.05	-82.68%
As	6.67		8.7	43.93%		2.5	-62.28%		2.4	-56.39%
Ba	979		2800	215.59%		978	0.53%		1130	39.91%
Be	2.3		1.4	-32.83%		3.6	57.51%		1.2	-36.76%
Bi	0.43		0.6	53.97%		0.4	-6.39%		0.2	-43.62%
Cd	0.2		0.1	-44.83%		0.1	-49.69%		0.05	-69.70%
Ce	93		119	41.19%		89	-3.70%		63	-17.89%
Co	6.2		5.3	-5.67%		6.4	3.88%		4.1	-19.84%
Cr	99.7		152	68.23%		92	-7.14%		157	90.88%
Cs	2.1		1.3	-31.69%		1.6	-23.33%		0.5	-71.14%
Cu	18.23		25	51.32%		67.4	272.05%		18.9	25.67%
Dy	3.99		3.36	-7.08%		3.92	-1.14%		3.46	5.11%
Er	2.12		1.88	-1.99%		2.12	0.79%		1.94	11.10%
Eu	1.35		1.98	61.84%		1.3	-3.10%		0.83	-25.48%
Ga	17.73		12.5	-22.22%		15.6	-11.48%		13.5	-7.72%
Gd	4.53		4.74	15.55%		4.42	-1.74%		3.12	-16.45%
Ge	1.33		1.2	-0.69%		1.2	-9.43%		1.2	9.09%
Hf	5.60		5.5	8.37%		6.6	18.60%		4.1	-11.26%
Hg	0.23		0.6	183.74%		0.05	-78.44%		0.05	-74.03%
Ho	0.95		0.8	-7.08%		0.91	-3.61%		0.79	0.80%
La	49		71	59.89%		45	-7.59%		32	-20.84%
Lu	0.37		0.4	20.38%		0.4	9.78%		0.3	-0.83%
Mo	1.9		2.4	39.38%		1.8	-4.67%		1.5	-4.31%
Nb	9.7		10	13.76%		10	3.74%		0.5	-93.75%
Nd	33.17		41.1	36.74%		32.4	-1.70%		20.2	-26.18%
Ni	19		4	-76.77%		6	-68.22%		6	-61.72%
Pb	21.13		10.5	-45.17%		16.8	-19.99%		5.81	-66.67%
Pr	10.14		12.9	40.38%		10.2	1.22%		6.4	-23.50%
Rb	194		389	121.26%		207	7.37%		176	9.97%
Sb	1.3		11	833.69%		2	54.81%		1	-6.76%
Sc	7		4	-36.95%		7	0.63%		3	-48.05%
Se	0.67		0.5	-17.65%		0.5	-24.90%		0.5	-9.54%
Sm	5.26		6.04	26.71%		5.45	4.26%		3.29	-24.18%
Sn	1.28		3.8	227.59%		3.5	175.16%		4.6	335.61%
Sr	206		123	-34.11%		166	-18.91%		27	-84.11%
Ta	1.6		1.61	11.03%		1.46	-8.18%		2.28	72.73%
Tb	0.7		0.68	7.19%		0.69	-0.81%		0.54	-6.49%
Te	0.05		0.05	10.34%		0.05	0.63%		0.05	21.21%
Th	22.03		24.3	21.71%		22.3	1.86%		32.9	81.02%
Tl	0.005		0.005	10.34%		0.005	0.63%		0.005	21.21%
Tm	0.39		0.34	-3.80%		0.38	-1.95%		0.33	2.56%
U	5.98		6.27	15.70%		6.82	14.76%		13.2	167.56%
V	38.3		29	-16.45%		35	-8.04%		13	-58.86%
W	24		68	212.64%		4	-83.23%		20	1.01%
Y	23.1		20.4	-2.55%		21.7	-5.47%		21.5	12.82%
Yb	2.33		2.24	6.08%		2.33	0.63%		2.08	8.21%
Zn	46		0.5	-98.80%		94	105.63%		0.5	-98.68%
Zr	195		178	0.73%		200	3.21%		109	-32.25%
Al ₂ O ₃ (wt.%)	16		14.5	0.00%		15.9	0.00%		13.2	0.00%
CaO	2.49		0.07	-96.90%		1.81	-26.85%		0.18	-91.24%
Fe ₂ O ₃	3.51		4	25.75%		3.8	8.94%		2.14	-26.10%
MgO	1.15		0.3	-71.21%		1.2	5.00%		0.26	-72.60%
MnO	0.07		0.005	-92.12%		0.11	58.13%		0.01	-82.68%
P ₂ O ₅	0.07		0.03	-52.71%		0.07	0.63%		0.005	-91.34%
K ₂ O	5.11		11.5	148.33%		5.15	1.42%		6.58	56.08%
Na ₂ O	3		0.18	-93.38%		2.86	-4.07%		3.23	30.51%
TiO ₂	0.43		0.35	-10.18%		0.43	0.63%		0.19	-46.44%
SiO ₂	66.7		68.2	12.83%		66.2	-0.13%		73.5	33.57%
LOI	1.5		0.6	-55.86%		1.5	0.63%		0.4	-67.68%

Mass change

10.34%

0.63%

21.21%

Average Least Altered Rhyodacite			97124		97129		97138	
Elements	Least altered C _i ⁰	Altered C _i	% Gain or Loss ΔC _i %	Altered C _i	% Gain or Loss ΔC _i %	Altered C _i	% Gain or Loss ΔC _i %	
Au (ppb)	4	3	-20.00%	1	-72.03%	16	357.14%	
Ag (ppm)	0.35	0.05	-84.76%	0.05	-84.02%	0.9	193.88%	
As	6.67	11.3	80.71%	8.1	35.88%	24.9	326.64%	
Ba	979	679	-26.02%	1450	65.72%	1030	20.24%	
Be	2.3	1.3	-39.71%	1.1	-46.49%	2.3	14.29%	
Bi	0.43	1.6	296.90%	0.1	-73.98%	1.7	351.83%	
Cd	0.2	0.1	-46.67%	0.05	-72.03%	0.05	-71.43%	
Ce	93	226	159.21%	111	33.54%	66	-18.89%	
Co	6.2	29.6	409.25%	8.6	55.20%	48	784.79%	
Cr	99.7	195	108.63%	145	62.73%	166	90.29%	
Cs	2.1	0.4	-79.68%	0.4	-78.69%	0.4	-78.23%	
Cu	18.23	113	561.18%	60.9	273.78%	1290	7987.14%	
Dy	3.99	8.93	138.73%	3.15	-11.67%	3.68	5.41%	
Er	2.12	4.37	120.22%	1.82	-3.79%	1.91	3.13%	
Eu	1.35	2.39	88.84%	1.21	0.28%	0.8	-32.28%	
Ga	17.73	18.6	11.88%	12.6	-20.50%	15.2	-2.04%	
Gd	4.53	12.8	201.62%	3.85	-4.84%	3.4	-14.16%	
Ge	1.33	2.1	68.00%	1	-16.08%	1.2	2.86%	
Hf	5.60	5.5	4.76%	4.2	-16.08%	4.6	-6.12%	
Hg	0.23	0.05	-77.14%	0.1	-52.05%	2	879.59%	
Ho	0.95	1.9	113.33%	0.74	-12.85%	0.84	1.05%	
La	49	119	159.05%	61	39.29%	36	-16.03%	
Lu	0.37	0.7	103.64%	0.3	-8.46%	0.3	-6.49%	
Mo	1.9	6.2	248.07%	4.9	188.55%	2.4	44.36%	
Nb	9.7	0.5	-94.50%	0.5	-94.23%	0.5	-94.11%	
Nd	33.17	95.2	206.17%	35.4	19.42%	22.7	-21.78%	
Ni	19	11	-38.25%	6	-64.67%	27	62.41%	
Pb	21.13	11	-44.47%	6.12	-67.59%	3.22	-82.58%	
Pr	10.14	27.2	186.13%	11.5	26.89%	6.99	-21.22%	
Rb	194	89.8	-50.63%	214	23.42%	186	9.57%	
Sb	1.3	6	392.31%	2	72.14%	1	-12.09%	
Sc	7	9	37.14%	5	-20.08%	5	-18.37%	
Se	0.67	1	59.20%	0.5	-16.50%	0.5	-14.71%	
Sm	5.26	17	244.74%	4.96	5.51%	3.59	-22.00%	
Sn	1.28	8.8	633.33%	1.6	39.86%	5.3	373.21%	
Sr	206	191	-1.10%	42	-77.19%	28	-84.47%	
Ta	1.6	1.56	4.00%	1.76	23.08%	1.75	25.00%	
Tb	0.7	1.73	163.62%	0.57	-8.89%	0.58	-5.31%	
Te	0.05	0.3	540.00%	0.05	11.89%	0.4	814.29%	
Th	22.03	20	-3.16%	25.6	30.02%	25.4	31.77%	
Tl	0.005	0.005	6.67%	0.005	11.89%	0.005	14.29%	
Tm	0.39	0.78	113.33%	0.33	-5.33%	0.34	-0.37%	
U	5.98	11.6	106.91%	10.2	90.85%	10.7	104.49%	
V	38.3	47	30.90%	28	-18.20%	37	10.41%	
W	24	11	-51.11%	51	137.76%	560	2566.67%	
Y	23.1	50	130.88%	19.8	-4.10%	20.4	0.93%	
Yb	2.33	4.85	122.03%	2.2	5.65%	2.26	10.85%	
Zn	46	26	-39.71%	6	-85.41%	2	-95.03%	
Zr	195	178	-2.63%	122	-30.00%	139	-18.53%	
Al ₂ O ₃ (wt.%)	16	15	0.00%	14.3	0.00%	14	0.00%	
CaO	2.49	6.68	186.16%	0.41	-81.58%	0.39	-82.10%	
Fe ₂ O ₃	3.51	5.82	76.87%	2.76	-12.02%	5.6	82.34%	
MgO	1.15	0.39	-63.83%	0.38	-63.03%	0.37	-63.23%	
MnO	0.07	0.1	52.38%	0.02	-68.03%	0.01	-83.67%	
P ₂ O ₅	0.07	0.1	52.38%	0.03	-52.05%	0.05	-18.37%	
K ₂ O	5.11	3.45	-27.98%	8.5	86.12%	6.82	52.53%	
Na ₂ O	3	2.72	-3.29%	2.6	-3.03%	3.59	36.76%	
TiO ₂	0.43	0.61	51.32%	0.29	-24.54%	0.3	-20.27%	
SiO ₂	66.7	63.9	2.19%	70	17.42%	68	16.51%	
LOI	1.5	1.4	-0.44%	0.5	-62.70%	0.7	-46.67%	

Mass change

6.67%

11.89%

14.29%

Average Least Altered Rhyodacite		97143	
Elements	Least altered C_i^0	Altered C_i	% Gain or Loss $\Delta C_i\%$
Au (ppb)	4	11	205.56%
Ag (ppm)	0.35	0.05	-84.13%
As	6.67	34.2	469.72%
Ba	979	1070	21.44%
Be	2.3	1.8	-13.04%
Bi	0.43	0.3	-22.48%
Cd	0.2	0.1	-44.44%
Ce	93	118	40.98%
Co	6.2	20.2	262.01%
Cr	99.7	163	81.66%
Cs	2.1	0.4	-78.84%
Cu	18.23	106	546.07%
Dy	3.99	3.37	-6.15%
Er	2.12	2.01	5.51%
Eu	1.35	1	-17.70%
Ga	17.73	15	-6.02%
Gd	4.53	3.61	-11.39%
Ge	1.33	1.2	0.00%
Hf	5.60	4.7	-6.75%
Hg	0.23	0.05	-76.19%
Ho	0.95	0.83	-2.92%
La	49	65	47.39%
Lu	0.37	0.3	-9.09%
Mo	1.9	6.6	285.96%
Nb	9.7	0.5	-94.27%
Nd	33.17	37.5	25.63%
Ni	19	11	-35.67%
Pb	21.13	5.06	-73.39%
Pr	10.14	12.3	34.78%
Rb	194	146	-16.38%
Sb	1.3	3	156.41%
Sc	7	4	-36.51%
Se	0.67	0.5	-17.08%
Sm	5.26	4.94	4.35%
Sn	1.28	0.05	-95.66%
Sr	206	25	-86.52%
Ta	1.6	1.84	27.78%
Tb	0.7	0.57	-9.52%
Te	0.05	0.1	122.22%
Th	22.03	27	36.18%
Tl	0.005	0.005	11.11%
Tm	0.39	0.34	-3.13%
U	5.98	9.48	76.14%
V	38.3	31	-10.07%
W	24	8	-62.96%
Y	23.1	20.9	0.53%
Yb	2.33	2.12	1.10%
Zn	46	0.5	-98.79%
Zr	195	143	-18.52%
Al ₂ O ₃ (wt.%)	16	14.4	0.00%
CaO	2.49	0.42	-81.26%
Fe ₂ O ₃	3.51	3.62	14.59%
MgO	1.15	0.25	-75.85%
MnO	0.07	0.01	-84.13%
P ₂ O ₅	0.07	0.04	-36.51%
K ₂ O	5.11	5.95	29.38%
Na ₂ O	3	4.52	67.41%
TiO ₂	0.43	0.31	-19.90%
SiO ₂	66.7	69.7	16.11%
LOI	1.5	0.4	-70.37%

Mass change

11.11%

Abbreviations: C_i^0 = concentration of compound/element I in least altered rock, C_i = concentration of

Curriculum Vitae

Name:

Mark Hamilton

Post-secondary Education and Degrees:

Brandon University
Brandon, Manitoba, Canada
2016 M.Sc., Environment and Life Science

Brandon University
Brandon, Manitoba, Canada
2014 B.Sc., Geology

University of Manitoba
Winnipeg, Manitoba, Canada
2010 B.A. Physical Geography

Related Work Experience:

Laboratory Teacher & Teaching Assistant
Brandon University
2013 - 2016

Microanalytical Laboratory Assistant
Brandon University
2014 – 2015

Geologist Assistant
BFR Copper & Gold
2013 (summer program)

Geologist Assistant
Manitoba Geological Survey
2012 (summer program)